SCUOLA DI DOTTORATO
UNIVERSITA' DEGLI STUDI DI MILANO-BICOCCA

Dipartimento di
Fisica

Dottorato di ricerca in Fisica, Ciclo XXIX
Curriculum in fisica subnucleare

Search for double-beta decay of ^{130}Te to the excited states of ^{130}Xe in CUORE-0

Pozzi Stefano
Matricola 720057

Tutore: Prof.ssa Maura Pavan

Coordinatore: Prof.ssa Marta Calvi

Anno accademico 2016/17

CONTENTS

Introduction

CUORE is a ton-scale bolometric detector whose main scientific goal is the search for neutrinoless double-beta decay ($0\nu\beta\beta$) in ^{130}Te. During my PhD I've worked on the CUORE-0 experiment, a small scale version of CUORE consisting of 52 TeO_2 crystals arranged in a single tower. CUORE-0 was operated from 2013 to 2015 in the Gran Sasso National Laboratories (LNGS), in central Italy. In this time period I've contributed to the construction of CUORE and the development of procedures that were included in the official CUORE-0 analysis, as well as the optimization of the Monte Carlo tools used by the collaboration.

The quality of the data produced by CUORE-0 makes the search for rare processes other than $0\nu\beta\beta$ possible. The main focus of my work is the search for double beta decay of ^{130}Te on the excited states of ^{130}Xe. This process is characterized by the emission of two electrons, followed by a γ cascade. Due to the granularity of the CUORE-0 tower this decay likely involves more than one crystal, giving it a very peculiar signature. This thesis describes in detail all the analysis techniques required to properly detect this signature, using both real and simulated data.

The first chapter of this work is dedicated to the description of neutrinoless double-beta decay and of its importance in the search for physics beyond the Standard Model. Chapters 2 and 3 fully characterize the CUORE-0 experiment, including the experimental technique, the structure of the detector and the analysis procedures used to extract useful information from recorded events. Parts of the data analysis procedure that are of particular interest for the decay under consideration are examined in depth: the pulse shape analysis algorithm, which I've developed to automatically reject non-physical signals, is described in chapter 4; chapter 5 illustrates how CUORE-0 handles simultaneous events on multiple crystals.

The Monte Carlo software used for the production of simulated data are described in chapter 6. This chapter focuses on `MCuoreZ`, the `Geant4`-based MC software in use by the collaboration, and `g4cuore`, a code that I've written to include characteristics specific to detector behaviour and analysis procedures in the simulated data. In chapter 7 I illustrate the reconstruction, using simulations, of measurements performed in CUORE-0 using radioactive sources, a powerful tool for MC benchmarking. Chapter 8 contains a full description of the CUORE-0 background model, one of the most successful practical applications of the CUORE-0 simulations. The background model leads to a complete determination of the location and activity of the sources of radioactive background which have a significant impact on CUORE-0 data.

Finally, chapter 9 contains the main analysis of this work. In particular, I focus on the double-beta decay of ^{130}Te to the first 0^+ excited state of ^{130}Xe, both with and without the

emission of neutrinos. The two processes are studied separately, as the different signatures they produce require a dedicated treatment. As a form of blinding, all the optimization procedure for the data selection is not performed on real spectra, but on simulated data coming from the background model. The results of this analysis are combined with the previous ones from Cuoricino, which set the most stringent limit on these decays half-life in year 2012. The final outcome of this work will result in a publication by the CUORE collaboration.

CHAPTER

1

DOUBLE-BETA DECAY

Double-beta decay is a rare nuclear process in which two nucleons simultaneously decay and emit two electrons. The allowed Standard Model version of this process, which involves the emission of two neutrinos, is the slowest process ever directly observed. Neutrinoless double-beta decay, the same process but without the emission of neutrinos, has not been observed yet and is not allowed by the Standard Model. Its observation, however, would have profound implications for physics beyond the Standard Model, including lepton number violation, the neutrino mass hierarchy and the nature of neutrinos themselves. fIn this chapter I'll describe the first signs of neutrino physics beyond the Standard Model, specifically regarding their mass. Then, I'll describe how the observation of neutrinoless double-beta decay could solve some of the open questions regarding neutrinos.

1.1 Neutrino masses

The original formulation of the Standard Model includes three massless neutrinos, ν_e, ν_μ and ν_τ, which, together with their anti-particles $\bar{\nu_e}$, $\bar{\nu_\mu}$ and $\bar{\nu_\tau}$, are always associated to their corresponding charged leptons e, μ and τ.

The first hints of the incompleteness of this picture came in the late 1960s with R. Davis' Homestake experiment [1]. The measured flux of electron neutrinos coming from the sun was ~ 3 times lower than expected from Bahcall's standard solar model [2], giving rise to the so-called *solar neutrino problem*. Either the experiment had some unaccounted

for systematic error, the solar model was incorrect or some new physical process had been discovered; the latter explanation was the least popular at the time. Further measurements by other experiments (SAGE [3], Gallex-GNO [4], Kamiokande and Super-Kamiokande [5]) confirmed the deficit of solar neutrinos; at the same time, other solar measurements supported the solar model [6][7].

The solution to the solar neutrino problem came in 2002 from the SNO experiment [8]: the missing neutrinos didn't disappear, but were *oscillating* to a different flavour, becoming undetectable by experiments sensitive to ν_e.

1.1.1 Neutrino oscillations

The non-conservation of neutrino flavour observed in SNO is explained by neutrino oscillations which, however, cannot exist in the framework of the Standard Model. This process, in fact, can only occur for massive neutrinos: it arises from the fact that neutrino flavour eigenstates, $|\nu_f\rangle$, do not coincide with mass eigenstates, $|\nu_k\rangle$. Flavour and mass eigenstates are related by the Pontecorvo-Maki-Nakagawa-Sakata (PMNS) neutrino mixing matrix U_{fk}:

$$|\nu_f\rangle = \sum_{k=1}^{3} U_{fk}^{*} \, |\nu_k\rangle \,, \qquad f = (e, \mu, \tau), \quad k = (1, 2, 3). \tag{1.1}$$

A common parametrization for the PMNS matrix is

$$\begin{aligned} U = &\begin{bmatrix} 1 & 0 & 0 \\ 0 & c_{23} & s_{23} \\ 0 & -s_{23} & c_{23} \end{bmatrix} \times \begin{bmatrix} c_{13} & 0 & s_{13}e^{-i\delta} \\ 0 & 1 & 0 \\ -s_{13}e^{-i\delta} & 0 & c_{13} \end{bmatrix} \times \begin{bmatrix} c_{12} & s_{12} & 0 \\ -s_{12} & c_{12} & 0 \\ 0 & 0 & 1 \end{bmatrix} \\ &\times \begin{bmatrix} e^{i\phi_1/2} & 0 & 0 \\ 0 & e^{i\phi_2/2} & 0 \\ 0 & 0 & 1 \end{bmatrix}, \end{aligned} \tag{1.2}$$

where $c_{ij} = \cos\theta_{ij}$ and $s_{ij} = \sin\theta_{ij}$. The mixing angles θ_{ij} are related to the amplitude of the $i \to j$ flavour transition, the phase δ is non-zero only if neutrino oscillations violate CP conservation and $\phi_{1,2}$ are Majorana phases, which are meaningful only if neutrinos are Majorana particles (i.e. coincident with their antiparticles), but have no effect on oscillations.

A neutrino produced with a well-defined flavour f at time $t = 0$ will be composed, at

the generic time t, by a mixture of the three flavours:

$$|\nu_f(t)\rangle = \sum_{k=1}^{3} U_{fk}^* e^{iE_k t} |\nu_k\rangle = \sum_{k=1}^{3} \sum_{f'=e,\mu,\tau} U_{fk}^* U_{kf'} e^{iE_k t} |\nu_{f'}\rangle \,. \tag{1.3}$$

There is a certain probability of detecting a neutrino of flavour f' at time t, if it has been produced with flavour f at time $t = 0$. In a simple case with only two neutrinos flavours (ν_f, $\nu_{f'}$) and mass eigenstates (ν_1, ν_2), the mixing matrix can be expressed as a function of a single θ and no phases are present. In this approximations, the transition probability is

$$P(\nu_f \to \nu_{f'}; t) = \sin^2(2\theta) sin^2 \left(\frac{\Delta m^2}{4E} L \right). \tag{1.4}$$

In equation 1.4 $\Delta m^2 = m_2^2 - m_1^2$, the energy for relativistic neutrinos has been approximated as $E_i = \sqrt{p + m_i} \simeq p + \frac{m_i}{2E}$ and time has been replaced by spacial distance L. There are several things to note about equation 1.4. First, the transition probability vanishes for massless neutrinos, as $\Delta m^2 = 0$. The probability amplitude depends exclusively from θ, is maximal for $\theta = 45$ and zero for $\theta = 0$. The period of the oscillation depends on the squared mass difference and on the L/E factor, which places severe constraints for experiments looking for neutrino oscillations; ideally, a detector should be placed at a distance from the source that maximizes the oscillation probability, increasing the sensitivity.

Plenty of experiments looking to determine the parameters of the PMNS matrix have been conducted or are still ongoing. Depending on the chosen neutrino source (solar, cosmic, reactor neutrinos...) and on the detection technique, each experiment is sensitive only to a subset of parameters. A summary of the most recent results of these searches is given in table 1.1. The difference between normal and inverted ordering, as well as the reason why only two of the three squared mass differences are reported, are explained in the following section.

NuFIT 3.0 (2016)

	Normal Ordering (best fit)		Inverted Ordering ($\Delta\chi^2 = 0.83$)		Any Ordering
	bfp $\pm 1\sigma$	3σ range	bfp $\pm 1\sigma$	3σ range	3σ range
$\sin^2\theta_{12}$	$0.306^{+0.012}_{-0.012}$	$0.271 \to 0.345$	$0.306^{+0.012}_{-0.012}$	$0.271 \to 0.345$	$0.271 \to 0.345$
$\theta_{12}/^\circ$	$33.56^{+0.77}_{-0.75}$	$31.38 \to 35.99$	$33.56^{+0.77}_{-0.75}$	$31.38 \to 35.99$	$31.38 \to 35.99$
$\sin^2\theta_{23}$	$0.441^{+0.027}_{-0.021}$	$0.385 \to 0.635$	$0.587^{+0.020}_{-0.024}$	$0.393 \to 0.640$	$0.385 \to 0.638$
$\theta_{23}/^\circ$	$41.6^{+1.5}_{-1.2}$	$38.4 \to 52.8$	$50.0^{+1.1}_{-1.4}$	$38.8 \to 53.1$	$38.4 \to 53.0$
$\sin^2\theta_{13}$	$0.02166^{+0.00075}_{-0.00075}$	$0.01934 \to 0.02392$	$0.02179^{+0.00076}_{-0.00076}$	$0.01953 \to 0.02408$	$0.01934 \to 0.02397$
$\theta_{13}/^\circ$	$8.46^{+0.15}_{-0.15}$	$7.99 \to 8.90$	$8.49^{+0.15}_{-0.15}$	$8.03 \to 8.93$	$7.99 \to 8.91$
$\delta_{\rm CP}/^\circ$	261^{+51}_{-59}	$0 \to 360$	277^{+40}_{-46}	$145 \to 391$	$0 \to 360$
$\frac{\Delta m^2_{21}}{10^{-5}\ \text{eV}^2}$	$7.50^{+0.19}_{-0.17}$	$7.03 \to 8.09$	$7.50^{+0.19}_{-0.17}$	$7.03 \to 8.09$	$7.03 \to 8.09$
$\frac{\Delta m^2_{3\ell}}{10^{-3}\ \text{eV}^2}$	$+2.524^{+0.039}_{-0.040}$	$+2.407 \to +2.643$	$-2.514^{+0.038}_{-0.041}$	$-2.635 \to -2.399$	$\begin{bmatrix}+2.407 \to +2.643\\ -2.629 \to -2.405\end{bmatrix}$

Figure 1.1: Values for the parameters of the PMNS matrix, obtained by the combination of results from different experiments as of August 2016. Data taken from the NuFit website(`http://www.nu-fit.org/`)

1.1.2 Hierarchy, mass scale and nature of neutrinos

Oscillation experiments have given great contributions to neutrino physics, being able to measure most of the PMNS matrix parameters and to prove that neutrinos have mass. There are, however, some questions that remain unanswered. The sign of the mass splittings, necessary to determine the neutrino mass ordering, has not been measured yet, and the same can be said about the absolute scale of neutrino masses. Additionally, whether neutrinos are Dirac or Majorana particles is still unknown.

Mass hierarchy

Since three neutrino flavours are known, three differentx mass differences should be observed. Experimental searches are able to find only two mass splittings, a *small* one between the 1 and 2 mass eigenstates ($\Delta m^2_{12} \sim 7 \cdot 10^{-5}$ eV^2) and a *big* one between eigenstate 3 and either 1 or 2 ($\Delta m^2_{13} \simeq \Delta m^2_{23} \sim 2 \cdot 10^{-3}$ eV^2); the experimental sensitivity is not sufficient at the moment to tell apart Δm^2_{31} and Δm^2_{32}. Additionally, no experiment has managed to determine the sign of the mass differences or, in other words, the neutrino mass hierarchy. While the sign of Δm_{12} is negative ($m_{\nu 2} > m_{\nu 1}$), the sign of Δm_{13} is still an unknown and, based on its value, two possible scenarios might occur (figure 1.2):

- if $\Delta m_{13} > 0$, neutrino mass eigenstates are arranged according to the *normal* hier-

archy: $m_1 \simeq m_2 < m_3$;

- if $\Delta m_{13} < 0$, the *inverted* hierarchy holds: $m_3 < m_1 \simeq m_2$.

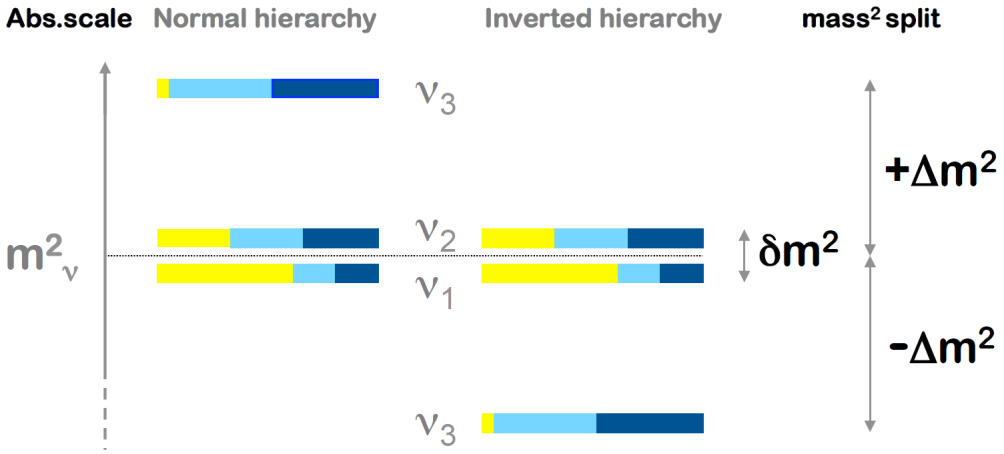

Figure 1.2: Schematic view of the normal and inverted hierarchy. The small mass splitting is denoted here as δm^2, while the big mass splitting is Δm^2.

Mass scale

Experiments sensitive to the mass splittings have no way to determine the absolute scale of the masses. A constraint on the sum of the three neutrino masses comes from cosmology, specifically from the observation of Cosmic Microwave Background anisotropies or the formation of large scale structures in our universe. The limits sets with these techniques range from a few eV to a few hundreds of meV, depending heavily on the chosen cosmological models.

Direct neutrino mass measurements are based on the analysis of particles emitted, together with neutrinos, in weak interactions. The most sensitive measurements are based on the determination of the endpoint of the continuous β spectrum after a β decay. These kind of measurements are sensitive to the *effective neutrino mass*, defined as

$$m_\beta^2 = \sum_{k=1}^{3} |U_{ek}|^2 m_k^2. \tag{1.5}$$

Currently, the best limit on m_β comes from the Mainz [9] and Troitsk [10] experiments, studying the β decay of tritium: $m_\beta < 2.1$ eV. Next generation experiments plan to constrain this value even more, improving it by around an order of magnitude (KATRIN [11], using tritium, or HOLMES [12], using ^{163}Ho).

Dirac and Majorana neutrinos

Oscillation experiments and direct searches for neutrino mass are not affected by the nature of neutrinos; their outcome is the same, regardless of whether neutrinos are Dirac or Majorana. The most promising approach to discriminate between these two possibilities is to search for neutrinoless double-beta decay ($0\nu\beta\beta$, or NDBD). As will be shown later, finding this decay would prove that neutrinos are Majorana particles. NDBD experiments are sensitive to the *effective Majorana mass*, $m_{\beta\beta}$:

$$m_{\beta\beta} = \left| \sum_{k=1}^{3} U_{ek}^2 m_k \right| = \left| \sum_{k=1}^{3} |U_{ek}|^2 e^{i\phi_k} m_j \right|. \tag{1.6}$$

In contrast to single beta decay, where m_β is a function of $|U_{ek}|^2$, $m_{\beta\beta}$ is sensitive to U_{ek}^2 and, therefore, to the Majorana phases ϕ_k. Since the U_{ek} are known from oscillation experiments, $m_{\beta\beta}$ can be written as a function of the two ϕ_k and on the mass of the lightest neutrinos.

The allowed values of $m_{\beta\beta}$, plotted as a function of the lightest neutrino mass, are shown in figure 1.3. The allowed values of $m_{\beta\beta}$ depend on the true hierarchy; observation of $0\nu\beta\beta$ would not only prove that neutrinos are Majorana particles, but also establish the mass hierarchy. This, however, is not true if $m_{lightest} \gtrsim 0.1eV$: in this region the allowed bands for the two hierarchies overlap, meaning that they cannot be distinguished by double beta decay alone.

Although the nature of neutrinos would be determined by an observation of $0\nu\beta\beta$, the same cannot be said in case the decay is not observed: this would not prove that neutrinos are Dirac particles. The vertical dip in the normal hierarchy plot means that, for some values of $m_{lightest}$, $m_{\beta\beta}$ vanishes, even if they are Majorana particles.

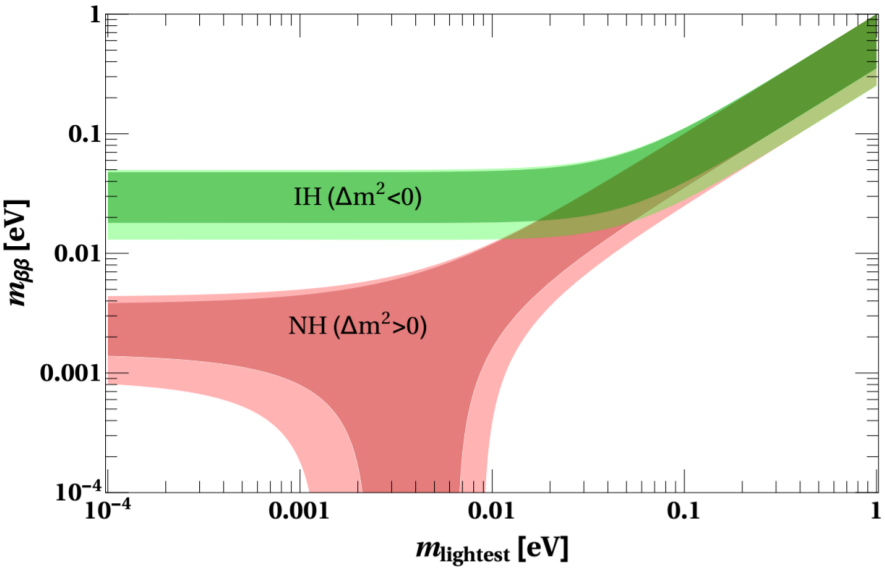

Figure 1.3: Allowed values for $m_{\beta\beta}$ as a function of the lightest neutrino mass, both in the normal and inverted hierarchy. The shaded areas correspond to 3σ regions due to error propagation of the uncertainties on oscillation parameters. Plot taken from [13]

1.2 Double-beta decay

Double beta decay is an extremely rare nuclear transition from a nucleus (A,Z) to its isobar (A,Z+2) with the emission of two electrons. Being a second order process, double beta decay has a slow decay rate and can be detected only on nuclei where the single β decay is forbidden; while it can happen on other nuclei, it is completely shadowed by single β decay. This happens when the parent nucleus (A,Z), is less bound than the daughter nucleus (A,Z+2), but more bound than the intermediate (A,Z+1). This condition is verified in nature for several nuclei with an even number of protons and neutrons (figure 1.4).

If accompanied by the emission of two neutrinos, double-beta decay is a process allowed by the standard model. As of now, it has been detected in 12 isotopes, with half-lives ranging from 10^{18} to 10^{24} years (table 1.1). This decay conserves lepton number, cannot discriminate between Dirac and Majorana neutrinos and does not depend significantly on neutrino masses.

There is also the possibility for double-beta decay to occur without the emission of neutrinos; since this process violates the conservation of lepton number, it is not allowed by the Standard Model. Neutrinoless double-beta decay can proceed through many different mechanisms [18] but, no matter which one holds, the observation of this decay would imply that neutrinos are Majorana particles [19]. This is shown in figure 1.5: the $0\nu\beta\beta$ decay

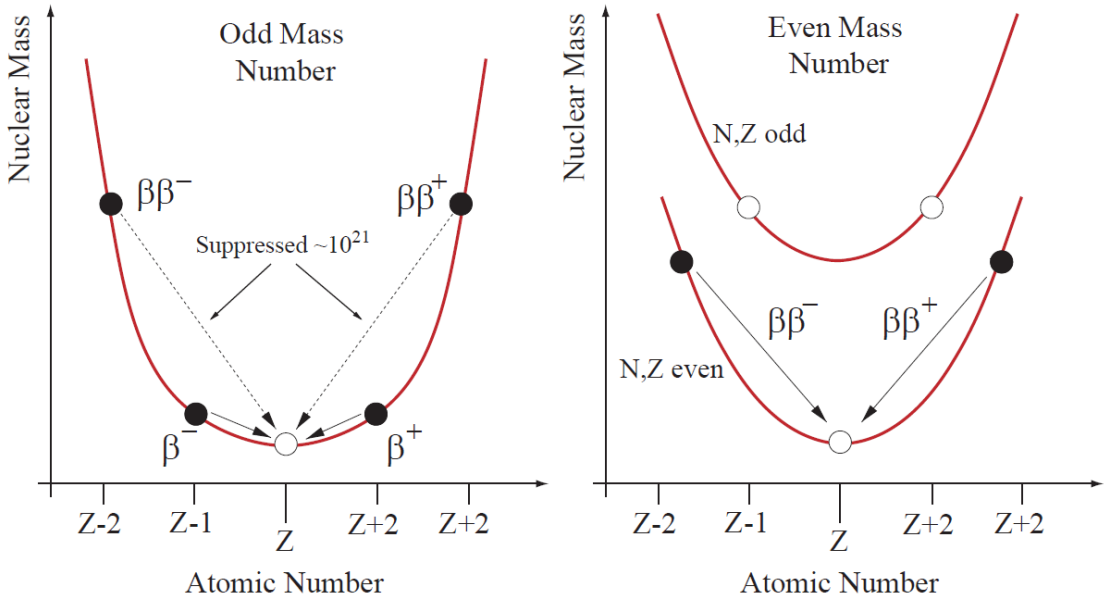

Figure 1.4: Nuclear mass as a function of the atomic number Z in the case of an isobar multiplet with A even (*left*) and A odd (*right*) (plot taken from [14]).

Nuclide	Half-life [10^{21} y]	Experiment
^{48}Ca	$0.064^{+0.007}_{-0.006} \pm ^{+0.012}_{-0.009}$	NEMO-3[15]
^{76}Ge	1.926 ± 0.094	GERDA[16]
^{78}Kr	$9.2^{+5.5}_{-2.6} \pm 1.3$	BAKSAN[16]
^{82}Se	$0.096 \pm 0.003 \pm 0.010$	NEMO-3[16]
^{96}Zr	$0.0235 \pm 0.0014 \pm 0.0016$	NEMO-3[16]
^{100}Mo	0.00693 ± 0.00004	NEMO-3[16]
^{116}Cd	$0.028 \pm 0.001 \pm 0.003$	NEMO-3[16]
^{128}Te	7200 ± 400	*geochemical*[16]
^{130}Te	$0.82 \pm 0.02 \pm 0.06$	CUORE-0[17]
^{136}Xe	$2.165 \pm 0.016 \pm 0.059$	EXO-200[16]
^{150}Nd	$0.00911^{0.00025}_{-0.00022} \pm 0.00063$	NEMO-3[16]
^{238}U	2.0 ± 0.6	*radiochemical*[16]

Table 1.1: List of the 12 isotopes for which $2\nu\beta\beta$ decay half-life has been measured.

can be inverted to produce a $\bar{\nu_e}$ going into a ν_e.

In the simplest case, $0\nu\beta\beta$ can be mediated by the exchange of a massive Majorana neutrino (figure 1.6). The rate of this process can be written as

$$[T_{1_2}^{0\nu}]^{-1} = G_{0\nu}|M_{0\nu}|^2\langle m_{\beta\beta}\rangle^2, \tag{1.7}$$

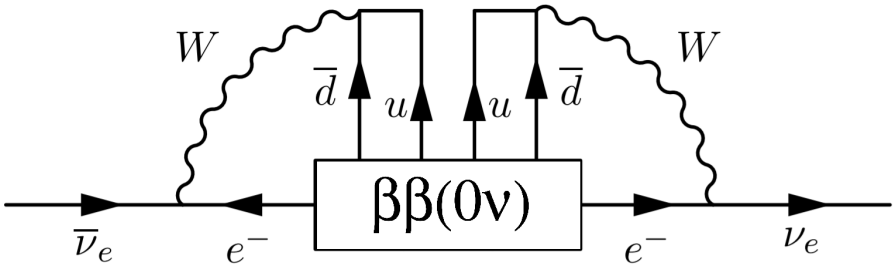

Figure 1.5: Conversion from $\bar{\nu_e}$ to ν_e by a $0\nu\beta\beta$ interaction. This diagram proves that the existence of the $0\nu\beta\beta$ decay would imply that neutrinos are Majorana particles, no matter the mechanism that produces the transition.

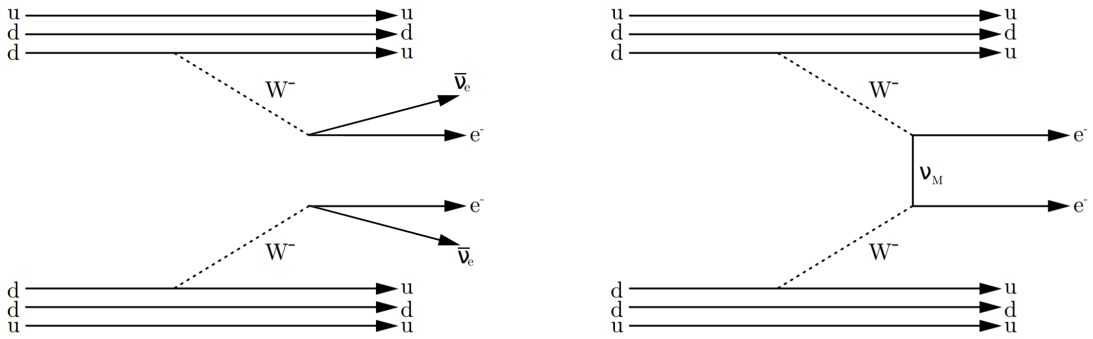

Figure 1.6: *Left*: Feynman diagram for double-beta decay with the emission of two neutrinos. *Right*: diagram for $0\nu\beta\beta$, mediated by the exchange of a massive Majorana neutrino, labeled ν_M (taken from [13]).

where $G_{0\nu}$ and $M_{0\nu}$ are the phase space factor and the nuclear matrix element for the transition respectively, and $m_{\beta\beta}$ comes from equation 1.6. The phase space factor depends on the charge, mass and available energy in the process; nuclear matrix elements depend on the structure of the parent and daughter nuclei.

In order to extract the value of $m_{\beta\beta}$ from an observation of neutrinoless double-beta decay, the values of $G_{0\nu}$ and $M_{0\nu}$ must be well known. While $G_{0\nu}$ can be calculated exactly, the value of $M_{0\nu}$ cannot be obtained analytically, but must come from the numerical solution of a many-body problem. The evaluation of nuclear matrix elements represents the biggest source of theoretical uncertainty in the evaluation of $m_{\beta\beta}$ [20].

1.2.1 $0\nu\beta\beta$ experiments

The amount of energy released in a double-beta decay is a fixed quantity, called the decay Q-value ($Q_{\beta\beta}$). In the $2\nu\beta\beta$ decay, part of the energy is carried away by neutrinos and is essentially undetectable: the energy spectrum for electrons is continuous between 0 and $Q_{\beta\beta}$. In the $0\nu\beta\beta$ decay, since no neutrinos are emitted, all the energy is carried by electrons. The signature of this decay, the monochromatic energy of the two electrons, is an energy deposition at the decay Q-value. Even if the signature is, in principle, very clear, the rarity of this decay makes its detection problematic. Several experimental parameters must be thoroughly kept under control in order to optimize the sensitivity.

Radiation produced by natural and cosmogenic radioactivity can generate events, indistinguishable from $0\nu\beta\beta$ ones, close to $Q_{\beta\beta}$. As this background can hide the signal and spoil the sensitivity of an experiment, it must be kept at a minimum. The maximization of the expected signal over the background is obtained by various techniques:

- using a large mass of active isotope to increase the expected number of $0\nu\beta\beta$ decays;
- building the detector with ultra-clean materials and including radiation shields in the design (*passive* background reduction techniques);
- developing analysis techniques to identify only events which are more likely to be produced by $0\nu\beta\beta$ (*active* background reduction techniques).

Energy resolution is another important feature of any experiment. A bad energy resolution can *smear* the signal, making it more difficult to detect over the background. Additionally, a good energy resolution helps to reduce the only source of background that cannot be removed, that is the tail of the $2\nu\beta\beta$ continuous energy distribution. Figure 1.7 shows the spectral shape produced by $0\nu\beta\beta$ and $2\nu\beta\beta$ decays in a calorimetric experiment where the sum kinetic energy of the two electrons is measured. If the energy resolution is low, as pictured in the insert, the signal from $0\nu\beta\beta$ can be covered by the $2\nu\beta\beta$ distribution.

If a $0\nu\beta\beta$ decay happened, the probability of actually detecting it (the detection efficiency) must be as high as possible. One of the best ways to keep its value high is to include the $0\nu\beta\beta$ candidate isotope under investigation in the detecting material itself.

The sensitivity of an experiment, defined as the half-life corresponding to the minimum number of signal events observable above background at a given confidence level, can be expressed in terms of the main experimental parameters as [21]:

$$T_{1/2}^{0\nu}(n_\sigma) \propto \frac{1}{n_\sigma}\frac{\epsilon \cdot i.a.}{A}\sqrt{\frac{M \cdot t}{b \cdot \Delta E}}. \tag{1.8}$$

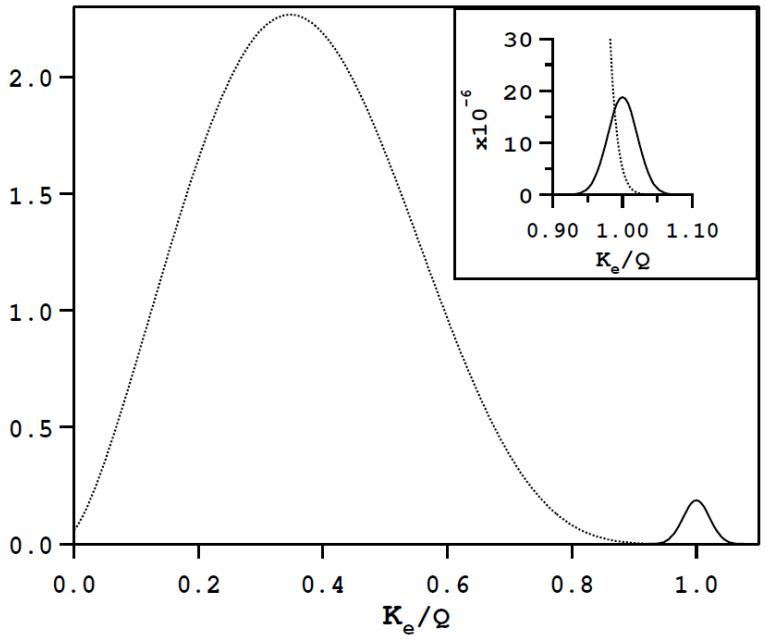

Figure 1.7: Energy spectra produced by $2\nu\beta\beta$ and from $0\nu\beta\beta$, with arbitrary amplitudes. In the insert, the effect of poor energy resolution on the detection of a signal in the $Q_{\beta\beta}$ region is shown (picture taken from [14]).

In equation 1.8, n_σ is the number of standard deviations corresponding to the required confidence level, ϵ the detection efficiency, *i.a.* the isotopic abundance of the isotope under investigation, A its atomic mass, M the active mass of the experiment, t the live time, b the background level and ΔE the energy resolution.

Only a few isotopes can undergo double-beta decay; not all of them, however, are equal from an experimental point of view. Two quantities, different between all the candidate isotopes, must be kept into consideration: the value of $Q_{\beta\beta}$ and the isotopic abundance of the chosen nuclide (figure 1.8).

The isotopic abundance enters directly in equation 1.8, meaning that the choice of an isotope with low I.A. represents a significant drawback. To overcome this issue the source material needs to be enriched in the required isotope, a procedure that can be costly and potentially introduce additional radioactive contaminants in the material, increasing the background.

The Q-value of the reaction is strictly related to the background that is expected in the energy region close to the detector. Generally speaking, the highest $Q_{\beta\beta}$, the lower the background induced by β and γ radioactivity. A particularly important threshold is represented by the 2615 keV γ line from ^{208}Tl, the highest energy naturally occurring γ

line. Above this value, the background becomes much lower, and mainly due to α decays. Experiments using isotopes whose $Q_{\beta\beta}$ is below this threshold generally have to employ active background rejection techniques to be competitive.

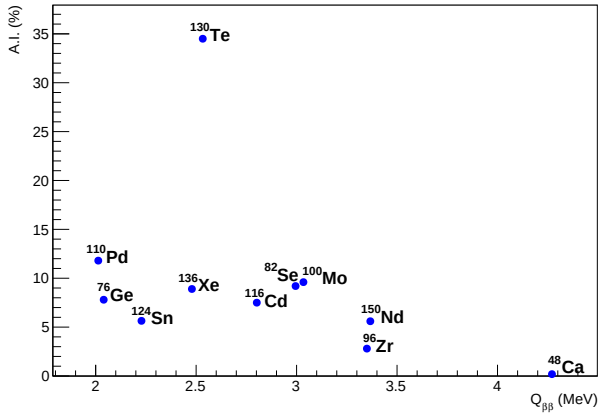

Isotope	$Q_{\beta\beta}$	I.A. (%)
^{48}Ca	4.271	0.187
^{76}Ge	2.040	7.8
^{82}Se	2.995	9.2
^{96}Zr	3.350	2.8
^{100}Mo	3.034	9.6
^{110}Pd	2.013	11.8
^{116}Cd	2.802	7.5
^{124}Sn	2.228	5.64
^{130}Te	2.527	34.1
^{136}Xe	2.479	8.9
^{150}Nd	3.367	5.6

Figure 1.8: Isotopic abundance and $Q_{\beta\beta}$ for the $0\nu\beta\beta$ candidate isotopes.

1.2.2 Current results

There are presently several large scale experiments trying to measure $0\nu\beta\beta$ decay in different isotopes, as well as multiple R&Ds for next-generation experiments. The current best limit on $m_{\beta\beta}$, $m_{\beta\beta} < (61 - 165)$ meV, comes from the KamLAND-Zen experiment [24], studying ^{136}Xe. The best results for other $0\nu\beta\beta$ decay candidates come from Gerda [23] for ^{76}Ge, NEMO-3 [25] for ^{100}Mo and CUORE-0 + Cuoricino [22] for ^{130}Te (figure 1.9).

The aim of the next generation of experiments is to reach the sensitivity required to start to investigate (or, possibly, cover completely) the inverted hierarchy band in the $m_{\beta\beta}$ vs. $m_{lightest}$ plot. This means reaching a sensitivity of about 10^{-2} eV for $m_{\beta\beta}$, an improvement of about an order of magnitude with respect to the current best results.

The complete investigation of the inverted hierarchy band would lead to two possible results: either $0\nu\beta\beta$ decay is observed, proving that neutrinos are Majorana particles and that the inverted hierarchy is correct, or the decay is not observed, which would only prove that, if neutrinos are Majorana particles, the hierarchy must be normal.

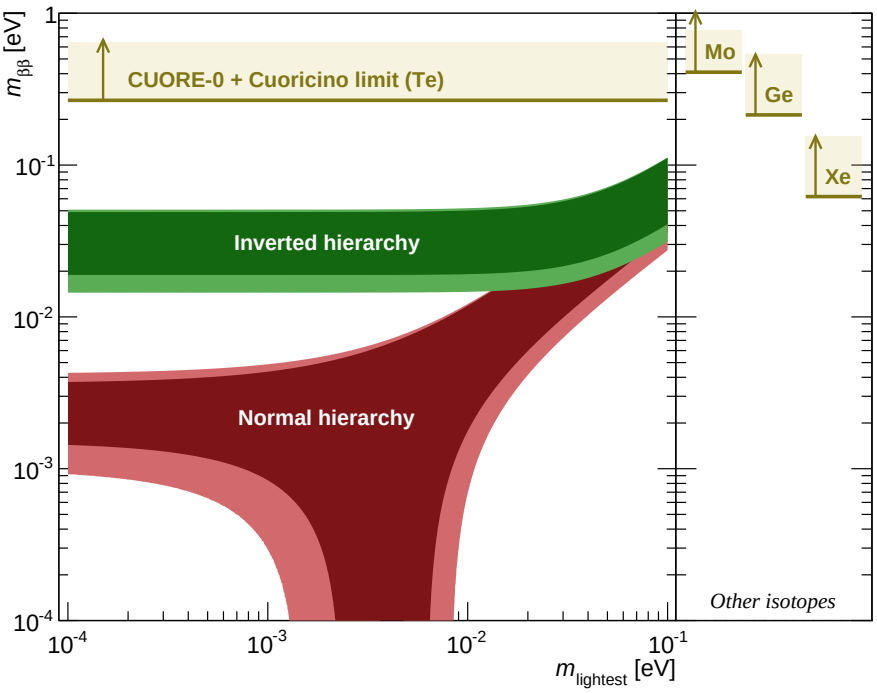

Figure 1.9: Limits on $m_{\beta\beta}$ for ^{130}Te (CUORE-0 + Cuoricino [22]), ^{76}Ge (Gerda [23]), ^{136}Xe (KamLAND-Zen [24]) and ^{100}Mo (NEMO-3 [25]). The width of the horizontal bands is related to the spread in the nuclear matrix element values.

CHAPTER

2

CUORE-0

The Cryogenic Underground Observatory for Rare Events (CUORE) [26][27][28] is a bolometric experiment located in the underground facilities of the INFN Gran Sasso National Laboratory (LNGS), in central Italy. At the time of writing, CUORE is starting to acquire data. Bolometric experiments have long been used for the search of neutrinoless double-beta decay in ^{130}Te; the best current limit on the half life of this process came from the combination of the results from two of said experiments, CUORICINO and CUORE-0 [22][29]. After a brief overview of the three aforementioned experiments, I'll describe in more detail the structure and the experimental technique used in CUORE-0, as it is the main focus of this thesis.

2.1 TeO_2-based detectors

The goal of any $0\nu\beta\beta$ experiment is to look for an excess of events at the decay Q-value. Bolometric experiments obtain the needed energy spectrum by detecting the temperature increase due to particle interactions inside the active volume of the detector. A more detailed description of the bolometric technique is given in section 2.2.1.

As already discussed in chapter 1, in order to increase the sensitivity to this process an experiment needs high mass and resolution, as well as a low background. CUORE, CUORE-0 and CUORICINO all use TeO_2 crystals as energy absorbers, which have long been used for $0\nu\beta\beta$ searches as they satisfy many of the key constraints necessary for a

sensitive experiment.

- The source isotope, ^{130}Te, is naturally contained in the detector medium, granting a high energy containment efficiency of the emitted electrons and avoiding the problems associated to the use of external source materials (additional radioactive background, potential resolution losses...)

- TeO_2 bolometers have an excellent energy resolution, comparable only to semiconductor devices: CUORE-0 reached a resolution of ~ 5 keV at 2.615 MeV.

- Among the possible candidates isotopes for $0\nu\beta\beta$ decay searches ^{130}Te has the highest natural isotopic abundance ($\sim 34.2\%$), making enrichment (a costly procedure that can introduce additional background sources in the crystals) not a necessity.

- The β/γ natural radioactive background is relatively low near the ^{130}Te endpoint energy ($Q_{\beta\beta}$), 2527.518 ± 0.013 keV [30][31][32].

- The technology required to produce TeO_2 crystals is well known; crystals that have low intrinsic background, excellent energy resolution and that fulfil all the mechanical and cryogenic requirements for a bolometric experiment can be grown reproducibly.

The CUORE detector consists of an array of 988 TeO_2 bolometers, corresponding to 206 kg of ^{130}Te. The 988 CUORE bolometers are arranged in 19 towers, each consisting of 52 crystals. They are housed inside a large cryostat, capable of reaching temperatures below 10 mK; at these temperatures, the small heat released by particle interactions becomes measurable. The goal of the experiment is to reach a 5 keV FWHM resolution at the Q-value and a background around 0.01 counts/(keV·g·y).

The experience needed to build and operate CUORE has been accumulated over many years, with the construction of several TeO_2 arrays with increasing mass[33][34][35][36]. The most important step towards a ton-scale detector came with CUORICINO experiment, which ran from 2003 to 2008 in Hall A at LNGS. The CUORICINO array consisted of a tower containing 62 TeO_2 crystals, for a total mass of 40.7 kg ($\sim$ 11 kg of ^{130}Te). More details on CUORICINO can be found in section 2.3.

CUORE-0 consisted of 52 bolometers arranged in a single tower, with a total active mass of $\sim$ 39 kg; the structure of CUORE-0 is identical to the towers currently used for CUORE. It was housed in the same cryostat that contained the CUORICINO array and ran from 2013 to 2015. One of the main purposes of CUORE-0 was the test of the CUORE assembly line, including the choice of materials and the procedure used to build the towers. The reproducibility of the technique also had to be checked, to ensure that all crystals shared the same level of performance. CUORE-0 also verified the effectiveness

of the improved material cleaning techniques employed after CUORICINO to reduce the radioactive background.

	Unit	**CUORICINO**	**CUORE-0**	**CUORE** (predicted)
Background	[counts/(keV·kg·y)]	0.169	0.058	0.01
Q-value resolution	[keV]	6.3	5.1	5
Mass (TeO_2)	[kg]	40.7	39	742
Mass (^{130}Te)	[kg]	11	10.8	206

Table 2.1: Summary table with the features of CUORE, CUORE-0 and CUORICINO.

2.2 CUORE-0

2.2.1 TeO_2 bolometers

A bolometer is an extremely sensitive low-temperature calorimeter [37]; its essential parts are an *absorber*, a *thermometer* and the *heat sink*. Energy deposited by interacting particles inside the absorber lead to a temperature increase, which is read by the thermometer; the excess heat is removed from the absorber by a weak thermal coupling to a heat sink, allowing the temperature to go back to its starting value (figure 2.1).

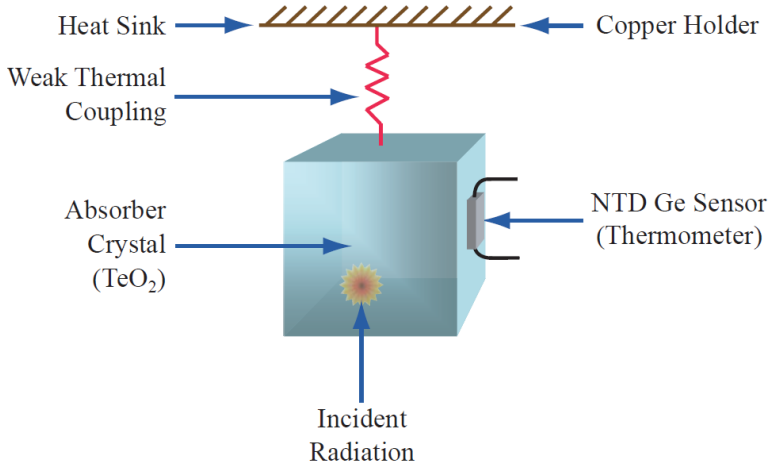

Figure 2.1: Schematic description of a CUORE bolometer. (Taken from [38])

Following the simplified model from figure 2.1, we can model the temperature increase

ΔT produced by a particle releasing energy E as

$$\Delta T = \frac{E}{C_{(T)}}, \tag{2.1}$$

where $C_{(T)}$ is the temperature-dependent heat capacity of the absorber. $C_{(T)}$ scales with the third power of the temperature, roughly following the Debye law [39]:

$$C_{(T)} \propto k_B \left(\frac{T}{\Theta_D}\right)^3 \tag{2.2}$$

where the Debye temperature Θ_D of TeO_2 is about 232 K[40]. Since the amount of energy released by typical interacting particles is small ($\sim$ 0.16 pJ for a 1 MeV photon), we need to keep the heat capacity as low as possible in order to detect a signal[1]. This is obtained by operating the detector at extremely low temperatures, around 10 mK; at this temperature $C_{(T)} \simeq 2$ nJ/K, resulting in a temperature increase of ~ 0.1 mK for a 1 MeV signal.

In CUORE-0, as in all other TeO_2-based bolometric experiments, each crystal is instrumented with a Neutron-Transmutation-Doped (NTD) germanium thermistor (figure 2.2). These devices convert the temperature changes in the crystals to a voltage signal, which is read out by the front-end electronics, located at room temperature. NTD thermistors were produced by neutron irradiation of germanium slabs at the University of Missouri Research Reactor; neutron activation on germanium dopes the semiconductor material with Ga, As and Se.

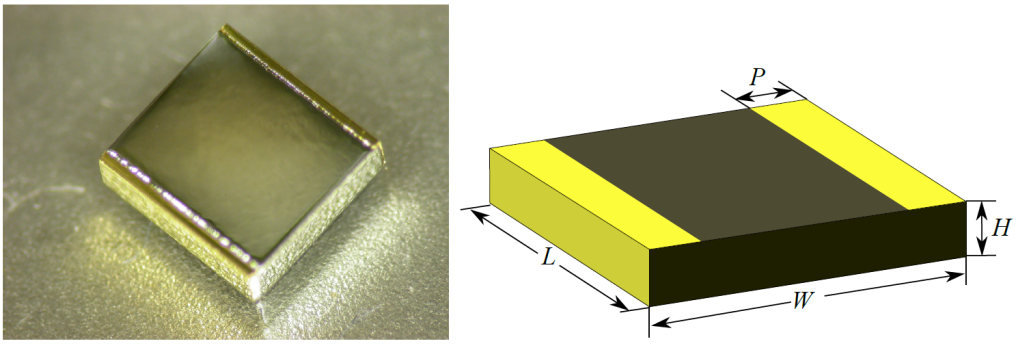

Figure 2.2: *Left*: photograph of a CUORE-0 NTD. *Right*: diagram for the thermistor geometry; the yellow parts on the thermistor sides are golden pads, used for electrical contacts. Typical values for the dimensions are L= 3.0 mm, W= 2.9 mm, H= 0.9 mm and P= 0.2 mm. (Taken from [38])

The doping density is a critical parameter in the production of NTD thermistors: a

[1] In order for a signal to be detected, its amplitude should also be higher than the normal temperature fluctuations in the detector, which provide a low energy threshold.

critical density exists, below which the conductivity goes to zero at zero temperature, and above which the conductivity is always finite [41][42]. In the former regime, the thermistor resistance has a very steep dependence on temperature [43]:

$$R_{(T)} = R_0 e^{(T_0/T)^\Gamma}, \tag{2.3}$$

where $\Gamma \simeq 0.5$, T_0 is determined by the doping level and R_0 depends on both the doping level and the geometry. The target values for CUORE-0 thermistors were $T_0 = 4$ K and $R_0 = 1\ \Omega$. With these values, a 0.1 mK increase in temperature over the base 10 mK reduces the thermistor resistance by almost 10%, making it easily detectable.

2.2.2 Detector structure

The CUORE-0 detector consists of 52 TeO_2 crystals in a single tower. The CUORE-0 bolometers are arranged in 13 floors, each consisting of four 5x5x5 cm^3 crystals, for a total active mass of ~ 39 kg. Each crystal is instrumented with a germanium thermistor and with a silicon heater, used to inject fixed-energy pulses in the detector, emulating particle interactions, to monitor slow drifts in the operating temperature.

The crystals are held together by a copper structure, specifically designed to reduce the amount of material near the detector to a minimum. The full structure, which consists of copper frames, columns and wire trays (figure 2.3) weights about 3.5 kg. The tower structure also holds a copper shield that serves both as radiation shield and as thermal radiation protection for the 10 mK stage of the cryostat (figure 2.3); this shield weighs about 10 kg.

Given the large amount of copper facing the detector directly, the tower structure and the innermost shield were manufactured from a high-purity Electrolytic Tough Pitch (ETP1) copper alloy, called NOSV. This alloy was selected for its low hydrogen content and extremely low contamination levels: $^{238}U < 5.3 \cdot 10^{-12}$ g/g (90% C.L.) and $^{232}Th < 5.0 \cdot 10^{-13}$ g/g (90% C.L.) [44]. Particular care was also given to surface cleaning of copper parts: an upper limit of $1.3 \cdot 10^{-7}$ Bq/cm^2 (90% C.L.) was measured for both ^{232}Th and ^{238}U .

The crystals are not directly in contact with the copper frames: small Polytetrauoroethylene (PTFE) spacers support them inside the copper structure and act as a weak thermal link to the heat sink (i.e. the frame itself), provided by the frames themselves.

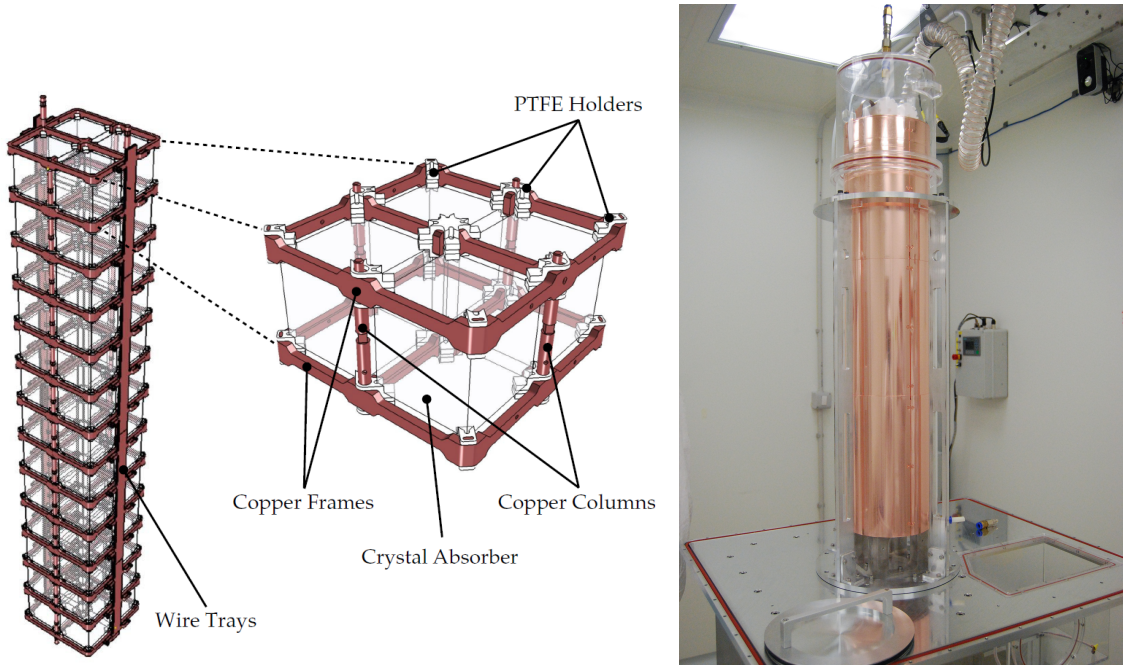

(1) (2)

Figure 2.3: *Left*: rendering of the CUORE-0 tower and detail of one of the floors. The two wire trays (one is shown, the other is on the opposite side of the tower) contain all the wiring that carries out the electrical signal from the crystals. *Right*: picture of the CUORE-0 tower, enclosed in the 10 mK shield.

2.2.3 Experimental setup and shielding

CUORE-0 was located in Hall A at LNGS, at a depth of $\sim$ 3600 m.w.e[2]., providing excellent shielding from both cosmic muons ($3 \cdot 10^{-8}$ $\mu/(\text{s}\cdot\text{cm}^2)$ [45]) and neutrons ($4 \cdot 10^{-6}$ $\text{n}/(\text{s}\cdot\text{cm}^2)$[46]).

In order to isolate the detectors from vibrations caused by the cryogenic equipment, the tower was connected to the cryostat via a stainless steel spring fixed to a plate thermalized at 50 mK[47]. In order to reach the operating temperature, the tower was thermally linked to the 10 mK stage of the cryostat by two thin (50 μm) copper foils.

The tower was enclosed in a set of nested cylindrical coaxial vessels which make up the thermal radiation shields for the cryostat. From the innermost, they are identified as the 50 mK, 600 mK and 4 K shields; the 4 K shield also formed the walls of the Inner Vacuum Chamber (IVC). The Outer Vacuum Chamber (OVC), the space between the outer IVC shield and the outermost, room-temperature vessel, contained five additional vessels along

[2] **M**eter **W**ater **E**quivalent; the $\sim$ 1400 m of rock on top of the LNGS underground labs provide shielding from cosmic rays equivalend to 3600 m of water.

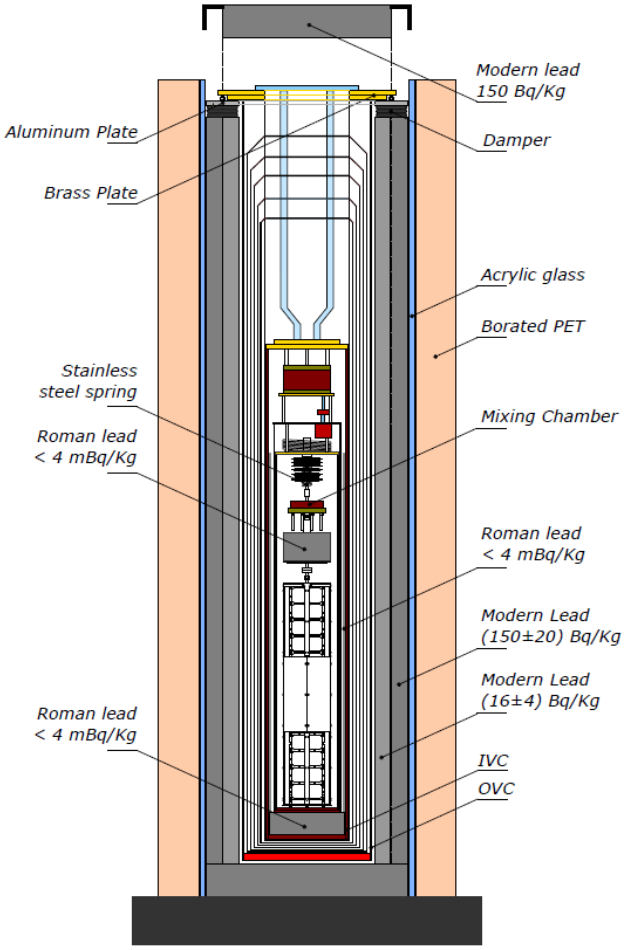

Figure 2.4: Sketch of the CUORE-0 cryostat (not to scale). The indicated activities refer to ^{210}Pb.

with several hundred thin aluminized mylar sheets, which acted as additional insulation.

Radiation shielding was provided by several lead layers. The tower was surrounded by a 1.4 cm-thick Roman lead cylindrical shield, whose ^{210}Pb activity was measured to be below 4 mBq/kg[48]. A Roman lead disk, 10 cm thick and 17 cm in diameter, was placed just above the tower; another disk, 8 cm thick and 19 cm in diameter was placed below the tower, to provide shielding from the laboratory floor.

Two additional lead layers were build outside the OVC: a 10 cm-thick modern lead layer, with a measured ^{210}Pb activity of 16 ± 4 Bq/kg, formed the inner shield, while another 10 cm-thick modern lead layer with a higher activity (150 ± 20 Bq/kg) was located on the outside. Finally, 10 cm of borated polyethilene provided shielding from neutrons coming from the rocks of Hall A.

The entire apparatus was enclosed in a Faraday cage to minimize local electromagnetic interference. The walls of the cage were then covered with sound and vibration absorbing material to reduce microphonic noise. A full drawing of the CUORE-0 cryostat can be found in figure 2.4.

2.2.4 Detector operation

The CUORE-0 experiment started taking data in March 2013. A first data-taking campaign, corresponding to a ^{130}Te exposure of 2.0 kg·y, started in March 2013 and lasted until September 2013; following this, the cryostat was shut down for maintenance. Detector operations resumed in November 2013, with improved noise and duty cycle thanks to the maintenance operations. CUORE-0 collected data for $0\nu\beta\beta$ analysis until March 2015, reaching a total ^{130}Te exposure of 9.0 kg·y (corresponding to 35.2 kg·y TeO_2 exposure). During the whole period one of the crystals, labeled as channel 49, was disconnected and provided no useful data, meaning that the exposure is obtained with 51 crystals only. Figure 2.5 shows the exposure accumulated by CUORE-0 over time.

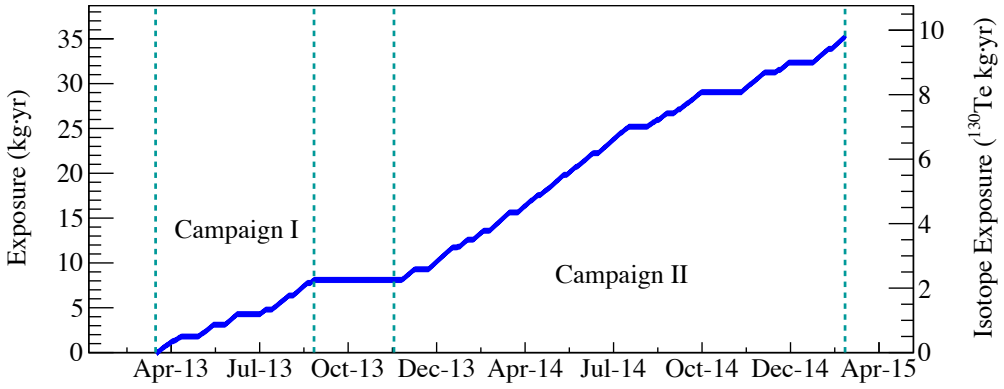

Figure 2.5: Plot of the accumulated statistics over time. The left Y axis reports the TeO_2 exposure.

The CUORE-0 data collection was organized in runs, with each run lasting approximately one day. Runs were grouped into datasets, each containing about three weeks of physics data. When possible, datasets started and ended with calibration measurements, used to determine the energy response of the detector; two wires containing ^{232}Th are inserted in the cryostat and the well-known γ lines produced by its decay chain are used to calibrate the system. Calibration measurements typically lasted three days; some datasets only have an initial calibration, due to problems in the cryogenics system that interrupted the data taking before the planned final calibration.

2.3 CUORICINO

Before CUORE-0, the best limit on $0\nu\beta\beta$ decay in ^{130}Te came from CUORICINO in 2011[29]. The CUORICINO detector was similar in structure to the CUORE-0 tower; it had a slightly higher active mass (40.7 kg) and its copper structure was heavier[3].

CUORICINO consisted of 62 TeO_2 crystals, few of which enriched in ^{130}Te, for a total ^{130}Te mass of ~ 11 kg. The CUORICINO tower included crystals of different sizes, including CUORE-sized crystals (5x5x5 cm^3) and smaller ones (3x3x6 cm^3). The tower was operated inside the same cryostat that was later used for CUORE-0, described in section 2.2.3.

CUORICINO ran from 2003 to 2008, collecting a total ^{130}Te exposure of 19.75 kg·y. Data-taking was split into two runs, Run I (1.18 kg·y ^{130}Te exposure) and Run II (18.57 kg·y ^{130}Te exposure), due to a major maintenance interruption.

The energy resolution varied depending on crystal type: the CUORE-sized crystals achieved the best results, while the smaller, enriched crystals yielded the worst resolution. The average ΔE_{FWHM} values can be found in table 2.2.

CUORICINO achieved a background in the $0\nu\beta\beta$ ROI of 0.169±0.006 counts/(keV·kg·y), most of which came from degraded α decays[4][49][50]. The background acquired in the $0-7$ MeV region is shown in figure 2.6.

Crystal type	$< \Delta E_{FWHM} >$
5x5x5 cm^3	6.3±2.5 keV
3x3x6 cm^3 (natural)	9.9±4.2 keV
3x3x6 cm^3 (enriched)	13.9±5.3 keV

Table 2.2: Average energy resolution at the 2615 keV line for the three CUORICINO crystal types. The CUORE-sized crystals (5x5x5 cm^3) achieved the best resolution.

The final result for the $0\nu\beta\beta$ analysis in CUORICINO are shown in figure 2.7. CUORICINO set a limit on the $0\nu\beta\beta$ half-life of ^{130}Te at $T^{0\nu\beta\beta}_{1/2} > 2.8 \cdot 10^{24}$ y (90% C.L.), which was the best available limit at the time[29].

[3]The copper structure used in CUORE-0 is an improvement over the CUORICINO one as it reduced the amount of material between crystals, strongly affecting the radioactive background

[4]α decays happening in a passive material (mainly copper) that deposit a random fraction of their energy in the originating volume, and the rest in a crystal.

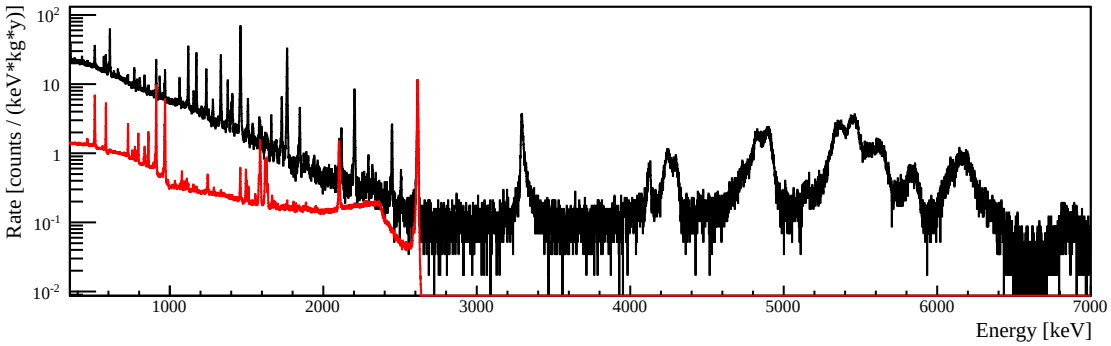

Figure 2.6: Energy spectrum acquired by the CUORICINO experiment. The calibration spectrum has been superimposed in red, normalized to the 2615 keV line.

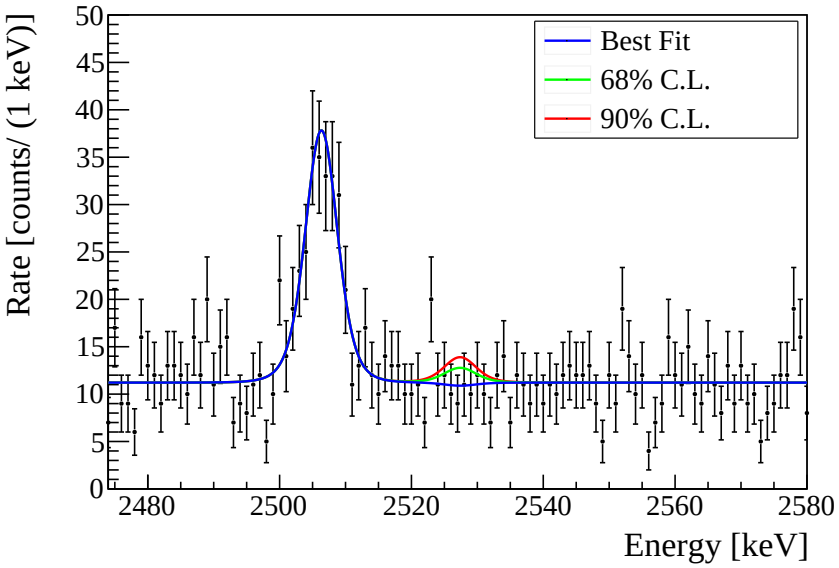

Figure 2.7: Final CUORICINO spectrum in the ROI with the fit results from the $0\nu\beta\beta$ analysis.

CHAPTER

3

CUORE-0 DATA ANALYSIS

In this chapter I will focus on the procedure used to produce the final data for the CUORE-0 experiment. The data production procedure is outlined in two sections, describing the steps that lead to the final data structure and the techniques used to select only events of interest for the analysis.

3.1 Data processing

Particle interactions inside TeO_2 bolometers produce a temperature increase that is read by a germanium NTD and transformed into an electrical signal (section 2.2.1). We acquire a continuous data stream from the detector with a 125 Hz frequency and pulses are detected with a software trigger which operates independently on each bolometer. Each triggered pulse is associated to a 5 second window: the one second of data preceding the trigger and the four seconds after.

Particle pulses have typical rise times of ~ 0.05 s and two decay time components, a fast (~ 0.2 s) and a slow one (~ 1.5 s). The former is related to the heat capacity of the crystal and the thermal conductivity to the thermal bath, while the latter depends on the heat capacity of the passive components (i.e. PTFE spacers, copper structure). A signal pulse can be seen in figure 3.1.

The first phase of the data processing takes the CUORE-0 data from a series of trig-

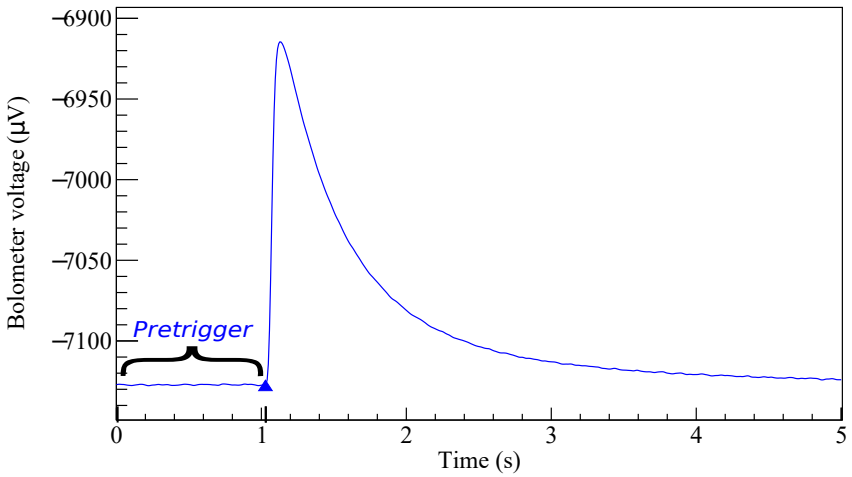

Figure 3.1: Typical pulse from CUORE-0, corresponding to an energy release of approximately 2615 keV. The data contained in the second preceding the signal pulse, called *pretrigger*, is also acquired.

gered pulses to a calibrated energy spectrum. In order to extract the deposited energy from the data, we first need to estimate the amplitude of each signal pulse, minimizing the effect of noise in order to improve energy resolution. The amplitude can be modeled as the product of two quantities: an energy-dependent amplitude $A(E)$ and a thermal gain, $G(T)$, which depends on the operating temperature of the detector. Since this temperature can vary during data acquisition, we need to stabilize the thermal gain against this variation. Using data acquired during the calibration runs performed at the beginning and at the end of each dataset, we model the energy dependence of $A(E)$.

In the later stages of the analysis additional quantities related to the shape of the pulses are calculated in order to improve the data quality; events that happen simultaneously on more than one crystals are also tagged with a specific quantity called `Multiplicity`. Finally, we blind the region of interest (ROI) to prevent any bias in the later stages of the analysis, such as cut optimization or determination of fitting algorithms.

3.1.1 Amplitude evaluation

To evaluate the amplitude of a pulse we employ the optimum filtering (OF) technique [51]. The OF is a frequency-based filter designed to maximize the signal-to-noise ratio, using the whole pulse to estimate the amplitude. We can model the signal shape $v_i(t)$ on each

bolometer, i, as the sum of a detector response function, $s_i(t)$, and a noise term, $n_i(t)$:

$$v_i(t) = B_i(E,T)s_i(t) + n_i(t) = [A_i(E) \times G_i(T)]\, s_i(t) + n_i(t), \tag{3.1}$$

where $B_i(E,T)$ is the amplitude of the signal. Up to a multiplicative gain, an OF pulse can be written as

$$V_i^{OF}(\omega) \propto e^{i\omega t_{max}} \frac{S_i(\omega)}{N_i(\omega)} V_i(\omega), \tag{3.2}$$

where $V_i(\omega)$ and $S_i(\omega)$ are the Fourier transforms of $v_i(t)$ and $s_i(t)$ respectively, $N_i(\omega)$ is the noise power spectra of the underlying noise sources and t_{max} is the time at which the pulse reaches its maximum. We derive the response function $s_i(t)$ by averaging hundreds of events from the ^{208}Tl 2615 keV line in calibration runs[1]. During data taking, 5 seconds wide windows that contain no event trigger are acquired every 200 seconds; those are averaged and used to estimate the noise power spectra, $N_i(\omega)$.

In addition to the optimum filter we use another technique, the decorrelating optimum filter (DOF). The DOF is a generalization of equation 3.2 that accounts for noise correlations between neighboring channels:

$$V_i^{DOF}(\omega) \propto e^{i\omega t_{max}} \sum_j S_i(\omega) C_{ij}^{-1}(\omega) V_j(\omega). \tag{3.3}$$

In equation 3.3, $C_{ij}^{-1}(\omega)$ is the i,j component of the inverted noise covariance matrix and the sum runs over a list of correlated bolometers.

The DOF typically outperforms the OF in physics runs but performs worse in calibration runs. The higher event rate of the calibration runs[2] leads to a higher probability of an event occurring in a neighboring channel within the 5 seconds window, producing an incorrect estimate of the correlated noise. Since calibration runs are essential in the evaluation of the energy resolution used as input for the $0\nu\beta\beta$ analysis, the DOF technique is problematic.

Despite this, for some bolometers, the benefits of the DOF still outweigh the effects of the increased event rate. In the final CUORE-0 data we use a combination of both OF and DOF: the DOF is chosen on those channels where the improvement in energy resolution at the 2615 keV line is significant at the $> 90\%$ level. With this requirement, the DOF is used in $\sim 20\%$ of the final data.

[1] The average pulse is calculated at the 2615 keV line as it is a strong γ line close to $Q_{\beta\beta} = 2527$ keV. Since there is a non-negligible relation between energy and pulse shape, this choice optimizes the filter performance.

[2] Physics runs have a typical event rate of 1 mHz/channel, while calibration runs reach ~ 60 mHz/channel.

3.1.2 Thermal gain stabilization

The thermal gain stabilization (TGS) compensates slow variations in the thermal gain of the bolometers, $G_i(T)$, due to temperature variations during operation. As with the amplitude evaluation we use two techniques in parallel: a heater-based TGS and a calibration-based TGS.

The heater-based TGS [52] uses the heater attached to each crystal to inject fixed-energy pulses in the detector every 300 s. Since the energy of these pulses is constant, variations in the recorded amplitude B_i^{ref} are exclusively linked to the thermal gain $G_i(T)$. The average voltage level of the bolometer V_{Bol}, measured from the pulse baseline (obtained by the pretrigger window of each pulse, as in figure 3.1), is used as a proxy of bolometer temperature. The $G_i(T)$ function, approximated by a polynomial, is evaluated by fitting the dependence of B_i^{ref} by the baseline and later used to stabilize the bolometric response against thermal drifts.

Two of the channels on the CUORE-0 towers didn't have a working heater attached, due to problems during detector installation. These two channels, which make up about 4% of the total exposure, cannot be stabilized with the heater-TGS. In addition, despite the TGS technique being effective in most cases, in some datasets the heater-TGS failed to stabilize certain bolometers. In these cases, if we hadn't come up with an alternative technique, we would have had to consider the whole dataset invalid for that particular bolometer, leading to a potential loss of $\sim 7\%$ of our exposure.

The reason for the heater-TGS failures lies in the electronics chain used to read the signal from the bolometers. While the relation between pulse amplitude and temperature should not change in time (if working conditions remain constant), the same is not true for some variables related to signal readout, which can suffer instabilities. Before the digitalization, the bolometric signal is amplified (with gain G) and a DC offset V_{Offset} is added in order to exploit the full range of the ADC. The pulse baseline V_{Bsl} can then be written as

$$V_{\mathrm{Bsl}} = V_{\mathrm{Offset}} - G \times V_{\mathrm{Bol}}. \tag{3.4}$$

While the gain G is very stable [53], V_{Offset} can drift and can also be adjusted manually to prevent signals from going outside the ADC range after significant temperature variations.

To address this issue we developed a calibration-based TGS algorithm that uses the 2615 keV γ line in calibration runs instead of heater pulses. We regress the gain dependence on $G \times V_{\mathrm{Bol}}$ measured in calibration runs against $G \times V_{\mathrm{Bol}}$ and use this to correct the amplitudes of events in both physics and calibration runs.

The calibration-TGS requires a precise and frequent measurement of V_{Offset} in order

to work properly, making the heater-TGS a better choice for most of our data. Still, the calibration-TGS allowed us to recover $\sim$ 80% of the exposure on the two heaterless channels and often outperformed the heater-TGS when large temperature drifts were observed, leading to the recovery of much of the 7% of exposure that would have been lost otherwise.

In 2.7% of the final exposure, however, both TGS algorithms failed significantly, due to abnormally large or sudden drifts in temperature; in those cases, the data were discarded for the rest of the analysis.

3.1.3 Energy calibration

For each dataset, we calibrate the energy response of each bolometer using the reconstructed positions of at least four of the main γ lines from the ^{232}Th decay chain (2615, 2104, 969 and 511 keV). This procedure consists in fitting each peak position using a Gaussian lineshape plus a first degree polynomial to model the background, and fitting the energy vs. amplitude curve with a second-order polynomial. More detail on calibration sources can be found in chapter 7. The energy spectrum from CUORE-0 is shown in figure 3.2.

The effectiveness of the calibration technique can be tested by computing the difference between the measured and expected energy for all the γ lines in the background spectrum in figure 3.2. This difference is shown in figure 3.3, and amounts to less than 0.1 keV at $Q_{\beta\beta}$.

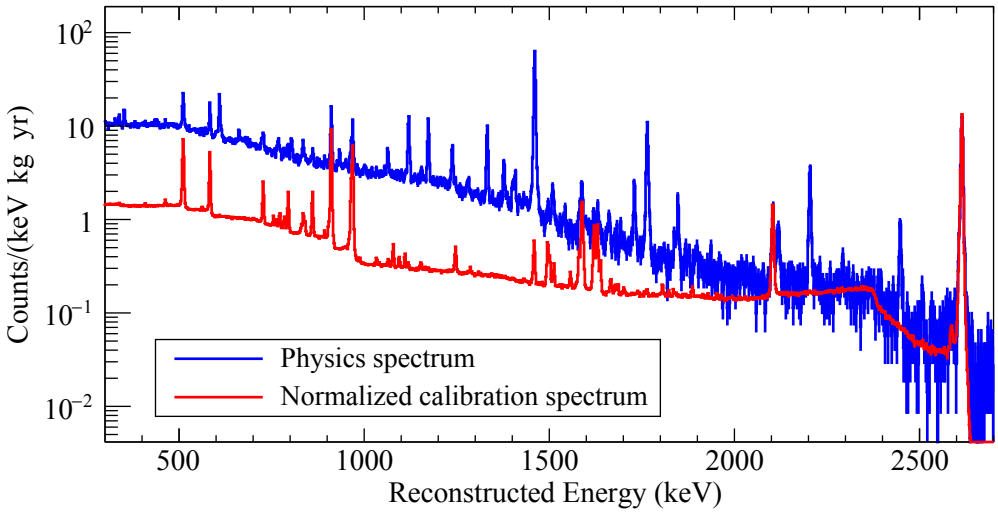

Figure 3.2: CUORE-0 energy spectrum in the γ region. The calibration spectrum is normalized at the 2615 keV line.

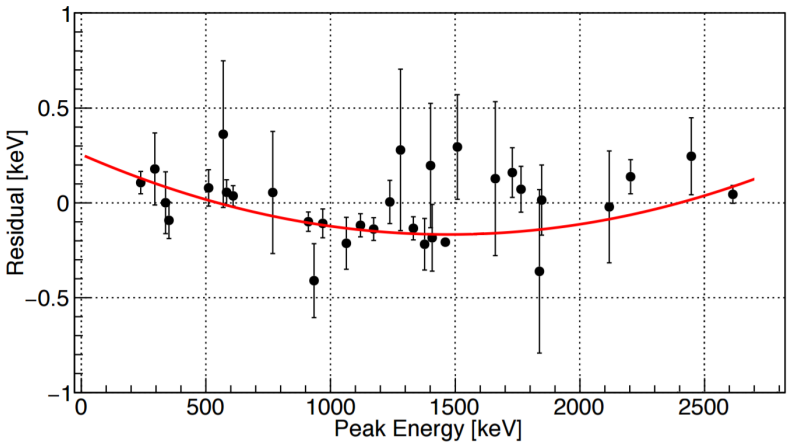

Figure 3.3: Difference between measured and expected energy for all the γ lines in the background spectrum. The points are fitted with a second degree polynomial.

3.1.4 Pulse shape discrimination

Pulses recorded by CUORE-0 aren't always clean like the one shown in figure 3.1. There are other categories of signals that can occur:

- spurious signals, which are not produced by particle interactions but, for instance, by random noise spikes. Since they are not associated to real events, the energy associated to these signals can, in principle, end up at any point in the spectrum, artificially increasing the background;
- signals due to real particles which are deformed, either by the superposition of other signals in a short time window (pile-up) or by the presence of excessive noise. The amplitude (and therefore, the energy) of these signals is not reconstructed correctly, since the OF technique uses the whole pulse to estimate signal amplitude.

The pulse shape discrimination algorithm was designed to identify and reject pulses that belong to these categories. The technique is based on pulse shape parameters, which either measure characteristic quantities of particle pulses (such as rise or decay time) or the resemblance of a signal to the average pulse. An in-depth description of the pulse shape discrimination algorithm is given in chapter 4.

3.1.5 Coincident events

The determination of the source of a particular event can benefit from the information related to the number of crystals that produced a trigger at the same time. For example,

a muon passing through the detector will likely produce triggers in more than one crystal, whereas $0\nu\beta\beta$, for which the only detectable energy is in the form of electrons, most likely happens within a single crystal. We call events that happen simultaneously *coincident* events, and the number of crystals involved in an event `Multiplicity`. A more detailed description of the coincidence analysis is given in chapter 5.

3.1.6 Blinding

The final step of the data processing is the blinding of the ROI. The blinding procedure is designed to mask any possible signal or fluctuation at $Q_{\beta\beta}^{130Te}$, in order to optimize the analysis procedure without bias. We use a form of data salting that randomly shifts the reconstructed energy of a fraction of events at the 2615 keV line by -87 keV to around $Q_{\beta\beta}^{130Te}$ and the same fraction of events from $Q_{\beta\beta}^{130Te}$ by +87 keV. Since the number of events under the ^{208}Tl line is much higher than that near $Q_{\beta\beta}^{130Te}$, this procedure creates an artificial peak in the ROI with the shape of a true signal peak. Each event's true energy is encrypted and stored, and only at the end of the analysis the unblinding procedure restores it to its original value.

3.2 Data selection, signal efficiency

Once the data processing is complete, we select the event of interest for our analysis with a set of cuts. These cuts mainly fall into three categories: time-based, event-based and multiplicity-based cuts.

3.2.1 Time-based cuts

We remove from the data time intervals where the detector behaviour was non-ideal (*Bad Intervals*); this either involves a single bolometer (for example during a period of excessive noise) or the whole tower (quick temperature fluctuations, due for example to an earthquake). The total exposure reduction due to this cut is around 3.5%. Additionally, we remove from the data the time intervals where some part of the data production procedure failed, for example when the TGS algorithm fails (section 3.1.2. This leads to the loss of an additional 2.7% of the total exposure.

3.2.2 Event-based cuts

We implement a set of event-based cuts that remove events that are either non-signal-like or are in some way not handled well by the data processing software. A first, basic set of cuts removes events which are clearly problematic, such as events that exceed the

dynamic range of the detector (due, for example, to high energy muons) or events that show more than one trigger in the 5 seconds window (pile-up). The pulse shape discrimination algorithm (section 3.1.2) removes additional pulses based on their resemblance to the average pulse.

The total number of signals in our data, N_{Tot}, is made up both by signals due to particle interactions (physical pulses), N_{Phys}, and spurious signals, N_{Sp}; after the application of cuts, both these quantities are reduced to N_{Sp}^{Cut} and N_{Phys}^{Cut}. The aim of the pulse shape cuts is to decrease N_{Sp}^{Cut} while keeping N_{Phys}^{Cut} as high as possible. We define the efficiency of pulse shape cuts, ϵ_{PS} as:

$$\epsilon_{PS} = \frac{N_{Phys}^{Cut}}{N_{Phys}}. \tag{3.5}$$

This efficiency is substantially constant at all energies above $\sim$ 100 keV and decreases steeply below this threshold. The calculation of this efficiency is discussed in section 4.4.

3.2.3 Multiplicity-based cuts

Multiplicity-based cuts use the `Multiplicity` variable to select events of use for a particular purpose. For example, the anti-coincidence cut used for the $0\nu\beta\beta$ analysis involves the removal from the spectrum of events that happen on more than one channel at the same time: therefore, we require that `Multiplicity`==1. However, we have to account for the rejection of valid events that happen to be close in time to another, uncorrelated event, and are accidentally considered as coincident.

The efficiency of this cut is evaluated using the γ line from ^{40}K (figure 3.4). When the decay follows the electron capture branch, a single γ is emitted. Since there is no other correlated energy emission, when this γ is fully contained in a single detector it must be a `Multiplicity` 1 (M1) event; any coincident event with a 1.46 MeV γ from ^{40}K must come from an accidental coincidence.

We compare the number of events that fall under the 1.46 MeV peak in the M1 spectrum and in the global spectrum; the ratio between these two quantities gives us the efficiency of the coincidence cut, which comes out to be $99 \pm 1\%$.

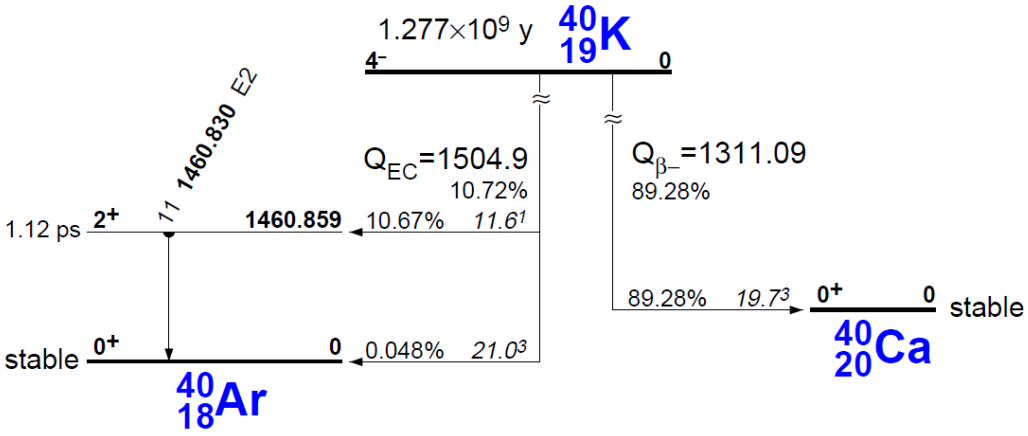

Figure 3.4: Decay scheme for ^{40}K. The decay follows two possible branches: a β^- decay on ^{40}Ca ($\sim$ 89% b.r.) and an electron capture decay on ^{40}Ar ($\sim$ 11% b.r.). About 96% of the EC decays end up on an excited state of ^{40}Ar, leading to the emission of a 1.46 MeV γ. Since only one γ is emitted, if it is fully contained within one crystal it must be a M1 event.

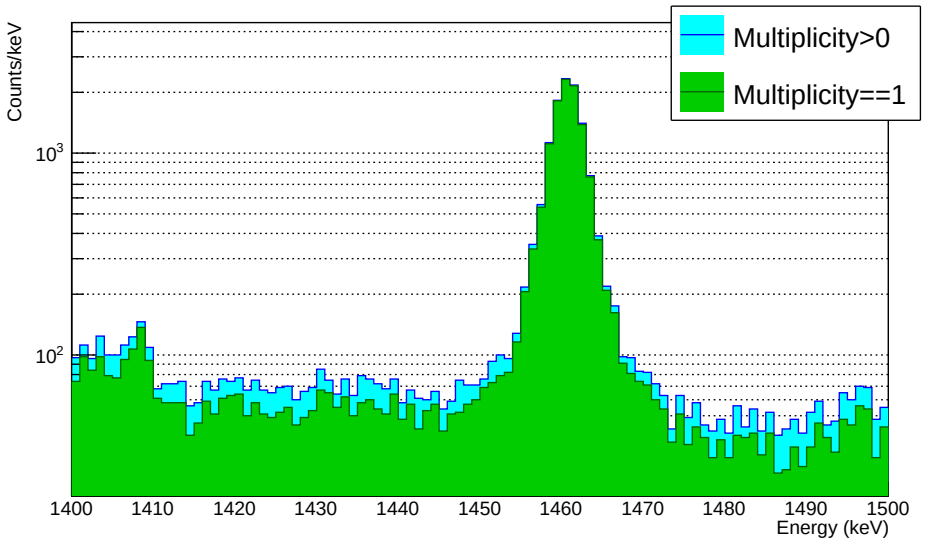

Figure 3.5: 1.46 MeV γ line from ^{40}K, shown in M1 (blue) and in the global spectrum (green).

CHAPTER

4

PULSE SHAPE ANALYSIS

The CUORE-0 data contains both events caused by particle interactions and spurious signals due, for example, to noise spikes. Even particle-related events can have their energy estimated poorly, due to possible deformations in their line shape that alter the amplitude evaluation (figure 4.1). We need to selectively reject events that belong in these categories, and we need to do so with the maximum possible efficiency. The quality of a signal can be evaluated thanks to several parameters that correspond to peculiar features of the pulse itself, such as the signal rise or decay time or the slope of the baseline on which the pulse grows. These pulse shape parameters can be used to discriminate *good* and *bad* signals. In this chapter I'll describe the procedure I worked on, and that has been used in the official CUORE-0 analysis, that makes this discrimination possible.

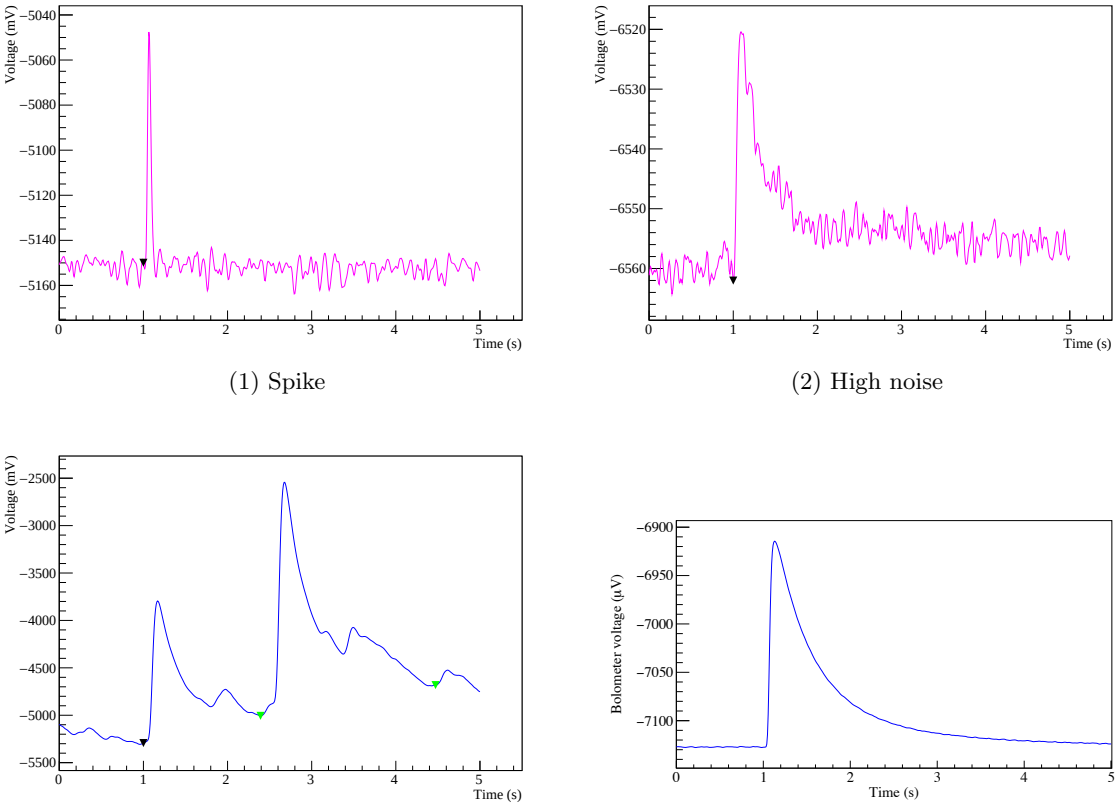

(1) Spike

(2) High noise

(3) Pile-up

(4) Clean signal

Figure 4.1: Examples (extracted from CUORE-0 data) of possible signals in CUORE-0. Among these, only (4) is useful for the final analysis, as it lies on a flat baseline and shows no deformation.

4.1 Pulse shape parameters

The first step of the pulse shape analysis (PSA) is the choice of which variables to use to best characterize a signal. We chose a set of six shape parameters that measure most of the features of physical pulses:

- `RiseTime`: the time required by the signal to rise from 10% to 90% of its amplitude;
- `DecayTime`: the time taken by the signal to decay from 90% to 30% of its amplitude;
- `BaselineSlope`: the slope of the pretrigger window just before the pulse;
- `Delay`: the time interval between the beginning of the pulse window and the pulse maximum;

- `TVL,TVR`: χ^2 values obtained by comparing the signal to the average pulse, calculated respectively on the left (`TVL` = *Test Value Left*) and on the right (`TVR` = *Test Value Right*) of the pulse maximum.

All shape parameters have a characteristic energy dependence (figure 4.2). These distributions are usually different from dataset to dataset and from channel to channel, but they retain the same general shape: for example, the `Delay` plot shown in figure 4.2:4 is always flat at high energy and drops at lower energies, but the position and the magnitude of the drop varies.

One of the common features is the broadening in the low energy region, which is due to the increasing contribution of noise to the parameter calculation. Another shared feature is the presence of outliers, which can either be spread out across the whole energy range or cluster together (as can be seen, for example, in the low energy region of the `Delay` vs. `Energy` plot in figure 4.2:4); these outliers represent the signals we wish to remove with appropriate cuts.

A simple solution would be to determine a lower and upper bound for each parameter and select events within these boundaries, regardless of energy. In the case of the *BaselineSlope* plot in figure 4.2:3, for example, this could work, as the parameter has a flat dependence on energy. In other cases however, such as the `TVL` or `TVR` plots (figure 4.2:5,6), fixing two boundaries would lead to two possible scenarios:

1. the bounds are optimized in order to maximize the rejection of outliers in a particular energy region, for example near $Q_{\beta\beta}$; the cut is efficient in that region, but removes a huge fraction of physical data at lower energies;

2. the bounds are broader, in order to maximize the amount of phisical data that is retained in the final spectrum; this way, the cut is almost meaningless, as most of the outliers would be kept in the data.

The PSA algorithm aims to model the energy dependence of pulse shape parameters, in order to set an energy-dependent cut that maximises efficiency and avoids the removal of large numbers of physical events.

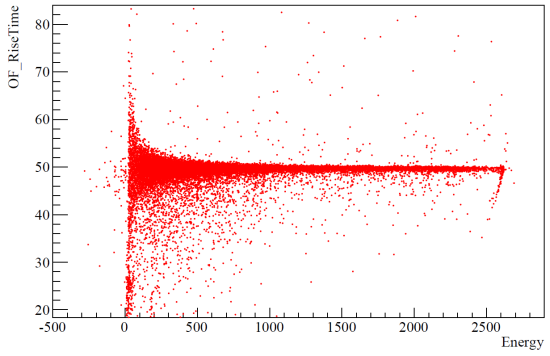

(1) Rise time

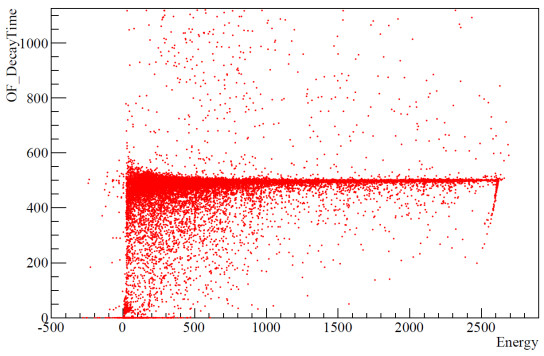

(2) Decay time

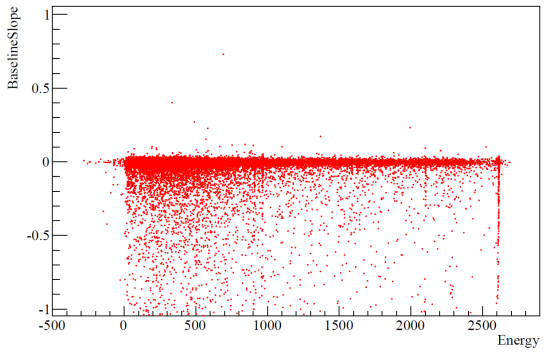

(3) Baseline slope

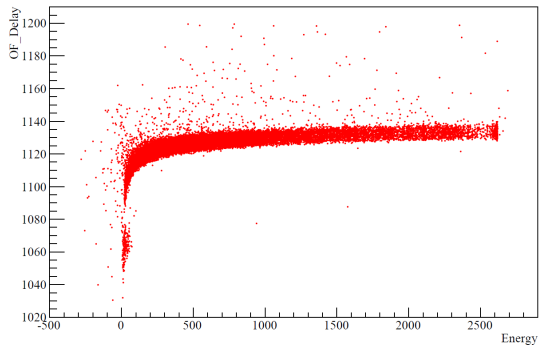

(4) Delay

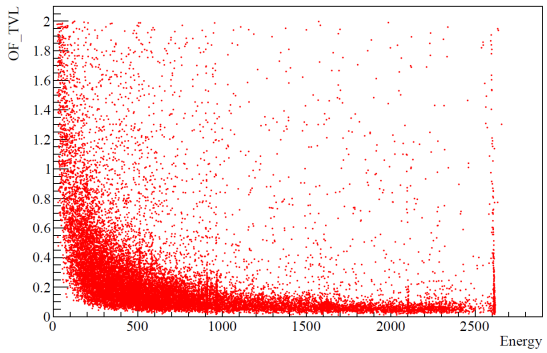

(5) TVL

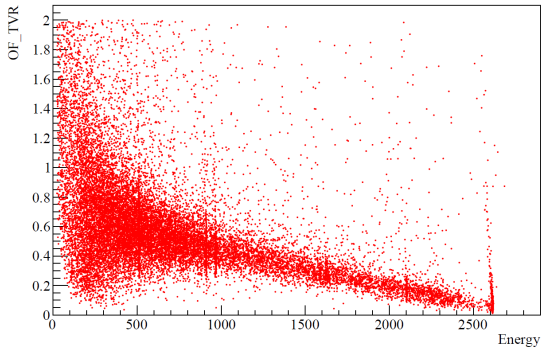

(6) TVR

Figure 4.2: Example energy dependence for the six pulse shape parameters, taken from a calibration measurement on a single channel. The shapes of these distributions can, in principle, change from dataset to dataset and from channel to channel.

4.2 Parameters linearization procedure

Parameter distributions such as the ones shown in figure 4.2 exhibit both a mean value and a width that are energy dependent. The goal of the procedure here described is to

remove this dependence through a linearization of the parameters, in order to obtain a flat distribution with constant width at all energies. The procedure can be summarized as follows:

1. the required energy range is split into bins;
2. for each obtained slice the average value and the width of the distribution are calculated;
3. ad-hoc functions are used to fit the energy dependence of both the average and the width;
4. a new, linearized pulse shape parameter is calculated for each data point.

The energy range under consideration is the one below 6 MeV, since there are substantially no events above this point; the low energy boundary is forced by the detection threshold of the detector. This energy range is, at first, split into 50 keV wide regions. If the number of data points contained in a slice is below a certain threshold the bin is merged with the following one, until either the required number of points is satisfied or the upper energy threshold is reached. This procedure ensures that each bin contains sufficient statistics to estimate the average and the width; the threshold value was set to 15 points per bin by simple trial and error. In order to improve statistics, both background and calibration data are used for this analysis.

The event distribution within an energy bin is often characterized by the superposition of a roughly bell-shaped distribution, mostly made up by physical events, and of a long tail, containing the non-physical or deformed pulses that need to be removed (figure 4.3). For this reason, the central value of the distribution cannot be estimated by a simple average, as this estimator would be strongly influenced by the presence of the tail. The median, on the other hand, is a better estimator for this kind of distribution; consequently, the width is estimated with the median absolute deviation (MAD).

Clusters of events that lie outside of the main distribution, such as the one shown in the low energy region in figure 4.2:4, contain mostly non-physical events: they can alter the median and lead to a wrong characterization of the energy dependence. The inclusion of these clusters can be avoided by using events from the `Multiplicity`==2 (M2) spectrum, for reasons that will be explained shortly.

`Multiplicity` has already been described in chapter 3 as a variable that keeps track of the number of crystals that have a signal trigger at the same time. Using M2 events, therefore, means that only events that involve two crystals at the same time are used. The distributions of pulse shape parameters obtained with M2 events are, in principle,

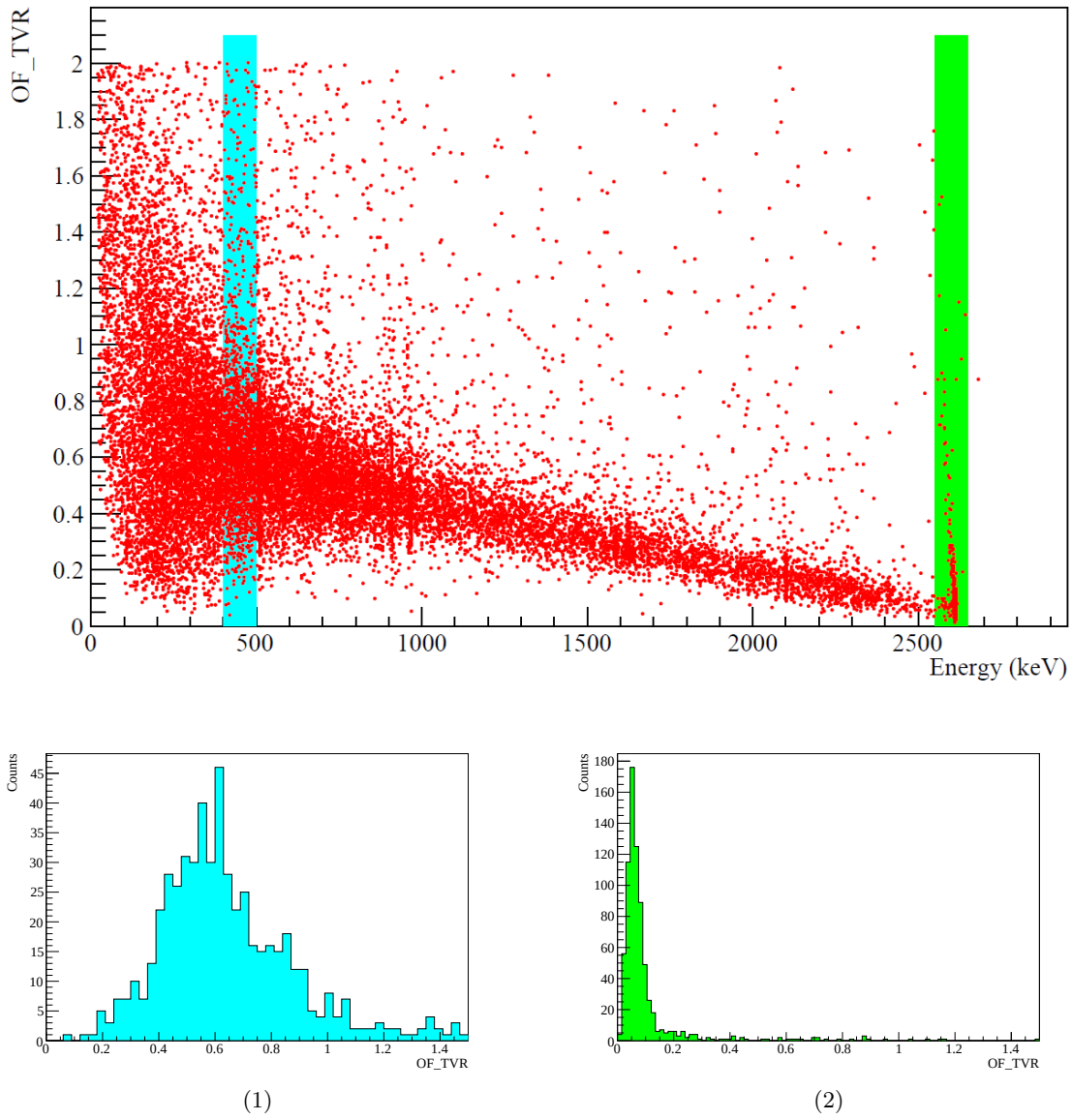

(1) (2)

Figure 4.3: Example `TVR` distribution in two energy regions. The median and the MAD of these distributions will be used to characterize the energy dependence in the relative region.

identical in shape to those obtained using any event: the presence of a simultaneous event on another channel doesn't alter the pulse shape.

M2 events can either come from a *real* coincidence (for example, a photon that undergoes Compton scattering in a crystal and is then absorbed in another) or from an *accidental* one, caused by the random occurrence of two signals at the same time. Since the objective is the removal of clusters of non-physical events, the issue only comes from

accidental coincidences, as real coincidences contain physical events by definition.

As will be shown in detail in chapter 5, the fraction of accidental coincidences in the M2 spectrum is $< 1\%$ in background data and $\sim 10\%$ in calibration data. Among these, a fraction is produced by the random occurrence of two physical events at the same time which, again, are not relevant for the problem at hand. This means that, regardless of the number of spurious events present in the total spectrum, only a small fraction ends up in the M2 spectrum. As it can be seen in figure 4.4, the aforementioned cluster disappears when M2 data is used: in order to maximize the capability of the PSA algorithm to reconstruct the energy dependence of shape parameters, M2 events are the best choice.

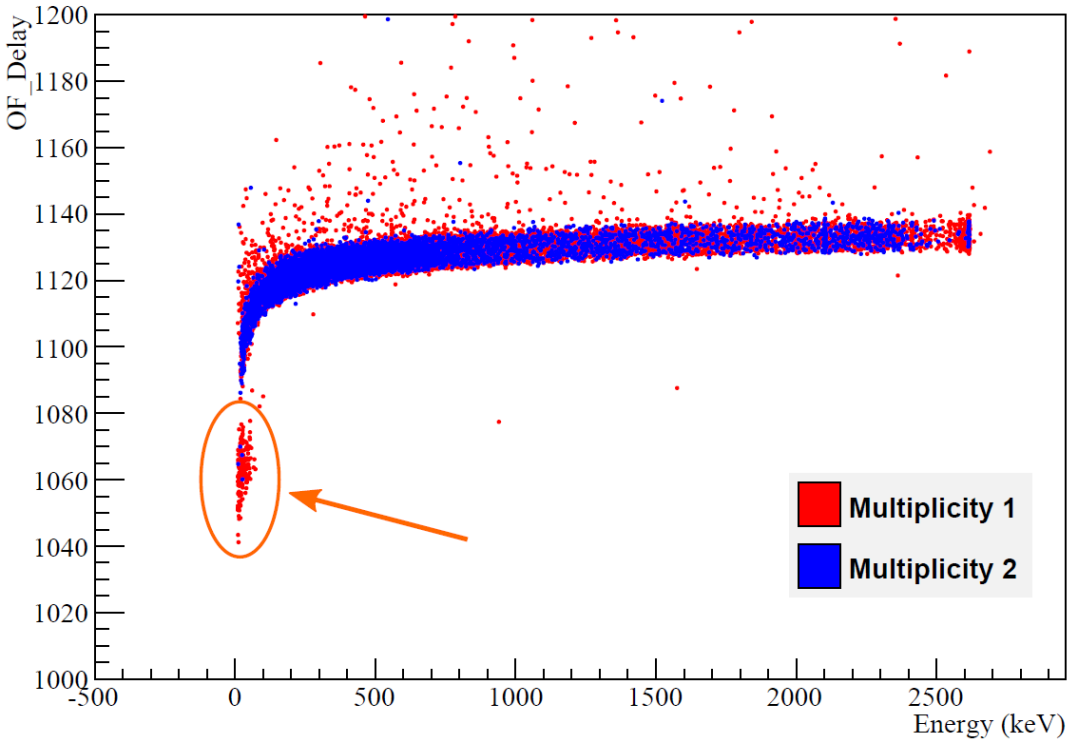

Figure 4.4: Comparison between the event distributions of M1 and M2 events. The cluster of events we wish to remove, highlighted in the circle, is not present in the M2 distribution.

After the median values are calculated for each bin their energy dependence is obtained by fitting(figure 4.5); since no model can currently predict the shape of the parameter distributions, fenomenological functions are used instead. The same process is repeated for the MAD dependence on energy.

Once the energy-dependent functions for the parameter average ($P_{Avg}(E)$) and for the MAD ($MAD(E)$) are obtained, the linearized parameters P_{lin} are calculated for each data

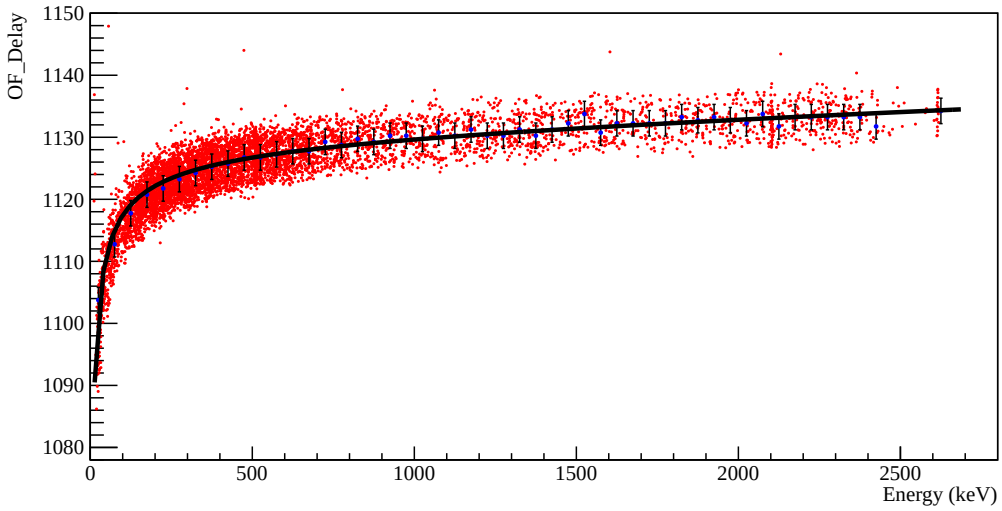

Figure 4.5: Example fit of the `Delay` distribution. The fit model is a square root function summed to a first degree polynomial.

point i as

$$P^i_{lin} = \frac{P^i - P_{Avg}(E)}{MAD(E)}. \tag{4.1}$$

These new, linearized variables (which are called `NormTVL`, `NormTVR`, etc.) are evenly distributed around 0 at any energy, at least for physical pulses, as can be seen in figure 4.6.

With the sole exception of `Delay`, every shape parameter has asymmetrical outliers, either below (`RiseTime`, `DecayTime`, `BaselineSlope`) or above (`TVL`, `TVR`) the main distribution. These outliers are not the same events for every distribution: outliers for one parameter may lie in the middle of the distribution for another. Different shape parameters are useful at identifying different types of *unwanted* signals, and we can use the location of the aforementioned outliers to understand this:

- outliers from the `NormRiseTime` and `NormDecayTime` distribution have predominantly negative values. These events have rise/decay times faster than the average, and are likely noise spikes;
- the `NormBaselineSlope` distribution also has negative outliers. Since the slope of the baseline is centered at 0 (figure 4.2(3)), these events grow on a downwards baseline; pile-up events that rise on the tail of a previous pulse share this trait. Since the temperature (and, therefore, the thermal gain) is changing in the time

period where these pulses rise, their amplitude reconstruction is likely wrong.

- `NormTVR` and `NormTVL` distributions have positive outliers. Since both TVL and TVR are χ^2 values, these events are the least similar to the average pulse, and are therefore either deformed (leading to an incorrect amplitude estimate by the Optimum Filter) or non-physical.

Some parameter distributions show prominent structures in the energy region below $\sim$ 100 keV, visible especially in the `NormRiseTime` and `NormDecayTime` plots. These clusters contain spurious events that are not efficiently identified by said parameters; setting a cut on `NormRiseTime` only would not get rid of them. On the other hand, some other parameter (for example, `NormTVR`) might be more efficient in removing that particular cluster: for this reason, all cuts on pulse shape parameters must be optimized and applied together.

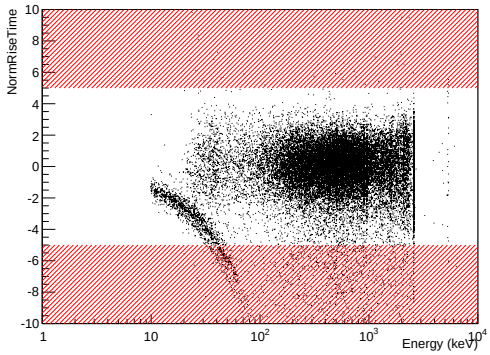

(1) `NormRiseTime`

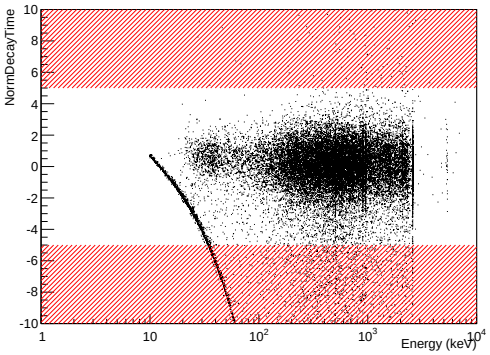

(2) `NormDecayTime`

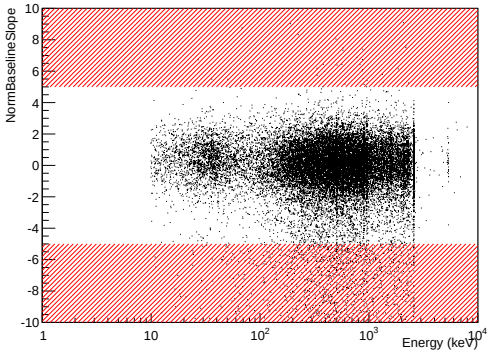

(3) `NormBaselineSlope`

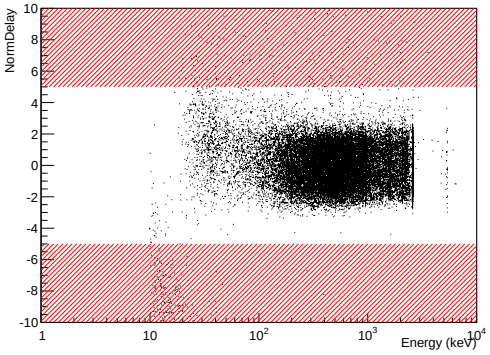

(4) `NormDelay`

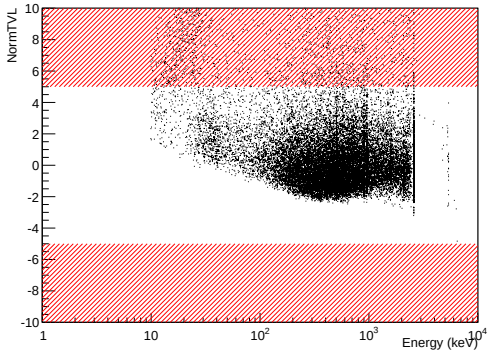

(5) `NormTVL`

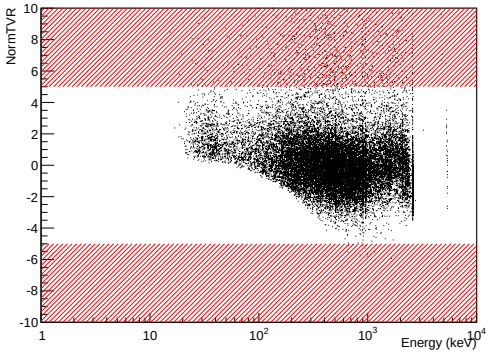

(6) `NormTVR`

Figure 4.6: Normalized parameter distributions. The red bands lie at ±5·MAD.

4.3 Cut optimization

After linearizing the distribution of pulse shape parameters, outliers need to be removed with the maximum possible efficiency. In order to exclude non-physical events from the spectrum acceptance levels on the normalized pulse shape parameters have to be set. For instance, only events for which `NormTVL` lies between -5 and 5 could be accepted; looking at figure 4.6:5, this is the same as requiring that any point that lies in the red region is excluded from the final spectrum.

Whichever value is chosen as a boundary, both non-physical and physical events would be removed: the former naturally lie outside the distribution; the latter because of the small fraction that, statistically, lie far away from the median value. The boundary choice has to be optimized in order to find the best equilibrium between those two effects.

Events that lie under a peak in the spectrum, produced either by a γ or α particle, are likely coming from physical pulses. Non-physical or deformed events can, in principle, have their energy at any value, ending up at any point in the continuum over which peaks grow. The number of events under a peak can be estimated by taking the integral of the energy spectrum in a region around it, for example within $\pm 3\sigma$ from the mean energy of the peak. The continuum does, however, inflate this integral; its contribution can be estimated by taking the integral in the background regions close to the peak and scaling this number to the size of the energy interval where the signal integral has been taken (figure 4.7).

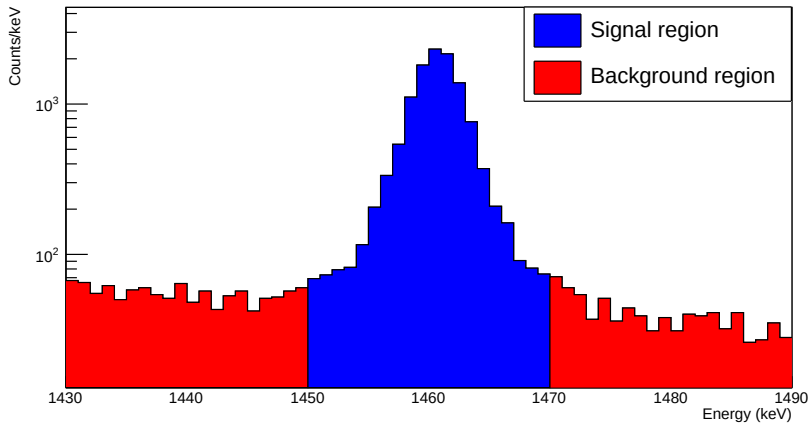

Figure 4.7: Regions used to estimate the number of events under a peak. The integral in the background region (red) is used to estimate the contribution of background to the signal region (blue).

If we call N_s^{tot} the number of events under any peak (after background subtraction)

before the application of cuts and n_s^{cut} the same number evaluated after cuts, we define the *signal efficiency* ϵ_s as

$$\epsilon_s = \frac{n_s^{cut}}{N_s^{tot}}. \tag{4.2}$$

This number represents the fraction of physical events that isn't affected by cuts. Similarly we define the *background efficiency* ϵ_b as

$$\epsilon_b = \frac{n_b^{cut}}{N_b^{tot}}, \tag{4.3}$$

where N_b^{tot} and n_b^{cut} are the number of events in a region of the spectrum without any visible peak, before and after the application of cuts.

Since ϵ_s has to be maximized to keep most physical pulses in our spectrum and ϵ_b must be minimized to remove badly reconstructed and non-physical events, a *score* S can be assigned to the peak by taking the ratio

$$S = \frac{\epsilon_s}{\sqrt{\epsilon_b}}. \tag{4.4}$$

By varying the cut levels for normalized pulse shape parameters the value of S is modified; given the above considerations, S must be maximized to obtain the best performance.

Ideally S should be the same across the whole spectrum, due to the cut linearization procedure; since fit functions are chosen heuristically, this is not always the case (see, for example, the residual energy dependence of `NormTVR` in figure 4.6:6). In order to optimize the cuts across the whole energy spectrum a set of 8 peaks is chosen, ranging from 146 to 5450 keV[1], and the total is score given by:

$$S_{tot} = \sum_{i=1}^{8} S_i = \sum_{i=1}^{8} \frac{\epsilon_s^i}{\sqrt{\epsilon_b^i}}, \tag{4.5}$$

where the sum is performed over the 8 peaks. The background contribution to the peak integral is calculated by integrating the continuum in the peak sidebands, at lower and higher energies; these regions have widths ΔE_{low} (containing n_{low} events) and ΔE_{high} (containing n_{high} events) respectively. The background efficiency ϵ_b^i is then given by:

[1]Specifically, the γ lines at 146, 511, 911, 1460, 2204 and 2615 keV, and the α lines at 3290 and 5450 keV.

$$n_{avg} = 0.5 \cdot \left(\frac{n_{low}}{\Delta E_{low}} + \frac{n_{high}}{\Delta E_{high}} \right),$$
$$\epsilon_b = \frac{n_{avg}^{cut}}{n_{avg}^{tot}}, \tag{4.6}$$

where the convention for n^{cut} and n^{tot} is the same used in equation 4.3. The region around the peak of width ΔE_{peak} contains n_{peak} events; the signal efficiency ϵ_s is then:

$$n_{bkg} = \frac{n_{avg}}{\Delta E_{peak}},$$
$$\epsilon_s = \frac{n_{peak}^{cut} - n_{bkg}^{cut}}{n_{peak}^{tot} - n_{bkg}^{tot}}. \tag{4.7}$$

Different sets of cut levels are tested in order to find the maximum value of S_{tot}. As pointed out in section 4.2, outliers from the parameter distributions have common features: specifically, outliers for `NormTVR` and `NormTVL` tend to have positive values, whereas outliers for the other parameters tend to have negative values. For this reason, the cut boundaries are asymmetric, in order to have a different threshold for negative and positive outliers; additionally, the same cuts are set for parameters with common features. This way only four values have to be determined, TV_{low}, TV_{high}, O_{low} and O_{high} (where O stands for *Other*), so that

$$TV_{low} < \texttt{NormTVR} < TV_{high}$$
$$TV_{high} < \texttt{NormTVL} < TV_{high}$$
$$O_{low} < \texttt{NormBaselineSlope} < O_{high}$$
$$O_{low} < \texttt{NormRiseTime} < O_{high}$$
$$O_{low} < \texttt{NormDecayTime} < O_{high}$$
$$O_{low} < \texttt{NormDelay} < O_{high}.$$

The values of the four parameters are varied between 3 and 6 in 0.05 steps, evaluating the score S_{tot} for each permutation. Since the maximum value of S_{tot} was obtained with $TV_{high} = 6$ and $O_{low} = 3$, both at their limits, their range was extended in order to look for a better maximum: TV_{high} varied between 3 and 7, whereas O_{low} between 2 and 6.

The dependence of S_{tot} on the various parameters is shown in figure 4.8; each plot shows the maximum S_{tot} value obtained by varying three parameters, as a function of the fourth.

There are a few considerations to be made regarding the plots shown in figure 4.8, all in agreement with what was expected from them. In the S_{tot} vs. TV_{low} plot, a saturation

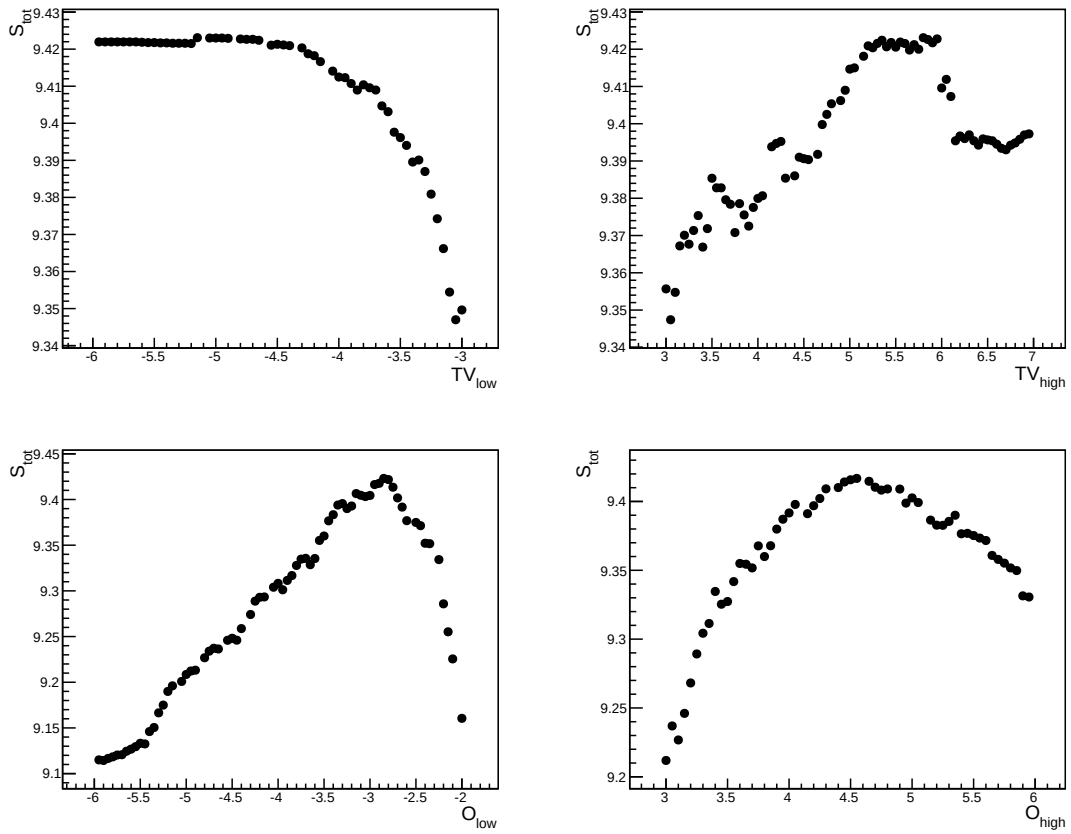

Figure 4.8: Dependence of S_{tot} on TV_{low}, TV_{high}, O_{low} and O_{high}. Each data point is obtained by maximizing the score with the other three parameters only.

effect sets in for values of TV_{low} below ~ -4.5. Since both the `TV` parameters are χ^2 values, most of the outliers should have positive `NormTV` (pulses that don't look like the average pulse have high chi^2 values). Negative values come predominantly from tails of the physical pulses distribution. Therefore, no improvement in S_{tot} can be found by pushing TV_{low} below a certain value, after ∼all the physical pulses have been included. The value of O_{low} for which S_{tot} reaches its maximum is, taken as an absolute value, lower than all other parameters; since the outliers for `NormRiseTime`, `NormDecayTime` and `NormBaselineSlope` have mostly negative values (figure 4.6(1,2,3)), a more stringent cut is preferred in order to eliminate most of them.

The maximum score is obtained with the following values, which are used as the final threshold cuts for pulse shape parameters:

$$TV_{low} = -5.1 \qquad TV_{high} = 5.8$$
$$O_{low} = -2.85 \qquad O_{high} = 4.6.$$

4.4 Cut efficiency

The application of pulse shape cuts implies the removal of a small fraction of physical events. This has to be taken into account in order to be able to reconstruct the real event rate of any process of interest. We define the pulse shape cut efficiency as the fraction of real signal events that remain in the data after the application of pulse shape cuts. As already stated before the M2 spectrum is a good place to look for physical pulses, as the accidental coincidences probability in our system is very low. The selection can be further improved by requiring that the sum of the energies of an M2 couple lies within a small range of one of the main γ lines in the spectrum.

This time, only the background data is used to estimate the efficiency. Calibration data, while still useful for the optimization of cut levels, contains a higher fraction of pile-up events and would artificially decrease the efficiency. Also, since the amount of data on single channels in background runs is low, the total spectrum is used and a single, global efficiency for the whole tower is calculated.

Some of the most intense γ lines in the spectrum, ranging from 911 to 2615 keV, are chosen for the efficiency calculation: only M2 events whose total energy lies within 3σ of one of these lines are kept into account (figure 4.9).

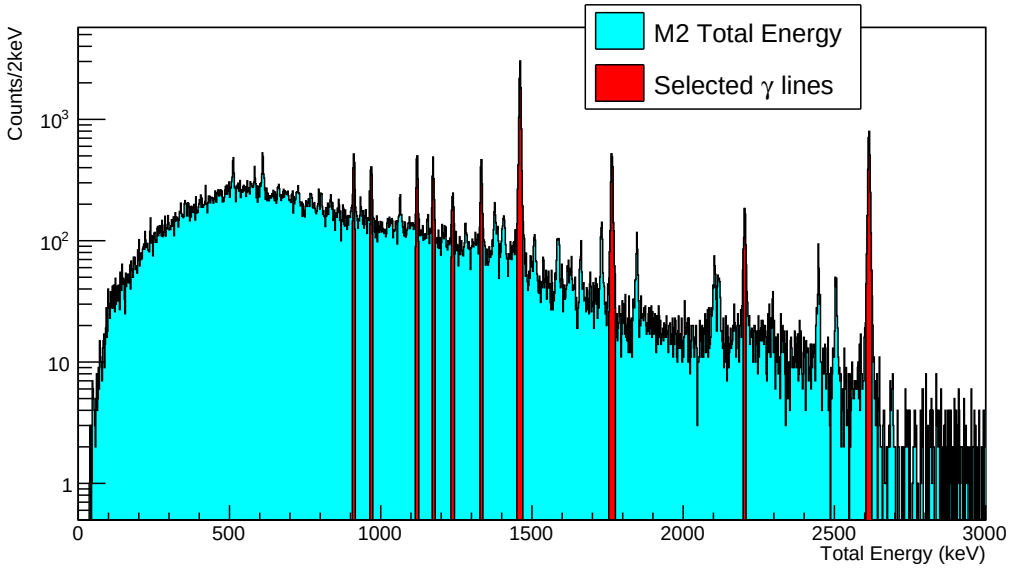

Figure 4.9: M2 Total Energy spectrum from CUORE-0; the γ lines used for the efficiency analysis are highlighted.

The efficiency ϵ_{ps} is estimated simply by taking the ratio of the number of events

accepted after the application of pulse shape cuts (N_{acc}) and in the total spectrum (N_{tot}), with the thresholds chosen during the optimization procedure. In order to evaluate the efficiency energy dependence, the data is split into 5 keV wide energy bins and the efficiency is calculated for each of them.

Since the events that make up the spectrum after cut applications are also present in the total spectrum, N_{acc} and N_{tot} are heavily correlated. Therefore, the error on ϵ_{ps}, $\sigma_{\epsilon_{ps}}$, cannot be calculated by simply taking

$$\sigma_{\epsilon_{ps}} \neq \frac{N_{acc}}{N_{tot}} \sqrt{\frac{1}{N_{acc}} + \frac{1}{N_{tot}}}. \tag{4.8}$$

If N_{rej} is the number of events rejected after the application of pulse shape cuts, N_{tot} can be written as as $N_{tot} = N_{acc} + N_{rej}$. Since N_{acc} and N_{rej} are now made up by different events, we can rewrite ϵ_{ps} and $\sigma_{epsilon_{ps}}$ as:

$$\begin{aligned} \epsilon_{ps} &= \frac{N_{acc}}{N_{tot}} = \frac{N_{acc}}{N_{acc} + N_{rej}} \\ \sigma_{epsilon_{ps}} &= \sqrt{\left(\frac{\partial \epsilon_{ps}}{\partial N_{acc}} \cdot \sigma_{N_{acc}} \right)^2 + \left(\frac{\partial \epsilon_{ps}}{\partial N_{rej}} \cdot \sigma_{N_{rej}} \right)^2} \\ &= \sqrt{\frac{N_{acc} \cdot N_{rej}}{(N_{acc} + N_{rej})^3}}. \end{aligned} \tag{4.9}$$

Figure 4.10 shows the efficiency evaluated in the 0-1000 keV energy range; the distribution is fitted with a simple exponential function superimposed to a flat background, $p0 + p1 \cdot e^{p2 \cdot E}$.

The efficiency of pulse shape cuts is substantially constant at 94.1% almost in the whole energy range, with the exception of the region below $\sim$ 80 keV. This number is slightly different than the one used in the standard CUORE-0 analysis, 93.7%: this is because the official data processing was done with an older version of the PSA code, which produced a slightly lower efficiency. Since all the analysis in this thesis is done with official CUORE-0 data, the correct 93.7% efficiency will be used for the rest of this thesis.

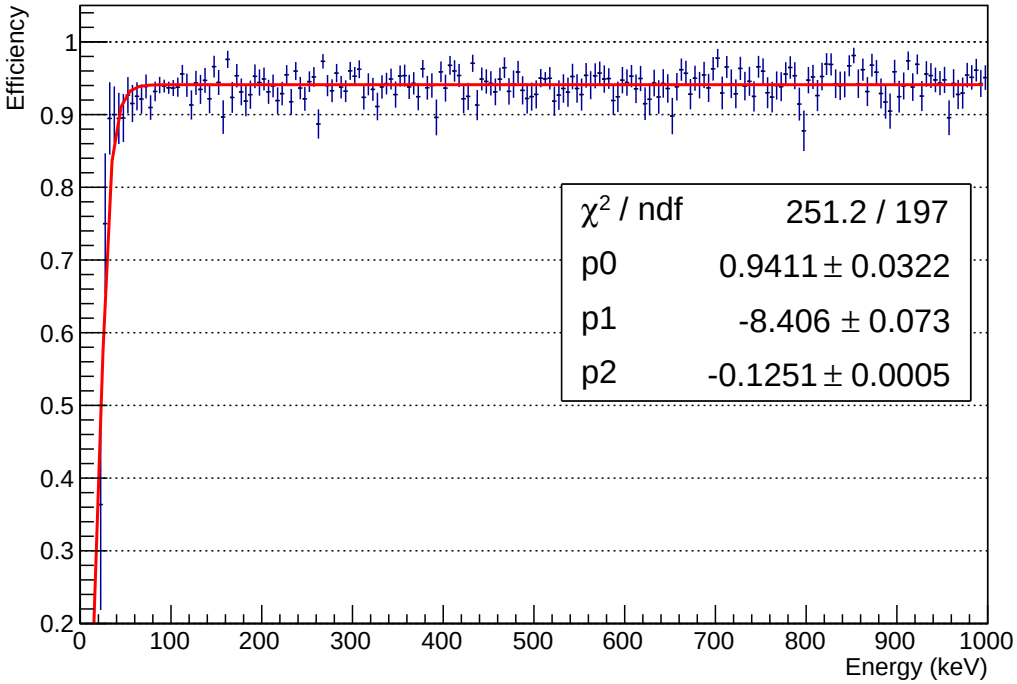

Figure 4.10: Pulse shape cut efficiency in the 0-1000 keV range. The fit function is an exponential with a flat background: $p0 + p1 \cdot e^{p2 \cdot E}$

4.5 Effect of cuts

As it was mentioned in section 4.2, after the parameter linearization some structures due to non-physical events showed up in the low energy region. This can be seen again in figure 4.11:1, where the `NormDecayTime` distribution is shown; even after the application of the optimized cut, whose boundaries are shown in red in the figure, part of the low energy structure would survive. `NormDecayTime` is not efficient in removing this particular cluster of events.

When all optimized cuts are applied together, however, the situation changes. Figure 4.11:2 shows the same `NormDecayTime` plot, but with all the pulse shape cuts applied. The low energy structure completely disappeared, removed by some other parameter.

Figure 4.12 shows the same plots from figure 4.2, but with all the optimized cuts in place. All the low energy structures that showed up before now disappear, leaving only a band of events distributed around zero, as expected. The `NormTVL` and `NormTVR` plots show some residual non-linearity due to imperfect choices in the fit functions, but the effect is small and easily compensated by the cut optimization procedure, which sets slightly higher

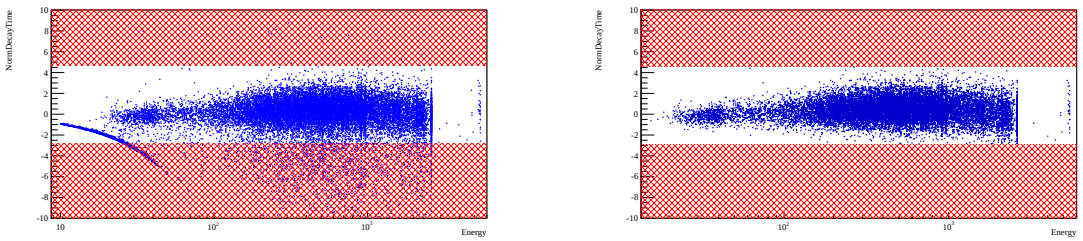

(1) `NormDecayTime`: No PSA cut

(2) `NormDecayTime`: All PSA cuts

Figure 4.11: Comparison between the `NormDecayTime` distribution before and after the application of all the PSA cuts combined. Most notably, the structure at low energy completely disappears. The red bands represent the region that would be removed with the application of the `NormDecayTime` cut only.

boundaries for these parameters.

Figure 4.13 shows the comparison between the M1 energy spectrum before and after the application of pulse shape cuts. The most prominent effects of the cuts can be seen in the low energy region, below ~ 500 keV, and near the 3.2 MeV α peak from ^{190}Pt. In the rest of the spectrum only a small fraction of events, most likely due to physical events, is lost, compatibly with the 94% efficiency of the algorithm.

The low energy region can be observed, zoomed in, in figure 4.14. All the structures visible in the total spectrum (the γ lines at $\sim 350, 300, 240, 150$ keV) remain unchanged in the cut spectrum, while the background that surrounds them is strongly reduced, making these γ lines more prominent in the spectrum. Additionally, some lower-energy structures that were completely submerged by background, such as the count excess around 100 keV (due to nuclear recoils of several α-decaying isotopes), are now visible.

Figure 4.15 shows a zoomed in plot of the ^{190}Pt α line. The shape of the peak changes visibly after the application of the pulse shape cuts, with the high and low energy tails of the peak disappearing. While the shape of the peak is clearly improved, the source of the removed tails is still not completely clear. A possible explanation has to do with how the CUORE-0 crystals were built.

^{190}Pt is a naturally occurring, unstable isotope, with a natural abundance of 0.01% and a half life of $6.5 \cdot 10^{11}$ years. Small fragments of platinum can end up in the bulk of the TeO_2 crystals during their growth. A decay coming from these small Pt inclusions can have a different shape than other pulses on the same channel. This, in turn, would lead to an improper amplitude reconstruction from the Optimum Filter, giving rise to the tails of the ^{190}Pt peak; the pulses in the tails are then identified and removed by the pulse shape algorithm. As an additional hint that the ^{190}Pt peak comes from slightly *odd* pulses, the

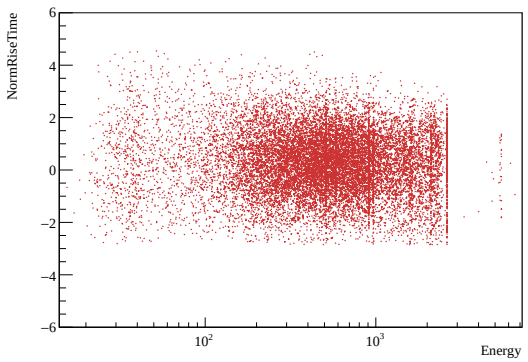

(1) `NormRiseTime`

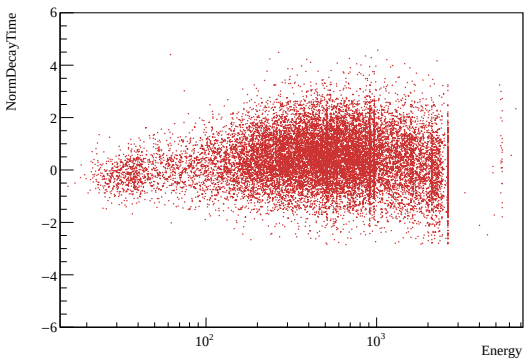

(2) `NormDecayTime`

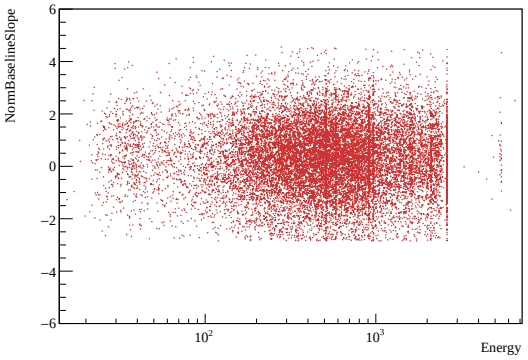

(3) `NormBaselineSlope`

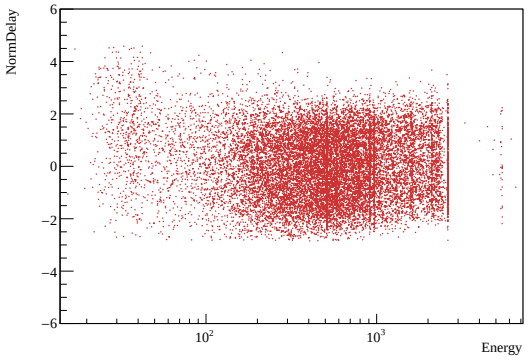

(4) `NormDelay`

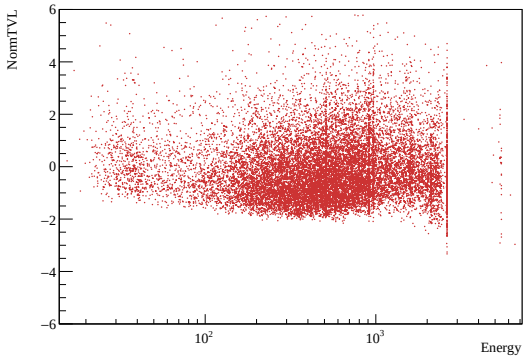

(5) `NormTVL`

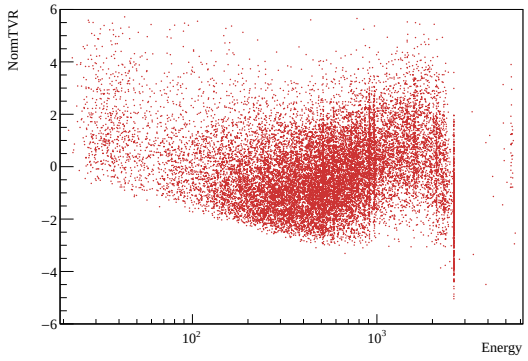

(6) `NormTVR`

Figure 4.12: Normalized parameter distributions after the application of the optimized cuts.

Q-value of its decay is 3249 keV, while the peak observed in the spectrum is about 50 keV

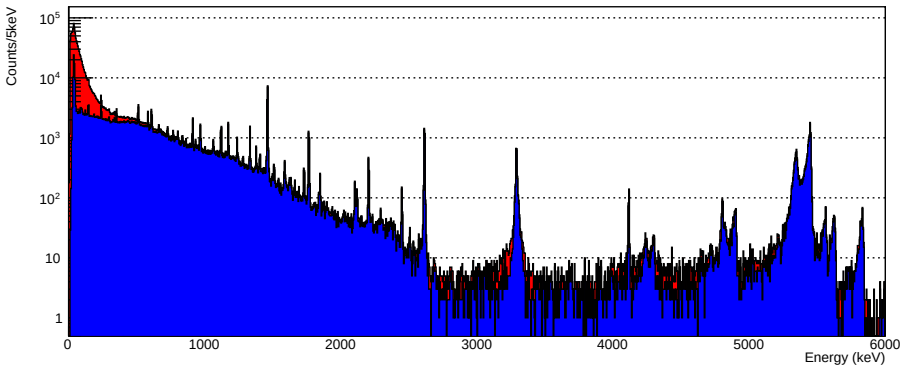

Figure 4.13: Effect of pulse shape cuts on the M1 spectrum. The total M1 spectrum is shown in red, the cut spectrum in blue.

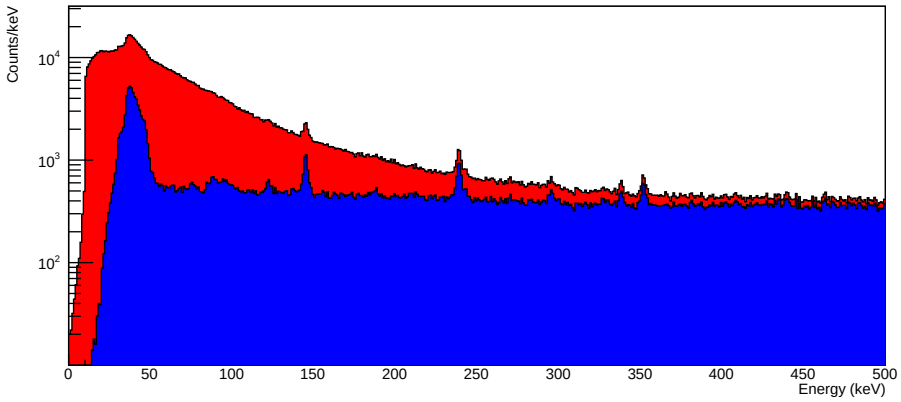

Figure 4.14: Effect of pulse shape cuts on the M1 spectrum, zoomed on the low energy region. The total M1 spectrum is shown in red, the cut spectrum in blue.

higher[2].

Finally, figure 4.16 shows the comparison between the total and the cut spectrum in M2. The effect of the cuts is much less evident here than in the M1 spectrum: only a small fraction of events is removed from the region below ~ 100 keV. This is in agreement with what was stated before: the M2 spectrum mostly contains physical events and, with the exception of a few pulses that suffered accidental deformations, most of it survives the application of the pulse shape cuts.

[2]Actually, all structures in the α region have slightly higher energy than expected, but the shift for ^{190}Pt is still inconsistent with what observed for every other line. This is discussed in more detail in chapter 8

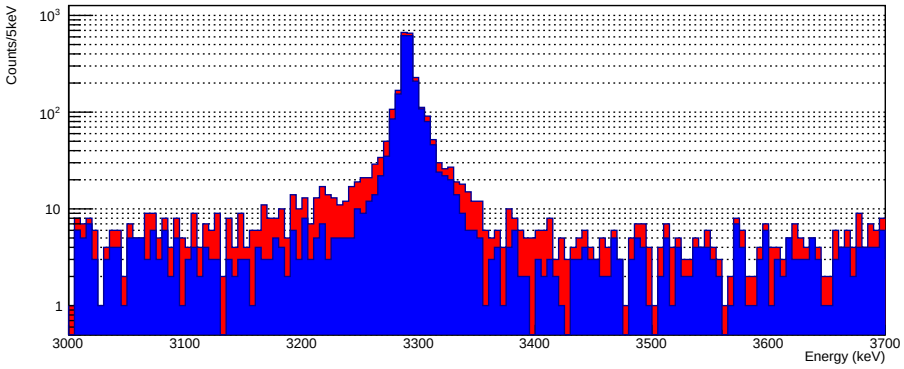

Figure 4.15: Effect of pulse shape cuts on the M1 spectrum, zoomed on the α region. The total M1 spectrum is shown in red, the cut spectrum in blue.

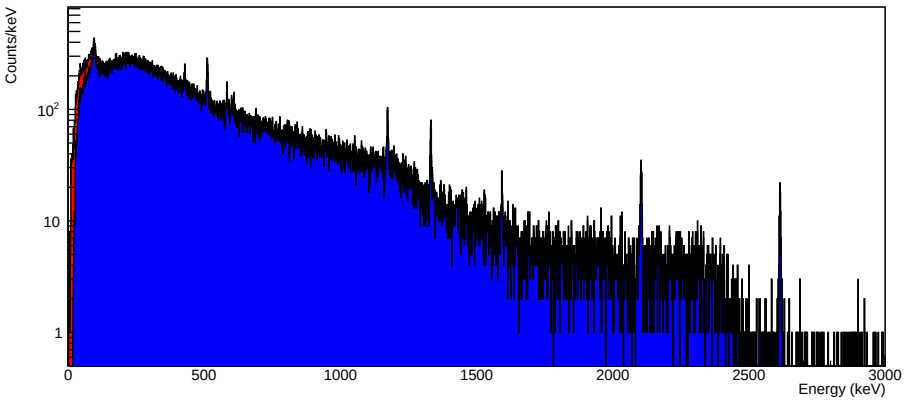

Figure 4.16: Effect of pulse shape cuts on the M2 spectrum. The total M2 spectrum is shown in red, the cut spectrum in blue.

CHAPTER

5

COINCIDENT EVENT ANALYSIS

The study of events that happen simultaneously on different crystals is fundamental for several purposes, including the $0\nu\beta\beta$ analysis (both on the ground and excited state) and the interpretation of the radioactive background, since it provides fundamental information for the identification and localization of sources. In this chapter I'll describe what causes simultaneous events, how they are identified and how they are influenced by the cuts used in the analysis.

5.1 Simultaneous events

Simultaneous events are produced when the same particle traverses more crystals (e.g. a cosmic muon) or, more often, when multiple particles are emitted in the same radioactive process. α, β or $\beta\beta$ radioactive decays often leave the daughter nucleus on an excited state; the de-excitation of this state can lead to the emission of a γ ray. If the de-excitation doesn't lead immediately to the ground state of the daughter nucleus, additional γs can be emitted in a cascade. Typical lifetimes of excited states are of the order of hundreds of picoseconds.

The rise time of signals in a TeO_2 detector is of the order of tens of milliseconds. This means that when two γs produced within less than a ns from each other (as in most γ decays) strike the detector, this time difference is way below the detector time resolution; effectively, they are simultaneous. A common example of γ cascade is the decay of ^{60}Co

on ^{60}Ni (figure 5.1): the decay branch with the highest probability ($> 99\%$) leads to the emission of a 1173 keV and 1332 keV γ in quick succession.

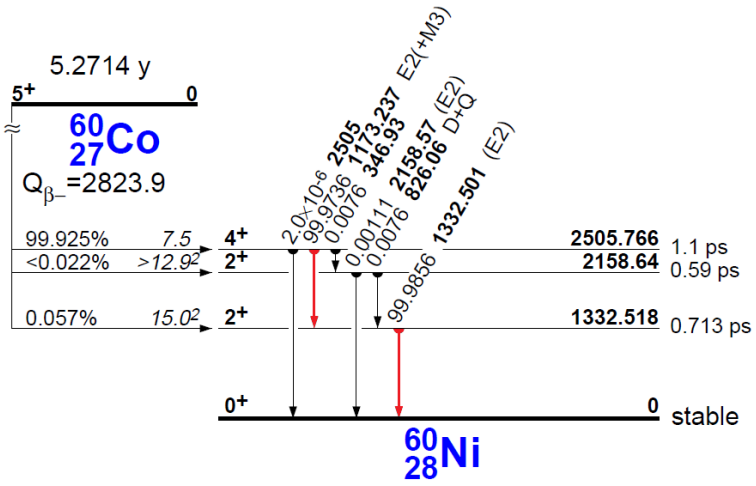

Figure 5.1: Decay scheme for ^{60}Co. The most probable branch ($> 99\%$, in red) leads to the emission of two γs in a quick cascade ($\Delta t < 1$ ns).

There are other possible situations, all coming from natural radioactivity, that can produce events in different crystals within a short timeframe:

- after an α decay occurring in a crystal, the recoiling nucleus can deposit energy in a crystal and the emitted α particle in another;
- a γ undergoing Compton scattering in a crystal and depositing the rest of its energy in another;
- a particle shower produced by a high energy muon interacting in the detector shielding;
- and so on.

Radioactivity is, however, not the only source of coincident events; they can also happen by chance, when two uncorrelated events strike the detector at the same time. These occurrences are called accidental coincidences.

A first estimate of the rate of accidental R_{acc} coincidences on the detector can be derived with simple probability laws. Assuming an uniform event rate across the whole tower, the rate on each channel is the same, R_{ch}. Given an event on channel A, the

probability of another event happening on another detector within a time window Δt is:

$$P = 1 - e^{-(N_{ch}-1)R_{ch}\Delta t}, \tag{5.1}$$

where the exponential is the Poisson probability of no event happening within Δt, N_{ch} is the total number of channels and the -1 is there to exclude the case where the additional events happen on channel A again. The rate of accidental coincidences across the whole tower is then given by

$$R_{acc} = N_{ch}R_{ch}\left(1 - e^{-(N_{ch}-1)R_{ch}\Delta t}\right). \tag{5.2}$$

Equation 5.2 provides a theoretical estimate of the accidental coincidences rate, assuming a uniform rate on all channels. When applied to experimental data, however, several factors can make it less precise, including the non-uniformity of event rate R_{ch} and the effect of some event-based cuts, which is analysed in more detail in section 5.4. Both effects are very significant for calibration runs but have a low impact on background data, as will be shown later; equation 5.2 can be used for background data with only a negligible error. A more precise way of directly measuring R_{acc} in both calibration and background data is described in section 5.3.

5.2 Finding coincidences

The simplest way of detecting simultaneous events is to define a coincidence time window Δt and, whenever an event happens, to look for other events within Δt. This was the method used for the Cuoricino analysis and in the early stages of CUORE-0. In both those cases, the chosen Δt was 100 ms.

From equation 5.1, the probability to have an accidental coincidence in CUORE-0, given an event rate $R_{ch} \simeq 0.001$ Hz (typical average value for background runs), $N_{ch} = 52$ and $\Delta t = 0.1$ s is roughly 0.5%. While this quantity is not necessarily troublesome for CUORE-0, it would cause a great deal of issues in CUORE, where the number of crystals increases to 988, leading to a $\sim 10\%$ probability of accidental coincidences; the coincidence window Δt needs to be lower.

The procedure adopted to efficiently reduce the coincidence window in CUORE-0 starts by considering `Multiplicity`==2 (M2) events where the sum of the two energies lies close to the 2615 keV line from ^{208}Tl (specifically, in the $2600 - 2630$ keV energy range). With the exception of a few accidental coincidences, these events are most likely produced by the Compton scattering of a 2615 keV photon in a crystal, followed by the deposit of the rest of the energy in another. Looking at the distribution of the time intervals between

each of these pairs of events (figure 5.2), a roughly gaussian structure centered around zero over a flat background, given by accidental coincidences, is expected. Instead, the distribution is broad between -50 and +50 ms, and characterized by several fine structure at specific time intervals.

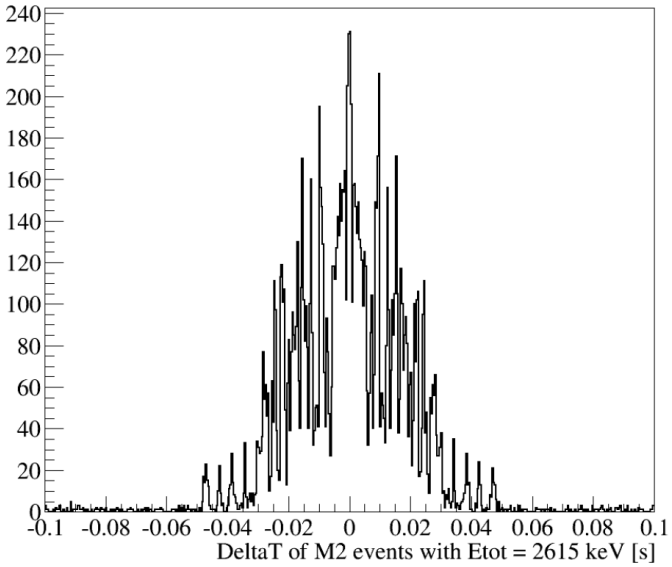

Figure 5.2: Distribution of Δt for M2 events whose total energy is around 2615 keV (taken from [59]). All data is taken from a calibration run.

Each channel has a different rise time t_{rise}: when two events are triggered on channels 1 and 2 the recorded time interval between depends on $\Delta t^{12}_{rise} = t^1_{rise} - t^2_{rise}$. Each pair of crystals has a characteristic Δt^{ij}_{rise}, leading to the substructures observed in figure 5.2; this characteristic rise time difference is the *jitter* between said channels.

Averaging the Δt of the same events described above (M2 events whose total energy is $\sim$ 2615 keV) the jitter between each pair of crystals can be estimated. This, however, cannot be done directly for far away crystal couples: the probability of a photon scattering in a crystal on the bottom floor of the tower and then being absorbed on the top floor is extremely low. To go around this, jitters are first calculated between detectors on the same floor; then, between neighboring floors by taking the crystal couple that leads to the smallest error; finally, a crystal on the bottom floor of the tower is arbitrarily chosen as reference, and the previously calculated variables are used to evaluate the jitter between each channel and the reference one.

The final distribution of Δt, narrower and more regular than the one in figure 5.2, is shown in figure 5.3.

The jitters calculated with the method described above are used to evaluate coinci-

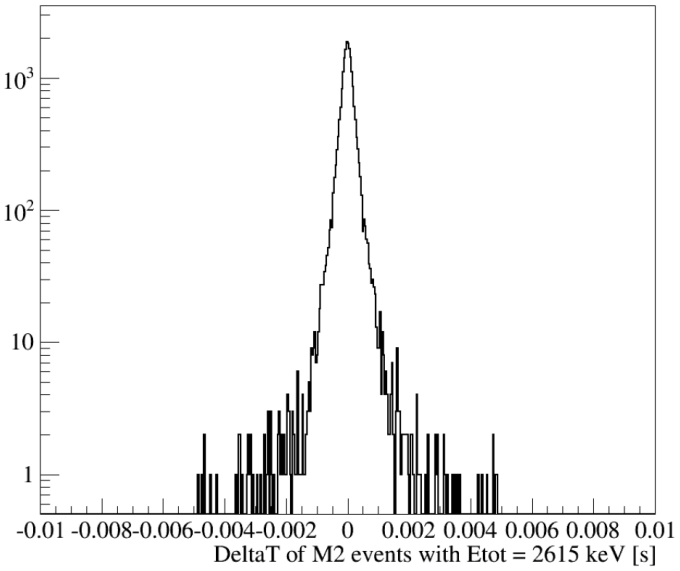

Figure 5.3: Distribution of Δt for M2 events whose total energy is around 2615 keV, after channel synchronization (taken from [59]). All data is taken from a calibration run.

dences with a much narrower time window of 10 ms; this reduced the accidental coincidence probability by roughly a factor of 10, consequently improving the anti-coincidence efficiency.

5.3 Measuring accidental coincidences

The evaluation of accidental coincidences that led to equation 5.2 doesn't take into account the different event rate on each channel and the effect of cuts on the data. I've worked on a simple method that considers all these effects by using the data production software directly.

The procedure is basically the opposite of what was described in section 5.2. The jitters are not calculated automatically by the software, but manually set to values much higher than normal: instead of being within the ± 50 ms range, the new values are all > 500 ms. When the data production software tries to correct event times to keep jitters into account, instead of synchronizing channels it de-synchronizes them. All events with a short-time correlation are decorrelated, meaning the final spectra do not contain any *real* coincidence. However, since the accidental coincidences rate R_{acc} depends only on the total event rate, and this de-synchronization procedure doesn't affect it, R_{acc} is not varied. The final spectrum allows a direct measurement of R_{acc}, having excluded any other coincidence.

At first this technique was used on a calibration run, to benefit from the increased statistics. Figure 5.4 shows the M2 spectrum evaluated with synchronized data (blue) and the one obtained with de-synchronized data (red). The spectrum of true coincidences is obtained by subtraction of the two.

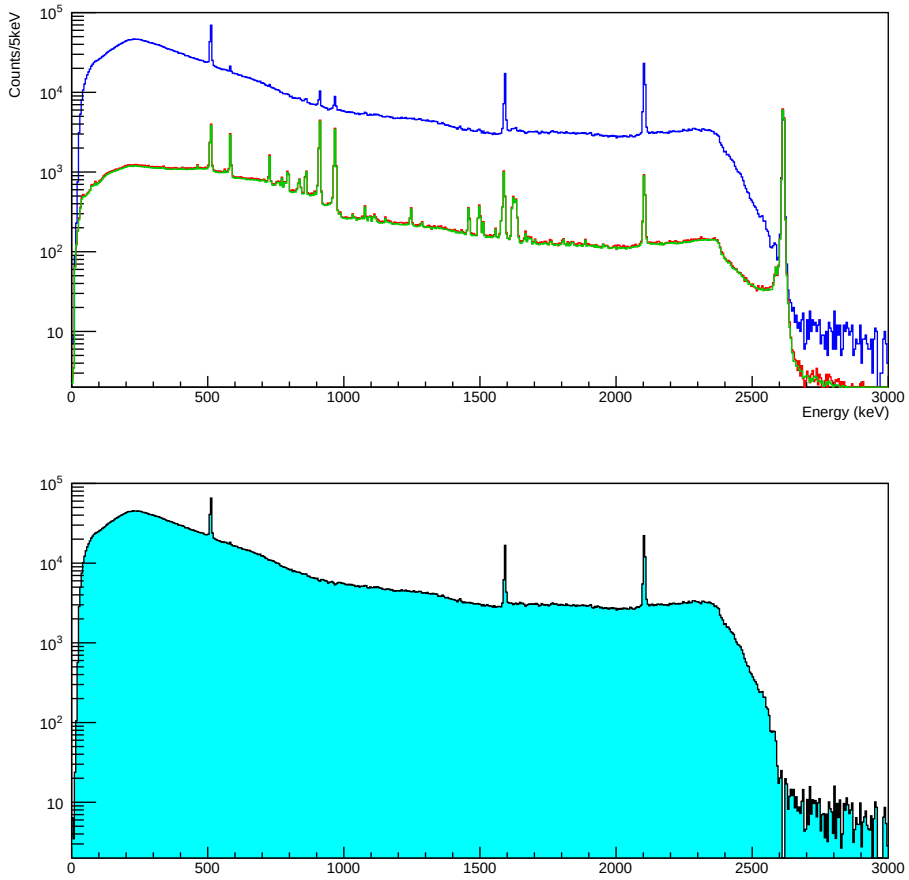

Figure 5.4: *Top*: M2 spectrum, calculated with the standard jitters (blue) and with the de-synchronization (red). The M1 spectrum (obtained by events that involve a single crystal) is shown as well (green), scaled down; it has the same shape as the spectrum from accidental coincidences. *Bottom*: subtraction between the blue and green histograms, representing the predicted spectrum from real coincidences.

The M1 spectrum, containing events that involve a single crystal, is also shown in figure 5.4, conveniently scaled: this is just to show that it has the same shape as the spectrum given by accidental coincidences. This is expected, since accidental coincidences come from events that should have been detected on a single crystal and, therefore, should be M1.

The fraction of M2 events that come from accidental coincidences is not constant at all energies: while the average value of this fraction is $\sim 5\%$, it becomes substantially higher near some of the main γ lines, especially the 2615 keV line from ^{208}Tl. This decay could, in principle, produce M2 events, since a 583 keV photon is promptly emitted after the 2615 keV one. However, since calibration sources are positioned outside the cryostat (see chapter 7), the low energy γ is more likely to be absorbed in the detector shielding: the higher energy photon reaches the detector more often, making almost every coincidence that involves it an accidental one.

Some other lines disappear in the *real* coincidences spectrum, such as the one at 969 keV, produced by the decay of ^{228}Ac. Since no other γ is emitted together with the 969 keV one, this lines wouldn't even be present in the M2 spectrum if not for accidental coincidences.

The effect of accidental coincidences can also be seen in the `Total Energy` spectrum of M2 events, obtained by plotting the sum of the energies of coincident events. The comparison between coincidences with and without synchronization, obtained using the same calibration data, can be seen in figure 5.5.

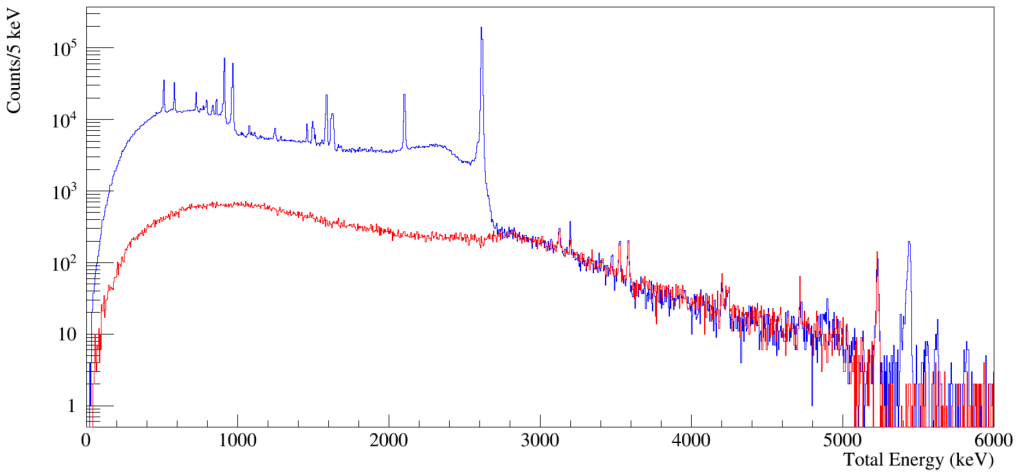

Figure 5.5: Total Energy spectra for M2 events, obtained with the standard jitters (blue) and with the de-synchronization (red). The line at 5230 keV, produced by the sum of two 2615 keV photons, is an example of a structure produced entirely by accidental coincidences.

Almost all the background above the 2615 keV line comes from accidental coincidences. The main exceptions are some lines above 4800 keV: those are not produced by the calibration source but by α decays of contaminations located on crystal surfaces.

The comparison between total and accidental coincidences for background data is shown in figure 5.6. The M1 spectrum is shown as well, this time scaled in order to make

its rate match the accidental coincidences rate; the scaling factor is R_{acc}/R_{M1}, where R_{M1} is the original M1 rate and R_{acc} comes from equation 5.2.

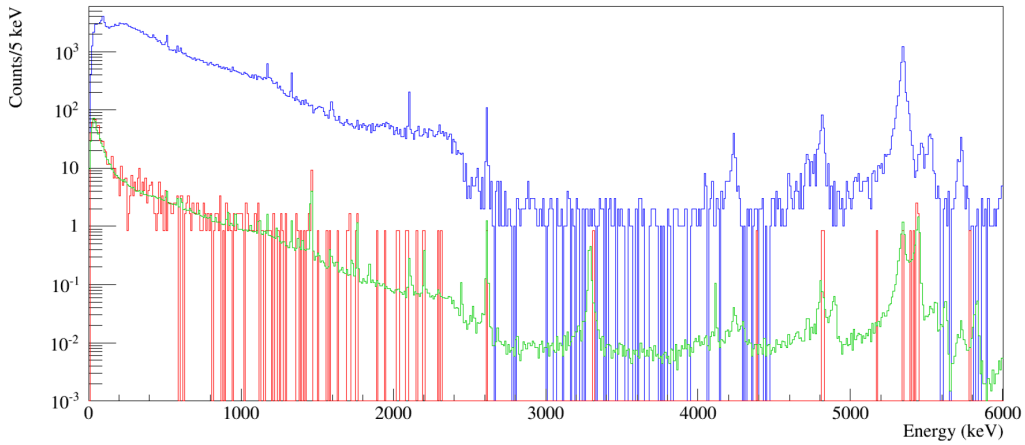

Figure 5.6: M2 spectra, calculated with standard jitters (blue) and de-synchronization (red), for background runs. The M1 spectrum is shown as well, scaled down (as described in the text).

The fraction of accidental coincidences for background data is much lower than the one obtained in calibration ($< 0.5\%$), thanks to the lower event rate. The behaviour near the main γ lines is also different: the 2615 keV line, for example, is much less prominent in the accidental coincidences spectrum. While in calibration this line was produced by a source far away from the detector, leading to the loss of the accompanying 583 keV photon. In background runs, ^{208}Tl is much closer to the detector, leading to a much higher rate of real coincidences between the 2615 and 583 keV line, which is less likely to be absorbed by the detector shielding.

5.4 Effect of cuts on multiplicity

In the CUORE-0 analysis cuts are used to remove bad quality events from the data. The output of the coincidence analysis can be heavily affected by cuts, depending on the moment when the cuts are applied: some of them are applied before the calculation of coincidences, while other are applied after, with different effects on the final outcome. Broadly speaking, cuts involving the rejection of pile-up are applied before the calculation of coincidences, while pulse shape cuts and bad intervals (see sections 3.1.4,3.2.1) are applied afterwards.

5.4.1 Pile-up rejection

Pulses in CUORE-0 are associated to a 5 seconds wide window (figure 5.7:1). The first second is acquired just before the event trigger (and is therefore named *pretrigger*) and is used to evaluate the shape of the baseline on which the signal is growing. A 1 second long dead time window is also present after each triggered pulse, completely preventing the trigger from firing.

Pile-up is observed when an event happens within a short time interval from the following one, on the same channel (figure 5.7:2). The pile-up probability P_{pu} can be estimated with the same approach used for the derivation of equation 5.1, and turns out to be

$$P_{pu} = 1 - e^{-R_{ch}\Delta t}, \tag{5.3}$$

where R_{ch} is the total event rate on a channel and Δt is the time window within which an event is considered as a pile-up. For CUORE-0, $\Delta t = 4$ s, corresponding to the 5 seconds window assigned to each pulse, minus one second of pretrigger.

The Optimum Filter used to reconstruct signal amplitude uses the whole pulse to do so; the presence of a second pulse in the same window leads to an incorrect estimate of amplitude and, therefore, energy. The influence of pile-up on data quality depends, of course, on the total event rate; a low-rate measurement will suffer little to no damage from pile-up. Therefore, its effects are substantial during calibration runs, where the average per-channel event rate is $\sim$ 60 mHz, and less noticeable in background runs, with an average rate of $\sim$ 1 mHz.

If the trigger fires multiple times within the time window associated to an event a dedicated flag, named `SingleTrigger(ST)` is set to false (figure 5.7:2); most of the CUORE-0 analysis, including the coincidence calculation, ignore pulses with `ST==false`.

The combination of these features leads to a few possible scenarios:

1. if a pulse (A) is triggered at time t_A and no other pulse is present within the corrisponding 5 seconds window, then A has the `ST` flag set to `true`; it will be used for the coincidence analysis and, unless removed by some pulse shape cut, will be present in the final data (figure 5.7:1).

2. If a second event (B) happens at time t_B, and $\Delta t_{BA} < 1$ s, then B falls within A's dead time window; B isn't triggered and, effectively, doesn't exist in the data. A still has `ST = true`: it will be used for the coincidence analysis but will be most likely removed by some pulse shape cut and won't be present in the final data (figure 5.7:2).

3. If $\Delta t_{BA} > 1$ s, B is also triggered. A has the `ST` flag set to `false`, and is ignored by the coincidence analysis. B, on the other hand, has `ST` = `true`, since A is outside of B's pretrigger window; B will be used for coincidences and likely be removed later by pulse shape cuts, since it grows on the tail of another pulse and not on a flat baseline (figure 5.7:3).

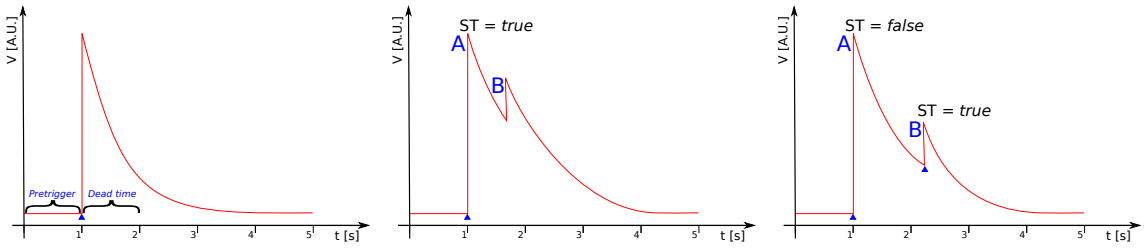

(1) Standard pulse (2) Dead time (3) Pulse with pile-up

Figure 5.7: *Left*: standard CUORE-0 pulse, with the pretrigger and dead time windows shown (case 1). *Middle*: signal B happens within 1 second from signal A; B is not triggered, `ST` is `true` for A (case 2). *Right*: $\Delta t_{BA} > 1$ s, B is also triggered; $\texttt{ST}_A$=`false`, $\texttt{ST}_B$=`true` (case 3).

Case	Pulse	Δt_{BA}	Triggered	`ST`	Used for multiplicity	Used in final data
1.	A	-	Yes	`true`	Yes	Yes
2.	A	-	Yes	`true`	Yes	No
	B	< 1 s	No	-	No	No
3.	A	-	Yes	`false`	No	No
	B	$1 - 4$ s	Yes	`true`	Yes	No

Table 5.1: Summary table for pile-up handling

A schematic view of all the possible scenarios that might occur is given in table 5.1.

To summarize, dead time and the `ST` flag can prevent some events to be even considered in the coincidence analysis. Most of the time, this is useful: if a crystals suffers from high noise in a certain time period, leading the trigger to potentially fire at a high rate, dead time and `ST` avoid the processing of useless data. However, if some physical events happen simultaneously and one of them is removed by these cuts, the correct information about the event multiplicity is lost.

A schematic example of this situation is shown in figure 5.8. Event A (red, channel 1) and event C (red, channel 2) are two physical events in coincidence, so they belong in

the M2 spectrum. By chance, B (blue, channel 1) happens close in time to A; the events on channel 1 fall in case #1 from table 5.1, so $\texttt{ST}_A$=`false`, meaning that it is ignored for coincidences. Event B, since no other simultaneous event is found, is flagged as M1. The inefficiency introduced by this procedure, albeit small, must be kept into account.

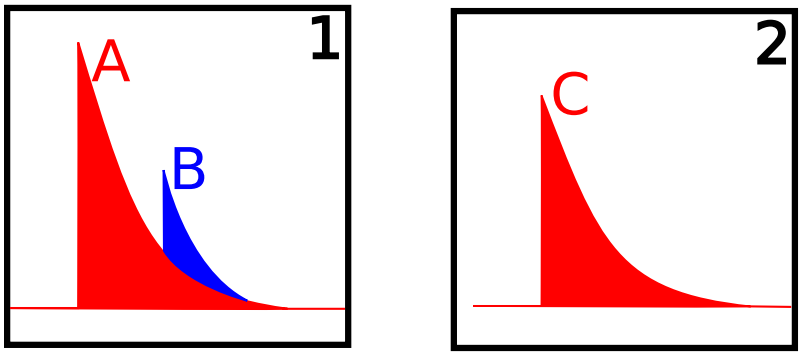

Figure 5.8: Schematic view of the possible loss of a M2 event. 1 and 2 are two bolometers that simultaneously record two correlated events A and C, while B accidentally takes place at a short time distance from A on bolometer 1.

If an event falls within the dead time window opened by a previous signal (table 5.1, case 2), it is not triggered and isn't considered for coincidences. The probability P_{DT} of this happening, since the dead time window t_{DT} is 1 second, is

$$P_{DT} = 1 - e^{-R_{ch} \cdot t_{DT}} = 1 - e^{-R_{ch}}, \tag{5.4}$$

where R_{ch} is the event rate on any channel (here assumed uniform across the whole tower).

As mentioned before, the `ST` flag is set to false for an event when a second pulse happens on its tail, but not if the time difference between the two is less than 1 second (see table 5.1, cases 2 and 3). This flag is activated only if the time difference is between 1 and 4 seconds. The probability P_{PU} of this happening is then

$$P_{PU} = e^{-R_{ch}} - e^{-4 \cdot R_{ch}}. \tag{5.5}$$

The probability P_{Good} that an event is not removed from any of the previous cuts is

$$P_{Good} = 1 - P_{PU} - P_{DT}. \tag{5.6}$$

In order for two events to be correctly recognized as M2, both of them must pass these cuts. Therefore, assuming that before the application of any cut the number of M2 events

is N_{M2}, the number of actual M2 events n_{M2} recorded by the CUORE-0 analysis will be

$$n_{M2} = N_{M2} \cdot P_{Good}^2 = N_{M2} \cdot (1 - P_{PU} - P_{DT})^2 \,, \tag{5.7}$$

or, in other terms, that the efficiency ϵ_{M2}, defined as the fraction of M2 events that survive after the application of cuts, is given by

$$\epsilon_{M2} = \frac{n_{M2}}{N_{M2}} = P_{Good}^2. \tag{5.8}$$

Using the average event rate of background runs, $R_{ch}^{Bkg} = 0.001$ Hz, $\epsilon_{M2}^{Bkg} = 99.2\%$. For calibration runs, where the average event rate is much higher ($R_{ch}^{Cal} \simeq 0.060$ Hz), the efficiency is significantly lower: $\epsilon_{M2}^{Cal} = 61.8\%$.

The calculation described above is not constrained to work only for M2 events; the efficiency for an event of multiplicity N is simply

$$\epsilon_{MN} = P_{Good}^N, \tag{5.9}$$

where P_{Good} is defined exactly as in equation 5.6.

5.4.2 Pulse shape and bad intervals

The coincidence analysis is independent of both pulse shape cuts and bad intervals[1]; in other words, these cuts are applied after multiplicities are calculated. For example, if one of the two signals part of a M2 event is removed by pulse shape, the other retains the information about multiplicity, but it will lose its companion. For some pulses, therefore, there is a difference between the number of coincident signals that made it into the final data and the value reported by the `Multiplicity` variable.

In the final data the total number of M2 events that pass all the cuts is 154876. Around 12000 events, less than 10%, pass both pulse shape and bad interval cuts, but their companion doesn't. This is expected, since pulse shape cuts alone, with an efficiency of $\sim 94\%$ (see chapter 4), lead to the removal of 6% of the final data.

5.5 Summary

In this chapter I've outlined how the occurrence of random events can alter the contents of the final data. The effect of accidental coincidences and event cuts can be summarized as follows:

[1] Actually, some bad intervals are considered by the coincidence analysis, such as periods of time where the detector heats up and reaches saturation. Time periods with high noise or where the baseline is unstable, which make up the vast majority of bad intervals, are ignored by the coincidence analysis.

- **Accidental coincidences** take events that should be M1 and shift them to higher multiplicities, M2 with the highest probability. This also modifies the expected shape of the M2 spectrum, adding peaks and structures that wouldn't be there otherwise.
- Events that suffer from **pile-up** are removed from the data and are not considered for the multiplicity analysis, shifting events from the M2 to the M1 spectrum: if an event within an M2 pair is removed by pile-up, the other is registered as an M1 event.
- **Pulse shape** cuts remove events that suffered from bad reconstruction, but this is done after multiplicities are calculated. If an event within an M2 pair is removed by PSA cuts, the information regarding the event multiplicity is preserved by its companion.

Among these effects, accidental coincidences and pile-up are strongly related to the experimental event rate. Their impact is far more significant on calibration measurements than it is in the standard background data.

Understanding the way that random events are handled by the CUORE-0 analysis is not only useful to account for lost events, but also to properly build a Monte Carlo model of the detector. Including every feature of the data analysis in Monte Carlo simulations is crucial for the exact reconstruction of the observed spectra. This will be discussed in detail in the following chapters, dedicated to the description and uses of the Monte Carlo tools developed for CUORE-0.

CHAPTER

6

MONTE CARLO TOOLS

In this chapter I'll describe the tools used to perform Monte Carlo simulations in CUORE-0. I'll mainly focus on `MCuoreZ`, a `Geant4` based code that simulates particle propagation and interaction in the CUORE geometry, and `g4cuore`, a tool I've written that is used to reprocess MC data adding all detector-related features, such as energy resolution, thresholds, coincidences, and others. `g4cuore` is based on a previously existing software that was used for the same purpose, but that lacked several features needed to properly reproduce the CUORE-0 data processing.

6.1 The Monte Carlo code: `MCuoreZ`

`MCuoreZ` is the code used to simulate the effect of particle interactions in the CUORE-0 detector. It is fully written in `C++` and is based on `Geant4`, a well-known toolkit for the simulation of the passage of particles through matter developed by CERN[54].

`Geant4` version 9.6.p03 was used for most of the simulations cited in this work. For special purposes (described later), however, libraries more recent than the ones shipped with version 9.6.p03 had to be used (chapter 7). A modification that had to be done to the `Geant4` code itself to correct a significant bug in particle generation will also be discussed (section 6.1.5).

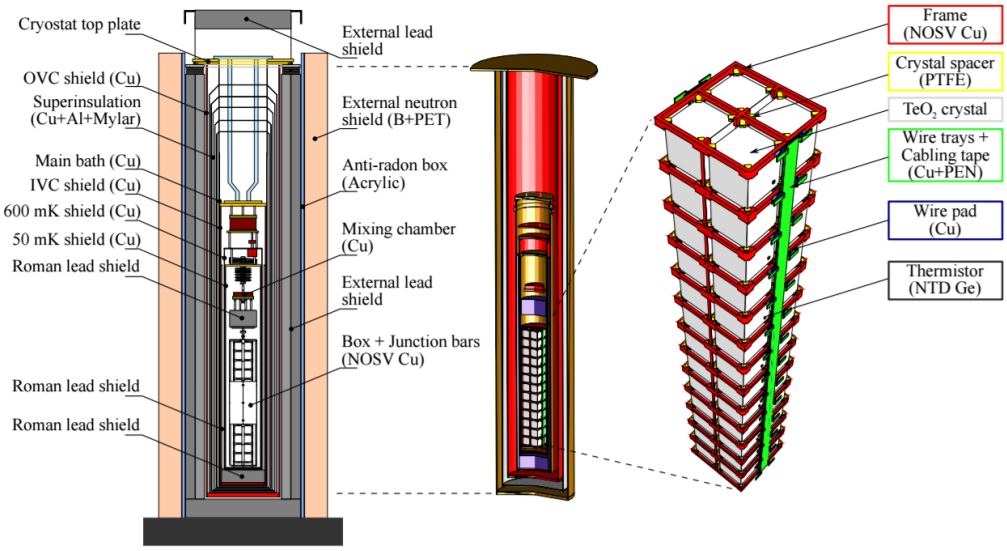

Figure 6.1: CUORE-0 geometry as implemented in `MCuoreZ`. The whole cryostat is shown on the left, while the structure of one of the tower is detailed on the right. (taken from [17])

6.1.1 Detector geometry

Exploiting the `Geant4` classes for material and geometry definition, we've included the full CUORE-0 cryostat and detector geometry in `MCuoreZ`. The whole structure has been reproduced with great care and precision to ensure the best possible resemblance between Monte Carlo and real data. The structure of the CUORE-0 cryostat, as implemented in `MCuoreZ`, is shown in figure 6.1. A list of all elements that are included in the simulation, as well as their surface, volume and mass, can be found in table 6.1.

Element	Volume [dm^3]	Surface [dm^2]	Mass [Kg]
External Lead Shield	2177.6	2338.9	24694
External Neutron Shield	1385.3	2859.2	2770.3
Concrete Pedestal	1051.3	710.5	3153.8
Main Bath	16.3	692.7	145.0
Superinsulation	18.3	728.0	163.2
OVC Shield	53.2	894.6	474.8
IVC	5.1	278.3	45.6
600 mK	22	178.7	19.8
Roman Lead Shield	17.8	198.7	202.3
Mixing Chamber	0.5	4.3	3.8
50 mK	1.9	154.8	16.9
10 mK	0.8	93.3	6.8
Copper Frames	0.3	23.5	2.6
TeO_2 crystals	6.5	78.0	39.0
NTD	4.7×10^{-4}	0.2	0.002
Wire pads	3.1×10^{-4}	0.6	0.003
Wire trays	0.1	14.4	0.6
PEN tapes	2.2×10^{-2}	5.8	0.04
PTFE spacers	0.1	12.6	0.2

Table 6.1: CUORE-0 elements included in `MCuoreZ`, with the respective volume, surface and mass.

6.1.2 Particle generation

Through a simple command line interface, `MCuoreZ` offers a variety of options for particle generation. All the possible options, which can also be combined together, are listed here.

- **Single particles**: this options allows to generate electrons, positrons, photons, muons, neutrons or alpha particles; the source can either be monochromatic or follow a specific energy distribution.
- **Single decay**: a single decaying nucleus, identified by its A and Z, can be chosen as the source; particles produced during the transition from the father to the daughter nucleus are also produced and propagated.
- **Decay chains**: natural radioactivity mainly proceeds via chains of decays. The process involves a sequence of unstable nuclei, each decaying on a daughter nucleus with its own lifetime, until reaching a stable one. By specifying each nucleus in the sequence, the user can either require the production of a full decay chain (e.g. ^{232}Th or ^{238}U) or just part of it, to reproduce the effect of secular equilibrium breaks.

- **Double beta decay**: various double beta decay schemes can be generated, depending on user needs. Decays with and without the emission of neutrinos or Majorons, both from the ground state or from the 2+ excited state, are possible choices. The theoretical shape for the double beta events is extracted from [55]; the user can also choose to use more detailed numerical calculations for the electron spectrum (from Kotila-Iachello[56]).

For all the previously listed source options the starting particle position inside the cryostat, from here on called the initial *vertex*, must be specified. Any solid reported in table 6.1 can be used as a source, with particles coming either from its full volume or from its surface. The contaminant density for surface contaminations can be chosen to be uniform in a layer of thickness λ (zero thickness layers are possible) or to be exponential, with characteristic length λ. The exponential contamination profile is given by

$$p(x) = e^{-\frac{x}{\lambda}}, \tag{6.1}$$

where x is the distance from the closest surface of the source solid. The exponential profile has been used for all CUORE-0 surface simulations, as it is the one predicted for contaminant diffusion through a surface. Other possibilities for source definition include point-like sources and simple geometrical shapes, such as wires, disks, tubes and spheres.

`MCuoreZ` also implements the possibility to generate muons with the same spectrum measured underground at LNGS. Muons are generated on a hemisphere and are distributed according to the differential flux and zenith angle dependence measured by the LVD[57] and MACRO[58] experiments in the LNGS cavern.

6.1.3 Particle propagation

`Geant4` provides a wide choice of physics processes and models that describe particle propagation through matter. The user is free to decide how much detail should go in the physics modeling, weighing precision against CPU time required by the simulation. This is done by choosing one of the available *physics lists* in the `Geant4` toolkit, or building a new one. Physics lists define which models should be used for particle production and transport, allowing the choice of lighter (and less precise) models for processes which are not under investigation. Plenty of physics lists for both high and low-energy physics are available; among those, the Livermore physics list, based on the data libraries developed at LLNL[1], has been chosen, as it is recognised as one of the most efficient for low energy physics.

[1] Lawrence Livermore National Laboratory

It is often possible to improve the simulation performance, without hindering the quality of the results, by setting appropriate cuts on particle tracking. Tracking in `Geant4` is done by following each particle through a series of steps; the distance covered by the particle between said steps is calculated by `Geant4` based on particle type, energy and material composition. The user can set two different cuts that influence particle propagation distance:

- absolute range: if the distance for the next step is below a certain threshold, the particle is immediately absorbed. This cut is defined within the chosen physics list and affects any volume in the simulation in the same way;
- threshold for secondary particle production: if the distance for the next step is below a certain threshold, no secondary particles are produced. Different thresholds can be set for different regions of the detector.

Given its inherent flexibility, in `MCuoreZ` the cut on secondary particle production has been used to optimize simulation performance. As far as threshold choices go, the cryostat can be split in two parts: anything that is within the inner roman lead shield and anything that is outside, roman lead included. Volumes that are within the roman lead shield are the closest to the detector itself. High precision is needed in this zone, in order to reconstruct correctly any interaction. Low thresholds are chosen here, letting particles propagate and interact until their energy reaches a few keV. Volumes that are outside the roman lead shield, on the other hand, don't need this kind of precision. Particles with energies up to a few hundreds of keV have an extremely low probability of passing through the lead shield; therefore, it's pointless to track them when they reach these kinds of energies. Therefore, higher thresholds can be chosen to reduce CPU time. Threshold values for the main `MCuoreZ` materials can be found in table 6.2.

Material	Particle	Threshold [μm]
Lead	γ	10^4
(external and Roman)	e_-,e_+	10^4
Aluminium	γ	10^3
(Superinsulation)	e_-,e_+	10^3
Outer copper	γ	10^3
(outside Roman Lead)	e_-,e_+	10^3
Inner copper	γ	10
(inside Roman Lead)	e_-,e_+	1
TeO_2	γ	10
(crystals)	e_-,e_+	1

Table 6.2: Distance thresholds for secondary particle production, for the main `MCuoreZ` materials.

6.1.4 Output file format

`MCuoreZ` outputs ROOT files that contain information on the initial conditions for the simulation and all the useful data regarding energy deposition in the detector. For quick reference to the actual file content the input command line is stored, as well as the number of simulated particles and/or decay chains. Each energy deposition inside the detector is stored inside a ROOT `TTree` containing data to be used in the following steps of data processing or for debugging purposes:

- **Channel**: number used to identify the TeO_2 crystal where the energy deposition occurred;
- **Chain Number**: number of the chain that generated the event;
- **Time**: time interval with respect to the previous event in the same chain. The first event in the chain is set at time $T = 0$, while the times for the rest of the chain depend on the related half-life;
- **Energy**: total energy deposited in the crystal;
- **Particle Energy**: deposited energy per particle type (i.e. 10% γ, 90% e_-);
- **Particle Name**: name of the primary particle that generated the interacting particle;
- **Starting Energy**: initial energy of the primary particle;
- **Coordinates**: starting (X, Y, Z) coordinates of the primary particle;

- **Direction**: direction cosines associated to the emission direction of the primary particle.

6.1.5 Surface generation correction

In order to produce complex geometrical shapes `Geant4` implements *Boolean Solids*, which allow the user to combine more basic volumes by union, subtraction or intersection. This feature has been used extensively in `MCuoreZ`; the frames that sustain the CUORE-0 tower, for instance, are obtained by repeated subtractions from an initial, full parallelepiped (figure 6.2).

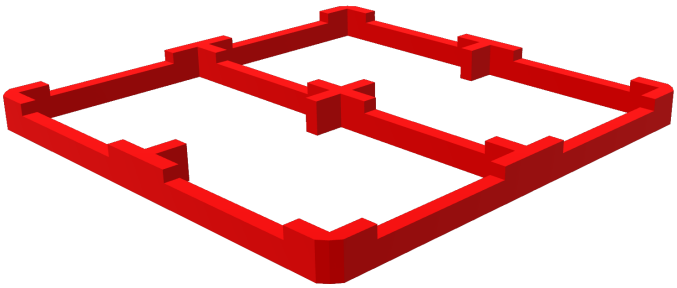

Figure 6.2: CUORE-0 frame as reproduced by `MCuoreZ`.

Particle generation inside or on the surface of boolean solids requires a small discussion. The structure in figure 6.3, which shows the union $AB = A \cup B$ between two solids A and B, will be used as a reference.

The procedure used to generate particles from the whole volume of AB is simple. `Geant4` produces a *bounding box* (black outline in figure 6.3), a simple shape that encloses all the involved solids; points are generated randomly and uniformly inside the bounding box and, if a point is inside either A or B, it is chosen as a vertex for particle generation. This technique can be inefficient for solids with a lot of empty space (such as the CUORE-0 frame), but guarantees the uniform distribution of points inside every part of the boolean solid. As long as the bounding box is modified accordingly, this doesn't change by performing more boolean operations.

The generation of particles from the surface of a boolean solid is slightly more complex. `Geant4` generates points on the surface of either A or B and then checks if these points are on the external surface of AB (and not, for example, on the common surface between the A and B). In order to guarantee uniformity across the whole surface, the probability of generating the vertex on the surface of A or B cannot be the same; if S_A and S_B are

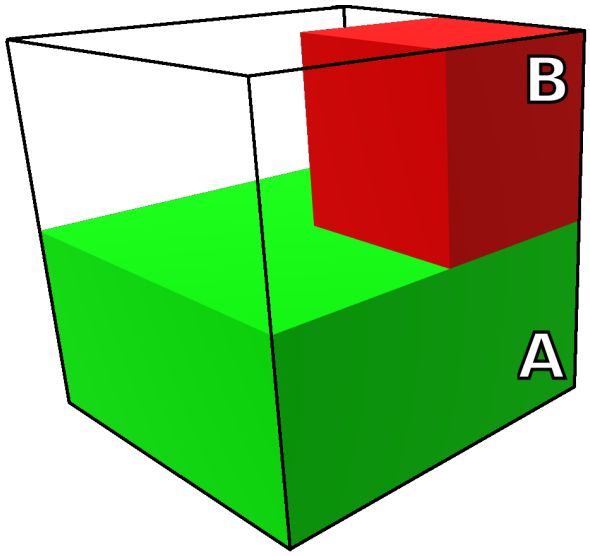

Figure 6.3: Example of a boolean solid, obtained by the union of A and B. The black outline is the *bounding box* of the total solid.

the surface areas of A and B respectively, a point will lie on A with a probability

$$p_A = \frac{S_A}{S_A + S_B} \tag{6.2}$$

and, consequently, it will lie on B with $p_B = 1 - p_A$. Therefore, in order to properly generate vertices uniformly on the surface of a boolean solid the surface area of all the sub-solids that make it up has to be well known. If A and B are simple volumes, like the boxes in the previous example, this is easily done.

If an additional boolean operation is needed, for instance the addition of a third solid C to the union AB, then surface generation would require the knowledge of S_{AB}, which is obviously different from $S_A + S_B$. While the surface area evaluation for simple solids is done correctly by `Geant4`, the same is not true for boolean solids like AB. This leads to a non-uniform distribution of surface events whenever more than one boolean operation is applied in sequence.

In the standard `Geant4` implementation the vertex distribution for a simulation of the CUORE-0 frames is like the one shown in figure 6.4. In the top half of the figure, point density across the XY plane is shown; even though the source volume is symmetrical, the density is higher for positive X/negative Y values and lower for negative X/positive Y values. This is more clearly visible in the bottom plot, which show the X coordinates of starting points: ideally, the distribution should be symmetrical with respect to 0 but the

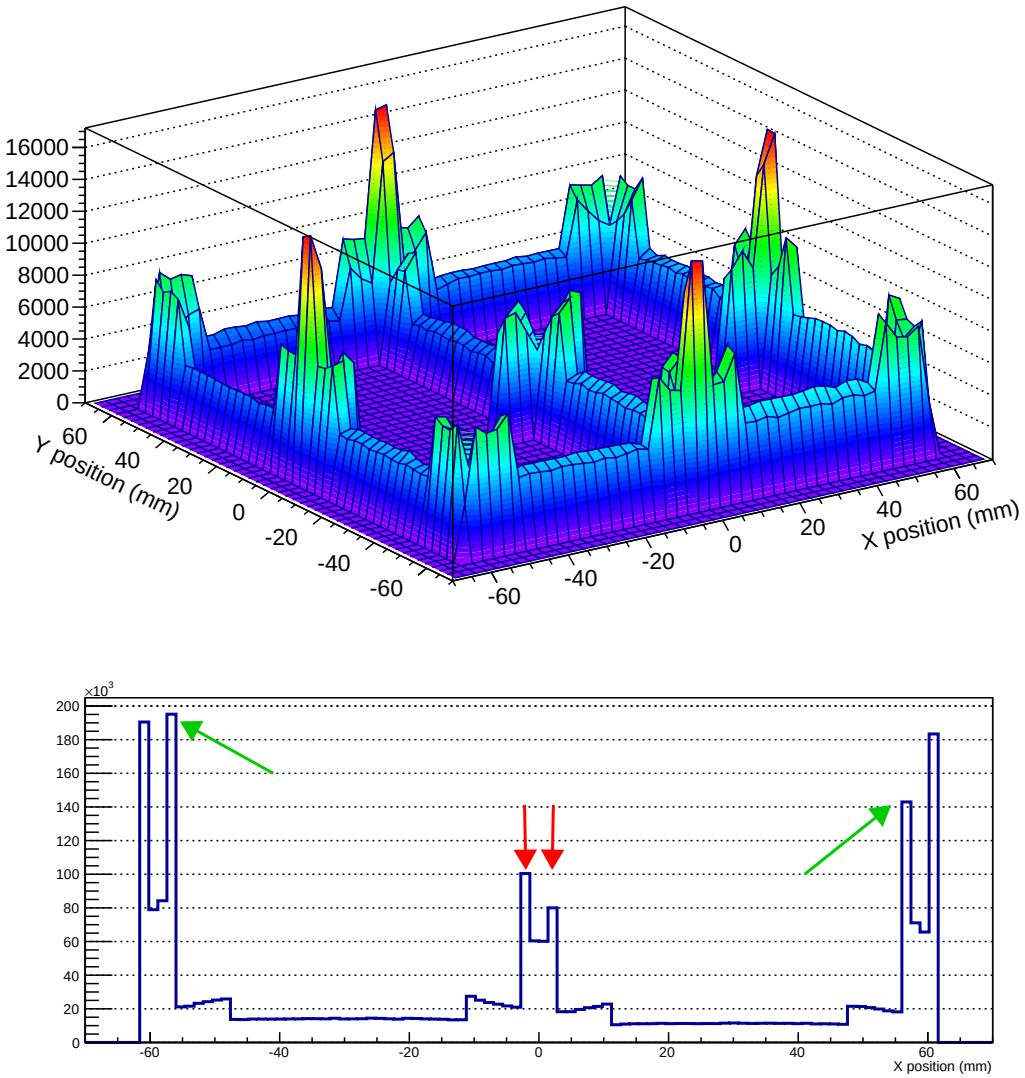

Figure 6.4: *Top*: starting vertex density across the XY plane for surface generation on the frame, obtained with the standard `Geant4` algorithm. *Bottom*: X coordinates of starting vertices. The distribution should be symmetric with respect to zero but it isn't, as highlighted by the colored arrows.

structures highlighted by the arrows clearly aren't.

To overcome this problem in CUORE-0 (and CUORE) simulations, a different algorithm for the numerical estimation of boolean solid surfaces has been implemented. Whenever a boolean operation is performed the surface of the newly created solid is calculated with a simple *hit and miss* Monte Carlo; this way, the surface of composite solids

like AB is always known, after any amount of boolean operations. This method is slightly slower than the one used originally in `Geant4` but, since surface calculations are performed once at the beginning of the simulation, the additional overhead is completely negligible when compared to total simulation time.

The vertex distribution with the improved surface calculation algorithm is shown in figure 6.5; all plots now show the expected symmetries.

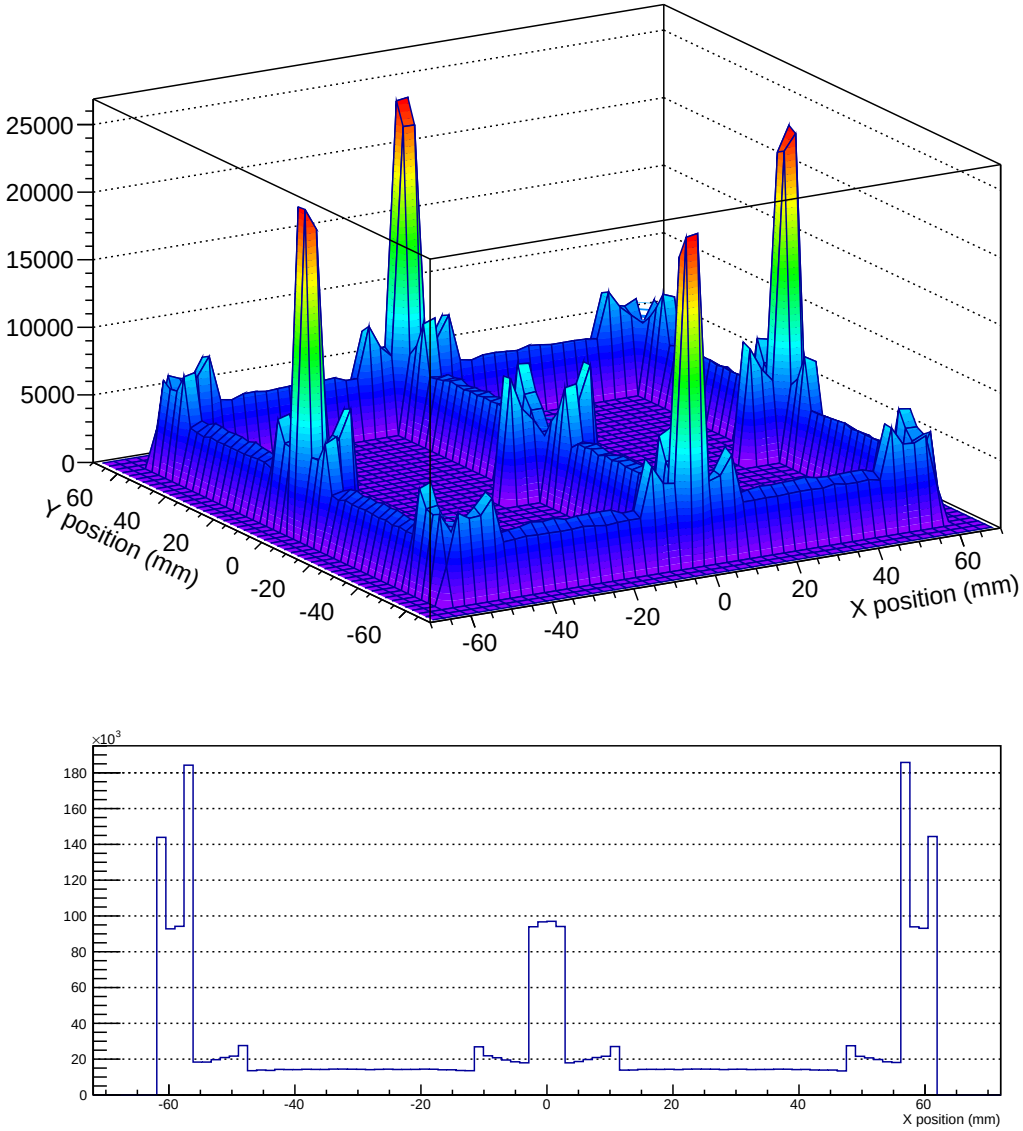

Figure 6.5: *Top*: vertex density for surface generation on the frame, obtained with the modified `Geant4` algorithm. *Bottom*: X coordinates of vertices. All asymmetries shown previously disappear.

6.2 Reconstruction software: `g4cuore`

The raw data contained in `MCuoreZ` output files cannot be compared directly with real CUORE-0 data. Detector features such as energy resolution or threshold, as well as data analysis procedures, need to be taken into account and modelled accordingly. During my

thesis I developed a new software, `g4cuore`, dedicated to the step of MC data handling. `g4cuore`, based on an older software that did not implement all the features now required for a proper simulation on events, is used to process the raw data from `MCuoreZ` and turn it into a CUORE-like format. `g4cuore` attempts to reproduce every aspect of the CUORE-0 data: characteristics of the detector itself (energy resolution or threshold, particle quenching factor), algorithms for pulse timing and multiplicity evaluation and application of cuts. This sections outlines

6.2.1 Energy resolution

The curve relating energy resolution and energy can be passed to `g4cuore` in order to reproduce the correct σ at all energies. A first degree polynomial has proven to reproduce correctly this dependence for CUORE-0 data, and is therefore the default choice. If an event with energy E is reported in the MC data, `g4cuore` assigns it a new energy E^* extracted randomly by a gaussian probability distribution $P(E^*)$:

$$P(E^*) = \frac{1}{\sqrt{2\pi\sigma^2}} e^{-\frac{(E-E^*)^2}{2\sigma^2}}. \tag{6.3}$$

An example application of a 5 keV FWHM is given in figure 6.6.

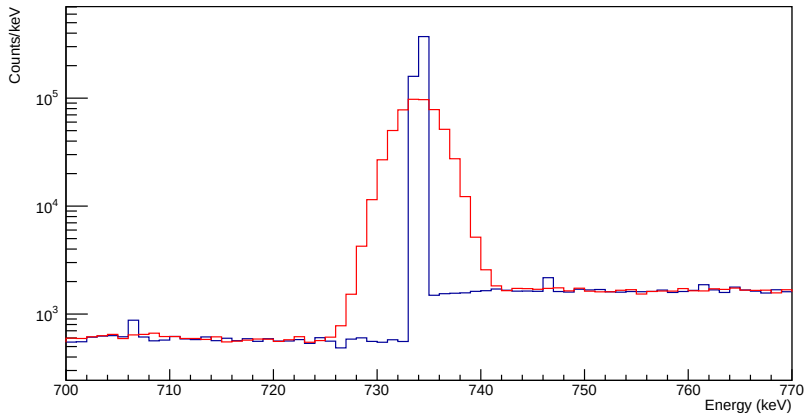

Figure 6.6: Effect of energy resolution in `g4cuore`. The blue spectrum is obtained without any resolution, while the red one with a 5 keV FWHM.

6.2.2 Energy threshold

Each of the CUORE-0 crystals has a different trigger threshold, due mainly to the measured noise level. These thresholds are measured periodically during the CUORE-0 data

taking by means of what is called an *N-pulses* measurement. The heater, present on every CUORE-0 bolometer (see chapter 2), is connected with a voltage pulser able to fire signals at different amplitudes, close to each crystal's threshold. The fraction of triggered pulser events as a function of energy is used to produce a threshold vs energy curve, modeled as a sigmoid function (figure 6.7):

$$F(E) = \frac{1}{2}\left(1 + \mathrm{erf}\left(\frac{x-\mu}{\sigma\sqrt{2}}\right)\right). \tag{6.4}$$

The sigmoid parameters for every channel can be passed to `g4cuore` to produce the threshold curves; an event with energy E^* is then kept in the data with a probability $F(E^*)$.

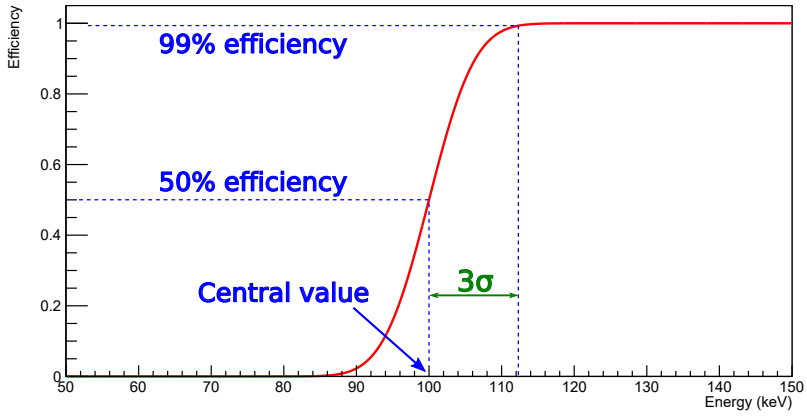

Figure 6.7: Sigmoid function used for reproducing the energy threshold. The central value and σ of the function can be passed as arguments to `g4cuore`.

6.2.3 Timing

Timing data contained in the MC output files isn't readily usable. If a single particle is simulated, no time information at all is given; if a single decay or a chain are requested, each event contains the time interval with respect to the previous element in the chain, but for natural decay chains this can typically exceed 10^9 years. In the timescale of CUORE-0, time intervals of this magnitude are meaningless.

In order to properly produce timing information `g4cuore` requires the user an event rate r. After reading through the MC data, which contains only Δt information, the following procedure is applied:

1. if the MC file contains N events, an *equivalent* total time $T_{tot} = \frac{N}{r}$ is calculated. Given the event rate r, T_{tot} is the time that CUORE-0 would require, on average,

to measure N events;

2. a random absolute time, extracted from a uniform distribution between 0 and T_{tot}, is assigned to any event with time $T = 0$ in the MC file. If a chain is simulated, this involves the first particle of any chain; if single particles are produced, all of them have $T = 0$.

3. the treatment of Δt_i for decay chain simulations depends on its magnitude. If $\Delta t_i < T_{corr}$ (where T_{corr} is a user-definable quantity set by default at 3600 s) the time interval isn't changed, in order to maintain short-time physical correlations between events; the i-th event is assigned an absolute time $T_i = T_{(i-1)} + \Delta t_i$. If $\Delta t_i > T_{corr}$, time correlations are assumed to be irrelevant and T_i is randomly assigned between 0 and T_{tot};

4. events are ordered according to their absolute time, producing a timeline that spans from 0 to T_{tot}.

Once meaningful times have been assigned to all MC events, `g4cuore` can perform several timing-related operations to reproduce the real detector, DAQ and analysis behaviour, which are listed here. In all the following examples, A and B refer to two different pulses that happen at time t_A and t_B respectively.

- **Dead time**: CUORE-0 detectors have a 1 second dead time after each pulse; within this window, the trigger cannot fire again. If A and B happen on the same channel and $\Delta t_{BA} < 1$ s B is removed from the data; A is flagged for later removal, since it would be probably flagged by pulse shape cuts.

- **Integration**: if A and B are on the same channel and $\Delta t_{BA} < t_{int}$[2], the two events are added together and produce a single event with energy $E_{tot} = E_A + E_B$. This reproduces the effects of pile up on the pulse rise time; if Δt_{BA} is short enough, the combination of the two pulses is indistinguishable from a single pulse with energy E_{tot} and therefore passes all pulse shape cuts.

- **Coincidence**: if A and B are on different channels and $\Delta t_{BA} < t_{coinc}$[3], the two events are considered coincident; their `Multiplicity` is set to 2 (or higher, if more than 2 events are coincident).

- **Pile-up**: the same procedure for pile-up rejection described in chapter 5 is applied in `g4cuore`, mimicking the application of the `SingleTrigger` flag, by setting an appropriate pile-up time t_{pu}.

[2]The *integration time* t_{int} can be set by the user and defaults to 10ms

[3]The *coincidence time* t_{coinc} can be set by the user and is 10 ms in the CUORE-0 standard analysis

- **Pulser**: heater pulses are produced every 300 s in CUORE-0. If the time interval between A and a multiple of 300 s is less than t_{pu}, A is treated as a pile-up pulse.

6.2.4 PSA cut efficiency

In chapter 4 the procedure used to optimize pulse shape cuts has been discussed, together with the calculation of the PSA efficiency vs energy curve (figure 4.10). The parameters of the efficiency curve $F(E)$ can be passed as an argument to `g4cuore`; each event i can then be removed from the data with a probability $1 - F(E_i)$.

6.2.5 Other operations

There are several other simple operations that can be performed on MC data by `g4cuore`:

- *Excluded channels*: channels can be shut off completely, preventing any signal on them to be analyzed. Channel 49 in the CUORE-0 tower, which was disconnected during data-taking, is treated this way.
- *Line shape*: the line shape in CUORE-0 is not gaussian (this will be described in detail in chapter 8). A secondary, *satellite* peak is visible slightly below the most prominent γ lines in the spectrum, weighting about 5% of the total peak area. This line shape can be reproduced in `g4cuore`.
- *Distance cuts*: if needed, event multiplicity can be calculated only between crystals that lie within a certain distance between each other.
- *Quenching factor*: the MC output contains information about the interacting particle for each event. `g4cuore` can modify the energy deposited by all particles of the same type can be modified by a multiplicative factor. This is used mainly for α particles, which produce slightly higher pulses than expected on the CUORE-0 crystals. This property of α particles will be discussed in more detail in chapter 8.

6.2.6 Order of operations

As mentioned before, the objective of `g4cuore` is to reproduce the whole CUORE-0 data analysis chain. To do so properly, it is extremely important that the order in which operations are performed on the data is respected.

1. all events are read from the MC file;
2. excluded channels are shut off, events on them are ignored;

3. a first integration step is performed, merging simultaneous signals on the same channel;
4. line-shape and resolution are applied;
5. low-energy threshold is applied and events are removed accordingly;
6. absolute times for all events are calculated, then events are sorted;
7. events falling in the dead time window of a previous signal are removed;
8. second integration step to merge events that, after time randomization, become simultaneous on the same channel;
9. pile-up analysis, removing events with the rules set for the `SingleTrigger` flag;
10. multiplicity calculation for coincident event on different channels;
11. PSA cut efficiency curve is applied and events are removed accordingly;
12. final data are written to the output file.

The order in which steps 3 and 5 are performed requires particular attention. Let's suppose that an event with energy $E_1 = 50$ keV and another event with energy $E_2 = 500$ keV happen simultaneously on the same bolometer. What happens in the CUORE-0 data is that the two pulses are added together and a single signal is recorded, with energy $E_{tot} = E_1 + E_2 = 550$ keV. If the first integration step (#3) wasn't performed by `g4cuore`, the threshold evaluation (#5) would consider E_1 and E_2 as separate events; E_1 has a high probability of being removed due to its low energy, with the final result of having a single 500 keV pulse instead of a 550 keV one.

CHAPTER

7

MONTE CARLO RECONSTRUCTION OF SOURCE MEASUREMENTS

Source measurements can be used as a powerful benchmarking tool for Monte Carlo simulations, since they can be measured independently to know their activity and their description in the MC code is relatively simple. Some of the systematics associated to MC simulations can be evaluated this way.

During the CUORE-0 data-taking several source measurements were undertaken, the most common of which has been the calibration runs, performed at the beginning and at the end of each dataset with a high-rate ^{232}Th source. In order to study the energy response of the detectors and the effects of pile-up, measurements with ^{60}Co, ^{56}Co and low-rate ^{232}Th sources were also performed.

In this chapter I'll describe the techniques used to reproduce source measurement with the MC tools described in section 6. At first I'll list the parameters used for data processing with `g4cuore`, together with the way they were obtained. Then, a comparison between real and simulated data is shown for every available source measurement.

7.1 Analysis technique

Background measurements in CUORE-0 typically have an event rate of around 1 mHz per crystal; most of the timing-related issues that might occur, such as pile-up or accidental

coincidences, have a low impact on data. Calibration measurements, on the other hand, are performed with much higher event rates, which range from 20 to almost 200 mHz per crystal; at these event rates, pile-up becomes a significant issue. All the features of the CUORE-0 data processing, including the way pile-up is kept into account, are handled by `g4cuore`. The parameters used for data processing with `g4cuore` are obtained in the following way:

- *Energy resolution*: the most prominent γ lines in the CUORE-0 spectrum are fitted and the relation between their FWHM and energy is fitted with a first degree polynomial (figure 7.1). The parameters of the polynomial are passed to `g4cuore`. The FWHM at energy E is given by $\mathrm{FWHM}(E) = \mathrm{FWHM}(2615) \cdot (0.49 + 2.22 \cdot 10^{-3} E)$.
- *Energy threshold*: thresholds are evaluated periodically during data taking by performing an *N-pulses* measurement (see section 6.2.2). The parameters of the sigmoid function used to reproduce the threshold behaviour, plotted in figure 7.2, are passed to `g4cuore`. Since no information is available for the thresholds on channels 1 and 10, a 50 keV value has been assumed.
- *Dead time*: the standard dead time of 1 second for all channels is used during MC data processing.
- *Integration time*: the default value is used (10 ms).
- *Coincidence window*: the default value is used (10 ms).
- *Pile-up*: pulses which occur within less than 4 seconds from a previous one are treated as pile-up.
- *Excluded channels*: channel 49 is disabled.
- *Pulser*: the effects of a pulser event every 300 seconds (the default pulser frequency in CUORE-0) are applied.

Together with these quantities, the event rate also has to be defined. Additionally, the effect of events coming not from the source under investigation but from contaminations in the cryostat needs to be kept into account. These two additions are discussed in the following sections.

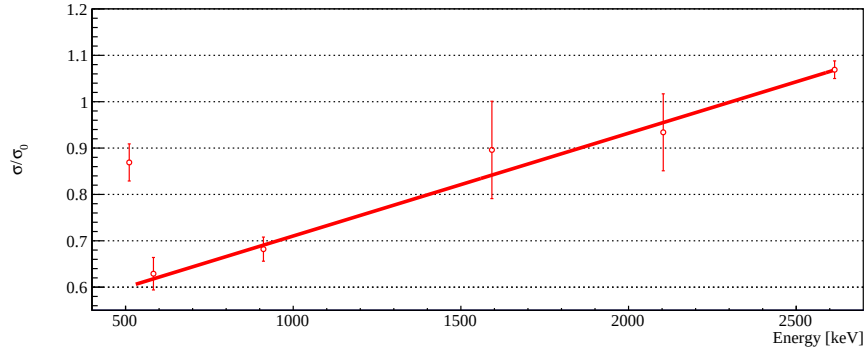

Figure 7.1: Resolution vs energy curve measured in CUORE-0. The resolution is given in terms of the 2615 keV line FWHM in calibration runs, which is used here with its average value, 4.9 keV [60]. The 511 keV line is not used in the fit, as it has a naturally broader energy resolution.

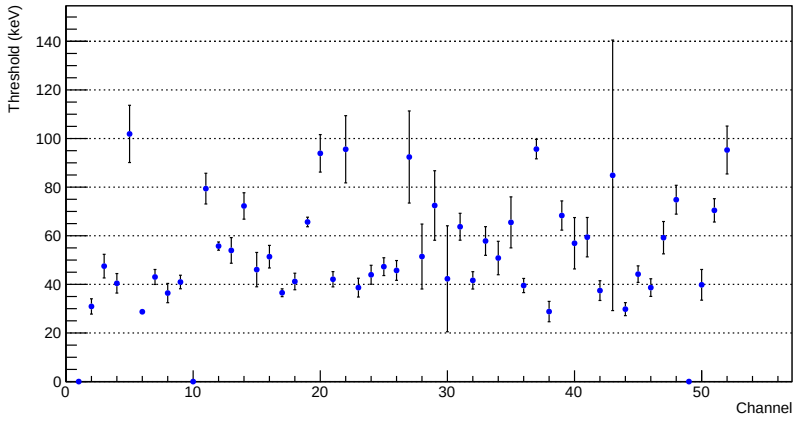

Figure 7.2: Energy threshold parameters for all the CUORE-0 channels. The points correspond to the center of the sigmoid and the error bars to its σ. Channels 1 and 10 have no working pulser, so their threshold curve could not be calculated. Channel 49 is shut off for the whole CUORE-0 data taking.

7.1.1 Rate evaluation

Due to the presence of 1 second of dead time, in a high-rate scenario a significant fraction of events is lost; therefore, the event rate can't be simply evaluated as the ratio between the number of signal triggers and the measurement live time. Instead, the event rate R is estimated by taking the time intervals between subsequent events on each channel and

fitting the Δt distribution with an exponential function(figure 7.3):

$$y = A \cdot e^{-\frac{\Delta t}{R}}. \tag{7.1}$$

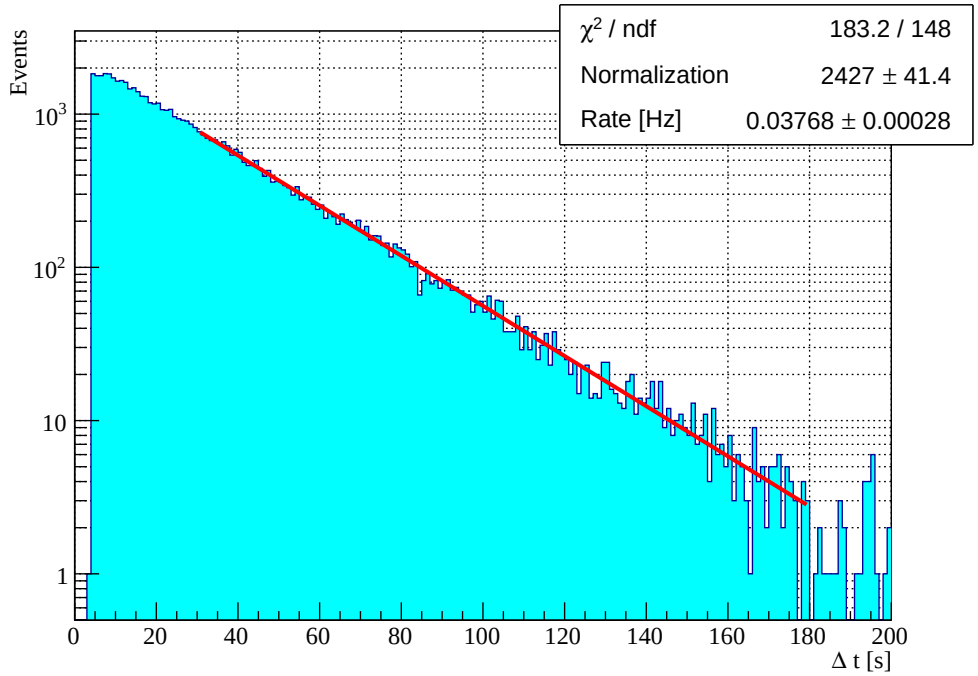

Figure 7.3: Example fit of the Δt distribution. The ratio between signal triggers and measurement live time would give a 34 mHz rate; the correct rate, given by the fit, is around 38 mHz.

The presence of a 1 second wide dead time window can alter the Δt distribution, as shown in figure 7.4: in this scenario, instead of measuring two separate Δt values a longer time interval is observed, which ignores the existence of the pulse removed by dead time. This leads to a systematic over-estimation of time intervals, which in turn can alter the rate obtained by fitting the Δt distribution.

A simple toy Monte Carlo was used to verify if this systematic effect is significant for the case under study. Given an initial event rate, the corresponding Δt distribution is generated, keeping the 1 second dead time window into account (figure 7.5:1); the distribution is then fitted with equation 7.1 to obtain the "measured" event rate. As shown in figure 7.5:2, significant differences between the predicted and measured event rate show up only for initial rates higher than 600 mHz. Since calibration rates in CUORE-0 never

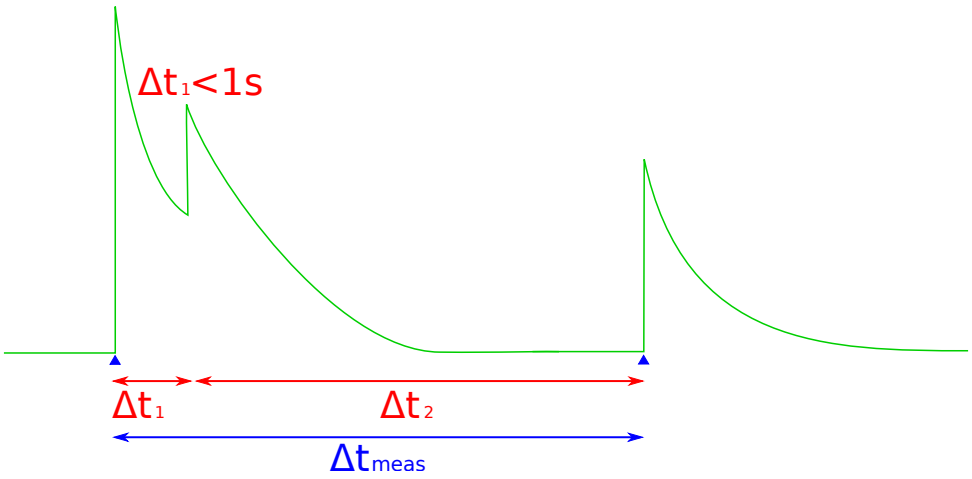

Figure 7.4: Dead time effect on Δt evaluation. If $\Delta t_1 < 1$ second, instead of correctly measuring Δt_1 and Δt_2, $\Delta t_{meas} = \Delta t_1 + \Delta t_2$ is observed.

exceeded 200 mHz per crystal, this systematic effect can be safely ignored.

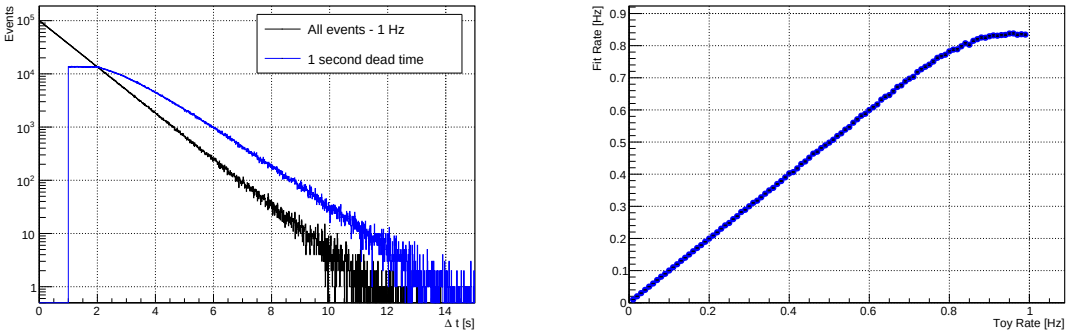

(1) Toy Δt distributions with $R = 1$ Hz, with and without dead time

(2) Toy fit results, with starting rate ranging from 0.01 to 1 Hz

Figure 7.5: Results of the toy MC to test the effect of dead time on rate evaluation. As shown in the right plot, the systematic decrease in the fitted rate is significant only for toy rates greater than ~ 600 mHz.

The experimental rates for each of the four calibration measurements are reported in table 7.1.

Calibration	Event rate [Hz]
^{232}Th - High rate	3.35
^{232}Th - Low rate	0.40
^{60}Co	2.60
^{56}Co	4.48
Background	0.055

Table 7.1: Total event rates (on the whole CUORE0 tower) for the four calibration measurements under examination. The background contribution is also given for comparison.

7.2 Combination with background data

Radioactivity coming from the detector and the cryostat, which normally contributes to the *background* spectra taken from CUORE-0, shows its effects in source measurements too. For this reason, this analysis cannot be performed using Monte Carlo data alone, but real CUORE-0 data has to be included to account for the background contribution. In order to easily combine MC and *real* data files, they have to be produced in a similar format.

The background event rate is generally pretty low, 55 mHz on average on the whole tower; its contribution is therefore substantially negligible for most of the calibration measurements (table 7.1). However, for the low rate ^{232}Th calibration, whose total rate is ~ 400 mHz, this contribution is significant, since background makes up roughly 15% of the total data. To account for this effect, Monte Carlo simulations were combined with real CUORE-0 data using the following procedure:

1. a Monte Carlo is produced containing N total events.
2. `g4cuore` is run on the MC file using an event rate r. The event rate must be as close as possible to the measured one to properly reproduce pile-up and accidental coincidences.
3. An *equivalent* time $t_{eq} = \frac{N}{r}$ is calculated: if this were a real measurement, counting N events with an event rate r, then it would have lasted a time t_{eq}.
4. A subset of CUORE-0 data, spanning a total time t_{eq} and starting from a random moment during the data acquisition, is selected.
5. The selected set of CUORE-0 events is merged with the Monte Carlo data, after being formatted in an identical way, as if coming from the same source.
6. `g4cuore` is run on the whole data, performing timing operations (pile-up, coincidences...) without making a distinction between Monte Carlo and CUORE-0 data.

This way, background contributions can be added without ignoring random occurrences, such as pile-up and accidental coincicences.

7.3 Results

In this section the comparison between CUORE-0 and simulated data will be shown. The spectral shape for M1 and M2 data is compared; the source activity is also estimated and compared with values measured with HPGe detectors. For all the reported simulations the `9.6.p03` version of `Geant4` was used.

The reconstruction of the ^{232}Th measurements showed an issue: a γ line at 1153 keV was present in the simulated data but completely absent in real data (figure 7.6). The default data libraries that come with `Geant4 v9.6.p03` were found to be the cause; substituting them with the more up-to-date libraries coming with `Geant4 v10.01.p02` completely solved the issue.

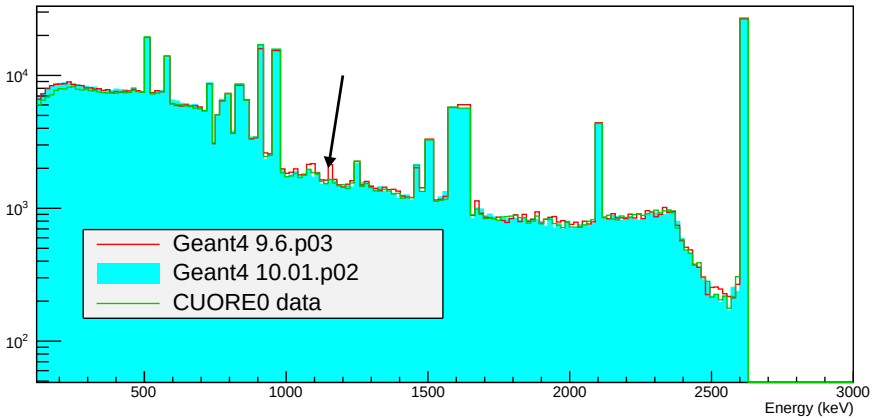

Figure 7.6: Comparison between CUORE-0 data and simulated data obtained with two different sets of libraries. The data comes from the high rate ^{232}Th calibration performed for dataset 2085. The arrow points at the 1153 keV line, which is overestimated when using the libraries that come with `Geant4 v9.6.p03`

7.3.1 Energy binning

Each plot showing the comparison between the energy spectra coming from experimental data and their Monte Carlo reproduction follows the same logic when it comes to energy binning. This can be summarized as follows:

- main γ lines are enclosed in a 3σ wide bin, in order to avoid including the exact line shape and the channel-dependent resolution in the MC reconstruction;
- background regions between γ lines are split into equally-sized bins, with a minimum width of 15 keV.

7.3.2 Activity evaluation

The Monte Carlo reconstruction has been used to evaluate the total activity of the radioactive sources. The activity value is calculated as follows:

$$A = \frac{N_{chain}^{MC}}{\tau} \cdot \left\langle \frac{N_{events}^{exp}}{N_{events}^{MC}} \right\rangle_{\gamma}, \tag{7.2}$$

where N_{chain}^{MC} is the number of full radioactive chains that have been simulated, τ is the measurement livetime and the average is performed over several γ lines, each of which had N_{events}^{exp} experimental counts and N_{events}^{MC} Monte Carlo counts.

7.3.3 ^{232}Th - High rate

High-rate ^{232}Th calibrations were performed using two thoriated wires, placed outside the cryostat but inside the external lead shield (figure 7.7). The two wires have the same activity and their position is symmetrical with respect to the center of the cryostat. The wires are ~ 1.04 meters long and are symmetric with respect to the center of the tower.

The high rate ^{232}Th measurement was the standard calibration procedure for CUORE-0; it has been repeated roughly every month, at the beginning and at the end of each dataset. As shown in figure 7.8, in some datasets the calibration wasn't performed in ideal conditions: apparently the thoriated wires weren't completely inserted, producing an asymmetry in the channel distribution of events. Since the MC simulation is performed with ideally positioned sources, a meaningful comparison can only come from datasets where the channel distribution best resembles the one coming from the Monte Carlo. For this reason, the calibration from dataset 2085 was chosen as a reference.

The comparison between experimental data and the Monte Carlo reproduction is shown in figures 7.9 (for the M1 spectrum) and 7.10 (M2). The normalization factor for the MC data was chosen in order to minimize the combined χ^2 value of the two spectra in the $120 - 3000$ keV range. There's a very good agreement between the MC and experimental data, both in M1 and M2. The only exception is the low energy region (below 300 keV) in the M1 spectrum (figure 7.9), where the MC systematically overestimates the background shape by about 10%.

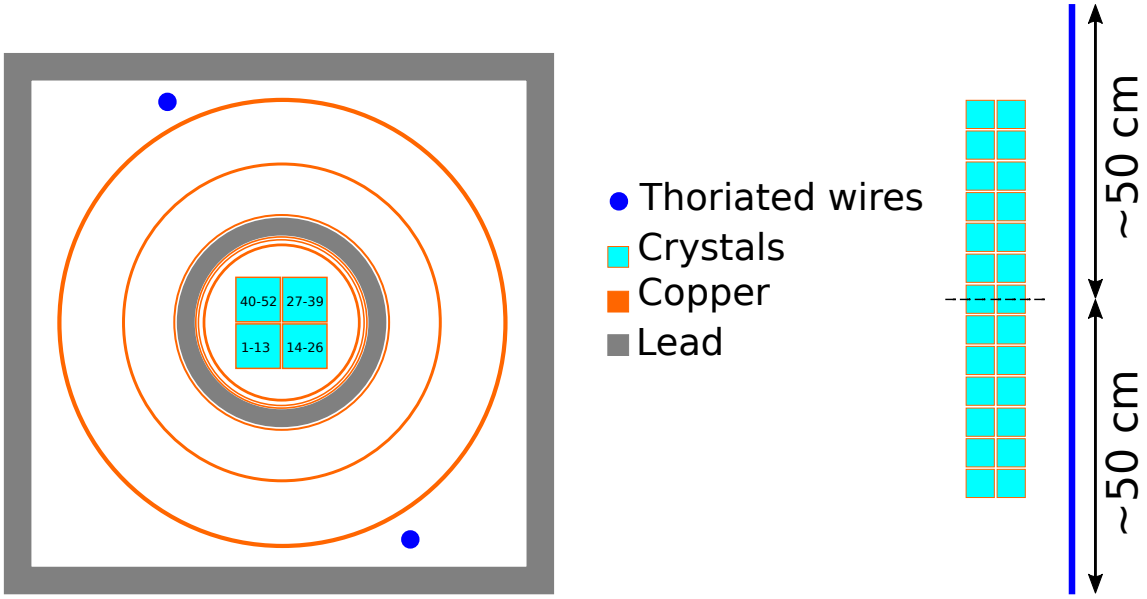

Figure 7.7: Schematic top-view (left) of the CUORE-0 cryostat and shielding, with the location of the ^{232}Th wire sources. Crystals are numbered starting from the bottom floor. On the right, vertical symmetry of the calibration wires.

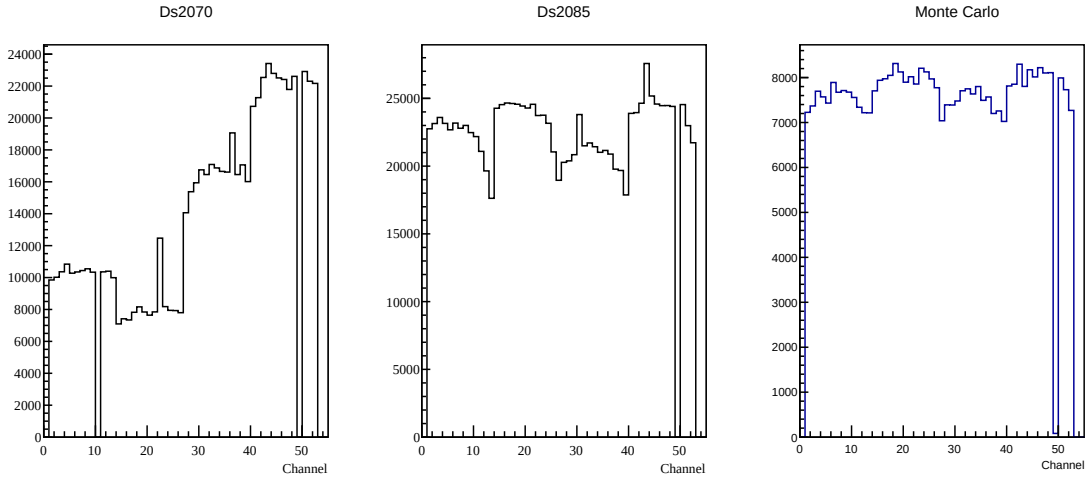

Figure 7.8: Channel distribution of events from two ^{232}Th calibrations (datasets 2070 and 2085), compared with the ideal distribution, coming from the Monte Carlo simulation. Ds 2070 is an example of a dataset where the calibration source is not in the ideal position.

The average source activity is $\sim$ 237 Bq (figure 7.11), roughly 120 Bq for each wire assuming they have the same activity. The wires have also been measured with HPGe detectors; the measured activities were 122 ± 7 Bq and 117 ± 7 Bq, making them perfectly compatible with the Monte Carlo reconstruction result.

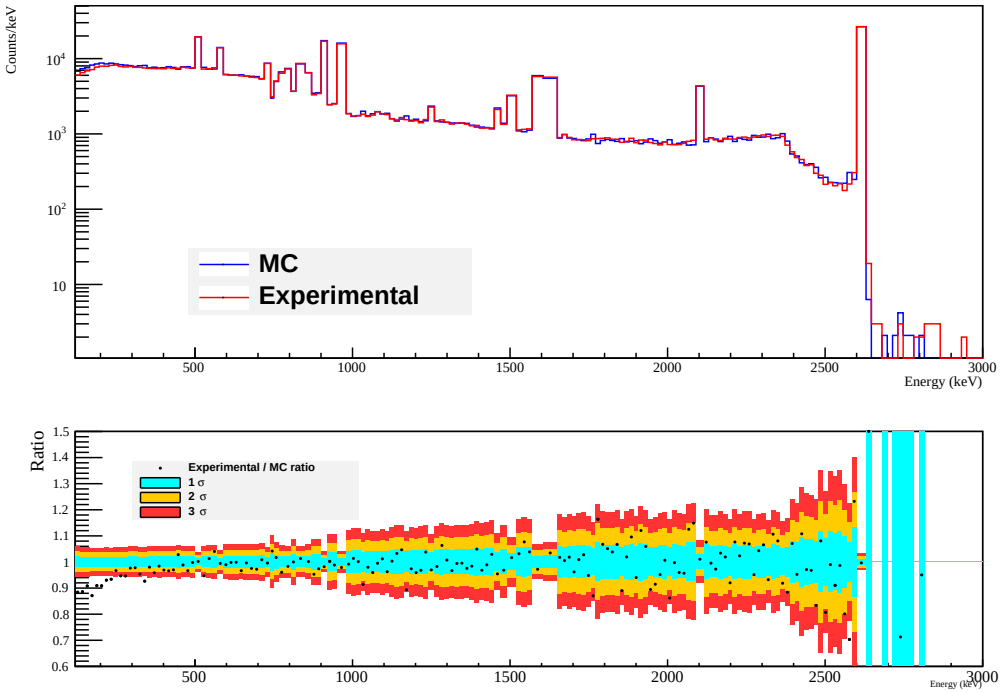

Figure 7.9: Comparison between the high rate ^{232}Th calibration and the MC simulation; M1 spectrum. The top plot shows the energy spectrum; the bottom plot shows the ratio between experimental and Monte Carlo data versus energy.

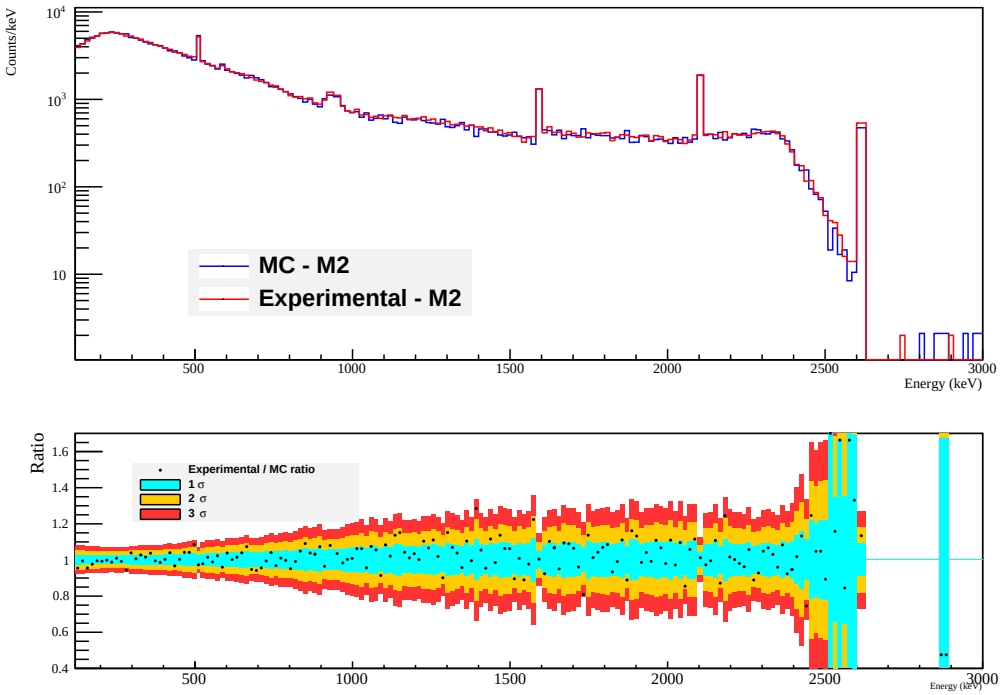

Figure 7.10: Comparison between the high rate ^{232}Th calibration and the MC simulation; M2 spectrum. The top plot shows the energy spectrum; the bottom plot shows the ratio between experimental and Monte Carlo data versus energy.

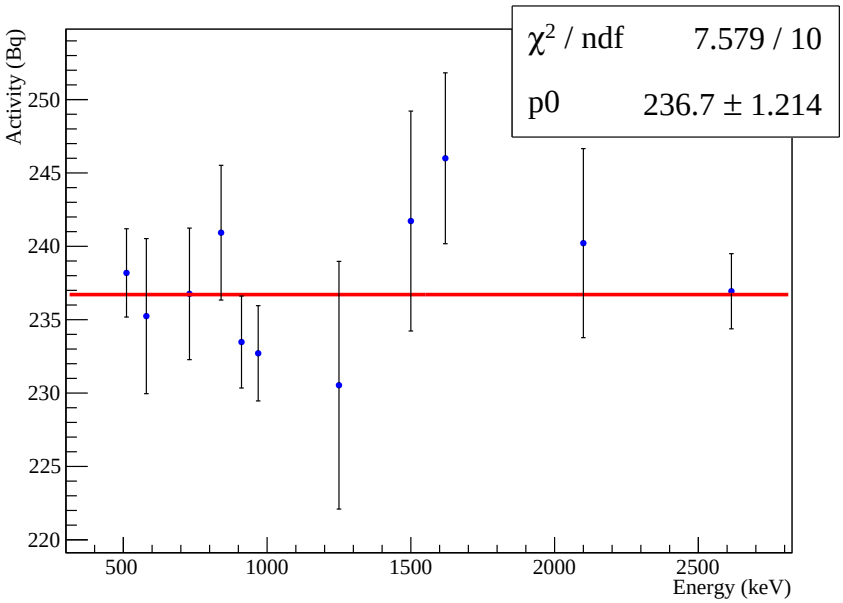

Figure 7.11: Calibration ^{232}Th source activity, evaluated over the main γ lines.

7.3.4 ^{60}Co

^{60}Co measurements were performed with a single source, located in the Main Bath (figure 7.12). This wire is ~ 1 meter long and is symmetrical along the vertical axis with respect to the center of the tower. The source was produced by neutron activation of an Al-Co wire at an experimental nuclear reactor; the source activity, measured with HPGe detectors, is 21 ± 2 Bq. Since the source is now asymmetric with respect to the center of the cryostat, the event rate distribution should not be uniform across the whole detector, as it happened for the ^{232}Th measurements (figure 7.8). Instead, columns 3 (channels from 27 to 39) and 4 (channels from 40 to 52) should see a higher event rate, being closer to the source and shielding the other two columns.

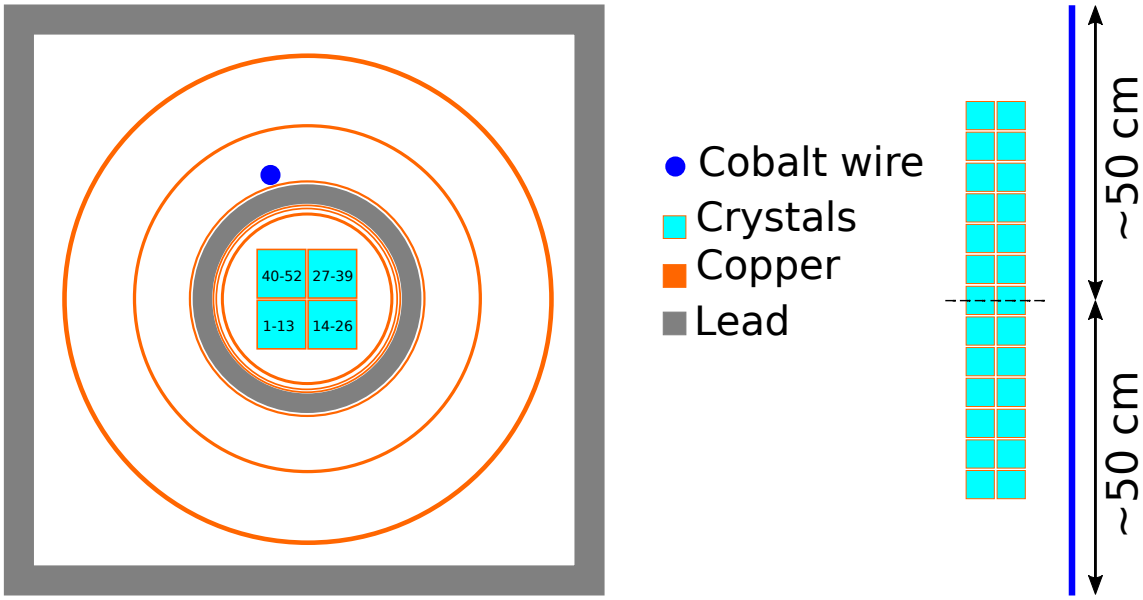

Figure 7.12: Schematic top-view (left) of the CUORE-0 cryostat and shielding, with the location of the ^{60}Co wire source. Crystals are numbered starting from the bottom floor. On the right, vertical symmetry of the calibration wire.

Due to the vertical symmetry of the source wire, a roughly flat distribution of events across each column of the CUORE-0 tower (as shown in the Monte Carlo prediction, in figure 7.13:1) should be expected. The experimental distribution, however, shows a different structure (figure 7.13:2); on the third column, the lower floors have higher event rates than the ones on the top of the tower, and the fourth column has the opposite behaviour. This suggests that the source probably wasn't inserted vertically, but at an angle.

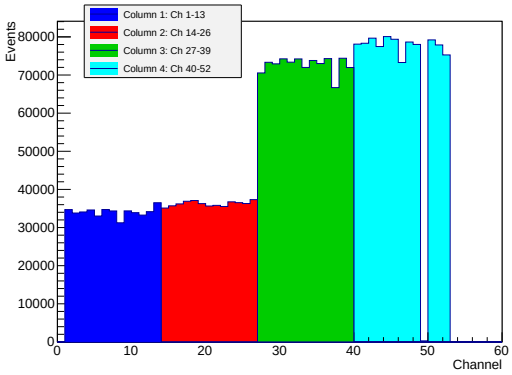

(1) Monte Carlo channel distribution

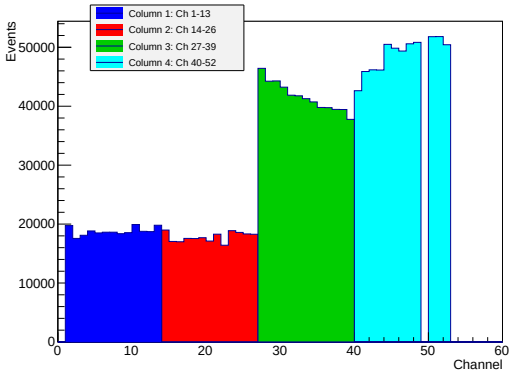

(2) Experimental channel distribution

Figure 7.13: Comparison between the experimental and Monte Carlo channel distribution for the ^{60}Co measurement. The four columns of the CUORE-0 tower are highlighted. The experimental event distribution on columns 3 and 4 shows that the source wasn't in the ideal position.

The comparison between experimental data and the Monte Carlo reproduction is shown in figures 7.14 (for the N1 spectrum) and 7.15 (M2). The normalization factor for the MC data was chosen in order to minimize the combined χ^2 value of the two spectra. There's a very good agreement between the MC and experimental data, both in M1 and M2.

The average source activity, evaluated on the two main γ lines from ^{60}Co, is 26.1 ± 0.1 Bq. The difference between this value and the measured one (21 ± 2 Bq) can probably be linked to the systematic error due to the unknown real position of the source.

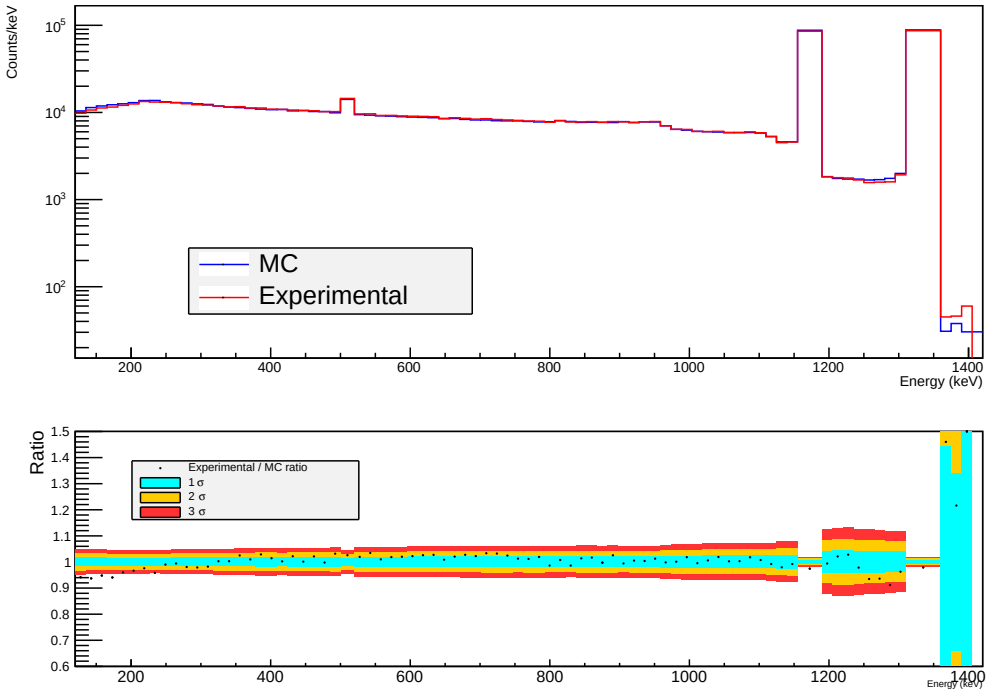

Figure 7.14: Comparison between the ^{60}Co calibration and the MC simulation; M1 spectrum.

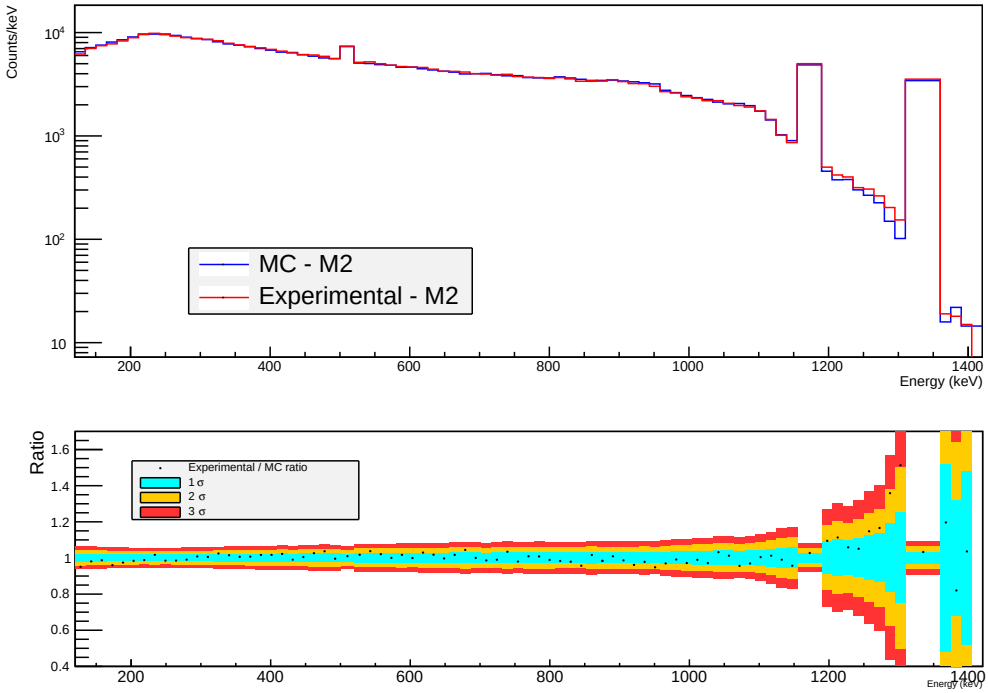

Figure 7.15: Comparison between the ^{60}Co calibration and the MC simulation; M2 spectrum

7.3.5 ^{56}Co

The ^{56}Co measurement was performed with two wire sources, one located in the Main Bath (MB) and the other outside the OVC (figure 7.16). Both wires are ~ 1 meter long and are symmetrical with respect to the center of the tower. The wires were produced by proton irradiation on a ^{56}Fe target; the measured activities are 31 ± 3 Bq for the MB wire and 61 ± 6 for the one outside the OVC.

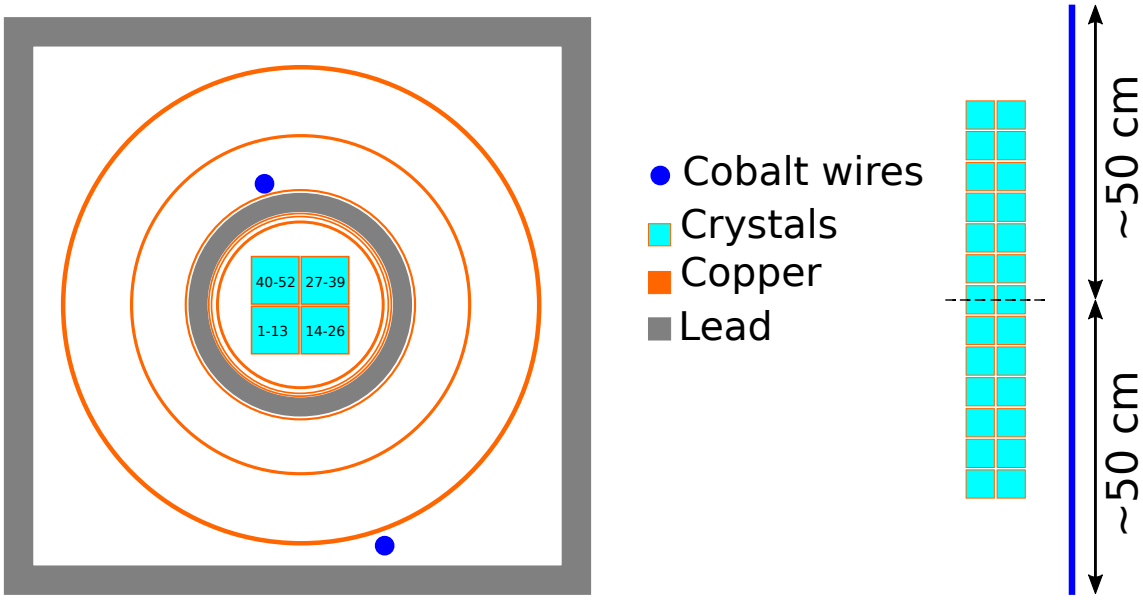

Figure 7.16: Schematic top-view (left) of the CUORE-0 cryostat and shielding, with the location of the ^{56}Co wire sources. Crystals are numbered starting from the bottom floor. On the right, vertical symmetry of the calibration wire.

As in the case of the ^{60}Co calibration, the source is not symmetric with respect to the center of the cryostat, so a higher event rate is expected on the columns closer to the MB source (columns 3 and 4). Again, due to the vertical symmetry of the wire disposition, great rate variations across a single column are not expected.

The distribution of events across the crystals is shown in figure 7.17, both for the Monte Carlo and for the experimental data. There's a great difference between the experimental behaviour and the expected one, across the whole tower; this is most likely due to an uneven activity distribution on both source wires.

The activity disuniformity on both sources has a strong effect on the Monte Carlo reconstruction, as the source geometry couldn't be reproduced correctly. Figures 7.19 and 7.20 show the comparison between experimental data and Monte Carlo reconstruction for

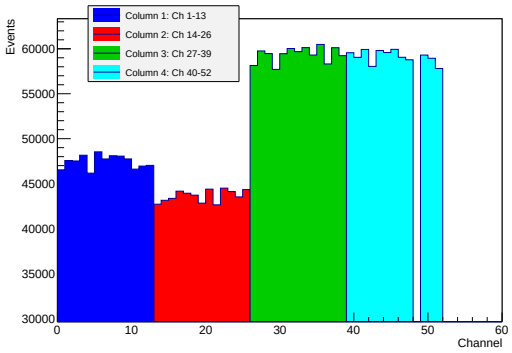

(1) Monte Carlo channel distribution

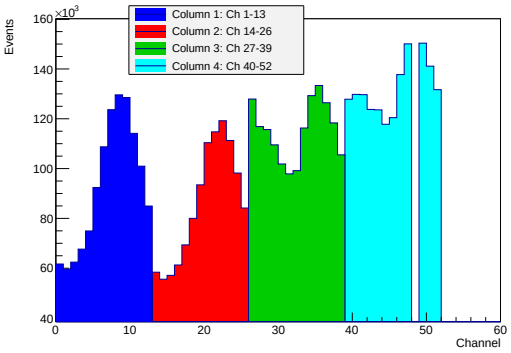

(2) Experimental channel distribution

Figure 7.17: Comparison between the experimental and Monte Carlo channel distribution for the ^{56}Co measurement. The four columns of the CUORE-0 tower are highlighted. The experimental event distribution shows that the source was strongly non-uniform.

the M1 and M2 spectra respectively. The general background shape is roughly reproduced both in M1 and in M2, with the major differences (around $\pm 10\%$) found in the region below 1 MeV. However, differences up to $\sim 20\%$ are observed for several γ lines in the M1 spectrum.

Due to these problems, the source activity estimate is not perfect. As shown in figure 7.18, most of the activity values obtained for single γ lines are incompatible between each other; they range from 70 to 90 Bq, with the average value being 80.4 ± 0.2 Bq. Given all the problems that affected the reconstruction of this measurement, a 10% difference between the estimated activity and the measured one (~ 90 Bq) is more than satisfactory.

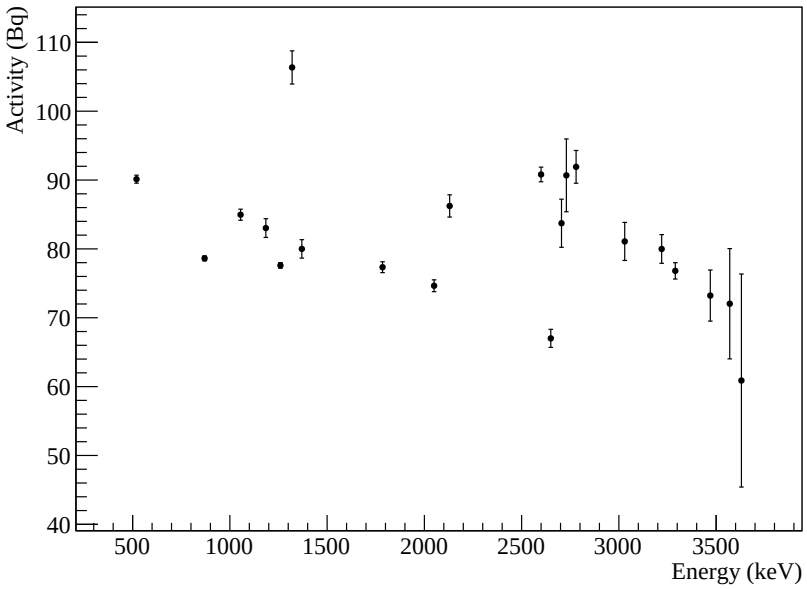

Figure 7.18: ^{56}Co sources activity, evaluated at the main γ lines.

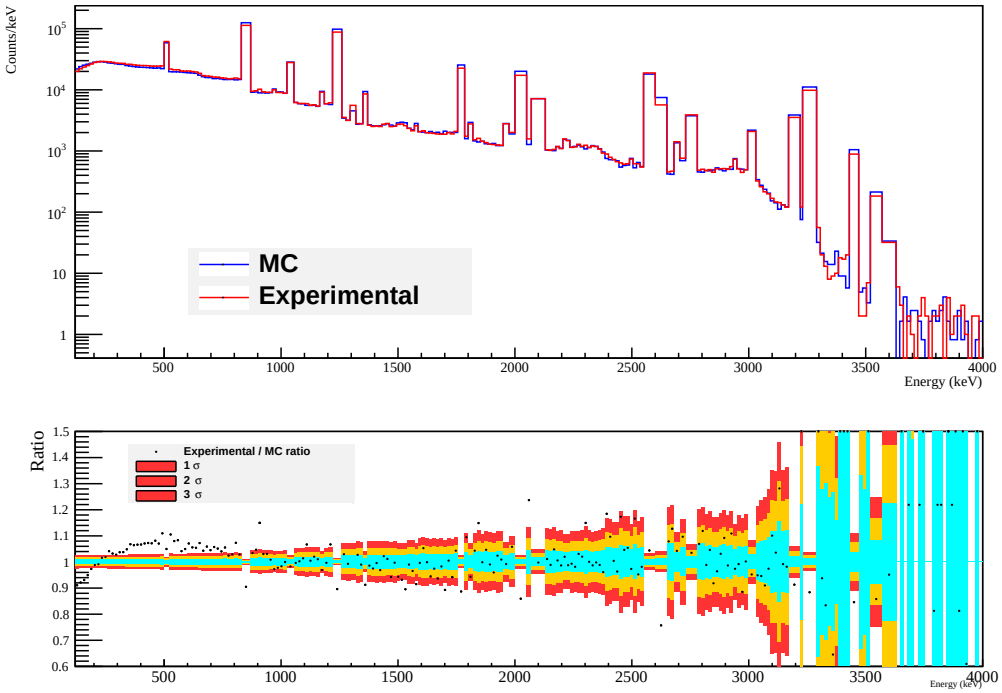

Figure 7.19: Comparison between the ^{56}Co calibration and the MC simulation; M1 spectrum

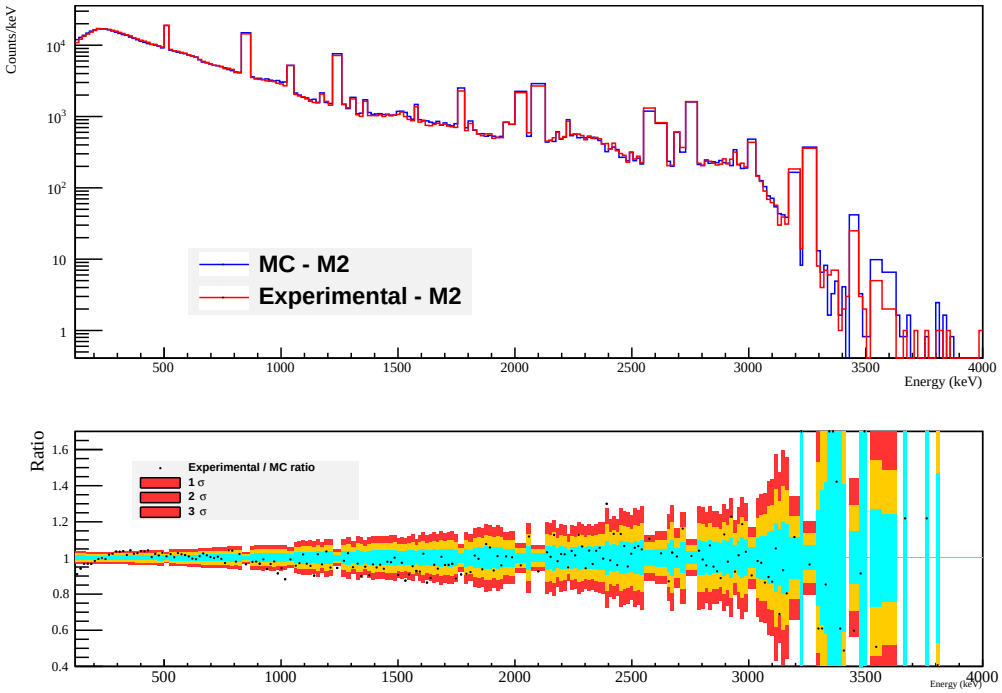

Figure 7.20: Comparison between the ^{56}Co calibration and the MC simulation; M2 spectrum

7.3.6 ^{232}Th - Low rate

The low rate ^{232}Th measurement was performed with two wire sources, whose position was the same as the one used in the high rate ^{232}Th calibrations (figure 7.7). These sources were shorter than the ones used for the standard ^{232}Th calibrations, being only $\sim$ 70 cm long; their position is still symmetrical with respect to the center of the tower (figure 7.21). The activity of each source is $\sim$ 9.7 Bq.

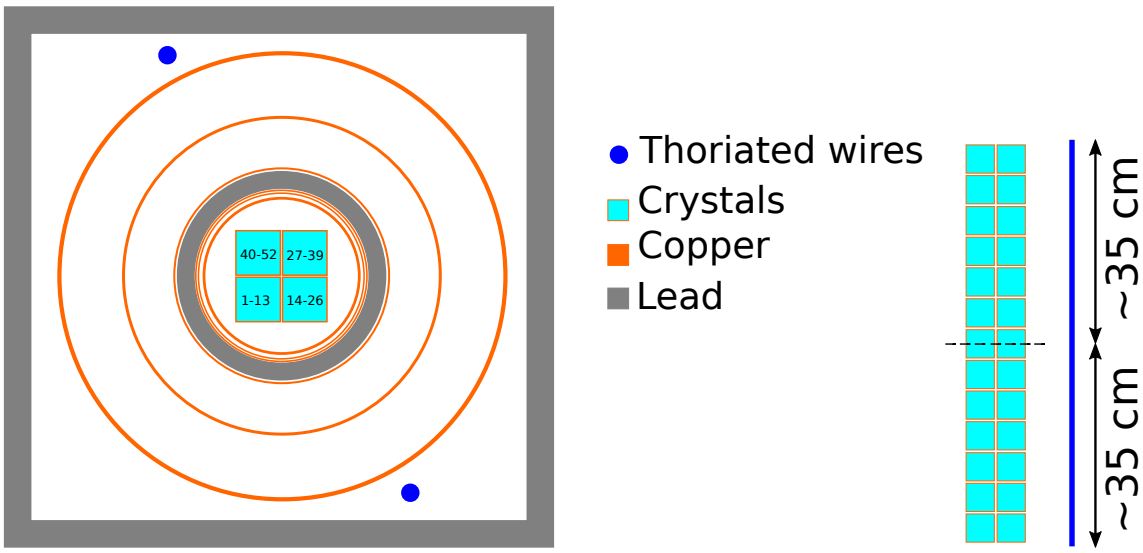

Figure 7.21: Schematic top-view (left) of the CUORE-0 cryostat and shielding, with the location of the ^{56}Co wire sources. Crystals are numbered starting from the bottom floor. On the right, vertical symmetry of the calibration wire.

The comparison between the experimental spectra and the Monte Carlo reproduction are shown in figures 7.22 (for M1) and 7.23 (M2). The agreement is generally very good, with the sole exception of the low energy region in the M1 spectrum. This is the same systematic effect observed in the high rate ^{232}Th measurement (figure 7.9).

The activity estimate is shown in figure 7.24: a small energy dependence can be observed, and the activity varies between $\sim$ 18 and $\sim$ 23 Bq, with an average value of 20.8 ± 0.1 Bq. This value is compatible with the expected one (19.4 Bq, corresponding to two 9.7 Bq wires) within 10%, which is a reasonable systematic value for the MC.

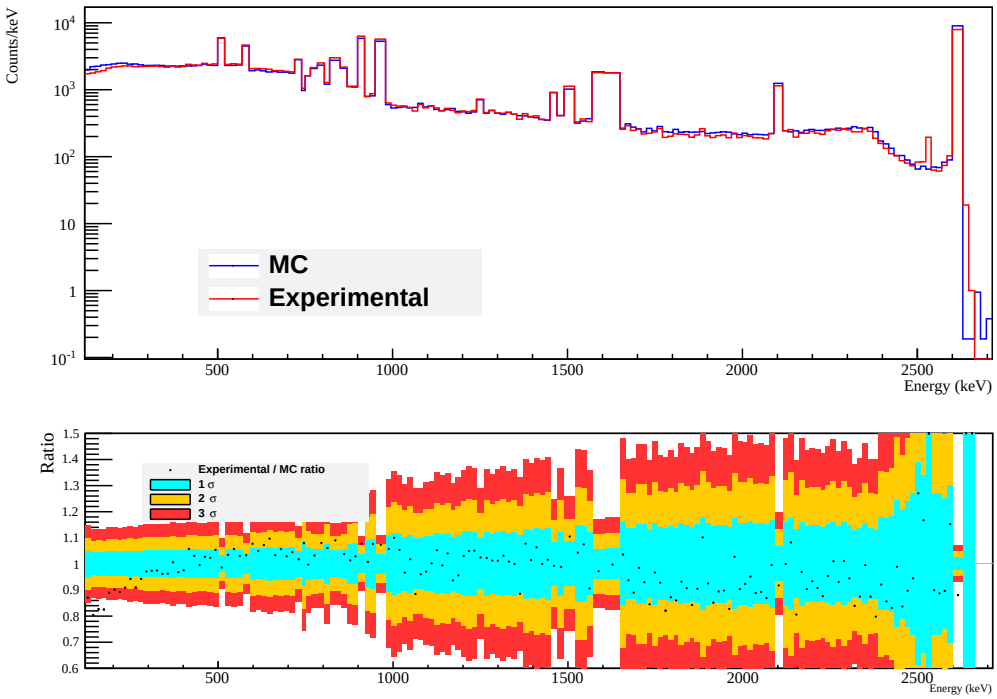

Figure 7.22: Comparison between the ^{232}Th low rate measurement and the MC simulation; M1 spectrum. The line at $\sim$ 2500 keV comes from data blinding, as the low rate calibration has never been officially unblinded.

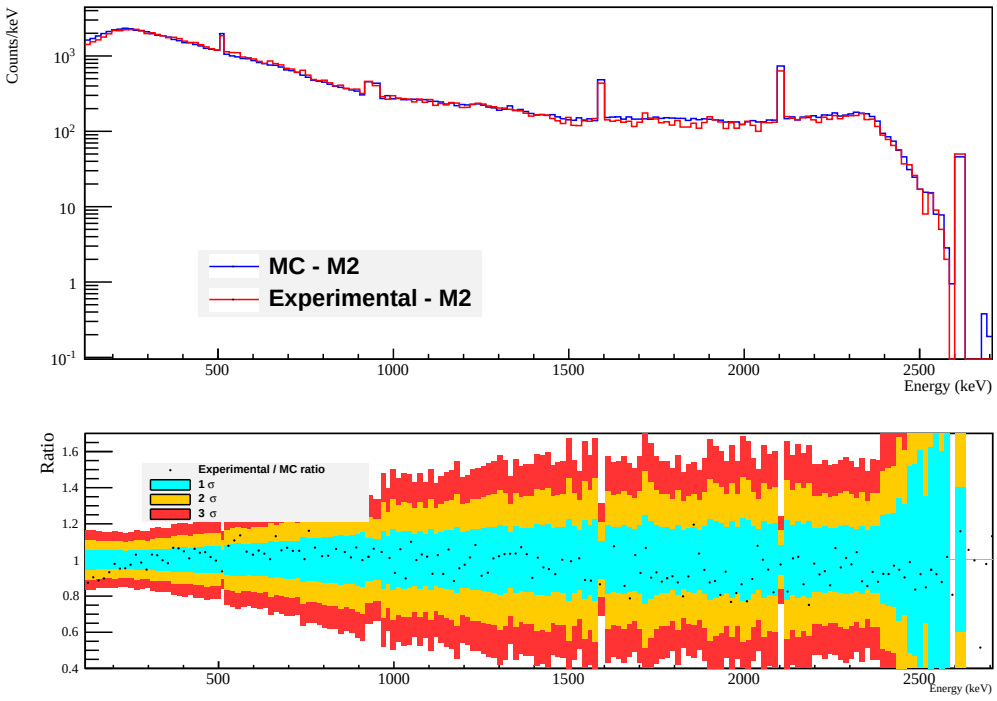

Figure 7.23: Comparison between the ^{232}Th low rate measurement and the MC simulation; M2 spectrum

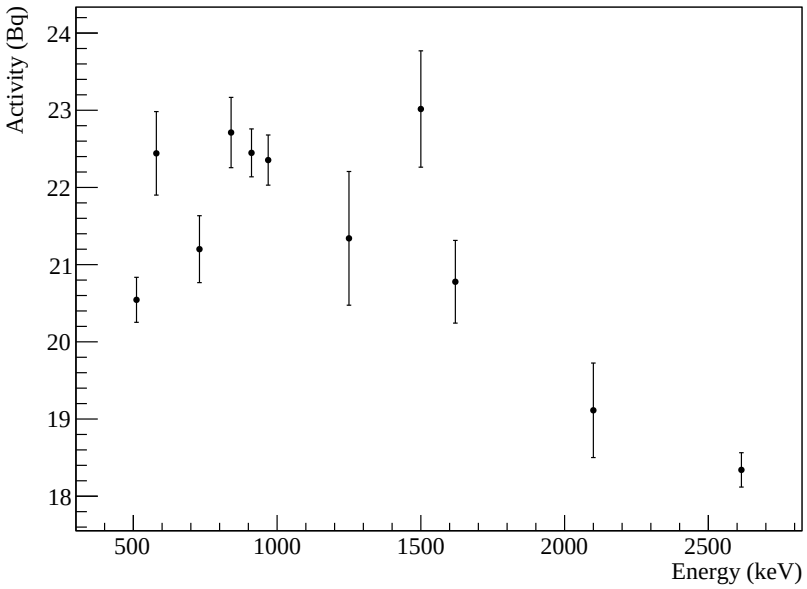

Figure 7.24: Low rate ^{232}Th sources activity, evaluated at the main γ lines.

7.4 MC systematics

The Monte Carlo code is able to reconstruct source measurements with good accuracy in most cases, with the main inaccuracies coming from source non-idealities that are complicated to simulate correctly. Table 7.2 shows a summary of the results of the reconstructed source measurements.

Source	Activity (HPGE) [Bq]	Activity (MC) [Bq]	Comments
^{232}Th - High Rate	239 ± 9	236.7 ± 1.2	Standard calibration
^{60}Co	21 ± 2	26.1 ± 0.1	Source at an angle
^{56}Co	92 ± 7	$80 - 100$	Source activity not uniform
^{232}Th - Low Rate	19.4	$18 - 23$	

Table 7.2: Summary table of the four reconstructed source measurements.

One flaw that appeared in every case studied was the inability of the Monte Carlo to reproduce the shape of the M1 spectra in the region below ~ 300 keV. Some possibilities have been investigated to try and motivate this discrepancy. This effect appears in every source measurement including the low rate ^{232}Th calibration, meaning that the issue is

probably not related to the increased event rate and, therefore, to some timing issue.

The shape of the energy spectra might suggest that the trigger efficiency VS energy is involved, as it is described with a sigmoid function. For this to be true, however, the noise level would have to be significantly higher in source measurements with respect to background runs; since this is not observed, this possibility should be ruled out. Additionally, this would impact both the M1 and the M2 spectra, but the M2 spectrum doesn't show the same behaviour at low energies.

Another possible cause is an inaccuracy in the geometrical reconstruction of the cryostat. The parts of the cryostat that could be responsible for this effect are the ones inside the roman lead shield, since the issue is found in the low energy region; low energy photons produced outside this layer are absorbed by lead and do not reach the detector.

MC simulations have been produced with different thicknesses of copper in the internal shields of the cryostat; since the Monte Carlo has the best performance when reconstructing the high rate ^{232}Th calibration, it has been used in this comparison.

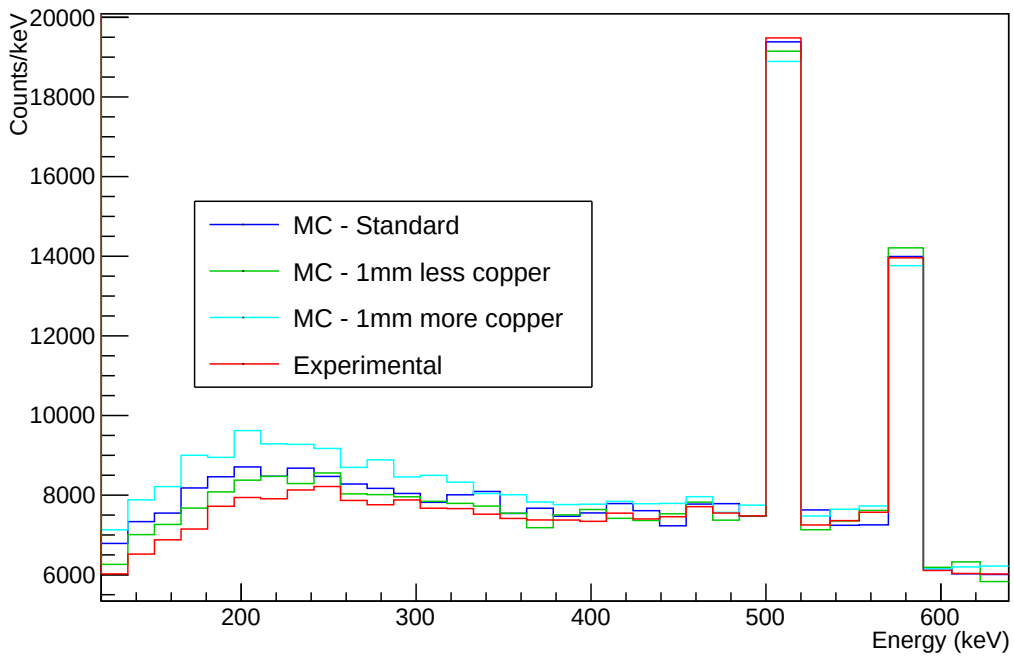

Figure 7.25: High rate ^{232}Th calibration, comparison of the measured M1 spectrum (red) with three different MC spectra: standard (blue, the same one used in section 7.3.3), with more copper added to the internal shields (cyan) and with less copper in the internal shields (green). The best adaptation to the experimental spectrum is obtained by removing copper.

In figure 7.25 a comparison between the experimental M1 data and three different Monte Carlo spectra is shown: the standard one (the same used in section 7.3.3), one with more copper and one with less copper. The best adaptation in the low energy region is clearly obtained by removing 1 mm copper from the internal shields. The amount of copper to be removed, however, is significant; the internal shields (10 mK, 50 mK, 600 mK) add up to a total 5 mm thickness of copper, and an error of the order of 20% seems excessive. Even if this approach could lead to a solution of the low energy issue, unless a direct measurement of the shield thickness proves otherwise, it is not a feasible approach.

CHAPTER

8

THE CUORE-0 BACKGROUND MODEL

One of the parameters that affect the sensitivity of a detector to $0\nu\beta\beta$ is the radioactive background. The choice of materials for detector construction can affect greatly the performance of the experiment, but it isn't always possible to measure precisely the activity of said materials beforehand. The background levels needed for a competitive experiment are so low that often standard techniques can only yield upper limits on contaminations. The most sensitive way to determine contamination levels of materials used for the construction of CUORE-0 can be CUORE-0 itself.

The aim of the CUORE-0 background model is the reconstruction of the sources that can account for the observed experimental background, giving a precise description of their location and activity. This is done by properly combining Monte Carlo spectra simulating the effect of various contaminants in all the parts of the cryostat. The combination is performed with a Bayesian approach, using the previous knowledge about material contamination as a *prior* for the model [17].

In this chapter I'll outline the construction of the CUORE-0 background model, describing how background sources were selected, the way MC files are processed and how they're combined in the final fit.

8.1 Background sources

The sources responsible for background can be cosmic rays, natural or artificial radioactive contaminations in the laboratory environment and in the experimental setup and finally the radioimpurities contained in the detector itself. The impact that each background source has on the final data strongly depends on its origin and intensity. These, however, are not the only unknowns: some sources might not have been identified from previous measurements but they can be present and affect the detector nonetheless. CUORE-0 data are, however, a powerful tool to investigate the presence of these sources, identified from the characteristic features of their decay, such as the presence of α or γ lines, time variation of the counting rate or multiplicity patterns.

8.1.1 Screening of CUORE-0 materials

Based on the experience accumulated with Cuoricino [61][62] the most important sources of background are expected to come from the detector tower and the cryostat. Natural radioactive chains (^{232}Th, ^{238}U, ^{40}K) are expected to play an important role, as well as surface implantation of ^{210}Pb due to the decay of environmental ^{222}Rn. A thorough screening campaign was performed on the materials used for the construction of every part of the detector, looking for these specific contaminants [61]. A summary of the result of the screening can be found in table 8.1 for bulk contaminations and in table 8.2 for surface ones.

Component	^{232}Th [Bq/kg]	^{238}U [Bq/kg]	^{40}K [Bq/kg]
TeO_2 crystals	$< 8.4 \cdot 10^{-7}$	$< 6.7 \cdot 10^{-7}$	
Epoxy glue[1]	$< 8.9 \cdot 10^{-4}$	$< 1.0 \cdot 10^{-2}$	$< 47 \cdot 10^{-3}$
Au bonding wires	$< 4.1 \cdot 10^{-2}$	$< 1.2 \cdot 10^{-2}$	
Si heaters	$< 3.3 \cdot 10^{-4}$	$< 2.1 \cdot 10^{-3}$	
Ge thermistors	$< 4.1 \cdot 10^{-3}$	$< 1.2 \cdot 10^{-2}$	
PTFE supports	$< 6.1 \cdot 10^{-6}$	$< 2.2 \cdot 10^{-5}$	
Cu NOSV	$< 2.0 \cdot 10^{-6}$	$< 6.5 \cdot 10^{-5}$	$7 \pm 2 \cdot 10^{-4}$
Roman lead	$< 4.5 \cdot 10^{-5}$	$< 4.6 \cdot 10^{-5}$	$< 2.3 \cdot 10^{-5}$
External lead	$< 2.6 \cdot 10^{-4}$	$< 7.0 \cdot 10^{-4}$	$< 5.4 \cdot 10^{-3}$

Table 8.1: Measurements and limits on bulk contaminations of the various detector components. Error bars are 1 sigma, limits are 90% C.L. upper limits. ([1]: epoxy glue is used to fix the Ge thermistors and the Si heaters to the crystals)

Component	Contamination depth [μm]	^{232}Th [Bq/cm^2]	^{238}U [Bq/cm^2]	^{210}Pb [Bq/cm^2]
TeO_2 crystals	$0.01 - 10$	$< 2 \cdot 10^{-9}$	$< 9 \cdot 10^{-9}$	$< 1 \cdot 10^{-6}$
Si heaters	$0.1 - 10$	$< 3 \cdot 10^{-6}$	$< 8 \cdot 10^{-7}$	$< 8 \cdot 10^{-7}$
Ge thermistors	$0.1 - 10$	$< 8 \cdot 10^{-6}$	$5 \cdot 10^{-6}$	$< 4 \cdot 10^{-5}$
PTFE supports	$0.1 - 30$	$< 2 \cdot 10^{-8}$	$< 7 \cdot 10^{-8}$	
Cu NOSV	$0.1 - 10$	$< 7 \cdot 10^{-8}$	$< 7 \cdot 10^{-8}$	$< 9 \cdot 10^{-7}$

Table 8.2: 90% C.L. upper limits for the surface contaminants of the most relevant elements facing the CUORE-0 detector.

8.1.2 Analysis of the γ region

The analysis of the region below the 2615 keV γ line from ^{208}Tl can yield important information about the presence of additional contaminants. While most of the observed γ lines come from the natural decay chains of ^{232}Th and ^{238}U, contributions from isotopes produced by activation (either by cosmic rays or neutrons) by fallout can be found.

TeO_2 crystals cosmogenic activation

The only visible contribution coming from cosmogenic activation of TeO_2 comes from ^{125m}Sb. This isotope is produced in the bulk of the TeO_2 crystals as a result of Te interactions with cosmic rays. ^{125}Sb undergoes β decay with a half life of 2.8 years with Q=766 keV; the decay also leads to the emission of several γ lines, among which the most prominent are at 428 keV (30% branching ratio) and at 600 keV (17% B.R.). Additionally, the daughter nucleus, ^{125m}Te, decays by internal transition with a 58 days half-life and a 145 keV Q-value.

The 145 keV line is clearly visible in the M1 spectrum (figure 8.1), while the two γ lines from ^{125}Sb are visible in the M2 spectrum (figure 8.2): these M2 events are produced when the β decay happens in a crystal and the γ deposits energy in another.

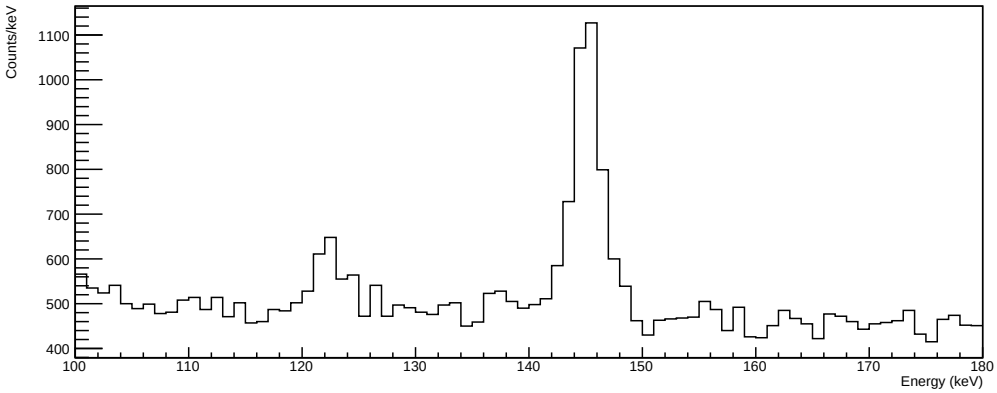

Figure 8.1: CUORE-0, M1 spectrum; the 145 keV line from ^{125m}Te and the 122 keV line from ^{57}Co are visible.

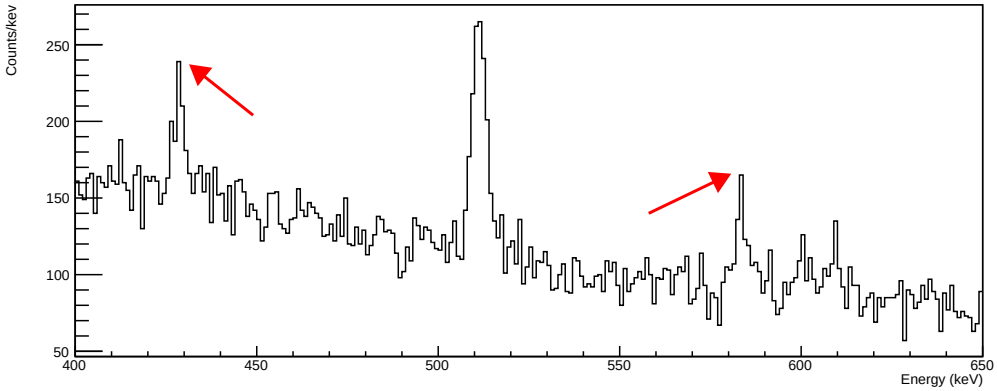

Figure 8.2: CUORE-0, M2 spectrum; the two main γ lines from ^{125}Sb are highlighted.

Copper cosmogenic activation

Three contaminants produced by cosmogenic activation in copper are relevant for CUORE-0: ^{60}Co, ^{57}Co and ^{54}Mn.

^{60}Co beta decays with a half-life of 5.27 years; its main signatures are two γ lines at 1173 and 1332 keV. Both the lines are clearly visible in the M1 and M2 spectrum; the sum of these two lines, located at 2505 keV, is also visible (figure 8.3).

^{57}Co decays by electron capture with a half life of 271.4 days, emitting in the process two γ lines, one at 122.1 keV (85.6% B.R.) and one at 136.5 keV (10.7% B.R.). The 122 keV line is clearly visible in the M1 spectrum, while the small structure slightly below the 145 keV line from ^{125m}Te, near 137 keV, could be ascribed to the γ with lower branching

ratio (figure 8.1).

^{54}Mn decays by electron capture with a half life of 312.5 days. A single γ is emitted by this decay, at 834.8 keV (99.98% B.R.). Although this line is clearly visible in the spectrum, it is not necessarily produced by ^{54}Mn only. ^{228}Ac, which is part of the ^{232}Th decay chain, produces several low-branching γ lines with similar energies: 830.5 (0.5% B.R.), 835.7 (1.6% B.R.) and 840.4 (0.9% B.R.). Analysis of the other γ lines from ^{228}Ac led to the conclusion that the 835 keV line cannot be caused by ^{228}Ac alone, meaning that part of it must come from ^{54}Mn (figure 8.4).

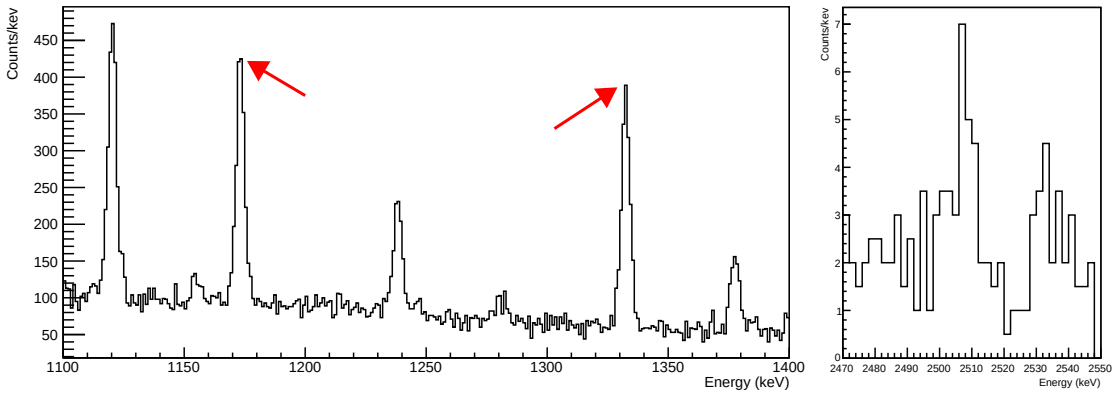

Figure 8.3: CUORE-0, M1 spectrum; on the left, the two main γ lines from ^{60}Co are highlighted; on the right, the sum line at 2505 keV is shown.

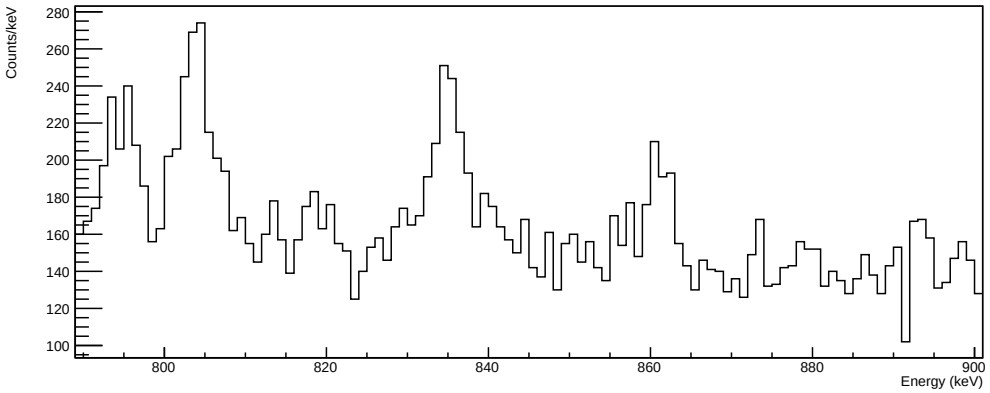

Figure 8.4: CUORE-0, M1 spectrum; the 835 keV line comes from the superposition of the single γ line from ^{54}Mn and three low-branching lines from ^{228}Ac.

Neutron activation

The most relevant neutron-produced source in CUORE-0 is ^{108m}Ag, located inside the roman lead shield. ^{108m}Ag decays by electron capture with a half life of 418 years, emitting three γs: 433.5 keV (90.5% B.R.), 614.3 keV (89.8% B.R.) and 722.9 keV (90.8% B.R.). While the three branching ratios are similar, the lower energy line is not clearly visible in the spectrum, while the other two show up as excesses on the tail of neighboring peaks (figure 8.5). This is likely due to the lower energy photon being absorbed with higher probability between the roman lead shield and the detector, and has been confirmed by simulations of ^{108m}Ag in the bulk of the roman lead shield.

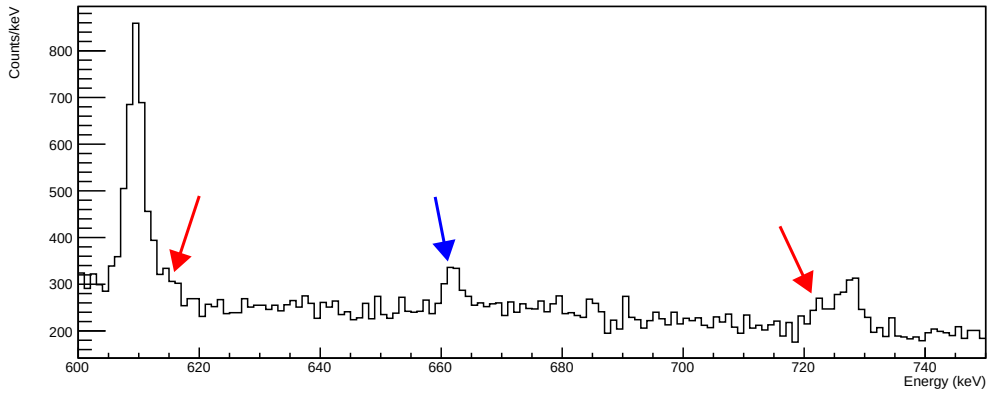

Figure 8.5: CUORE-0, M1 spectrum; the two γ lines from ^{108}Ag, showing up as excesses near the tails of neighboring peaks, are indicated by the red arrows. The blue arrow points to the 661 keV line from ^{137}Cs.

Fallout products

Two fallout products contribute to the CUORE-0 bakground: ^{137}Cs and ^{207}Bi. ^{137}Cs beta decays with a 30.2 years half life, producing a single intense γ line at 661 keV, visible in the M1 spectrum (figure 8.5). ^{207}Bi decays via electron capture with a half-life of 31.55 years, emitting two γ lines at 569.7 keV (97.75% B.R.) and 1063.7 keV (74.5% B.R.). Despite the higher branching ratio, the lower energy line is not visible in the spectrum; this suggests that this contamination is located in the outer lead shield, leading to the likely absorption of the 569 keV line by the inner lead shield (figure 8.6).

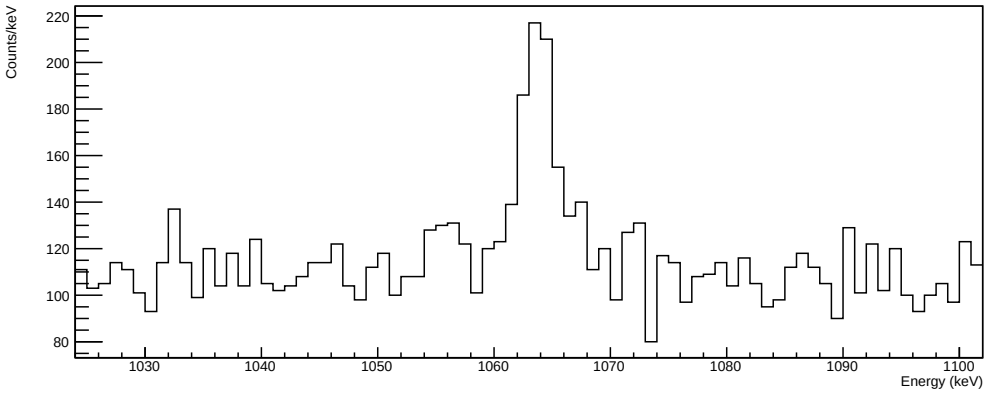

Figure 8.6: CUORE-0, M1 spectrum; the only visible line from ^{207}Bi, at 1063 keV.

8.1.3 Analysis of the α region

The energy region above the ^{208}Tl line contains mainly contributions from α decays coming from the ^{232}Th and ^{238}U decay chains, with a single line coming from ^{190}Pt. While the analysis of this region doesn't give information about the presence of additional contaminants, it can give strong hints regarding the location of ^{232}Th and ^{238}U in the cryostat. Since the range of α particles in matter is extremely short (a 5 MeV α has a range of about 10μm in copper), only the elements closest to the detector can populate this part of the spectrum: the innermost copper shield, the copper structure of the tower, the PTFE holders and the crystals themselves.

Event multiplicity can play an important role in determining source location. After each α decay a part of the energy is carried away by the recoiling nucleus: αs have energies in the 3-6 MeV range, while nuclear recoils carry about 70-100 keV. This produces several possible scenarios:

- if the contamination is in the crystal bulk, neither the α or the recoiling nucleus can escape the crystal. Both deposit their energy in the same spot, producing an M1 event whose energy is at the Q-value of the decay;
- when the contamination is closer to crystal surfaces, the α particle can leave the crystal. If the α is then absorbed in copper, an M1 event with the energy of the nuclear recoil is produced; if, on the other hand, the α interacts in another channel, the event is M2. The opposite can also happen, with the nuclear leaving the crystal, but this requires the contamination to be much closer to the surface;
- if the decay originates from the copper surface, the α can reach a crystal and produce

an M1 event. The energy deposited by this event depends on the depth of the original contamination. If the source is really close to copper surface, no energy is left behind and the M1 event contains the full energy of the α. If the contamination is deeper, part of the energy is left behind, undetected: this populates a low-energy tail of the α peak, extending as a flat continuum to lower energies, even in the γ region.

The analysis of the α region is not only useful in locating close sources but can also be used to verify if the ^{232}Th and ^{238}U chains are in secular equilibrium. A decay chain is in secular equilibrium if all its members have the same activity, or decay rate. Natural sources of ^{232}Th and ^{238}U are generally in equilibrium, unless some isotope belonging to the chain is somehow removed from the original material: this can be due, for example, to ^{222}Rn degassing. When this happens secular equilibrium breaks, making the activity of the various parts of the chain disuniform.

^{238}U chain

Almost all the main α lines from the ^{238}U chain are visible in the spectrum, both in M1 and in M2. Q-value lines, however, are not visible in the M1 spectrum. Based on previous considerations, this means that most of the ^{238}U contamination should lie near the crystal surface, with a small fraction probably coming from the surface of the copper structure.

The activity of some of the members of the chain is shown in figure 8.7. There is a major breakpoint at ^{230}Th, whose activity is far lower than that of its preceding isotopes, ^{238}U and ^{234}U. The following isotope, ^{226}Ra, has a much higher activity, compatible with ^{222}Rn and ^{218}Po, coming immediately after. A small quantity of ^{226}Ra has probably been added to the crystals surface during the cleaning process, presumably the ones involving water. Given the short lifetime of this isotope (1.6 years) and the age of the CUORE-0 crystals (7-8 years), secular equilibrium for the chain fraction below ^{226}Ra has been reinstated.

^{214}Po is missing from the chain as it is highly unlikely to observe the corresponding α line in the spectrum. ^{214}Po decays quickly (half-life 164μs) after the β decay of its predecessor, ^{214}Bi; since the time resolution of CUORE-0 is in the order of tens of ms, the βs from bismuth add up to the α from polonium, producing a signal that has a higher energy than the α alone.

The most prominent α line in CUORE-0, coming from ^{210}Po, deserves a discussion on its own. This isotope produces two lines in the CUORE-0 spectrum, one at the α energy (5304 keV), both in M1 and M2, and one at the Q-value (5407 keV) in M1 only. This means that there should be two components: one from the bulk of the crystals, populating the Q-value line, and one from the surface.

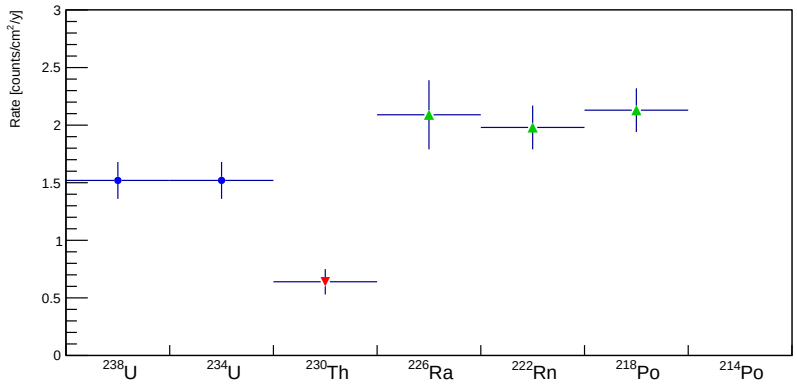

Figure 8.7: Activity of α-decaying parts of the ^{238}U chain. The main breakpoint is at ^{230}Th. The reason why ^{214}Po has no activity and ^{210}Po is missing is explained in the text.

The time dependence of the two lines is also different: while the α line is stable in time across the whole CUORE-0 data taking, the Q-value line appears to decay with the characteristic half-life of ^{210}Po, 138 days (figure 8.8). This means that there must be two components that produce these lines:

- a contamination of ^{210}Po itself, which is decaying with its normal half-life;
- a contamination of ^{210}Pb, a predecessor of ^{210}Po in the ^{238}U decay chain with longer half-life (22 years). This contamination is in secular equilibrium, meaning that the activity of both ^{210}Pb and ^{210}Po is the same and is constant in time (at least on the CUORE-0 timescale).

Both components are not in secular equilibrium with the rest of the chain, described previously, as their activity is much higher.

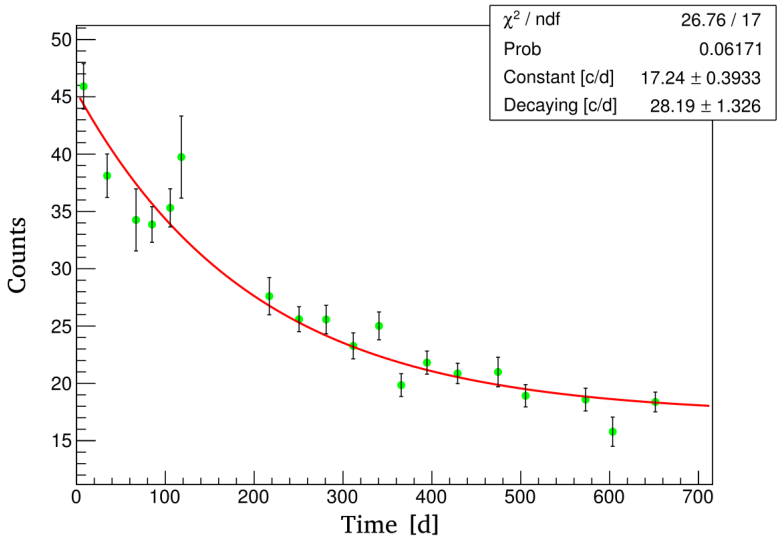

Figure 8.8: Time dependence of the ^{210}Po Q-value line. The half-life of ^{210}Po, 138 days, is kept constant in the exponential fit.

^{232}Th chain

The identification of secular equilibrium breakpoints is harder for ^{232}Th, since several isotopes in this chain decay quickly and produce pile-up events in CUORE-0. The analysis of the few available peaks leads to believe that secular equilibrium is maintained for most of the chain, with the exception of the progenitor itself, ^{232}Th.

- ^{232}Th: only the Q-value line in the M1 spectrum, with activity 5.92 counts/(kg·y), is visible, meaning that it's a bulk contamination only. All other contaminations come from the surface of the crystals.
- ^{228}Th: surface activity $1.82 \pm 0.18 \cdot 10^{-2}$ counts/(cm^2·y).
- ^{224}Ra: surface activity $1.68 \pm 0.17 \cdot 10^{-2}$ counts/(cm^2·y), in equilibrium with ^{228}Th.
- ^{210}Rn, ^{216}Po: the half-life of ^{216}Po is short (0.16 seconds), leading to pile-up on signals produced by ^{210}Rn most of the time. The lines produced by these two isotopes are not visible in the spectrum.
- ^{212}Bi: measured surface activity $0.52 \pm 0.10 \cdot 10^{-2}$ counts/(cm^2·y), but the α decay of this isotope has a 36% branching ratio; the real activity is then $1.44 \pm 0.27 \cdot 10^{-2}$ counts/(cm^2·y), compatible with ^{224}Ra and ^{228}Th and in secular equilibrium. Due to this fact, probably even ^{210}Rn and ^{216}Po are in secular equilibrium.

- ^{212}Po: the low half-life of this isotope (0.3μs) makes this α often add up to βs produced by its predecessor, ^{212}Bi. As for the situation described for ^{214}Po, in the ^{238}U chain, the activity from this isotope isn't easily measurable.

^{190}Pt

^{190}Pt is a naturally occurring isotope with low abundance (0.01%). Its α decay emits a 3180 keV α, but it is not visible in the CUORE-0 data; instead, the Q-value peak at 3249 keV is visible in M1, meaning that ^{190}Pt is entirely contained in the bulk of the crystals.

8.2 MC production

All the sources identified with the methods described in section 8.1 were simulated with high statistics and processed with `g4cuore`. The settings used for this processing are very similar to those used in chapter 7 to reconstruct source measurements:

- *Energy resolution*: the same resolution vs. energy is used (figure 7.1).
- *Energy threshold*: the same channel-dependent threshold parameters are used (figure 7.2).
- *Dead time*: 1 second.
- *Integration time*: 10 ms.
- *Coincidence window*: 10 ms.
- *Pile-up*: 4 seconds.
- *Excluded channels*: channel 49 is disabled.
- *Pulser*: one pulse every 300 seconds.

A significant difference between data processing for the background model and for source measurements is the event rate. For source measurement the event rate can be set as the measured one, since the contribution from background is negligible. For the simulations described in this chapter, no information on the event rate is available. While it is true that background measurements in CUORE-0 have an average event rate of 0.055 Hz (on the whole tower), this is due to the combination of every background source. Without knowing the relative weight of all the involved sources, it's impossible to assign a proper event rate to each simulation. Since `g4cuore` still needs an event rate to work

properly, a fixed rate of 10^{-4} has been chosen, assuming that it is low enough to have completely negligible effects from pile-up or accidental coincidences.

A parameter which wasn't used in the source measurements reconstruction was the quenching factor for α particles. This, as well as the parameter used to describe surface contamination profile, will be described in the following sections.

8.2.1 α quenching factor

When an α particle interacts in the detector it generates a pulse slightly higher than what would be expected from the standard calibration. All α lines are systematically shifted towards higher energies with respect to their nominal value. A fit of the relative energy difference $\Delta E/E$ is shown in figure 8.9; the average value for the quenching factor is $7.4 \cdot 10^{-3}$.

The line from ^{190}Pt has been excluded from the fit, since it shows a different behaviour. The quenching factor associated to this line is much higher than all the others, almost double. As discussed in chapter 4, this is a possible consequence of the nature of the Pt contamination. Small fragments of Pt can be included in the crystals during their growth, leading to a slightly different local response in the vicinity of the fragments.

The quenching factor has been included in the `g4cuore` processing of all simulations used in the background model. The simulation associated to platinum coming from crystal bulk has been treated with an appropriate quenching factor.

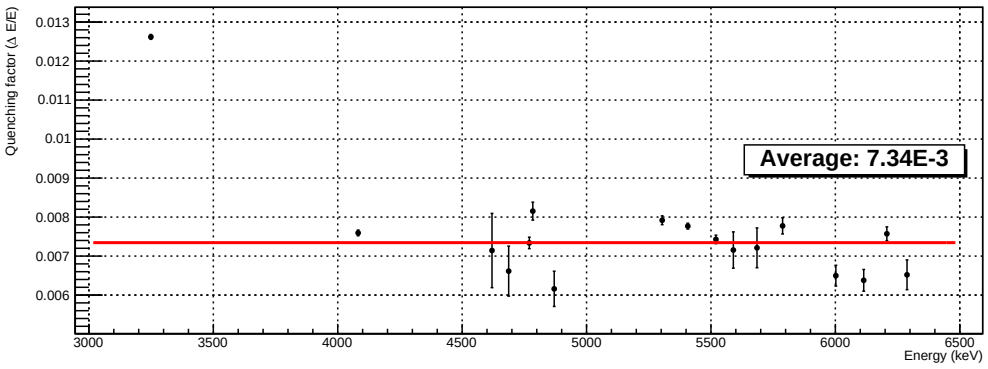

Figure 8.9: Quenching factor for αs. The first point, corresponding to ^{190}Pt, is not included in the fit.

8.2.2 Contamination depth

Contaminations in the bulk of materials are normally diffused uniformly across the whole volume, making the simulation of their effects simple. Surface contaminations, on the other hand, are not so easy to handle: depending on the chemical affinity between contaminants and the *host* material or on the techniques used for surface cleaning, the depth at which contaminations can be found may vary. While this is normally not a problem for β or γ emitters, as the involved depths normally vary in the range of a few microns, the situation is more complicated for α particles.

As discussed in section 8.1.3, α particles originating from copper elements close to the detector can leave part of their energy in the source volume, depositing the rest in TeO_2. This produces a low energy tail below the main peak, extending even to the γ region (figure 8.10).

The tail shape depends strongly on the depth of the original contamination. An example of three MC simulations run with different contamination depths is given in figure 8.11: the shape of the peak and of the tail changes considerably, to the point of making the peak almost disappear at higher depths. To best reproduce this effect in the background model, all surface simulations of α contaminants have been performed with different depths; the simulation which best resembles the actual measured tail shape is the one used in the final fit.

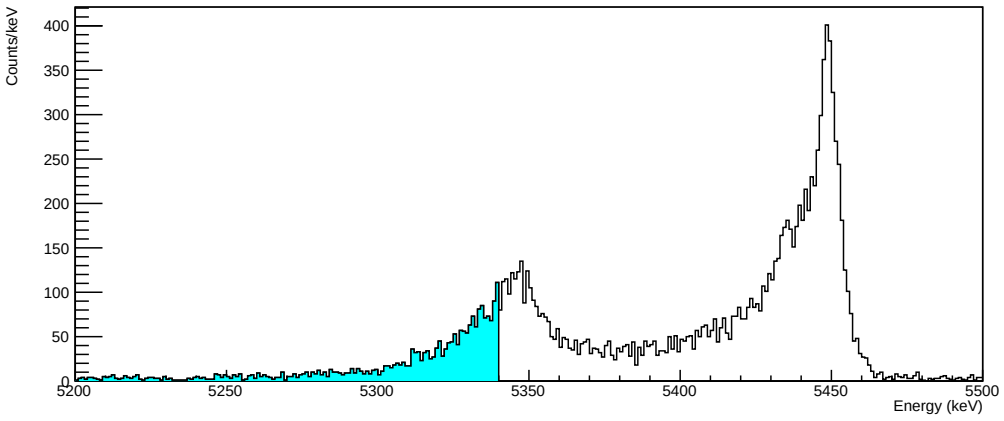

Figure 8.10: Low energy tail of the α line from ^{210}Po.

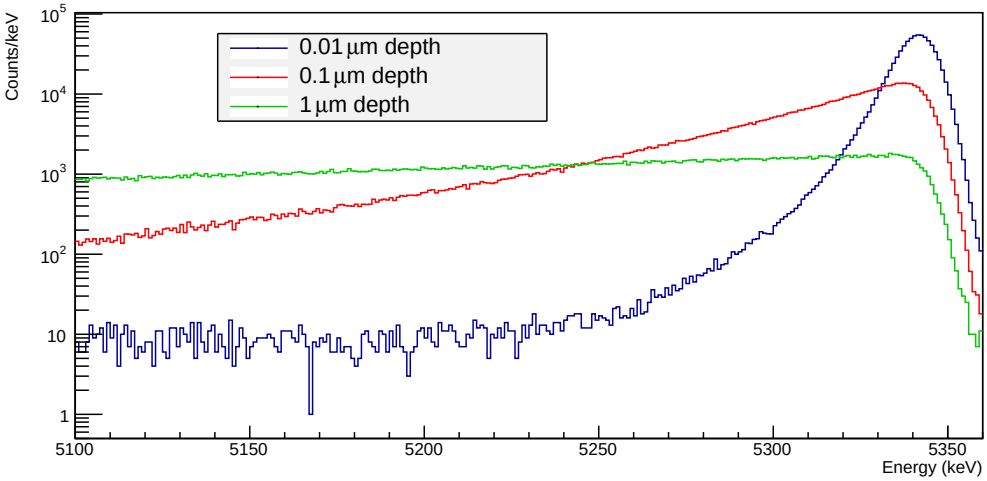

Figure 8.11: Effect of contamination depth on the simulation of α decays near the surface of copper. The α from ^{210}Po, located at 5349 keV (after the application of the quenching factor).

8.3 Bayesian model

The aim of the background model is to provide the most likely combination of sources generating the observed data. This is done with a Bayesian analysis tools, whose task is combining the simulated MC spectra of different background sources to obtain normalization coefficients N_j for each of them. Given an energy spectrum with N_{bin} bins, each of which is indexed by the letter i, the problem can be formalized with the following set of linear equations:

$$\langle C_i^{exp} \rangle = \sum_j^{N_{MC}} N_j \langle C_{ij}^{MC} \rangle . \tag{8.1}$$

In equation 8.1, $\langle C_i^{exp} \rangle$ is the expected value for the number of counts in bin i in the experimental spectrum, $\left\langle C_{ij}^{MC} \right\rangle$ is the same quantity evaluated for bin i of MC spectrum j and the sum is performed over all included MC spectra. The available data is the observed counts in each bin, (C_i^{exp}) and $\left(C_{ij}^{MC}\right)$, which can be viewed as random draws from Poisson distribution whose expectation values are $\langle C_i^{exp} \rangle$ and $\left\langle C_{ij}^{MC} \right\rangle$ respectively.

In general, Bayesian statistics are based on the following interpretation of Bayes' theorem [63]:

$$P(\theta|data) = \frac{P(data|\theta)}{P(data)} P(\theta). \tag{8.2}$$

In equation 8.2, θ is the set of parameters that have to be determined by doing an experiment with output *data*, $P(\theta|data)$ is called the *posterior* distribution, $P(data|\theta)$ is the *Likelihood* and $P(\theta)$ the *prior*. The desired outcome of the Bayesian analysis, the posterior, is obtained by combining the information available *a priori* (the prior) with the Likelihood.

The Bayesian software used for this analysis is JAGS (*Just Another Gibbs Sampler*[64]), a general purpose tool that easily allows the definition of all quantities required by the problem. In the case of the CUORE-0 background reconstruction, the Likelihood is defined as a Poisson PDF and the unknown variables θ are the normalization coefficients N_j. For what concerns the priors, they are generally uniform PDFs, to avoid any kind of bias towards any value. When previous results constrain the contamination level on some materials, for example those coming from the CUORE-0 material screening (tables 8.1 and 8.2), the prior distributions are modified accordingly.

JAGS output analysis

Each fit parameter in the JAGS output is associated to a marginalized posterior PDF. The marginalized PDF for each variable is obtained by integrating over all other unknowns: it's the PDF obtained when no information is available from the other parameters. Although, in principle, PDFs of any shape can be produced, four main groups of PDFs are usually obtained.

- A Gaussian shape (figure 8.13:1): the average value and standard deviation for N_j can be computed by simply fitting the posterior PDF with a Gaussian function.
- A truncated Gaussian (figure 8.13:2): in these cases the result is not so well-determined, but a gaussian fit can be used nonetheless to estimate mean and standard deviation of N_j.
- Decreasing profile truncated at zero (figure 8.13:3): this is what usually happens when the $j-$th MC spectrum is not needed by the fit. An upper limit for the corresponding contamination can be obtained by integrating to a certain confidence level.
- Increasing profile truncated at the upper limit (figure 8.13:4): this usually happens when a component is missing from the fit, causing some other coefficient to increase its value above the allowed limit to compensate.

Finally, the correlation between variables can be studied to further improve the fit results. It's not uncommon to observe highly anti-correlated variables, such as the ones

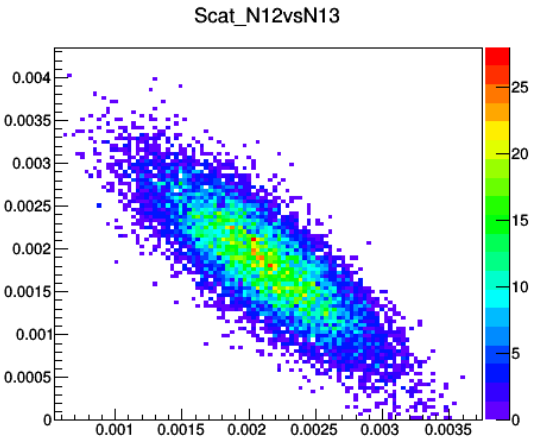

Figure 8.12: Example of two highly anti-correlated variables.

shown in figure 8.12. This means that the MC spectra linked to these variables have similar shapes which cannot be disentangled with good precision. A possibility in this case would be to perform a new fit with the two spectra merged together.

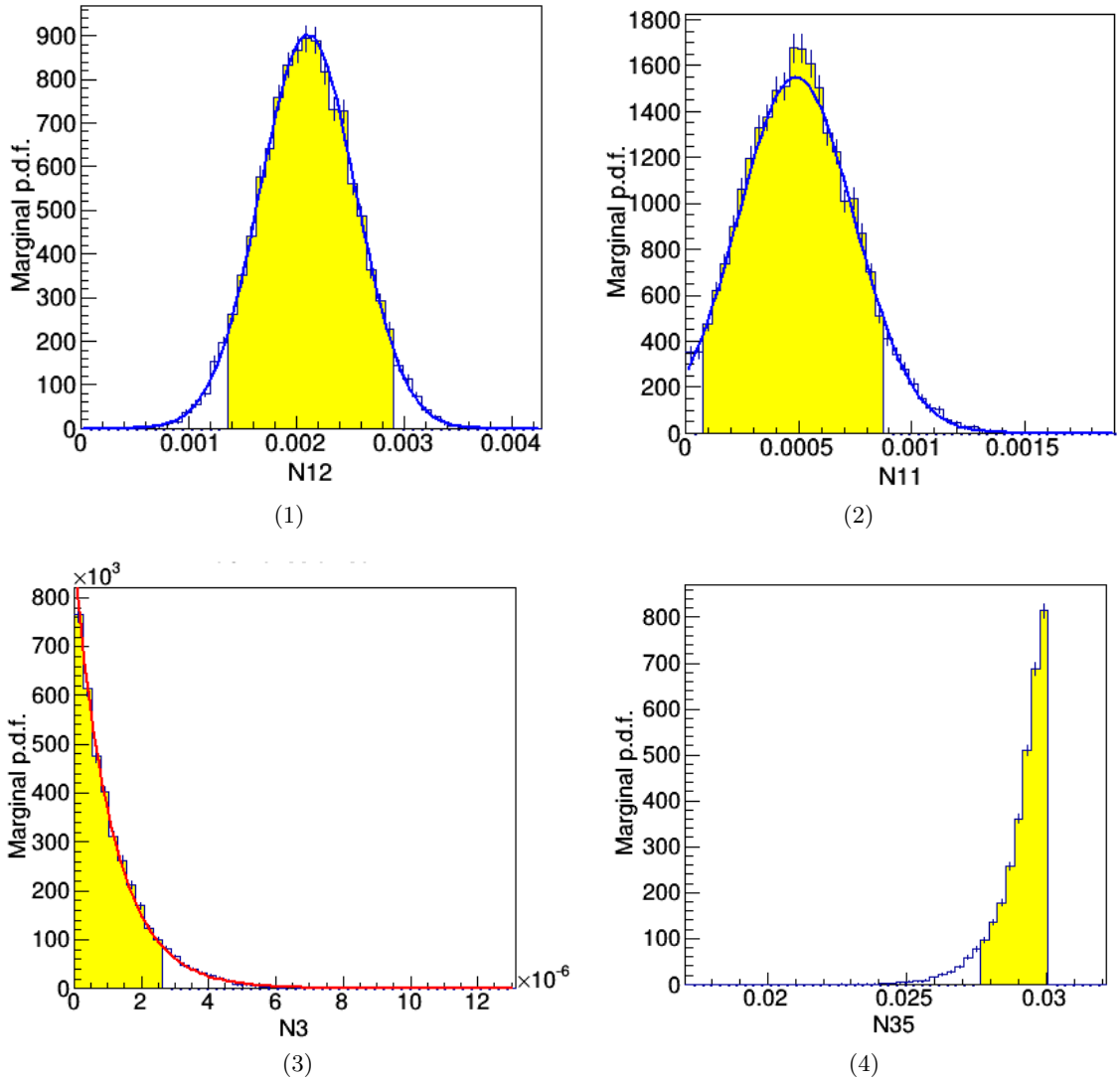

Figure 8.13: Examples of shapes obtained by marginal posterior PDFs.

8.4 Background model construction

The most critical point in the construction of the background model is the selection of sources to be used in the Bayesian fit. A missing source would lead to other components increasing their normalization coefficients to incorrect levels to try and compensate; on the other hand, the inclusion of unneeded or highly correlated sources would add nothing to the final result. In this section I'll describe the criteria used to define which subset of all the simulated contaminations is actually used in the final fit.

8.4.1 Sources and spectra

A *source* is identified by:

- the radioactive contaminant (^{238}U, ^{232}Th, ...)
- the contaminated volume (TeO_2 crystals, PTFE spacers, copper shields...)
- the density distribution of contaminants in the source volume (bulk or surface contamination, and depth for the latter)

Sources are determined either by direct observation of the CUORE-0 data, by previous measurements of involved materials, cosmogenic activation studies or results obtained by other experiments.

The background model operates on four different energy spectra, linked to different energy deposition patterns: **MAll** (events with any multiplicity), **M1** (events which hit a single crystal), **M2** (events involving two crystals at the same time) and **M2Sum** (total energy of M2 events). Higher multiplicity spectra have been used to help in the determination of the intensity of some background sources, but are not included in the final fit. The four spectra under consideration are not channel-dependent, but they are evaluated on the whole tower.

8.4.2 Degenerate sources

The MC code describes in detail the detector and the experimental setup, but not all volumes that in the simulation can be treated as independent produce distinguishable signatures in the spectra used for the fit. Some volumes are so similar to each other (due to their position, shape or composition) that their spectra are degenerate when normalized to available CUORE-0 data.

The example shown in figure 8.14 concerns two volumes close to the detector, the PTFE spacers holding the TeO_2 crystals and the copper structure (including the first cylindrical shield). The degeneracy exists because of the large statistical error in CUORE-0 data and because the detector is considered as a whole. Several other structures show the same level of degeneracy, so they have been grouped together in this set of non-degenerate volumes:

- **TeO_2 crystals**.
- **Copper holder**: it includes the copper structure and the first shield surrounding the tower, as they are all made of the same material (Cu NOSV). It also represents several smaller parts (NTDs, thermistors, gold wires...), which are expected to be completely negligible due to their small mass. The only exception are the PTFE

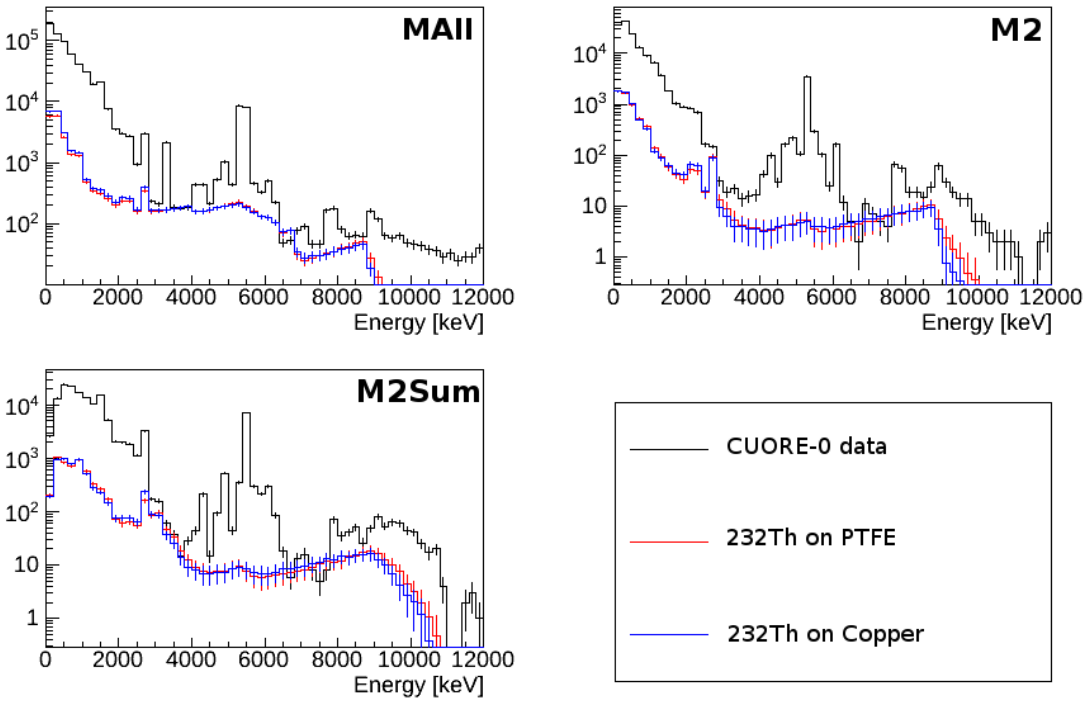

Figure 8.14: Degeneracy of ^{232}Th sources placed on PTFE spacers and on copper parts close to the detector. MC spectra are normalized to the maximum activity compatible with CUORE-0 data. Error bars are evaluated from real data fluctuations, showing that, with this statistics, these two contaminations cannot be disentangled.

spacers; they are too degenerate with the copper holder to be considered separately, but their contribution is considered in the evaluation of the *prior* PDF for the holder.

- **Internal shields**: union of the 50 mK, 600 mK and IVC shields, all made of the same copper. While the 50 mK and 600 mK shields are located inside the roman lead shield, the IVC shield is outside.
- **Roman lead**: contains both the lateral shield and the disks on the top and bottom of the tower.
- **External shields**: union of the external thermal shields of the cryostat, motivated by the degeneracy of the associated spectra.
- **External lead**.

8.4.3 Selection criteria for simulations

Some criteria applied for the selection of simulations to be used in the final fit have already been mentioned previously, such as previous knowledge of contaminations in materials, direct analysis of γ lines in the spectrum or localization of α contaminants based on their multiplicity pattern. A few other techniques used to further refine the model are listed here.

Floor dependence

Even if most of the volumes considered for the background model have a cylindrical symmetry, some count rate variations are observed between different channels of the tower. This can lead to the identification of additional, asymmetrical sources. This has been used in more than one case, but the case reported here concerns the main γ lines from the ^{232}Th chain.

The CUORE-0 tower contains 52 TeO_2 bolometers, divided in 13 floors with 4 crystals each. The analysis of the count rate of the main γ lines from ^{232}Th across the 13 floors showed a clear excess near floor #10 (figure 8.15). The excess is visible in the whole γ region, but it's more pronounced for lower energy lines. Additionally, no excess is observed in α line count rate.

The count rate of the γ lines changes considerably even between the various crystals of floor 10. The crystals on this floor are labeled 10, 23, 36 and 49. Channel 49 has not been active for the whole CUORE-0 data taking, so no information is available for it. Channels 23 and 36 show a similar count rate, while the one recorded on channel 10 is lower by a factor 200. The source that is causing the excess is not, therefore, cylindrically symmetric.

The combination of these considerations leads to a possible solution: a point-like source located in the vicinity of floor 10, located on the same side of the tower as channels 23 and 36. Since no variation is observed for α lines, the source cannot be inside the innermost copper shield; however, since strong variations are observed for low energy lines it cannot be too far away from the detector, otherwise those lines would be reduced in intensity by the additional shielding. To reproduce the observed behaviour, a point-like ^{232}Th source was added just outside the innermost copper shield; the activity of this source has been constrained in order to reproduce the observed count rate.

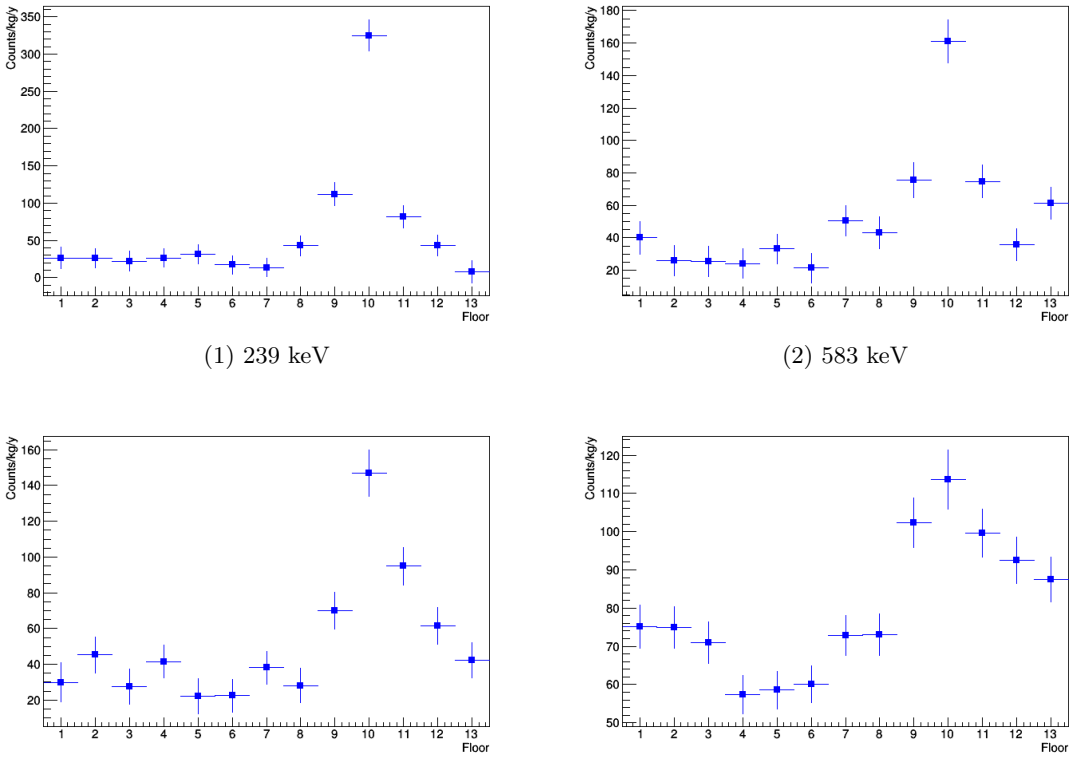

(1) 239 keV (2) 583 keV

(3) 911 keV (4) 2615 keV

Figure 8.15: Event rate distribution for four of the main γ lines from the ^{232}Th chain. An excess near floor #10 is visible in all plots, but is more pronounced at lower energies.

Line intensity ratio

The starting location of a decay can strongly influence the intensity of the various lines associated to it, as particles of lower energy are more likely to be absorbed by the shielding. A few examples of apparent branching ratio violations that were due to energy-dependent absorption rates were given in section 8.1.2. An even stronger information can come from the analysis of lines in the M2Sum spectrum.

Let's take as an example the decay of ^{60}Co, producing two γs in a quick succession, with energies 1173 and 1332 keV. If the two photons reach the detector and interact in two different crystals, a line in the M2Sum spectrum is observed at their sum energy, 2505 keV. Since the emission direction of these γs is not correlated, the probability of both of them interacting in the detector is strongly related the position where the decay takes place, depending on the solid angle under which the tower is seen. Sources close to the detector will produce the 2505 keV sum peak more often than sources located further away.

Figure 8.16 shows the ratio between the 1173 and 2505 keV lines, taken in different combinations between the M2Sum and MAll spectra. The ratio is calculated for CUORE-0 and for simulations performed on different shields, all the ones that are liable to contain ^{60}Co contaminations. In this particular case, the study of the ratios leads to the exclusion of the External Shields as a possible source for ^{60}Co.

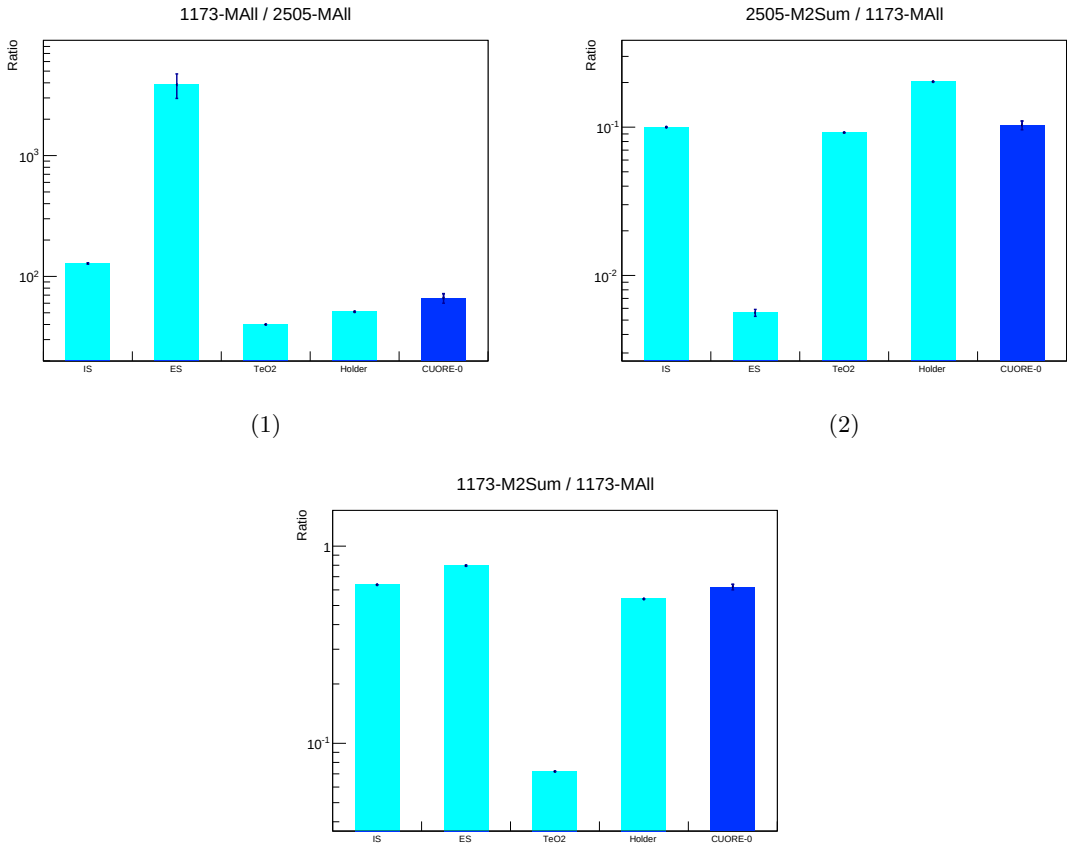

Figure 8.16: Ratio between main lines from ^{60}Co in MAll (all multiplicities) and M2Sum (total energy of M2 events). The ratio is evaluated on the CUORE-0 data and on four simulations coming from different volumes. *IS* stands for Internal Shields, *ES* for External Shields.

High multiplicity spectra

Muons are simulated according to their measured flux (see section 6.1.2). Since cosmic muons that pass through the tower are likely to interact with several crystals, the normalization coefficient can be strongly constrained by observing high multiplicity spectra.

Other contaminations have a low impact at high multiplicities, making muons the dominant background source. The `Multiplicity`>5 spectrum (figure 8.17) has been used to constrain the prior distribution for muons.

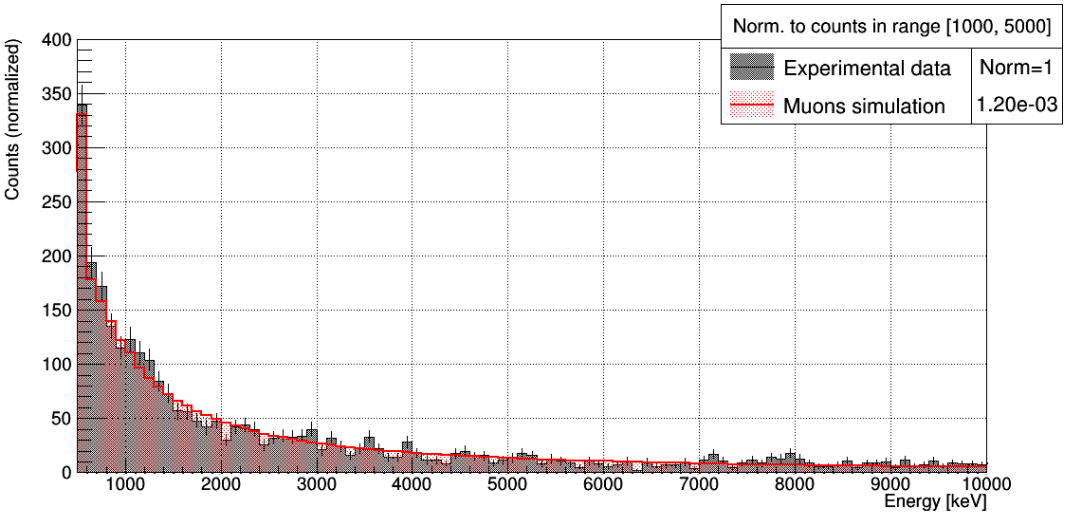

Figure 8.17: `Multiplicity`¿5 spectrum from the CUORE-0 data and MC spectrum from muons, normalized to the 1-5 MeV range.

8.4.4 Final list of simulations

The complete list of all sources used for the CUORE-0 background model is given in table 8.18. The prior distributions used for most of the simulations are also reported. When a measured value is available, a Gaussian prior with the given average and σ was used. When only a limit is available, the prior is a Gaussian centered at 0 and whose σ is defined so that 10% of the integral area is above the upper limit. Finally, if no information on the prior is given, it is defined as uniform in a range between 0 and an upper limit higher then the highest possible normalization compatible with the CUORE-0 data.

Crystal bulk	Prior (Bq/kg)	**Crystal surfaces**	
^{130}Te-$\beta\beta2\nu$		^{232}Th (only) – 0.01 μm	
^{210}Po	$(2.36 \pm 0.11) \times 10^{-6}$	^{228}Ra-^{208}Pb – 0.01 μm	
^{210}Pb		^{238}U -^{230}Th – 0.01 μm	
^{232}Th (only)		^{230}Th(only) – 0.01 μm	
^{228}Ra-^{208}Pb		^{226}Ra-^{210}Pb – 0.01 μm	
^{238}U -^{230}Th		^{210}Pb – 0.001 μm	
^{230}Th(only)		^{210}Pb – 1 μm	
^{226}Ra-^{210}Pb		^{210}Pb – 10 μm	
^{60}Co	$< 3 \times 10^{-7}$	^{232}Th – 10 μm	
^{40}K	$< 1 \times 10^{-3}$	^{238}U – 10 μm	
^{125}Sb			
^{190}Pt			
Holder bulk	Prior (Bq/kg)	**Holder surfaces**	
^{232}Th	$< 2 \times 10^{-6}$	^{210}Pb – 0.01 μm	
^{238}U	$< 6.5 \times 10^{-5}$	^{210}Pb – .1 μm	
^{60}Co	$(5 \pm 1) \times 10^{-5}$	^{210}Pb – 10 μm	
^{40}K	$(7 \pm 2) \times 10^{-4}$	^{232}Th – 10 μm	
^{54}Mn		^{238}U – 10 μm	
^{57}Co			
Internal Shields	Prior (Bq/kg)	**External Shields**	Prior (Bq/kg)
^{232}Th		^{232}Th	
^{238}U		^{238}U	
^{60}Co	$< 1.8 \times 10^{-4}$	^{60}Co	$< 4.2 \times 10^{-5}$
^{40}K		^{40}K	
^{137}Cs			
Roman Lead	Prior (Bq/kg)	**External Lead**	Prior (Bq/kg)
^{232}Th	$< 3.3 \times 10^{-5}$	^{232}Th	$< 2.6 \times 10^{-4}$
^{238}U	$< 4.5 \times 10^{-5}$	^{238}U	$< 7.0 \times 10^{-4}$
^{40}K	$< 2.3 \times 10^{-5}$	^{40}K	$< 5.4 \times 10^{-3}$
^{108m}Ag		^{207}Bi	
^{202}Pb		^{210}Pb	
Asymmetric sources	Prior (Bq)	**Internal Shields surfaces**	
^{232}Th Spot	$(2.4 \pm 0.2) \times 10^{-4}$	50+600mK-^{210}Pb	
^{40}K-BottomExtPb	16 ± 2	RomanLead-^{210}Pb	
Muons	(see Sec. 6.3)		

Figure 8.18: List of all the sources and priors used in the CUORE-0 background model. If not differently specified, ^{232}Th, ^{238}U and ^{210}Pb refer to the whole decay chains in secular equilibrium.

8.5 Results

In this section the results of the CUORE-0 background model will be discussed. First of all, the choices regarding energy binning and choices of low-energy threshold for the model

will be explained. After all, the results of the reference best fit will be discussed in detail.

8.5.1 Binning and energy threshold

In order to minimize the systematic errors due to the measured shape of γ and α peaks, a variable size binning has been used. The following approach was followed:

- each peak is included in a single bin. The edges of this bin lie at $\pm 3\sigma$ from the mean peak energy;
- a fixed size binning is chosen for the continuum between peaks, setting a minimum bin size to be used. If the number of events in a single bin is below 30, it is merged with the following one;
- a specific binning is applied to the α region, to account for the different structure of the peaks.

The energy range used in the fit extends from 118 keV to 7 MeV. The upper bound is chosen because the PSA cuts are not optimized above this range, while their efficiency is essentially constant below this point. The lower bound is chosen to avoid including the noise events at low energy (those that are not removed by pulse shape cuts) and the peaks from nuclei recoiling after an α decay, whose shape cannot be successfully reproduced by the MC software. This lower bound is not applied for events above 2.7 MeV in the M2Sum spectrum, as the information regarding the presence of a recoiling nucleus is essential in the proper reconstruction of the position of α sources.

8.5.2 Reference fit results

The results of the reference best fit are shown in figure 8.19 for M1, 8.20 for M2 and 8.21 for M2Sum. In each figure, the first plot shows the comparison between the experimental CUORE-0 data and the fit reconstruction. In the second plot the ratio between the number of counts in each bin in the experimental spectrum over the fitted one is shown, along with colored bands in correspondence of 1σ, 2σ and 3σ uncertainty.

The residuals were used to calculate χ^2 values for each of the fitted spectra:

- M1: $\chi^2/\text{nBins} = 245/200 = 1.22$;
- M2: $\chi^2/\text{nBins} = 191/177 = 1.08$;
- M2Sum: $\chi^2/\text{nBins} = 214/158 = 1.35$.

The global reduced-χ^2 of the fit is obtained by summing the chi^2 values for each spectra and dividing by the number of degrees of freedom, given by the difference between the total number of bins and the number of MC spectra used for the fit, 57:

$$\chi^2/d.o.f. = 650/478 = 1.36. \tag{8.3}$$

Both the figures and the χ^2 values prove the validity of the background model, which is able to reproduce the experimental spectrum in the whole range with great accuracy. The contamination levels obtained in the best fit are listed in table 8.22. In general, all posterior values are compatible with the available prior information.

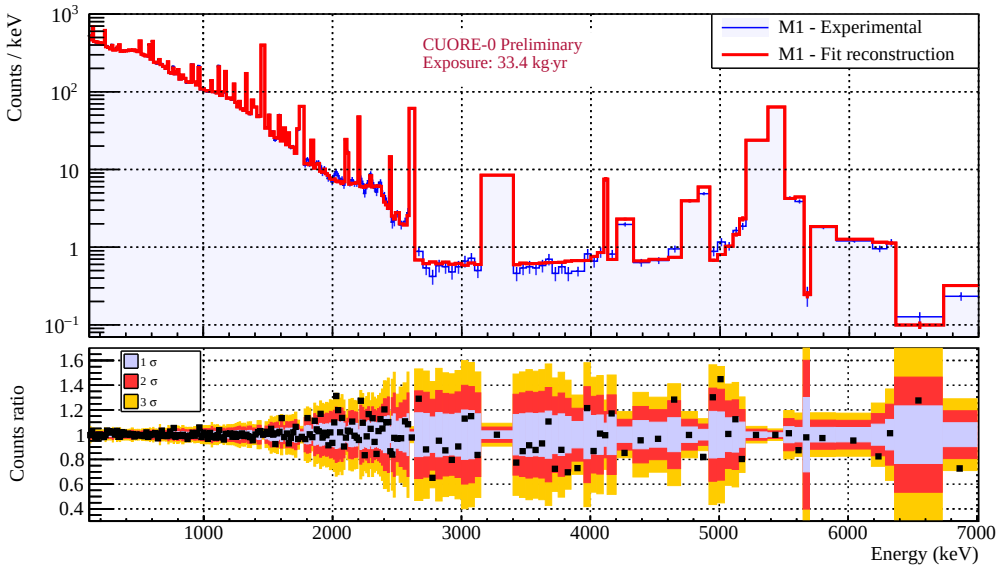

Figure 8.19: Background model reconstruction of the M1 spectrum.

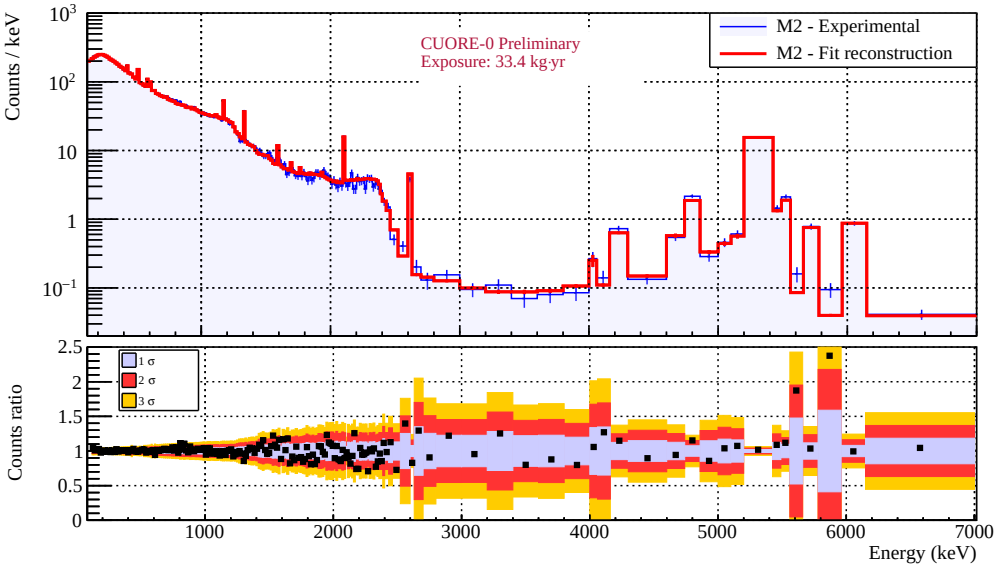

Figure 8.20: Background model reconstruction of the M2 spectrum.

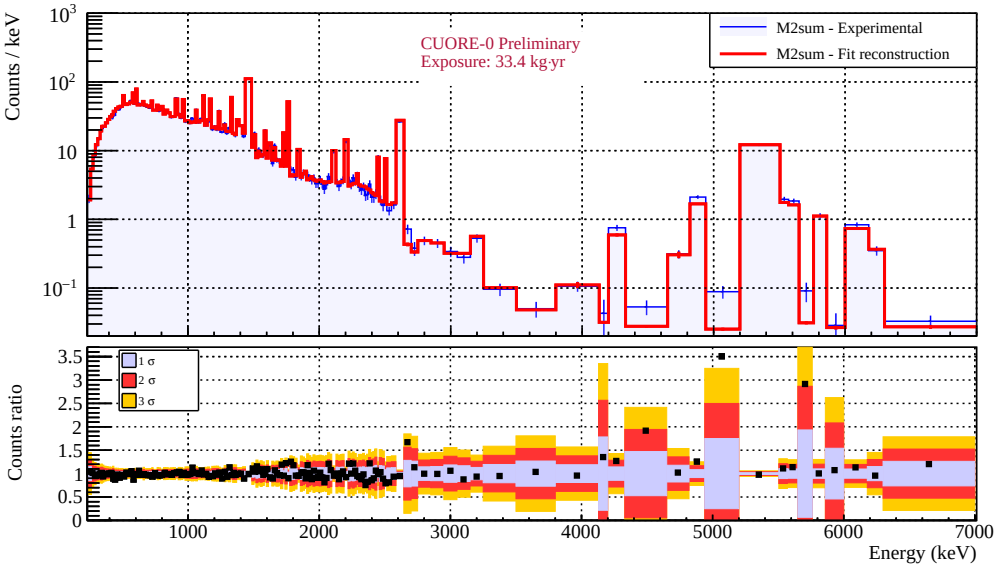

Figure 8.21: Background model reconstruction of the M2Sum spectrum.

Component	Index	Bulk sources	Prior [Bq/kg]	Posterior [Bq/kg]	Systematics [Bq/kg]
Crystals	1	^{130}Te-$\beta\beta2\nu$		$3.43(9)\times10^{-5}$	$3.1\times10^{-5} \div 3.7\times10^{-5}$
	2	^{210}Po	$2.36(11)\times10^{-6}$	$2.39(11)\times10^{-6}$	
	3	^{210}Pb		$1.37(19)\times10^{-6}$	$5.4\times10^{-7} \div 2.2\times10^{-6}$
	4	^{232}Th (only)		$7(3)\times10^{-8}$	$< 1.2\times10^{-7}$
	5	^{228}Ra-^{208}Pb		$<3.5\times10^{-8}$	$< 7.5\times10^{-8}$
	6	^{238}U-^{230}Th		$<7.5\times10^{-9}$	$< 3.6\times10^{-8}$
	7	^{230}Th(only)		$2.8(3)\times10^{-7}$	
	8	^{226}Ra-^{210}Pb		$<7.0\times10^{-9}$	$< 2.2\times10^{-8}$
	9	^{40}K		$5.1(14)\times10^{-6}$	$< 8.2\times10^{-6}$
	10	^{60}Co	$< 3.0\times10^{-7}$	$<5.1\times10^{-7}$	
	11	^{125}Sb		$9.6(4)\times10^{-6}$	$7.5\times10^{-6} \div 1.2\times10^{-5}$
	12	^{190}Pt		$2.00(5)\times10^{-6}$	$1.6\times10^{-6} \div 2.3\times10^{-6}$
Holder	13	^{232}Th	$< 2.0\times10^{-6}$	$<2.1\times10^{-6}$	
	14	^{238}U	$< 6.5\times10^{-5}$	$<1.2\times10^{-5}$	$< 2.2\times10^{-5}$
	15	^{40}K	$7(2)\times10^{-4}$	$8(2)\times10^{-4}$	
	16	^{60}Co	$5(1)\times10^{-5}$	$3.5(8)\times10^{-5}$	
	17	^{54}Mn		$1.0(2)\times10^{-5}$	$< 1.7\times10^{-5}$
	18	^{57}Co		$2.9(3)\times10^{-5}$	$2.3\times10^{-5} \div 3.7\times10^{-5}$
CryoIntS	19	^{232}Th		$<1.5\times10^{-5}$	$< 3.5\times10^{-5}$
	20	^{238}U		$<1.5\times10^{-5}$	$< 3.9\times10^{-5}$
	21	^{40}K		$1.1(3)\times10^{-3}$	
	22	^{60}Co	$< 1.8\times10^{-4}$	$2.4(10)\times10^{-5}$	
	23	^{137}Cs		$9.9(15)\times10^{-6}$	
IntPb	24	^{232}Th	$< 4.5\times10^{-5}$	$5.3(7)\times10^{-5}$	$1.7\times10^{-5} \div 6.6\times10^{-5}$
	25	^{238}U	$< 4.6\times10^{-5}$	$2.7(10)\times10^{-5}$	
	26	^{40}K	$< 2.3\times10^{-5}$	$<2.4\times10^{-5}$	$< 4.6\times10^{-4}$
	27	^{108m}Ag		$6.1(12)\times10^{-6}$	
	28	^{202}Pb		$6(3)\times10^{-6}$	
CryoExtS	29	^{232}Th		$<1.2\times10^{-4}$	$< 1.8\times10^{-4}$
	30	^{238}U		$2.4(6)\times10^{-4}$	$< 5.9\times10^{-4}$
	31	^{40}K		$<1.6\times10^{-3}$	$< 2.6\times10^{-3}$
	32	^{60}Co	$< 4.2\times10^{-5}$	$2.5(9)\times10^{-5}$	
ExtPbS	33	^{232}Th	$< 2.6\times10^{-4}$	$3.1(3)\times10^{-4}$	$2.1\times10^{-4} \div 3.5\times10^{-4}$
	34	^{238}U	$< 7.0\times10^{-4}$	$5.0(6)\times10^{-4}$	$3.5\times10^{-4} \div 6.2\times10^{-4}$
	35	^{40}K	$< 5.4\times10^{-3}$	$3.1(5)\times10^{-3}$	
	36	^{207}Bi		$5.9(5)\times10^{-5}$	$4.7\times10^{-5} \div 7.2\times10^{-5}$
	37	^{210}Pb		5.96(11)	$5.4 \div 6.3$
Component		Surface sources	Prior [Bq/cm^2]	Posterior [Bq/cm^2]	Systematics [Bq/cm^2]
Crystals	38	^{232}Th (only) – 0.01 μm		$3.0(10)\times10^{-10}$	
	39	^{228}Ra-^{208}Pb – 0.01 μm		$2.32(12)\times10^{-9}$	$2.1\times10^{-9} \div 2.7\times10^{-9}$
	40	^{238}U-^{230}Th – 0.01 μm		$2.07(11)\times10^{-9}$	$1.8\times10^{-9} \div 2.2\times10^{-9}$
	41	^{230}Th (only) – 0.01 μm		$1.15(14)\times10^{-9}$	
	42	^{226}Ra-^{210}Pb – 0.01 μm		$3.14(10)\times10^{-9}$	$2.9\times10^{-9} \div 3.5\times10^{-9}$
	43	^{210}Pb – 0.001 μm		$6.02(8)\times10^{-8}$	$4.8\times10^{-8} \div 7.2\times10^{-8}$
	44	^{210}Pb – 1 μm		$8.6(8)\times10^{-9}$	$7.2\times10^{-9} \div 1.1\times10^{-8}$
	45	^{210}Pb – 10 μm		$<2.7\times10^{-9}$	$< 4.9\times10^{-9}$
	46	^{232}Th – 10 μm		$7.8(14)\times10^{-10}$	
	47	^{238}U – 10 μm		$<3.3\times10^{-11}$	$< 1.2\times10^{-10}$
Holder	48	^{210}Pb – 0.01 μm		$2.9(4)\times10^{-8}$	$2.1\times10^{-8} \div 4.3\times10^{-8}$
	49	^{210}Pb – .1 μm		$4.3(5)\times10^{-8}$	$3.1\times10^{-8} \div 5.1\times10^{-8}$
	50	^{210}Pb – 10 μm		$<1.9\times10^{-8}$	$< 3.9\times10^{-8}$
	51	^{232}Th – 10 μm		$5.0(17)\times10^{-9}$	$< 1.0\times10^{-8}$
	52	^{238}U – 10 μm		$1.39(16)\times10^{-8}$	$8.4\times10^{-9} \div 1.6\times10^{-8}$
CryoIntS	53	^{210}Pb – 0.01 μm		$1.4(7)\times10^{-5}$	$< 2.7\times10^{-5}$
IntPbS	54	^{210}Pb – 0.01 μm		$5.1(18)\times10^{-5}$	$< 8.2\times10^{-5}$
Component		Other Sources	Prior [Bq]	Posterior [Bq]	
50 mK Spot	55	^{232}Th	$2.4(2)\times10^{-4}$	$2.41(18)\times10^{-4}$	
Bottom plate PbExtS	56	^{40}K	16.8(2)	18(2)	
Muons	57		(see text)		

Figure 8.22: Contamination values obtained by the reference fit for all the components.

Systematic errors

To check the stability of the background model, the dependence on provided prior distributions and systematic uncertainties a set of different fits with modified parameters were run:

- **Binning**: the minimum bin size used for the continuum between peaks is changed between 5 to 25 keV.
- **Low energy threshold**: the fit is performed with several low energy thresholds, ranging from 118 to 500 keV.
- **Contamination depth uncertainty**: different simulations performed with variable contamination depths are tested in the α region.
- **Dependence on priors**: another fit is performed by setting uniform priors for all components.
- **Selection of background sources**: the 14 undetermined sources that are quoted in the reference fit as upper limits are removed, fitting only with the rest.
- **Subset of data**: several fits were done with subsets of channels, looking for geometrical effects. For example, only the even floors are fitted, or the odd floors, or the top half of the tower...

In all these tests the overall goodness of the fits remains stable, while there are fluctuations in the magnitude of individual sources. These variations were used as an evaluation of the systematic uncertainties listed in table 8.22.

CHAPTER

9

DOUBLE-BETA DECAY ON THE EXCITED STATE

Even if the main scientific goal of CUORE-0 is the search for neutrinoless double beta decay of ^{130}Te on the ground state of ^{130}Xe, there are several other studies that can be carried out with this detector. In this chapter the analysis of ^{130}To double beta decay to excited states in CUORE-0 will be presented. The study of this process is not the best choice for the investigation of the Majorana nature of neutrinos; the associated available phase space (and, therefore, probability) is much lower than the corresponding one for decay on the ground state. However, since the decay to the excited states is always accompanied by the emission of photons, their detection can strongly improve the background rejection and increase the sensitivity to this process. The study presented in this chapter focused on the decay on the first 0^+ excited state of ^{130}Xe, both in the neutrinoless ($0\nu\beta\beta_{0+}$) and two-neutrino ($2\nu\beta\beta_{0+}$) channels. The work presented in this chapter is completely original, is currently undergoing revision by the CUORE collaboration and will be submitted for a publication.

9.1 Physical process and detectable signatures

The excitation levels of ^{130}Xe accessible by double beta decay from ^{130}Te are shown in figure 9.1. These levels are valid both for the $0\nu\beta\beta$ and $2\nu\beta\beta$ channels.

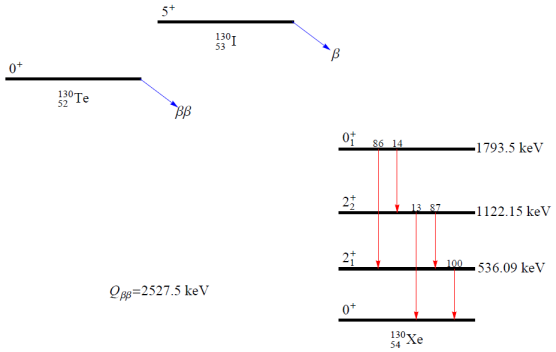

Figure 9.1: ^{130}Te→ ^{130}Xe decay scheme.

The maximum amount of energy carried by the electrons in the decay to the 0^+_1 level is the difference between the decay Q-value (2527.5 keV) and the level's excitation energy (1793.5 keV). In the case of the $0\nu\beta\beta_{0+}$ decay the two electrons carry the whole 734 keV, while in the $2\nu\beta\beta_{0+}$ decay scenario the sum of their energies lies between 0 and 734 keV.

The de-excitation of the 0^+_1 excited state leads to three possible γ cascades:

- 86% branching ratio: two γs, 1257.4 and 536.1 keV;
- $\sim$ 12% branching ratio: three γs, 671.3, 586 and 536.1 keV;
- $\sim$ 2% branching ratio: two γs, 671.3 and 1122.2 keV.

The emitted electrons and γs can interact in multiple crystals, producing a large number of different experimental scenarios depending on the number of bolometers involved and on the fraction of energy deposited in each of them. I restrict my search to a set of scenarios that must fulfil three specific requirements:

1. the full energy carried by the electrons is deposited inside the crystal where the decay occurred;
2. each emitted γ particle either deposits its full energy in a single crystal, or in no crystal at all (i.e. it fully escapes the detector). Scenarios where the photon Compton-scatters in a crystals and then deposits its energy elsewhere are ignored;
3. for the $2\nu\beta\beta$ decay, at least two crystals are involved.

Whatever the decay channel ($0\nu\beta\beta$ or $2\nu\beta\beta$) the fulfilment of these requirements imply thst at least one of the bolometers involved in the decay records a monochromatic peak.

This is the easiest condition for measuring the decay rate: fit a gaussian peak over a (very likely smooth) background and extrapolate the source half-life from the peak intensity.

A list of all the scenarios that fulfil the mentioned requirements is reported in tables 9.1 and 9.2. In the first table, scenarios that are possible for both the decay channels are listed, characterized by `Multiplicity`> 1 and involve 2, 3 or 4 bolometers. In the second table M1 scenarios are listed, possible for the $0\nu\beta\beta_{0+}$ channel only.

Scenario #	Multiplicity	Energy [keV]			
		Crystal A	Crystal B	Crystal C	Crystal D
86% **branching:** $\beta\beta$ + 536.1 **keV** + 1257.4 **keV**					
1	2	$\beta\beta$	1793.5		
2	2	$\beta\beta$	536.1		
3	2	$\beta\beta$	1257.4		
4	2	$\beta\beta + 536.1$	1257.4		
5	2	$\beta\beta + 1257.4$	536.1		
6	3	$\beta\beta$	536.1	1257.4	
2% **branching:** $\beta\beta$ + 671.3 **keV** + 1122.2 **keV**					
7	2	$\beta\beta$	1793.5		
8	2	$\beta\beta$	671.3		
9	2	$\beta\beta$	1122.2		
10	2	$\beta\beta + 671.3$	1122.2		
11	2	$\beta\beta + 1122.2$	671.3		
12	3	$\beta\beta$	671.3	1122.2	
12% **branching:** $\beta\beta$ + 536.1 **keV** + 586 **keV** + 671.3 **keV**					
13	2	$\beta\beta$	1793.5		
14	2	$\beta\beta$	536.1		
15	2	$\beta\beta$	586		
16	2	$\beta\beta$	671.3		
17	2	$\beta\beta$	1122.1		
18	2	$\beta\beta$	1207.5		
19	2	$\beta\beta$	1257.4		
20	2	$\beta\beta + 536.1$	671.3		
21	2	$\beta\beta + 536.1$	586		
22	2	$\beta\beta + 536.1$	1257.4		
23	2	$\beta\beta + 586$	671.3		
24	2	$\beta\beta + 586$	536.1		
25	2	$\beta\beta + 586$	1207.5		
26	2	$\beta\beta + 671.3$	536.1		
27	2	$\beta\beta + 671.3$	586		
28	2	$\beta\beta + 671.3$	1122.1		
29	2	$\beta\beta + 1122.1$	671.3		
30	2	$\beta\beta + 1207.5$	586		
31	2	$\beta\beta + 1257.4$	536.1		
32	3	$\beta\beta$	536.1	586	
33	3	$\beta\beta$	536.1	671.3	
34	3	$\beta\beta$	586	671.3	
35	3	$\beta\beta$	536.1	1257.4	
36	3	$\beta\beta$	586	1207.5	
37	3	$\beta\beta$	671.3	1122.1	
38	3	$\beta\beta + 536.1$	586	671.3	
39	3	$\beta\beta + 586$	536.1	671.3	
40	3	$\beta\beta + 671.3$	536.1	586	
41	4	$\beta\beta$	536.1	586	671.3

Table 9.1: Allowed scenarios for `Multiplicity`>= 2 events, available for both the $0\nu\beta\beta_{0+}$ and the $2\nu\beta\beta_{0+}$ channels. Here $\beta\beta$ stands for a monochromatic energy of 734 keV for $0\nu\beta\beta_{0+}$ and for a continuous spectrum in the 0-734 keV region for $2\nu\beta\beta_{0+}$. The crystals involved in the event are labeled A, B, C and D. Crystal A is the source crystal where the two electrons are fully contained.

Scenario #	Multiplicity	Energy [keV]
86% **branching:** $\beta\beta$ + 536.1 **keV** + 1257.4 **keV**		
42	1	$\beta\beta$
43	1	$\beta\beta$+536.1
44	1	$\beta\beta$+1257.4
45	1	$\beta\beta$+1793.5
2% **branching:** $\beta\beta$ + 671.3 **keV** + 1122.2 **keV**		
46	1	$\beta\beta$
47	1	$\beta\beta$+671.3
48	1	$\beta\beta$+1122.2
49	1	$\beta\beta$+1793.5
12% **branching:** $\beta\beta$ + 536.1 **keV** + 586 **keV** + 671.3 **keV**		
50	1	$\beta\beta$
51	1	$\beta\beta$+536.1
52	1	$\beta\beta$+586
53	1	$\beta\beta$+671.3
54	1	$\beta\beta$+1122.1
55	1	$\beta\beta$+1207.5
56	1	$\beta\beta$+1257.4
57	1	$\beta\beta$+1793.5

Table 9.2: All scenarios for M1 events, valid for $0\nu\beta\beta_{0+}$ only. Here $\beta\beta$ stands for a monochromatic energy of 734 keV.

9.2 Analysis procedure

The set of rules for the definition of an accepted scenario defined in the previous section make sure that every signature is characterized by the presence of a full-energy peak in one of at least one monochromatic peak in the spectrum of one of the involved bolometers.

The objective of this analysis is to fit said peaks to infer the value of the $\beta\beta_{0+}$ decay rate $\Gamma^{\beta\beta_{0+}}$. There are several steps that need to be taken in order to get to this point.

At first, events satisfying each of the signatures outlined in tables 9.2 and 9.1 have to be properly identified inside the CUORE-0 data. Cuts based on the deposited energy and on the event multiplicity are the main data selection tools used in this analysis.

After all signatures have been defined, some of them are removed. The expected sensitivity to $\Gamma^{\beta\beta}$ for each signature is evaluated with Monte Carlo simulations, used to reproduce both the background (from the CUORE-0 background model) and the effect of the decay under consideration. Signatures are then ranked based on this value and only the most significant scenarios are kept in the final fit. This leads to the removal of low-probability and/or high-background signatures that would give negligible contribution to the final sensitivity and potentially just slow down the fit.

The final step of this procedure is to project, for each signature, the energy spectrum selected for the fit. This is the spectrum of the channel that records a monochromatic peak and, in the case of more channels satisfying simultaneously this requirement, the one with the highest energy peak is chosen (as it usually has the lowest background). Taking as an example scenario #6 from table 9.1, the three involved crystals in the M3 event contain the two electrons, a 536 keV γ and a 1257 keV γ respectively. In this case, the fit is performed on the 1257 keV line only, as it is the one with the highest energy.

9.2.1 Fitting technique

A combined fit is performed on all selected signatures, with $\Gamma^{\beta\beta}$ as the only common parameter. The chosen fitting method is the Unbinned Extended Maximum Likelihood (UEML). As the name suggests, an unbinned fit doesn't require a binned histogram but instead operates on each event in the data directly. If the likelihood for each event i is given by $f(x_i; \boldsymbol{p})$, the unbinned likelihood for N observed events is given by

$$\mathcal{L}_u(\boldsymbol{p}) = \prod_{i=1}^{N} \frac{f(x_i; \boldsymbol{p})}{N}. \tag{9.1}$$

The extended likelihood implies that the normalization area of the distribution, previously given by N, is an additional parameter of the fit, $A(\boldsymbol{p})$. Assuming a Poisson variation for

the measured number of events, the extended likelihood becomes

$$\mathcal{L}_{ue}(\boldsymbol{p}) = \frac{A(\boldsymbol{p})^N e^{-A(\boldsymbol{p})}}{N!} \prod_{i=1}^{N} \frac{f(x_i;\boldsymbol{p})}{A(\boldsymbol{p})}. \tag{9.2}$$

After the removal of some constant terms, the more convenient logarithm of the likelihood is

$$-\ln \mathcal{L}_{ue}(\boldsymbol{p}) = -\sum_{i=1}^{N} lnf(x_i;\boldsymbol{p}) + A(\boldsymbol{p}). \tag{9.3}$$

9.2.2 UEML fit bias

The number of measured events associated to some of the scenarios is expected to be very low: for example, this could happen for signatures that involve M3 or M4 events, as the number of measured events decreases sharply in CUORE-0 as the multiplicity increases. I've set up a dedicated *toy* Monte Carlo to verify the effectiveness of the chosen fitting technique on low-statistics spectra.

A 100 keV interval is filled randomly with events taken from a flat distribution. The expected number of events N_{ev} is fixed at the beginning of the simulation, and then extracted randomly for each MC from a Poisson p.d.f. whose expected value is N_{ev}. An UEML fit is then performed on the obtained data, using the following fit function:

$$f(E) = p_0 + \frac{p_1}{\sqrt{2\pi\sigma^2}} * exp(-\frac{(E-E_c)^2}{2\sigma^2}, \tag{9.4}$$

where E_c is fixed at 50 keV and σ at $5keV$. The two free parameters represent the flat background level (p_0) and the number of events under the gaussian at 50 keV (p_1). An example of a MC with the fit superimposed is given in figure 9.2.

Since the generated events come from a flat distribution, the expected value of p_1 (the gaussian area) is 0. The fit will account for statistical fluctuations near the center of the window, so the value of p_1 will vary depending on the generated events; the final distribution of p_1 should be a gaussian centered at 0.

The number of generated events, N_{ev}, is varied between 5 and 200, in steps of 5. For each step, 5000 toy MC are generated and fitted with equation 9.4; the values of p_1 for each fit are shown in figure 9.3.

The results of the test depend strongly on the choice of N_{ev}. For high values of N_{ev} the results follow the expected trend, with the values of p_1 distributed uniformly around the expected value, 0. When N_{ev} is lower (more or less below 30), there is a clear preference for negative values of p_1. This can be seen in more detail in figure 9.4, which shows the

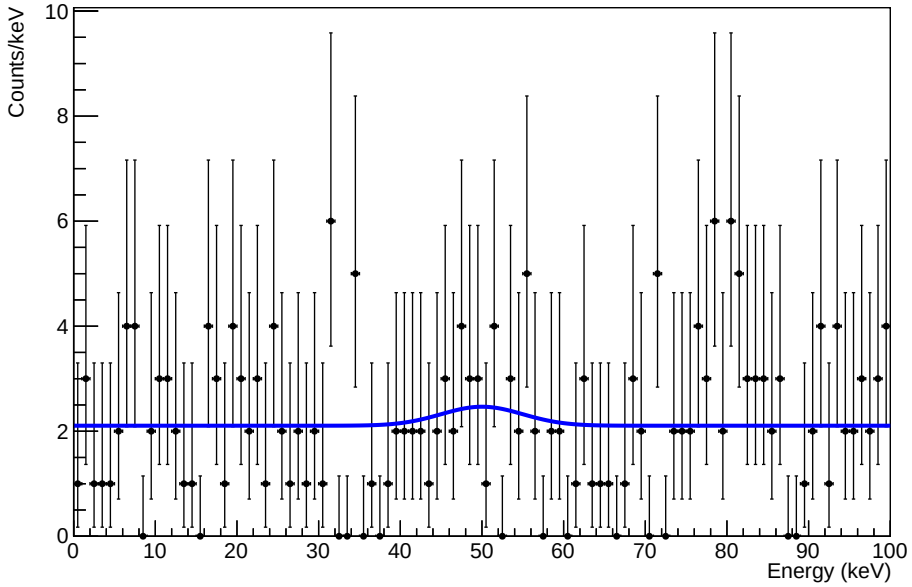

Figure 9.2: Example of a toy MC where 200 events are extracted from a flat distribution. The data is binned in the plot, but the fit is unbinned. The fit function contains a gaussian term, which follows a statistical fluctuation in the generated background.

comparison between the p_1 values obtained with $N_{ev} = 20$ and $N_{ev} = 200$. The former distribution has a clear bias towards negative values of p_1, while the latter is centered at the expected value.

Including signatures with low background in the final fit for $\Gamma_{\beta\beta}$ could lead to a significant bias of the result. Therefore, following the results of this toy MC test, the UEML technique described above is used only for signatures that contain more than 30 events per 100 keV, or 0.3 events/keV, in their fit window. For signatures containing less events, a different approach has been developed.

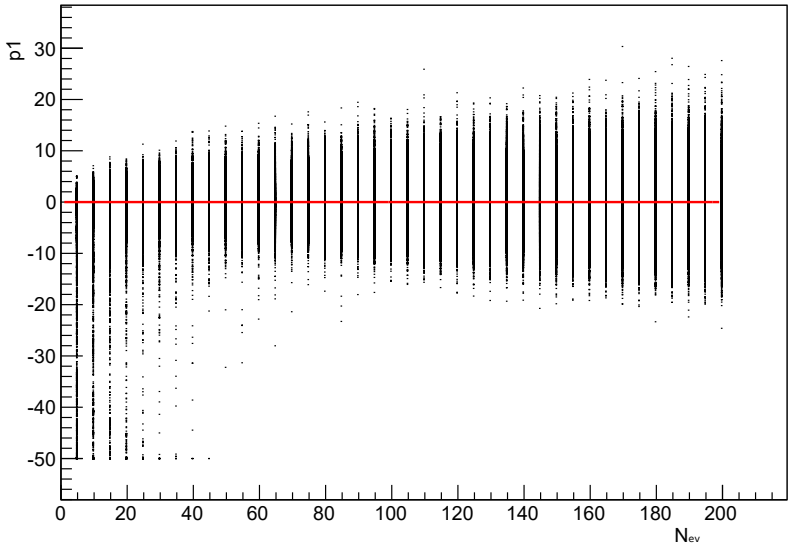

Figure 9.3: UEML technique bias, tested with toy MC. The number of generated events N_{ev} is on the X axis, while the gaussian area p_1 is on the y axis. The red line is set at the expected average value for p1, 0. Each vertical band contains the values of p_1 obtained by 5000 toy MC.

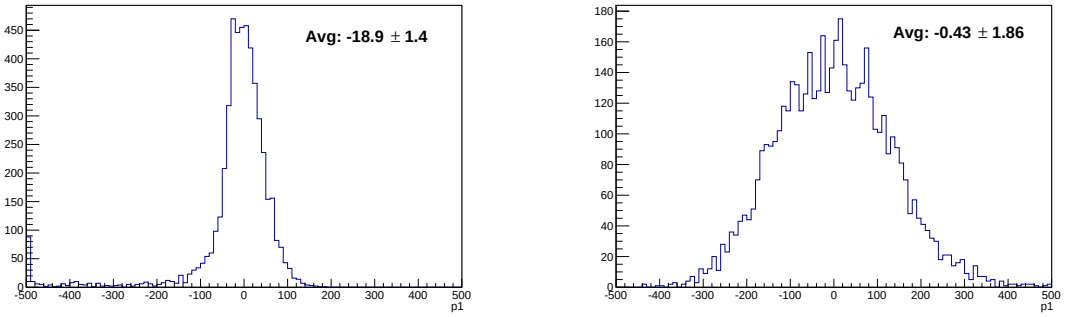

(1) $N_{ev} = 20$ (2) $N_{ev} = 200$

Figure 9.4: *Left*: p_1 values for $N_{ev} = 20$; the distribution is shifted towards negative values, as shown also by the negative average. *Right*: p_1 values for $N_{ev} = 200$; the distribution is symmetric and centered in zero, as expected.

9.2.3 Low statistics signatures

Let's take as an example scenario #3 from table 9.1, which would require the fit of a γ line at 1257 keV. In order to fit this peak properly, an 80 keV wide range is chosen around

its energy, between 1220 and 1300 keV. For the sake of this example, let's assume that after applying all the cuts only 5 counts are found in the 80 keV region: following the results of the bias test defined in section 9.2.2, this scenario cannot be fitted with the normal UEML algorithm without the risk of incurring in a significant bias. The procedure defined in this section is used to construct a likelihood function for $\Gamma_{\beta\beta}$ for low statistics scenarios without actually fitting the data.

This procedure is based on a simple assumption: events that lie close to the required energy (1257 keV in this case) either come from the decay of interest or from background. For the sake of this example, fake data has been generated in the region between 1220 and 1300 keV. The number N of events that fall within $\pm 5\sigma$ from the expected peak energy at 1257 are considered as potential signal candidates (figure 9.5).

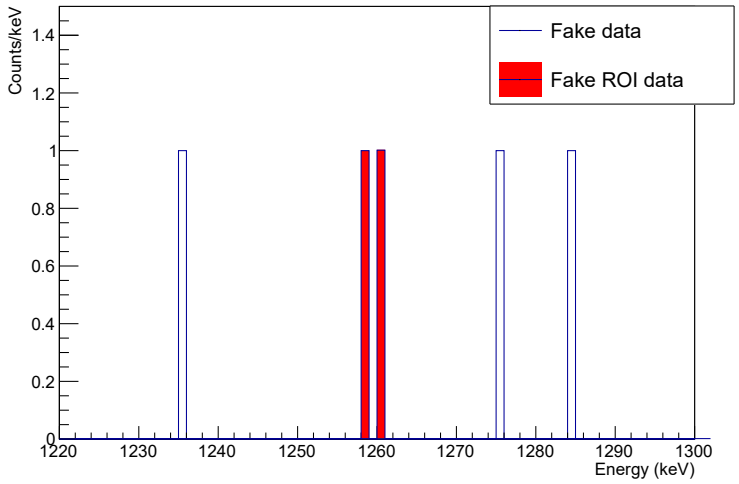

Figure 9.5: Region between 1220 and 1300 keV, centered around the expected peak at 1257 keV. The colored events are within $\pm 5\sigma$ from the expected peak energy. These events do not come from real CUORE-0 data, but are arbitrarily produced for the sake of this example.

In this example, N=2; these events can either be both produced by a $\beta\beta_{0+}$ signal, both by background or a combination of the two. The probability of observing N_{sig} signal events, given an expected number of events λ_{sig}, is given by a Poisson p.d.f.:

$$P(N_{signal}; \lambda_{sig}) = \frac{\lambda_{sig}^{N_{sig}} e^{-\lambda_{sig}}}{N_{sig}!}; \tag{9.5}$$

the same relation holds for the probability of observing N_{bkg} background events, given the

expectation λ_{bkg}:

$$P(N_{bkg};\lambda_{bkg}) = \frac{\lambda_{bkg}^{N_{bkg}} e^{-\lambda_{bkg}}}{N_{bkg}!}. \tag{9.6}$$

The expected number of background events, λ_{bkg}, can be estimated with events in the fit window that are outside the $\pm 5\sigma$ boundaries. If this number is denoted by N_{side}, then

$$\lambda_{bkg} = N_{side} \frac{\Delta E_{\pm 5\sigma}}{\Delta E_{Fit} - \Delta E_{\pm 5\sigma}}, \tag{9.7}$$

where $\Delta E_{\pm 5\sigma}$ is the width of the energy range close to the peak, and ΔE_{Fit} is the width of the whole range around the peak (in this case, 80 keV from 1220 to 1300 keV). The expected number of signal events, λ_{sig}, is unknown and can be written in terms of $\Gamma_{\beta\beta}$:

$$\lambda_{sig} = k \cdot \Gamma_{\beta\beta}; \tag{9.8}$$

the multiplication factor k is a constant that depends on the number of ^{130}Te atoms in the detector, on live time and on the detection efficiency. Going back to the example, the probability of observing two events in the $\pm 5\sigma$ band is given by:

$$\begin{aligned} \mathcal{L}(2) = & P(N_{bkg}=2)\cdot P(N_{sig}=0) \\ & + 2P(N_{bkg}=1)\cdot P(N_{sig}=1) \\ & + P(N_{bkg}=0)\cdot P(N_{sig}=2) \end{aligned} \tag{9.9}$$

Substituting equations 9.6 and 9.5, the likelihood becomes

$$\begin{aligned} \mathcal{L}(2) = & \left(\frac{1}{2}\lambda_{bkg}^2 e^{-\lambda_{bkg}}\right)\left(e^{-\lambda_{sig}}\right) \\ & + 2\left(\lambda_{bkg} e^{-\lambda_{bkg}}\right)\left(\lambda_{sig} e^{-\lambda_{sig}}\right) \\ & + \left(e^{-\lambda_{bkg}}\right)\left(\frac{1}{2}\lambda_{sig}^2 e^{-\lambda_{sig}}\right), \end{aligned} \tag{9.10}$$

which can be rewritten as

$$\mathcal{L}(N) = e^{-(\lambda_{bkg}+\lambda_{sig})}\left(\frac{1}{2}\lambda_{bkg}^2 + 2\lambda_{bkg}\lambda_{sig} + \frac{1}{2}\lambda_{sig}^2\right). \tag{9.11}$$

In the more general case, the likelihood related to the observation of N events is

$$\mathcal{L}(N) = e^{-(\lambda_{bkg}+\lambda_{sig})} \sum_{k=0}^{N} \binom{N}{k} \frac{\lambda_{bkg}^{N-k} \lambda_{sig}^{k}}{N!(N-k)!}. \tag{9.12}$$

The only variable in the likelihood defined in equation 9.12 is the decay rate $\Gamma_{\beta\beta}$, which is enclosed in λ_{sig}. The likelihood function obtained by fitting all the high-background scenarios is multiplied with the one coming from equation 9.12; the total likelihood thus obtained is used to estimate $\Gamma_{\beta\beta}$.

Summarizing, the procedure used for low background scenarios is the following:

1. apply all the needed selection cuts and select a region close to the required energy;
2. count the events that lie at more than 5σ from the peak energy and use them to estimate λ_{bkg} with equation 9.7;
3. count the events N within the $\pm 5\sigma$ band and calculate the likelihood $\mathcal{L}(N)$ according to equation 9.12;
4. combine $\mathcal{L}(N)$ with the likelihood obtained by fitting the high-background scenarios, producing a total likelihood $\mathcal{L}_{tot} = \mathcal{L}(N) \cdot \mathcal{L}_{Fit}$.

9.3 Neutrinoless channel

In this section I'll describe the procedure followed to estimate $\Gamma_{\beta\beta}$ for the $0\nu\beta\beta_{0+}$ decay. At first, I discuss the cuts used to select only events that might contribute to the process under study; then I describe the criteria used to select only signatures that contribute significantly to the final sensitivity. Finally, I will present the results of the fit, the way systematic errors are kept into account and the combination of the results from CUORE-0 and Cuoricino.

9.3.1 Data selection cuts

Data selection cuts for this analysis are used mainly for two purposes: removing non-physical or badly reconstructed signals and selecting only the events that might contribute to one of the signatures listed in table 9.2. This involves the time-based and event-based cuts described in chapter 3 and an additional set of specific, multiplicity-based cuts.

Time-based cuts

Time-based cuts remove time intervals where the detector doesn't operate correctly, for example during periods of high noise or baseline instability. These *bad intervals* are exactly

the same that were used for the standard CUORE-0 analysis: their contribution is kept into account in the total exposure of the detector, which amounts to 35.2 kg·y.

Event-based cuts

Event-based cuts are used to identify signals that are either non-physical or whose energy hasn't been properly reconstructed by the analysis chain. The basic pile-up rejection cuts, described in chapter 5, and the more advanced pulse shape cuts, described in chapter 4, are both used for this analysis. The previously discussed calculation of the pulse shape cut efficiency applies in the same way (figure 4.10).

Multiplicity-based cuts

Valid signatures for $0\nu\beta\beta_{0+}$ can either involve a single or multiple crystals, with the highest multiplicity scenario having M4. In order to optimize the selection of candidate events for each of them, different multiplicity-based cuts have to be set depending on the required scenario. For M1 signatures, a simple `Multiplicity`$== 1$ cut is applied. The efficiency of this cut is calculated with the same method described in section 3.2.3, using the ^{40}K 1460 keV γ line, and turns out to be $99 \pm 1\%$.

For M2 signatures, the `Multiplicity`$== 2$ cut is not enough; the chosen cut requires also that the sum of the energies of the two events in the M2 pair (the total energy, E_{tot} in the following) lies within a well-defined range. Let's take as an example scenario #1 from table 9.1: in this case the first crystal contains the two electrons, with energy 734 keV, and the second crystal a sum of γs, with energy 1793.5 keV. Only events whose total energy is close to $E_{tot} = 734 + 1793.5 = 2527.5$ can contribute to this scenario. If σ_1 is the energy resolution at 734 keV and σ_2 the one at 1793 keV, the resolution at energy E_{tot} is $\sigma_{tot} = \sqrt{\sigma_1^2 + \sigma_2^2}$. Only M2 events whose total energy lies within $\pm 5\sigma_{tot}$ from E_{tot} are accepted.

For M3 and M4 scenarios the cut on total energy is not as efficient. In these cases, in addition to the basic `Multiplicity`$== 3(4)$ cut, a requirement on the energy deposited on every single involved crystal is put in place. Let's consider an M3 scenario which involves the deposition of energies E_1, E_2 and E_3 on three separate crystals. If σ_1 and σ_2 are the energy resolutions corresponding to E_1 and E_2 respectively, the cut for M3 events is

- `Multiplicity`$== 3$;
- the energy deposited on a crystal in the triplet is within $E_1 \pm 5\sigma_1$;
- the energy deposited on another crystal in the triplet is within $E_2 \pm 5\sigma_2$;
- events on the remaining crystal are considered for the current signature.

For M4 events the cut works in the exact same way: boundaries are set for the energy deposited on three of the involved crystals, and the remaining event is considered for the signature.

The efficiency evaluation of the M2, M3 and M4 cuts is not so straightforward as for M1 events, since there is no equivalent to the ^{40}K γ line: while the 1460 keV γ from ^{40}K is guaranteed to be an M1 event, nothing in the CUORE-0 data is always supposed to be, for example, an M2 event. Therefore, the multiplicity cut efficiency can be estimated theoretically using equation 5.9 from chapter 5; the obtained values are 99.2% for M2, 98.8% for M3 and 98.4% for M4. The same value can also be calculated for M1 events, giving a 99.6% efficiency.

Fit energy range

The evaluation of the $0\nu\beta\beta$ half-life is done by evaluating the number of events that are possible decay candidates. The $0\nu\beta\beta$ signal is fitted in the spectrum of the crystal that, among those involved in the decay, records the highest energy signal. This is the most favourable condition since the signal to background ratio usually improves at higher energies.

Despite the presence of 57 different scenarios (tables 9.1 and 9.2), there are only a few recurring peaks that might appear in the detected spectra: 734, 1122, 1207, 1257, 1270, 1320, 1405, 1793, 1856, 1941, 1991 and 2527 keV. The fit of those peaks requires, for each of them, the selection of a fitting range wide enough to properly account for background contributions. To keep things as simple as possible, the fitting ranges are chosen to avoid the inclusion of any other prominent peak. The background model is used to select fit ranges in a blinded approach, i.e. without looking directly at the CUORE-0 data. The cuts defined in the previous sections are applied to the simulated data obtaining a background simulated spectrum later used to identify the fit range. An example is shown in figure 9.6: the spectrum of candidate events for scenario #1 is shown, along with the selected energy region for the 1793 keV line, which needs to be fitted in this case. The energy ranges for all the required peak energies are listed in table 9.3.

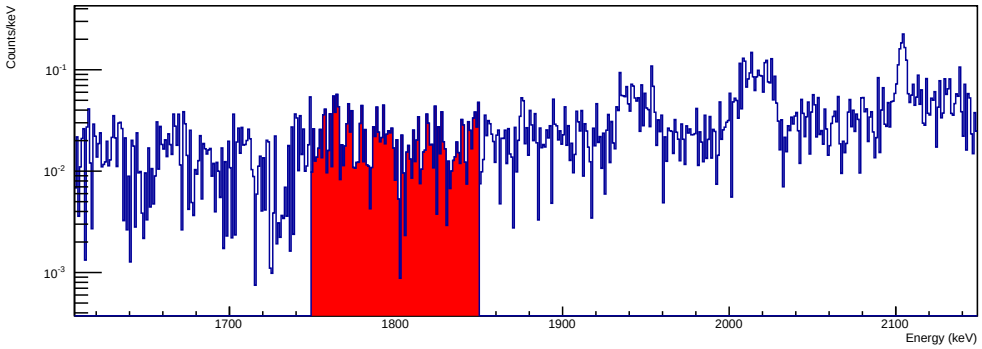

Figure 9.6: Simulated background spectrum for signature #1, table 9.1. This projection represents the spectrum where the highest energy line (at 1793 keV) should appear.

Energy [keV]	Lower fit boundary [keV]	Upper fit boundary [keV]
734	710	745
1122	1050	1150
1207	1150	1250
1257	1220	1300
1270	1220	1300
1320	1300	1350
1405	1380	1440
1793	1750	1850
1856	1820	1865
1941	1920	2000
1991	1960	2040
2527	2490	2560

Table 9.3: Fit ranges for all the lines required by the $0\nu\beta\beta_{0+}$ analysis.

9.3.2 Signature selection

As shown in section 9.1, there are tens of possibilities that lead to detectable signals for $0\nu\beta\beta_{0+}$. Not all of these scenarios are worth including in the fit; some can have a very low probability of happening and contribute nothing to the final result, while others could suffer from high background, again giving no significant contribution and slowing down the unbinned fit procedure. In this section I'll define the technique I've used to select only the most meaningful signatures to use in the final fit.

1405 keV line

Two of the scenarios listed in table 9.2, #47 and #53, are linked to a line in the M1 spectrum at energy $\beta\beta + 671 = 1405$ keV. Two lines, however, are present in the M1 spectrum at this energy, as shown by figure 9.7 (taken from the background model). For this reasons, scenarios 47 and 53 are immediately excluded from the analysis.

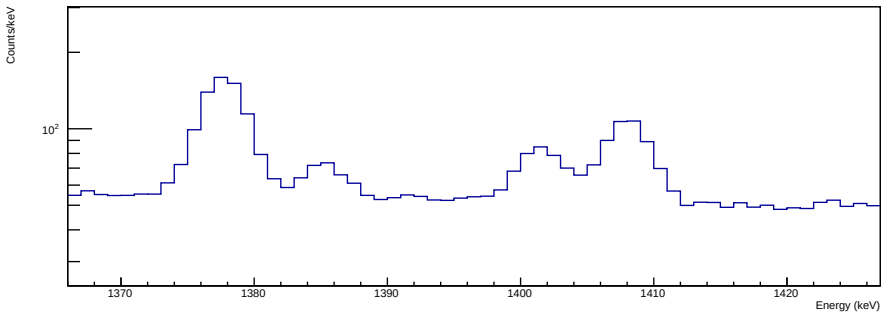

Figure 9.7: M1 spectrum from the background model, showing the structures close to 1405 keV.

Sensitivity

For all the cases that do not involve the 1405 keV line an acceptance criterion based on a sensitivity parameter is adopted. Signatures are ranked based on their predicted sensitivity. As already stated in chapter 1, the half-life sensitivity to double-beta decay can be expressed in terms of a number of experimental parameters as

$$T_{1/2} \propto \epsilon \sqrt{\frac{M \cdot t}{b \cdot \Delta E}}, \tag{9.13}$$

where ϵ is the efficiency, M the mass of the active isotope, t the live time of the experiment, b the background in the region of interest for the $\beta\beta$ signal and ΔE the energy resolution. Since every signature for the 0^+ decays is different, each of them has a different sensitivity. Some of the parameters in equation 9.13 are constant across all signatures: it's the case of the mass M and of live time t. Signatures can therefore be ranked by their expected sensitivity, expressed only in terms of efficiency, background and energy resolution.

The energy resolution scaling vs. energy is taken directly by the CUORE-0 data, with the same values already defined in chapter 7:

$$\mathrm{FWHM}(E) = \mathrm{FWHM}(2615) \cdot (0.49 + 2.22 \cdot 10^{-3} E). \tag{9.14}$$

The background index, expressed in terms of counts/keV, is taken from the simulated background: the selection cuts associated to each signature are applied to the simulated data and the background index is calculated in the fit ranges defined in table 9.3.

The efficiency represents the probability that an event coming from a $0\nu\beta\beta_{0+}$ decay is detected and properly reconstructed. It can be written as the product of several quantities:

- the probability that an event is triggered. In CUORE-0, it is basically the fraction of pulser events that are triggered and reconstructed at their correct amplitude. This efficiency is equal for all scenarios and its value is $98.529 \pm 0.004\%$. More details on the calculation can be found in [60].
- the pulse shape cut efficiency, already discussed in chapter 4;
- for M1 events, the anticoincidence cut efficiency is calculated using the ^{40}K line, as previously described;
- the probability of an M2/3/4 event actually being recorded as one, related to how pile-up is handled, has been discussed in chapter 5;
- the fraction of $0\nu\beta\beta_{0+}$ events that deposit energy according to a particular scenario (the energy confinement efficiency).

All these terms have been previously calculated, with the exception of the last one. Three MC simulations have been produced, one for each of the possible γ cascades described in section 9.1. They are then processed with `g4cuore`, using the same parameters defined in chapter 8 for the processing of simulations for the background model. The cuts associated to each signature are applied to these simulations and the energy containment efficiency for each of them is calculated. The pulse shape cut efficiency is included in this value, as the PSA efficiency vs. energy curve is used in the processing with `g4cuore`.

Once all quantities are available, a sensitivity *score* is calculated for each scenario, given by

$$S(\epsilon, \sigma, BI) = \frac{\epsilon}{b \cdot \Delta E}; \tag{9.15}$$

signatures are then ranked and evaluated based on this score. A summary of all the scores associated to the final signatures can be found in table 9.4.

Merging identical signatures

Some of the available signatures require the fit of the same line and use the exact same selection cuts, making them completely identical. Signatures #1, #7 and #13, for example, fall in this category: they all involve M2 events where the first crystal contains

the two electrons and the second a sum of γs with energy 1793 keV. The only difference between those three is the γ cascade by which they were produced. Identical signatures such as these require the application of the same data selection cuts and, therefore, select the same events; they cannot be fit separately, as if they were independent.

Identical signatures are merged together; the efficiency of the combined signature is the sum of the efficiencies of its components, weighted by the branching ratio of the respective γ cascade. In the previously illustrated example, the final efficiency is given by

$$\epsilon_{merge} = 0.86\epsilon_1 + 0.12\epsilon_7 + 0.02\epsilon_{13}. \tag{9.16}$$

Final set of signatures

The final set of signatures considered for the $0\nu\beta\beta_{0+}$ fit is presented in table 9.4. Signatures are ranked by their sensitivity score, obtained with equation 9.15. The contribution to the total sensitivity is calculated for each signature, and is reported as a percentage in the final column of table 9.4. Only the first three signatures, which contribute to the total sensitivity for more than 1%, are considered for the final fit.

Scenario # [1]	Multiplicity	Energy [keV]			B.I. [2]	ϵ^3	Resolution	Score	Score %
		Cr. A	Cr. B	Cr. C	[c/keV]		[keV]		
1	2	536	1991		4.65E-004	1.46E-002	1.93E+000	4.86E-001	65.33
2	3	734	536	1257	6.29E-005	3.02E-003	1.60E+000	3.02E-001	25.15
3	2	1257	1270		1.09E-002	2.23E-002	1.60E+000	1.69E-001	7.89
4	3	671	536	734	8.98E-005	1.71E-005	1.36E+000	1.55E-003	0.51
5	3	671	536	1320	1.84E-004	2.48E-005	1.63E+000	1.43E-003	0.45
6	2	734	1257		4.97E-002	1.21E-002	1.60E+000	4.30E-002	0.23
7	3	734	671	1122	7.50E-005	4.34E-004	1.53E+000	4.04E-002	0.22
8	2	536	734		6.29E-001	2.66E-002	1.36E+000	2.88E-002	0.08
9	1	2527			2.19E+000	6.23E-002	2.18E+000	2.85E-002	0.04
10	2	671	1270		6.18E-002	1.18E-004	1.60E+000	3.76E-004	0.04
11	2	1122	1405		1.53E-002	2.74E-003	1.66E+000	1.72E-002	0.02
12	2	671	1320		1.11E-001	1.00E-004	1.63E+000	2.36E-004	0.01
13	2	671	1856		2.08E-002	2.31E-003	1.87E+000	1.17E-002	0.01
14	2	734	1793		2.14E-002	2.25E-003	1.84E+000	1.13E-002	4.84E-003
15	2	536	1405		1.84E-001	1.00E-004	1.66E+000	1.81E-004	3.59E-003
16	2	536	1320		3.49E-001	1.23E-004	1.63E+000	1.63E-004	6.66E-004
17	1	1270			6.53E+001	9.11E-002	1.60E+000	8.91E-003	5.67E-004
18	1	1991			7.60E+000	2.77E-002	1.93E+000	7.24E-003	3.73E-004
19	1	1941			8.82E+000	4.03E-004	1.91E+000	9.81E-005	3.90E-005
20	2	1207	1320		2.55E-002	1.93E-005	1.63E+000	9.50E-005	1.54E-005
21	1	734			1.93E+002	7.38E-002	1.36E+000	4.57E-003	9.08E-006
22	2	734	1122		1.62E-001	2.09E-003	1.53E+000	4.18E-003	7.37E-006
23	2	671	734		6.64E-001	3.42E-003	1.36E+000	3.60E-003	2.66E-006
24	2	734	1207		8.16E-002	1.26E-005	1.57E+000	3.51E-005	2.49E-006
25	1	1320			5.94E+001	3.15E-004	1.63E+000	3.21E-005	3.41E-007
26	1	1856			1.15E+001	5.40E-003	1.87E+000	1.16E-003	2.84E-007

Table 9.4: Summary of all the final signatures for $0\nu\beta\beta_{0+}$, ranked by their sensitivity score. Only the first 3 contribute to the total sensitivity by more than 1%. [1] Scenario numbers defined here are not associated to those in tables 9.1 and 9.2. [2]Background Index. [3] The efficiency contains all terms listed in section 9.3.2.

9.3.3 Fit results

The only signatures that are included in the final fit are the first three ones in table 9.4. For all of them, no event is observed in the corresponding fit energy window. The likelihood for each signature i can be obtained by equation 9.12 and becomes simply

$$\mathcal{L}^i_{0\nu} = e^{-\lambda^i_{sig}} = e^{-k^i \cdot \Gamma_{0\nu}}. \tag{9.17}$$

The constant k^i depends on the total number of ^{130}Te nuclei N_{130Te}, on the live time T_l and on the efficiency of each selected signature ϵ_i, and can be written as

$$\begin{aligned} k^i &= N_{130Te} \cdot T_l \cdot \epsilon_i \\ &= \frac{M_{TeO_2}}{MM_{TeO_2}} \cdot N_{Av} \cdot i.a._{130Te} \cdot T_l \cdot \epsilon_i, \end{aligned} \tag{9.18}$$

where M_{TeO_2} is the total mass of the CUORE-0 crystals, MM_{TeO_2} the molar mass of TeO_2 (159.6 g/mol), $i.a._{130Te}$ the isotopic abundance of ^{130}Te (34.167%) and N_{Av} the Avogadro number. The product $M_{TeO_2} \cdot T_l$ is the exposure, which for CUORE-0 amounts to 35.2 kg·y. The efficiency ϵ_i can be taken directly from table 9.4. The values of k^i for the three selected signatures are listed in table 9.5.

Scenario #	Total Efficiency	k [$10^{24}y$]
1	1.47E-002	0.662
2	3.02E-003	0.137
3	2.23E-002	1.011
	Total	1.853

Table 9.5: Values of efficiency and of the constant k for the three selected signatures for the neutrinoless channel.

The combined likelihood for the 5 signatures is given by the product of all $\mathcal{L}^i_{0\nu}$:

$$\mathcal{L}^{tot}_{0\nu} = \prod_{i=1}^{5} \mathcal{L}^i_{0\nu} = e^{-\Gamma_{0\nu} \sum_{i=1}^{5} k^i} = e^{-\Gamma_{0\nu} K_{tot}}. \tag{9.19}$$

Since no evidence of signal is found, a 90% upper limit can be given for $\Gamma_{0\nu}$:

$$\int_0^{\Gamma^{90}_{0\nu}} e^{-\Gamma K_{tot}} \mathrm{d}\Gamma = 0.9 \int_0^{\infty} e^{-\Gamma K_{tot}} \mathrm{d}\Gamma \tag{9.20}$$

$$\Gamma_{0\nu} < 1.28 \cdot 10^{24} y^{-1}; \tag{9.21}$$

this can also be given as a half-life limit:

$$T_{0\nu}^{1/2} > 5.44 \cdot 10^{23} y. \tag{9.22}$$

9.3.4 Systematic errors

The only parameter used for the $0\nu\beta\beta_{0+}$ analysis which can introduce an error in the final result is the efficiency. The efficiency error depends on the PSA cut error (93.7±0.7% [60]), on the trigger efficiency ($98.529 \pm 0.004\%$ [60]) and on energy confinement, which changes depending on signature. The error values for confinement efficiency, total efficiency and k coefficients for each considered scenario are listed in table 9.6.

The total k coefficient is affected by less than 3‰; this has a completely negligible effect on the previously calculated limit.

Scenario	ϵ_{MC}	ϵ_{tot}	k
1	1.59E-02 ±7.12E-05	1.46E-02 ±6.52E-05	0.662 ± 0.003
2	3.33E-03 ±3.27E-05	3.02E-03 ±2.97E-05	0.137 ± 0.001
3	2.43E-02 ±8.85E-05	2.23E-02 ±8.12E-05	1.011 ± 0.004
		Total	1.810 ± 0.005

Table 9.6: MC confinement efficiency and relative error for each scenario used in the $0\nu\beta\beta_{0+}$ analysis; the values of the total efficiency ϵ_{tot} and of the coefficient k are also reported.

9.3.5 Combination with Cuoricino

This process was also studied in Cuoricino [66], obtaining a lower limit for the half life of

$$T_{1/2}^{0\nu} > 9.4 \cdot 10^{23} y \quad \text{(Cuoricino)}. \tag{9.23}$$

The limit obtained in CUORE-0 is worse than the pre-existing one, but this is expected. Very few events were observed also in Cuoricino, so the technique used to extract the limit was exactly the same: an exponential likelihood like the one in equation 9.17 was used for each signature, and the total likelihood was obtained as in equation 9.19. Since the structure of the tower is similar between CUORE-0 and Cuoricino, most of the quantities that define the constant k (equation 9.18) are similar between the two experiments, with the exception of the exposure. Cuoricino, in fact, accumulated much more data than CUORE-0 (almost double), leading to a better limit. It is, however, possible to combine the results obtained with the two experiments to provide an even more stringent limit.

The Cuoricino likelihood has the same exponential form of the one used here; the only additional information that is needed to fully characterize it is the coefficient at the exponent, K_{tot}. The K_{tot}^{Cino} coefficient for Cuoricino can be obtained by inverting equation 9.20; a combined likelihood can then be produced:

$$\mathcal{L}_{0\nu} = \mathcal{L}_{0\nu}^{Cino} \cdot \mathcal{L}_{0\nu}^{Cuore0} = e^{-(K_{Tot}^{Cino}+K_{Tot}^{Cuore0})\Gamma_{0\nu}}. \tag{9.24}$$

The combined lower limit for the process half-life is then

$$T_{1/2}^{0\nu} > 1.48 \cdot 10^{24} y \quad \text{(Cuoricino + CUORE-0)}, \tag{9.25}$$

which is the best current limit for the $0\nu\beta\beta_{0+}$ decay.

9.4 Two neutrino channel

In this section I'll describe the procedure followed to estimate $\Gamma_{\beta\beta}$ for the $2\nu\beta\beta_{0+}$ decay. While most of the procedure is similar to the one described for the 0ν channel, there are some differences in the data selection cuts and in the selection of signatures for the final fit.

9.4.1 Data selection cuts

The event-based and time-based cuts that were described in section 9.3.1 are exactly the same. Due to the different energy deposition by electrons with respect to the neutrinoless channel, however, the multiplicity-based cuts are different.

Multiplicity-based cuts

Scenarios listed in table 9.1 all involve more than one crystal, with multiplicity values ranging from 2 to 4. M2 scenarios are characterized by `Multiplicity`$== 2$ cut and by a cut on the total energy of the event. Let's take as an example scenario #1: in this case, the two electrons release their energy (between 0 and 734 keV) in the first crystal, while the γs produce a 1793.5 keV peak in the second. The chosen for the total energy variable E_{tot} (sum of the energies released in the two involved bolometers) is

$$1793.5 < E_{tot}^{S1} < 1793.5 + 734.$$

For M3 and M4 events, there is still a requirement on the energy deposited in each involved crystal. Scenario #6, for example, requires the production of an M3 event where

the deposited energies are $E_{\beta\beta} = 0 - 734$ keV, $E_1 = 536$ keV and $E_2 = 1257$ keV. M3 triplets in the data have to fulfil these requirements to be associated to this scenario:

- `Multiplicity`$== 3$;
- the energy deposited on one crystal must be within the boundaries set by $E_{\beta\beta}$;
- the energy on a second crystal must be within $\pm 5\sigma_1$ from E_1;
- the event on the third crystal is considered for the final fit.

The cut works in the same exact way for M4 events.

As in the 0ν case, the efficiency of these cuts is calculated theoretically using equation 5.9 from chapter 5: $\epsilon_{M2} = 99.2\%$, $\epsilon_{M3} = 98.8\%$ and $\epsilon_{M4} = 98.4\%$.

Fit energy range

Due to the continuous energy deposition from electrons, there are less recurring peaks required by the 41 scenarios available for $2\nu\beta\beta_{0+}$. As done for the $0\nu\beta\beta_{0+}$, the selection cuts used for each signature are applied to the background model, and suitable energy ranges for the fit are chosen from the obtained spectra. The peaks selected for the fit and the corresponding fit boundaries are reported in table 9.7.

Energy [keV]	Lower fit boundary [keV]	Upper fit boundary [keV]
536	520	560
586	550	590
671	620	720
1122	1050	1150
1207	1150	1250
1257	1220	1300
1793	1750	1850

Table 9.7: Fit ranges for all the lines required by the $2\nu\beta\beta_{0+}$ analysis.

9.4.2 Signature selection

Before proceeding with the selection of signatures based on their sensitivity an additional step has to be taken. Some of the signatures, in fact, are partially overlapping: unlike identical signatures described previously, they have different cuts and require the fit of different peaks, but are still not independent between each other. Additionally, some signatures can be removed right away due to the presence of a line in the spectrum close to the required energy.

586 keV line

Several signatures (#15, #21, #27, ...) require the fit of the γ line at 586 keV in the M2 spectrum. As shown by the background model (figure 9.8), a strong γ line close to this energy is expected, at 583 keV. This line is produced by ^{208}Tl and is emitted in a cascade with the already discussed 2615 keV photon. Since fitting two lines this close would be prohibitive, all signatures involving the 583 keV line are not considered for the final analysis.

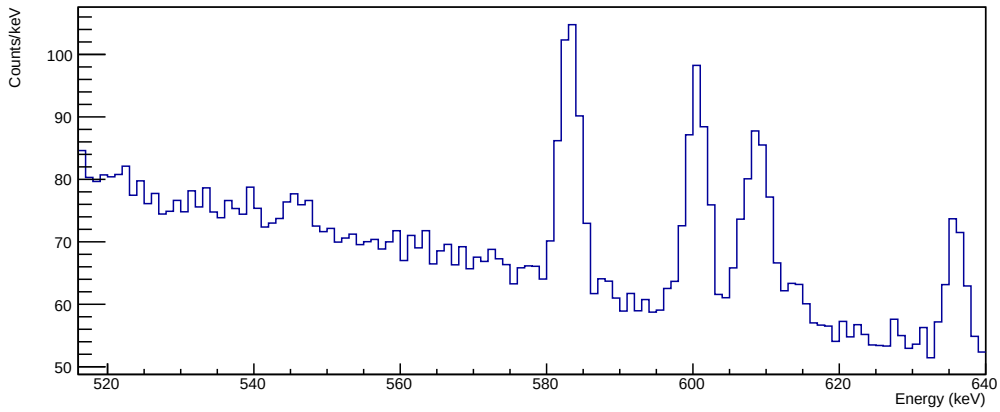

Figure 9.8: M2 spectrum from the background model, showing the prominent peak at 583 keV, preventing the fit of the 586 keV line.

Overlapping signatures

As an example of overlapping signatures, let's look at scenarios #3 and 4 from table 9.1, and summarized here in table 9.8. Since it is an M2 signature, the related total energy cuts are

$$1257.4 < E^3_{tot} < 1991.4,$$

$$1793.5 < E^4_{tot} < 2527.5.$$

Any M2 event whose total energy falls in the region between 1793.5 and 1991.4 keV is valid for both signatures and, as already stated for the case of identical signatures, would be counted twice in the final fit. In order to make them completely independent, the two scenarios are split in three: the new total energy cuts will be

$$1257.4 < E^{1*}_{tot} < 1793.5,$$

Scenario #	Multiplicity	Energy [keV]		Total Energy cuts[keV]	
		Crystal A	Crystal B	E_{tot}^{min}	E_{tot}^{max}
3	2	$\beta\beta$	1257.4	1257.4	1991.4
4	2	$\beta\beta + 536.1$	1257.4	1793.5	2527.5

Table 9.8: Definition of scenarios #3 and 4, with the respective total energy cuts.

$$1793.5 < E_{tot}^{2*} < 1991.4,$$

$$1991.4 < E_{tot}^{3*} < 2527.5.$$

This new division guarantees that no event is counted twice. Of course, if some duplicates are found among the newly created signatures, they are merged together as described previously. A visual representation of the split scenarios is given in figure 9.9.

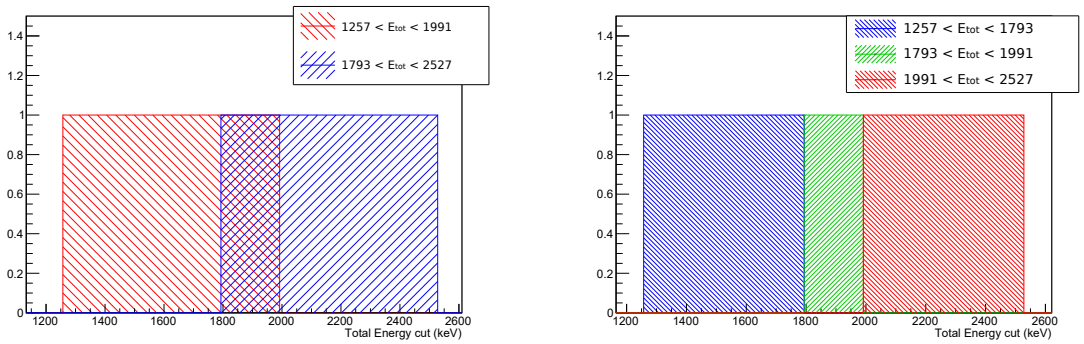

(1) (2)

Figure 9.9: Visual representation of the total energy intervals for scenarios 3 and 4, overlapping in the region between 1793.5 and 1991.4 keV. In the right plot, the two scenarios are split in three, independent ones.

Final set of signatures

The final set of signatures considered for the $2\nu\beta\beta_{0+}$ fit is presented in table 9.9. Signatures are ranked by their sensitivity score, obtained with equation 9.15. The contribution to the total sensitivity is calculated for each signature, and is reported as a percentage in the final column of table 9.9. Only the first eight signatures, which contribute to the total sensitivity for more than 1%, are considered for the final fit.

Scenario # [1]	Multi	Energy [keV]			B.I. [2]	ϵ^3	Resolution	Score	Score %
		Cr. A	Cr. B	Cr. C	[c/keV]		[keV]		
1	3	0-734	536	1257	2.15E-002	3.23E-003	1.60E+000	1.74E-002	62.16
2	2	734-1270	1257		2.14E+000	1.23E-002	1.60E+000	6.66E-003	9.08
3	2	536-734	1257		2.14E+000	1.17E-002	1.60E+000	6.31E-003	8.16
4	2	1405-1991	536		2.95E+000	1.13E-002	1.26E+000	5.82E-003	6.94
5	3	586-734	536	671	1.51E-002	7.42E-004	1.26E+000	5.37E-003	5.91
6	2	0-586	536		7.47E+001	3.09E-002	1.26E+000	3.18E-003	2.07
7	2	0-536	1257		2.04E+001	1.71E-002	1.60E+000	2.99E-003	1.83
8	3	734-1320	536	671	1.51E-002	3.13E-004	1.26E+000	2.26E-003	1.05
9	3	0-734	671	1122	2.31E-002	3.86E-004	1.53E+000	2.05E-003	0.86
10	2	1320-1405	536		2.95E+000	3.93E-003	1.26E+000	2.03E-003	0.85
11	3	0-586	536	671	1.21E-001	7.06E-004	1.26E+000	1.80E-003	0.67
12	2	1257-1320	536		2.95E+000	1.60E-003	1.26E+000	8.30E-004	0.14
13	2	0-734	1793		3.66E+000	1.92E-003	1.84E+000	7.37E-004	0.11
14	2	1320-1856	671		2.55E+000	9.58E-004	1.33E+000	5.21E-004	0.06
15	2	1122-1270	671		2.55E+000	6.56E-004	1.33E+000	3.57E-004	0.03
16	2	734-1257	536		2.82E+001	1.99E-003	1.26E+000	3.33E-004	0.02
17	2	734-1122	671		2.13E+001	1.53E-003	1.33E+000	2.87E-004	0.02
18	2	734-1405	1122		2.19E+000	5.18E-004	1.53E+000	2.82E-004	0.02
19	2	0-536	671		5.25E+001	1.57E-003	1.33E+000	1.88E-004	0.01
20	2	1270-1320	671		2.55E+000	3.00E-004	1.33E+000	1.63E-004	0.01
21	2	586-671	536		7.47E+001	1.15E-003	1.26E+000	1.19E-004	2.88E-003
22	2	671-734	536		7.47E+001	9.27E-004	1.26E+000	9.54E-005	1.86E-003
23	2	586-734	671		5.25E+001	7.24E-004	1.33E+000	8.67E-005	1.54E-003
24	2	0-671	1122		3.03E+001	5.82E-004	1.53E+000	8.53E-005	1.49E-003
25	2	586-734	1207		2.05E+000	1.20E-004	1.57E+000	6.68E-005	9.13E-004
26	2	734-1320	1207		2.05E+000	8.78E-005	1.57E+000	4.89E-005	4.89E-004
27	2	671-734	1122		2.19E+000	5.11E-005	1.53E+000	2.79E-005	1.59E-004
28	2	0-586	1207		2.58E+001	1.20E-004	1.57E+000	1.88E-005	7.26E-005
29	2	536-586	671		5.25E+001	1.11E-004	1.33E+000	1.33E-005	3.63E-005

Table 9.9: Summary of all the final signatures for $2\nu\beta\beta_{0+}$, ranked by their sensitivity score. Only the first 8 contribute to the total sensitivity by more than 1%. [1] Scenario numbers defined here are not associated to those in tables 9.1. [2]Background Index. [3] The efficiency contains all terms listed in section 9.3.2.

9.4.3 Fit results

The spectra obtained by applying the selection cuts required by the eight chosen signatures to the CUORE-0 data are shown in figures 9.10 and 9.11. Three of these spectra (1, 5 and 8) show only a few events, and therefore their likelihood will be obtained by equation 9.12. The other five signatures will be included in a combined fit to estimate $\Gamma^{2\nu}_{\beta\beta}$.

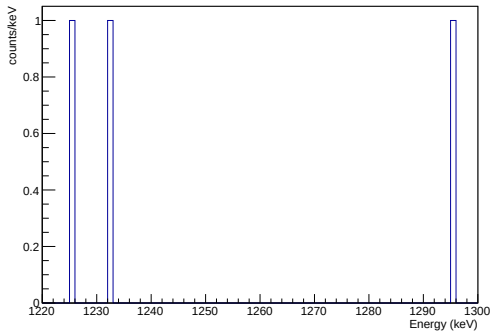

(1) Scenario 1

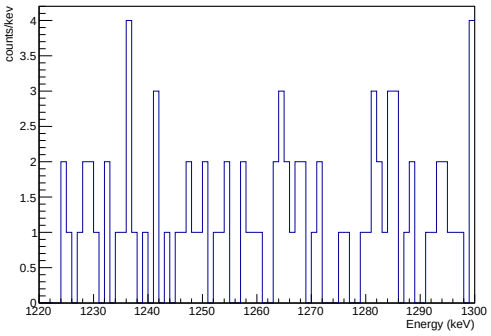

(2) Scenario 2

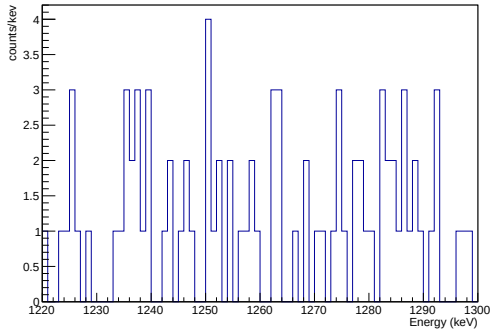

(3) Scenario 3

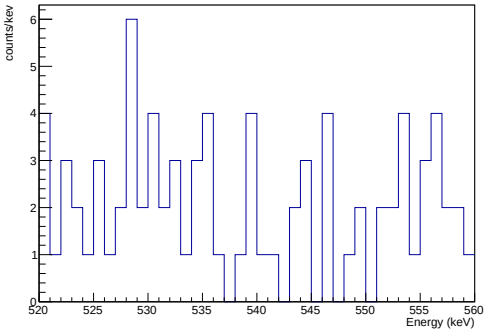

(4) Scenario 4

Figure 9.10: Energy spectra of selected scenarios for the $2\nu\beta\beta_{0+}$ fit. Scenarios 1, 5 and 8 are M3, the others are M2. (continues in figure 9.11)

For simplicity, let's start with the three M3 signatures. Since no event is observed in the region close to the required peak, the likelihood for each of the three is

$$\mathcal{L}^i_{2\nu} = e^{-\lambda_{bkg} - k^i \Gamma^{2\nu}_{\beta\beta}} = e^{-\lambda_{bkg}} e^{-k^i \Gamma^{2\nu}_{\beta\beta}} \tag{9.26}$$

The expected number of background counts λ_{bkg} can be calculated, but since it only appears as a multiplicative constant in the likelihood, it can be safely ignored as it doesn't contribute to the maximization of $\mathcal{L}_{2\nu}$. The combined likelihood for the three M3 signa-

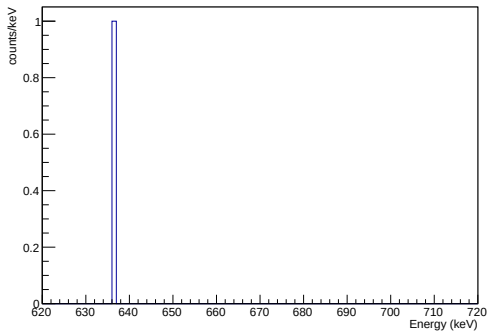

(1) Scenario 5

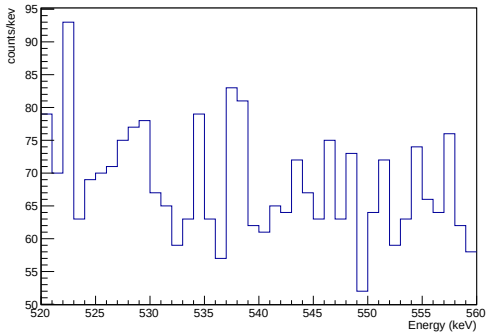

(2) Scenario 6

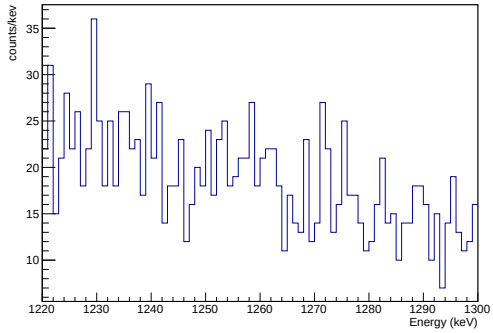

(3) Scenario 7

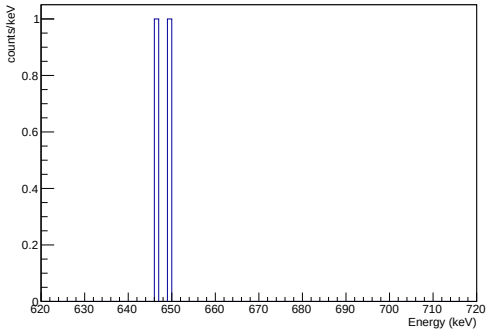

(4) Scenario 8

Figure 9.11: Energy spectra of the selected scenarios for the $2\nu\beta\beta_{0+}$ fit. Scenarios 1, 5 and 8 are M3, the others are M2.

tures is

$$\mathcal{L}_{2\nu}^{M3} = \prod_{i=1}^{3} \mathcal{L}_{2\nu}^{i} = e^{-\Gamma^{2\nu} \sum_{i=1}^{3} k^i} = e^{-\Gamma^{2\nu} K_{tot}}; \tag{9.27}$$

the values of k^i and K_{tot} are reported in table 9.10.

Scenario #	Total Efficiency	k $[10^{24}y]$
1	3.23E-003	0.146
5	7.24E-004	0.034
8	3.13E-004	0.014
	Total	0.194

Table 9.10: Values of efficiency and of the constant k for the three selected signatures for the two-neutrino channel.

The five remaining signatures are fit with a gaussian signal superimposed to a first degree polynomial, used to model the background:

$$F(E, \boldsymbol{p})_i = p_0 + p_1 E + \frac{k^i p_2}{\sqrt{2\pi\sigma_i^2}} e^{-\frac{(E - E^i_{center})^2}{2\sigma_i^2}}; \tag{9.28}$$

in the fit function, E_{center} is fixed at the required value, σ is obtained by the energy resolution vs. energy curve measured in CUORE-0 (chapter 7), while p_0, p_1 and p_2 are free parameters. The two parameters related to the background, p_0 and p_1, are independent between each signature; the event rate $p_2 = \Gamma^{2\nu}_{\beta\beta}$ is constrained to be identical for all signatures.

The results of the best fit for the selected signatures are shown in figure 9.13. The profile likelihood $\mathcal{P}_{2\nu}$ is shown in figure 9.12: the blue curve is the negative log-likelihood obtained by the fit, while the red curve comes from the combination with the result obtained by the M3 signatures. The best fit value for $\Gamma^{2\nu}_{\beta\beta}$ is

$$\Gamma - \beta\beta^{2\nu} = -1.03 \pm 2.72, \tag{9.29}$$

meaning that there is no evidence of a signal. A 90% upper limit for the event rate, $\Gamma^{90}_{2\nu}$, can be found by integrating $e^{-\mathcal{P}_{2\nu}}$:

$$\int_0^{\Gamma^{90}_{2\nu}} e^{-\mathcal{P}_{2\nu}} \mathrm{d}\Gamma = 0.9 \int_0^{\infty} e^{-\mathcal{P}_{2\nu}} \mathrm{d}\Gamma. \tag{9.30}$$

For the fitted signatures only, the upper limit on $\Gamma^{2\nu}_{\beta\beta}$ is

$$\Gamma_{2\nu} < 4.78 \cdot 10^{24} y^{-1}, \tag{9.31}$$

corresponding to a half-life lower limit of

$$T^{1/2}_{0\nu} > 1.48 \cdot 10^{23} y. \tag{9.32}$$

For the combined likelihood, including all the selected signatures, the limits become

$$\Gamma_{2\nu} < 3.73 \cdot 10^{24} y^{-1}, \tag{9.33}$$

$$T^{1/2}_{0\nu} > 1.86 \cdot 10^{23} y. \tag{9.34}$$

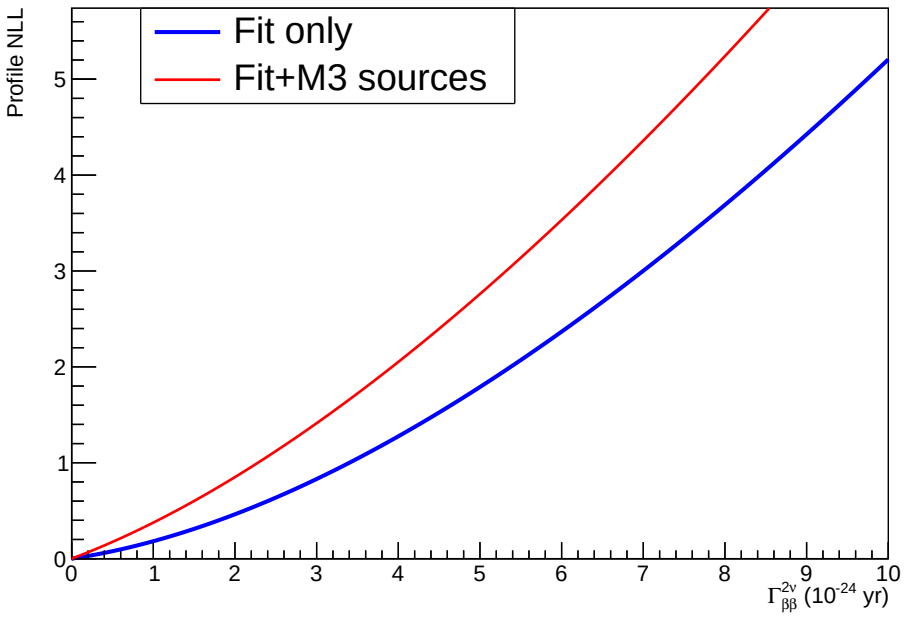

Figure 9.12: Negative log-likelihood for the $2\nu\beta\beta_{0+}$ analysis. In blue, the profile likelihood obtained with the fitted signatures only; in red, the combination with the low-background signatures.

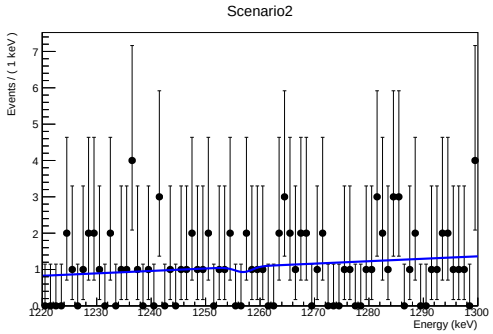

(1) Scenario 2

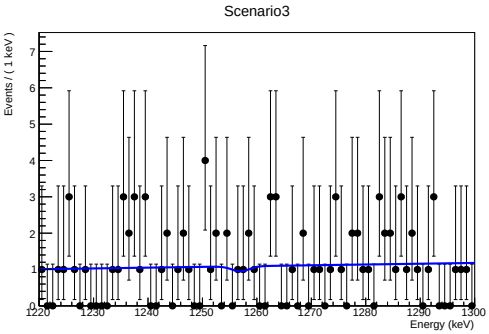

(2) Scenario 3

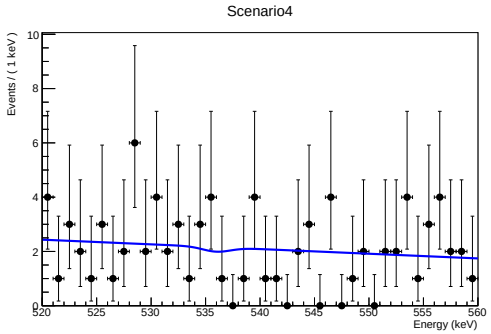

(3) Scenario 4

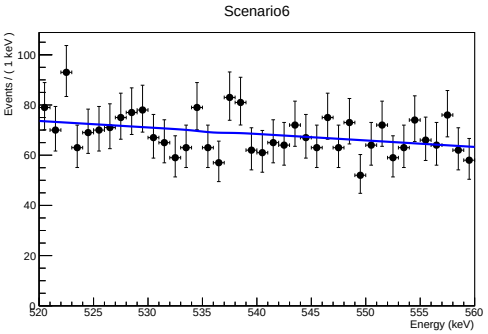

(4) Scenario 6

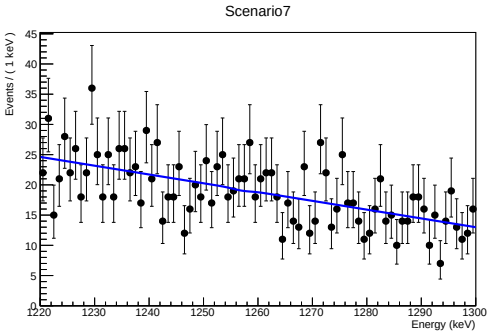

(5) Scenario 7

Figure 9.13: Results of the best fit for the selected $2\nu\beta\beta_{0+}$ signatures.

9.4.4 Systematic errors

The main sources of systematic errors in the $2\nu\beta\beta_{0+}$ analysis are the uncertainties related to energy resolution and efficiency. The method followed here to account for systematic errors is the same that was used in the main analysis of both CUORE-0 [60][67] and Cuoricino [49]. The likelihood obtained from the fit depends on Γ (the main parameter of interest) and on some parameters describing the background, $\boldsymbol{p}$. Calling $\hat{\Gamma}$ and $\hat{\boldsymbol{P}}$ the values of these parameters that maximize the likelihood function, it can be shown that the quantity

$$2\left(\min_{\boldsymbol{p}}\left(\ln\mathcal{L}(\hat{\Gamma},\hat{\boldsymbol{p}})-\ln\mathcal{L}(\Gamma,\boldsymbol{p})\right)\right) \tag{9.35}$$

follows a χ^2 distribution with one degree of freedom [65]. In terms of the profile likelihood $\mathcal{P}(\Gamma)$, which is obtained by maximizing the likelihood using $\boldsymbol{p}$ only, equation 9.35 becomes

$$\chi^2_{stat}=2\left(\ln(\mathcal{P}(\hat{\Gamma}))-\ln(\mathcal{P}(\Gamma))\right). \tag{9.36}$$

A χ^2 distribution can be constructed to account for systematic uncertainties in the following way:

$$\chi^2_{syst}(\Gamma)=\frac{(\Gamma-\hat{\Gamma})^2}{\sigma^2_{syst}}. \tag{9.37}$$

The magnitude of systematic error σ_{syst} can depend on the value of Γ; σ_{syst} can be expressed as the sum of an absolute and relative component:

$$\sigma_{syst}=\sigma^{abs}_{syst}+\sigma^{rel}_{syst}\Gamma. \tag{9.38}$$

Assuming all sources of error are independent, the total systematic error is the sum in quadrature of each σ_{syst}:

$$\sigma^2_{syst}(\Gamma)=(\sigma_{abs,1}+\sigma_{rel,1}\Gamma)^2+(\sigma_{abs,2}+\sigma_{rel,2}\Gamma)^2+... \tag{9.39}$$

A total χ^2_{tot} distribution, containing both statistical and systematic uncertainties, can be constructed by

$$\frac{1}{\chi^2_{tot}}=\frac{1}{\chi^2_{stat}}+\frac{1}{\chi^2_{syst}}. \tag{9.40}$$

A new profile negative log likelihood can be constructed using χ^2_{tot}:

$$\mathcal{P}(\Gamma)=\frac{1}{2}\chi^2_{tot}; \tag{9.41}$$

this function can be integrated and used to obtain a new lower limit for $T_{2\nu}^{1/2}$, accounting also for systematic uncertainties.

Systematic uncertainty sources

The main sources of systematics are the energy resolution and the efficiency; the impact of fit bias and calibration uncertainty[1] was tested, but was found to be completely negligible.

For each of the considered systematic error sources, the two components of σ_{syst} (equation 9.38) are obtained with the following procedure:

1. start with the parameters obtained by the best fit;
2. the parameter under investigation is modified by 1σ;
3. toy MC spectra are generated, using the best fit background parameters $\boldsymbol{p}$ and adding a simulated signal in the range $\Gamma_{\beta\beta} \in [0, 2 \cdot 10^{-22}]$ y^{-1};
4. the simulated spectra are fitted assuming the unmodified parameter under investigation.

For each systematic error source, the distribution of $\hat{\Gamma}_{MC}$ vs. the expected value of Γ is fitted with a first degree polynomial to obtain the values of σ_{syst}^{abs} and σ_{syst}^{rel}. When testing for fit bias the procedure is identical, but no parameter is modified. An example of the results for the fit bias toy MC is shown in figure 9.14.

Table 9.11 reports the values of the absolute and relative components of the systematic uncertainty for the most relevant sources.

Systematic source	σ_{syst}^{abs} $(10^{-24}y)$	σ_{syst}^{rel}
Fit bias	-	-
Calibration uncertainty	-	-
Energy resolution	0.029	0.41%
Efficiency	0.084	0.82%

Table 9.11: Absolute and relative components of the main sources of systematic errors for the $2\nu\beta\beta_{0+}$ analysis. The contribution from fit bias and calibration uncertainty is completely negligible, as both components of σ_{syst} are compatible with 0 within 1σ.

[1] The difference between the measured and expected energy in the γ region, which amounts to less than 0.2 keV in CUORE-0 on average.

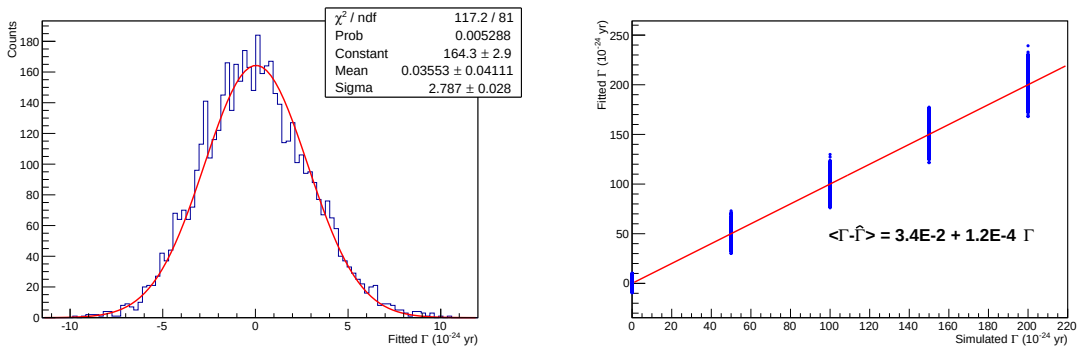

(1) $N_{ev} = 20$ (2) $N_{ev} = 200$

Figure 9.14: *Left*: distribution of fitted Γ for 5000 toy MC, obtained from the bias test with the simulated $\Gamma = 0$. *Right*: fitted vs. simulated Γ for the bias test. Both the parameters of the linear fit are compatible with 0 within 1 σ.

9.4.5 Combination with Cuoricino

Only three scenarios were considered for the $2\nu\beta\beta_{0+}$ analysis in Cuoricino, corresponding to scenarios #4, 5 and 6 from table 9.1. The procedure used to obtain the lower limit for the half-life of this process is similar to the one described in this thesis, involving an UEML fit of the spectra associated to the three selected scenarios. The obtained limit was

$$T_{1/2}^{2\nu,Cino} > 1.3 \cdot 10^{23} y [66]. \tag{9.42}$$

In order to combine this with what obtained in CUORE-0, the likelihood function obtained from the Cuoricino analysis is needed. Even tough the likelihood is not reported in the published paper, it is contained in an internal note from the Cuoricino collaboration, describing the analysis process in detail [68]. The plots are only available as an image, so they have been digitized in order to extract information from them. The likelihood functions from the three considered scenarios, as well as the combined likelihood, are shown in figure 9.15. The lower limit on $T_{1/2}^{2\nu}$ which comes from this combined likelihood is the same as the published one ($1.3 \cdot 10^{23}$ y).

The combination of the Cuoricino and CUORE-0 likelihood functions, with and without the effect of the CUORE-0 systematics, is shown in figure 9.16. With this combination, the limit on $2\nu\beta\beta_{0+}$ becomes

$$T_{1/2}^{2\nu} > 2.19 \cdot 10^{23} y \tag{9.43}$$

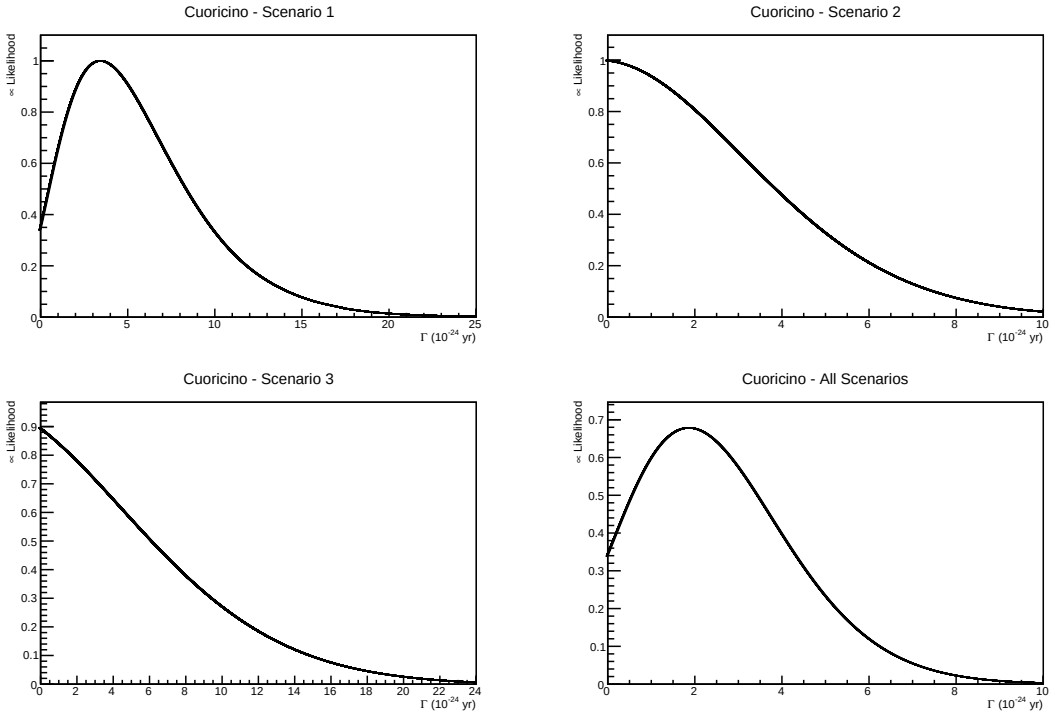

Figure 9.15: Likelihood obtained in Cuoricino on the three considered signatures and combination of the three, as a function of $\Gamma^{2\nu}_{\beta\beta}$. The first three plots are obtained by digitizing plots found in a Cuoricino internal note [CinoNote].

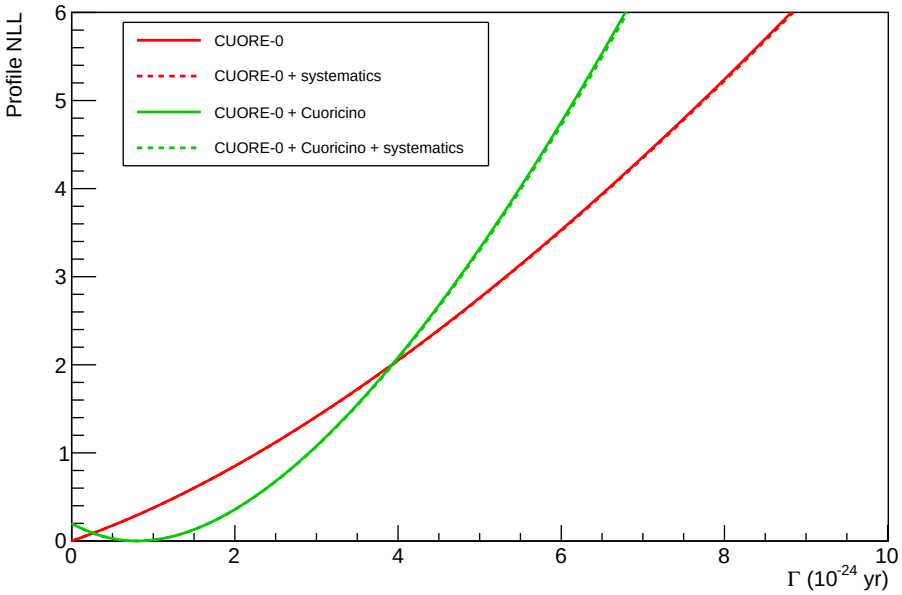

Figure 9.16: Profile NLL for the $2\nu\beta\beta_{0+}$ decay, for CUORE-0 and for the combination with Cuoricino, with (dashed line) and without (full line) systematic errors.

9.5 Final Results

The lower limit for the half-life of the $0\nu\beta\beta_{0+}$ decay obtained in CUORE-0, considering statistical and systematic uncertainties, is

$$\boxed{T^{0\nu}_{1/2} > 5.44 \cdot 10^{23} y \qquad \text{(CUORE-0)}}. \tag{9.44}$$

This result is worse than the one obtained in Cuoricino, due simply to the lower exposure accumulated in CUORE-0. The two limits can, however, be easily combined:

$$\boxed{T^{0\nu}_{1/2} > 1.48 \cdot 10^{24} y \qquad \text{(CUORE-0 + Cuoricino)}}; \tag{9.45}$$

this is the most stringent limit currently available for this process. For the two-neutrino channel, the lower limit on half-life obtained in CUORE-0, considering both statistical and systematic uncertainties, is

$$\boxed{T^{2\nu}_{1/2} > 1.85 \cdot 10^{23} y \qquad \text{(CUORE-0)}}. \tag{9.46}$$

This limit is better than the Cuoricino one, thanks to the improved analysis techniques. The combination of the two results yields an even better limit:

$$\boxed{T^{2\nu}_{1/2} > 2.19 \cdot 10^{23} y \qquad \text{(CUORE-0 + Cuoricino)}}; \tag{9.47}$$

this is the most stringent limit in the $2\nu\beta\beta_{0+}$ decay of ^{130}Te.

BIBLIOGRAPHY

[1] J. Davis, Raymond, D. S. Harmer, and K. C. Hoffman, Phys. Rev. Lett., vol. 20, pp. 12051209, 1968

[2] J. N. Bahcall, M. H. Pinsonneault, and S. Basu, Astrophys. J., vol. 555, pp. 9901012, 2001

[3] J. N. Abdurashitov et al., Phys. Rev., vol. C60, p. 055801, 1999

[4] M. Altmann et al., Phys. Lett., vol. B616, pp. 174190, 2005

[5] S. Fukuda et al., Phys. Rev. Lett., vol. 86, pp. 56515655, 2001

[6] J. Christensen-Dalsgaard and W. Dappen, Astronomy and Astrophysics Reviews, 4, p 267, 1992

[7] K. G. Librecht and M. F. Woodard, Science, 253, p 152, 1992

[8] Q. R. Ahmad et al., Phys. Rev. Lett., vol. 89, p. 011301, 2002

[9] C. Kraus et al., Eur. Phys. J., vol. C40, pp. 447468, 2005

[10] V. M. Lobashev et al., Nucl. Phys. Proc. Suppl., vol. 91, pp. 280286, 2001

[11] G. Drexlin, Nucl. Phys. Proc. Suppl., vol. 145, pp. 263267, 2005

[12] Alpert, B., Balata, M., Bennett, D. et al. Eur. Phys. J. C (2015) 75: 112, 2015

[13] S. DellOro, S. Marcocci, M. Viel, and F. Vissani, Advances in High Energy Physics, vol. 2016, Article ID 2162659, 2016

[14] S. Di Domizio, *Search for double beta decay to excited states with Cuoricino and data acquisition system for CUORE*, PhD thesis

[15] R. Arnold et al. (NEMO-3 Collaboration) Phys. Rev. D 93, 112008, 2016

[16] C. Patrignani et al. (Particle Data Group). Chin. Phys. C, 40(10): 100001, 2016

[17] C. Alduino, K. Alfonso, D. R. Artusa et al. Eur. Phys. J. C, 77: 13, 2016

[18] R. N. Mohapatra and P. B. Pal, *Massive Neutrinos in Physics and Astrophysics*, World Scientific, 3rd ed., 2004

[19] J. Schechter and J. W. F. Valle, Phys. Rev. D 25, 2951, 1982

[20] J. Menendez, A. Poves, E. Caurier, and F. Nowacki, *Deformation and the Nuclear Matrix Elements of the Neutrinoless Double Beta Decay*, 2008

[21] I. Avignone, Frank T., S. R. Elliott, and J. Engel, Rev. Mod. Phys., vol. 80, pp. 481516, 2008

[22] K. Alfonso et al. (CUORE Collaboration) Phys. Rev. Lett. 115, 102502, 2015

[23] M. Agostini et al. (GERDA Collaboration) Phys. Rev. Lett. 111, 122503, 2013

[24] A. Gando et al. (KamLAND-Zen Collaboration) Phys. Rev. Lett. 117, 082503, 2016

[25] R. Arnold et al. (NEMO-3 Collaboration) Phys. Rev. D 89, 111101(R), 2014

[26] E. Fiorini, Phys. Rept. 307, 1998

[27] R. Ardito et al., *CUORE: a cryogenic underground observatory for rare events*, hep-ex/0501010, 2005

[28] D. R. Artusa et al. (CUORE collaboration), Adv. High Energy Phys. 2015, 879871, 2015

[29] E. Andreotti et al. (Cuoricino collaboration), Astroparticle Physics, vol.34, issue 11, 2011

[30] M. Redshaw, B. J. Mount, E. G. Myers and F. T. Avignone, III, Phys. Rev. Lett. 102, 2009

[31] N.D. Scielzo et al., Phys. Rev. C 80, 2009

[32] S. Rahaman et al., Phys. Lett. B 703, 2011

[33] A. Alessandrello et al., Phys. Lett. B 335, 519, 1994

[34] A. Alessandrello et al., Nucl.Phys. B (proc. suppl.) 48, 238, 1996

[35] A. Alessandrello et al., Phys. Lett. B 433, 156, 1998

[36] C. Arnaboldi, et al., Phys. Lett. B 557, 167, 2003

[37] C. Enss and D. McCammon, J. Low Temp. Phys. 151, 2008

[38] C. Alduino et al. (CUORE collaboration), Journal of Instrumentation, vol.11, 2016

[39] C. Kittel, *Introduction to Solid State Physics* (Wiley, 2004), 8 ed.

[40] M. Barucci, C. Brofferio, A.Giuliani et al., J. Low Temp. Phys. 123 (5-6), 303, 2001

[41] P. W. Anderson, phys. Rev. 109, 1492, 1958

[42] N. F. Mott and W. D. Twose, Adv. Phys. 10, 107, 1961

[43] A. L. Efros and B. I. Shklovskii, J. Phys. C 8 L49, 1975

[44] M. Clemenza, A. Borio di Tigliole, E. Previtali and A. Salvini, AIP Conf. Proc. 1338, 37, 2011

[45] M. Ambrosio et al. (MACRO collaboration), Phys. Rev. D 52, 3793, 1995

[46] F. Arneodo et al., Nuovo Cim. A 112, 819, 1999

[47] S. Pirro et al., Nucl. Instrum. Meth. A 444, 331, 2000

[48] A. Alessandrello et al., Nucl. Instrum. Meth. B 142, 163, 1998

[49] A. D. Bryant, *A Search for Neutrinoless Double Beta Decay of 130Te*, Ph.D. thesis

[50] M. A. Carrettoni, *Data Analysis For Neutrinoless Double Beta Decay*, Ph.D. thesis

[51] E. Gatti and P. Manfredi, La Rivista del Nuovo Cimento, 9, 1, 1986

[52] A. Alessandrello et al., Nucl. Instr. Meth. A 412, 454, 1998

[53] M. Vignati, *Model of the Response Function of the CUORE Bolometers*, Ph.D. thesis

[54] S. Agostinelli et al., Nucl. Instr. Meth. A, vol. 506, no. 3, pp. 250-303, 2003

[55] F.Boehm and P.Vogel, *Physics of Massive Neutrinos*, Cambridge University Press, 1992

[56] J. Kotila and F. Iachello, Phys. Rev. C 85, 034316, 2012

[57] M.Aglietta et al., Phys. Rev. D 58, 092005, 1998

[58] S. Ahlen et al., MACRO Coll., Astrophys. J. 412, 412, 1993

[59] C. Tomei, *Coincidences with response synchronization in Diana*, CUORE internal note

[60] C. Alduino et al. (CUORE Collaboration) Phys. Rev. C 93, 045503, 2016

[61] C. Bucci et al., Eur. Phys. J. A 41, 155, 2009

[62] E. Andreotti et al. (Cuoricino Collaboration), Astropart. Phys. 34, 18, 2010

[63] A. Gelman et al., *Bayesian Data Analysis*, Chapman and Hall/CRC, 2004

[64] M. Plummer, *JAGS Version 3.3.0 User Manual*, 2012

[65] F. James, *Statistical Methods in Experimental Physics*, 2nd ed., World Scientific, 2006

[66] E. Andreotti et al. Phys. Rev. C 85, 045503, 2012

[67] J. L. Ouellet, *The Search for* $0\nu\beta\beta$ *Decay in* ^{130}*Te with CUORE-0*, Ph.D. thesis

[68] S. Di Domizio, C. Martinez, *CUORICINO results for double beta decay to excited states*, CUORE internal note